Millimeter Studies of Nearby Debris Disks

A dissertation presented

by

Meredith Ann MacGregor

to

The Department of Astronomy

in partial fulfillment of the requirements

for the degree of

Doctor of Philosophy

in the subject of

Astronomy & Astrophysics

Harvard University

Cambridge, Massachusetts

March 2017

Dissertation Advisor: Dr. David J. Wilner Meredith Ann MacGregor

Millimeter Studies of Nearby Debris Disks

Abstract

At least 20% of nearby main sequence stars are known to be surrounded by disks of dusty material resulting from the collisional erosion of planetesimals, similar to asteroids and comets in our own Solar System. The material in these 'debris disks' is directly linked to the larger bodies, like planets, in the system through collisions and gravitational perturbations. Observations at millimeter wavelengths are especially critical to our understanding of these systems, since the large grains that dominate emission at these long wavelengths reliably trace the underlying planetesimal distribution. In this thesis, I have used state-of-the-art observations at millimeter wavelengths to address three related questions concerning debris disks and planetary system evolution: 1) How are wide-separation, substellar companions formed? 2) What is the physical nature of the collisional process in debris disks? And, 3) Can the structure and morphology of debris disks provide probes of planet formation and subsequent dynamical evolution? Using ALMA observations of GQ Lup, a pre-main sequence system with a wide-separation, substellar companion, I have placed constraints on the mass of a circumplanetary disk around the companion, informing formation scenarios for this and other similar systems (Chapter 2). I obtained observations of a sample of fifteen debris disks with both the VLA and ATCA at centimeter wavelengths, and robustly determined the millimeter spectral index of each disk and thus the slope of the grain size distribution, providing the first observational test of collision models of debris disks (Chapter 3). By applying

an MCMC modeling framework to resolved millimeter observations with ALMA and SMA, I have placed the first constraints on the position, width, surface density gradient, and any asymmetric structure of the AU Mic, HD 15115, ϵ Eridani, τ Ceti, and Fomalhaut debris disks (Chapters 4–8). These observations of individual systems hint at trends in disk structure and dynamics, which can be explored further with a comparative study of a sample of the eight brightest debris disks around Sun-like stars within 20 pc (Chapter 9). This body of work has yielded the first resolved images of notable debris disks at millimeter wavelengths, and complements other ground- and space-based observations by providing constraints on these systems with uniquely high angular resolution and wavelength coverage. Together these results provide a foundation to investigate the dynamical evolution of planetary systems through multi-wavelength observations of debris disks.

Contents

List of Figures

List of Tables

Acknowledgments

A few pages of text can never fully express my gratitude to all of the people that have supported me over the past six years. Nobody ever said that getting a Ph.D. was easy. But, it would have been much harder without the support of my family, friends, and collaborators. Thank you to everybody that has helped me out along the way. I am immensely grateful.

When I began graduate school, I had never spent much time thinking about circumstellar disks. I arrived at Harvard in September 2011 knowing that I wanted to do something involving 'radio astronomy' and started emailing potential advisors. I feel very lucky that David Wilner was among the list of people I emailed. And, I feel even luckier that he decided to meet with me and discuss potential Research Exam projects. I spent some time looking back through my past notebooks and emails while compiling this thesis. It took me less than a week after my first meeting with David to decide that I wanted to work with him. A day after making that decision, he informed me that we would be receiving data in the first observing cycle of ALMA. Since that day, I have not regretted my decision for a minute. I have never wanted for access to data, attention, or resources throughout my entire time in graduate school. That is saying something, considering the many terabytes of disk space required to store all of the datasets that have gone into this thesis! David's guidance has helped me navigate scientific research as well as scientific politics. I have grown as a scientist and become an independent researcher, without fully realizing at the time that this transition had occurred. Thank you, David, for all of your wisdom and advice.

A special thank you is needed for the members of my thesis advisory committee: Sean Andrews, Scott Kenyon, Jim Moran, and Karin Öberg. All of you have taken time out of your schedules to meet with me every six months for the last several years. Each of these meetings has helped move my thesis forward and guided the direction of my research. I especially want to thank all of you for your advice and mentorship during the job application process this past fall. Please know that I carefully considered all of your comments and thoughts, and that they helped me obtain a position I am excited to have accepted. Sean, an extra thank you for skillfully responding to my emails about `CASA` and the oddities of visibility weights. Jim, thank you for providing me with a foundation in interferometry that I could never have obtained anywhere else. Thank you also to Aaron Boley, for joining my thesis committee as my external examiner. I am happy to have this opportunity to learn from you and build on our collaboration.

I have been very fortunate to have had many other mentors and teachers throughout graduate school. John Huchra taught my first course in astronomy, inspiring me to pursue a career in this field. Edo Berger mentored me through my first extended research project during my undergraduate career at Harvard, and has continued to provide career advice throughout graduate school. Philip Sadler opened my eyes to science education, and has made me a far better educator than I ever realized was possible. Steve Cranmer taught me my first course in stellar physics, and has answered every email I have sent him about stars ever since. Alyssa Goodman started off as my department advisor while I was an undergraduate, became my professor in graduate school, and has enabled my outreach activities by introducing me to WorldWide Telescope.

None of the research presented in this thesis would be possible without the hard work and insight of my collaborators. Thank you to Sarah Maddison for inviting me to visit Australia. I learned a tremendous amount in those few short weeks, and I look forward to our future collaborations. Thank you to Claire Chandler for working with me every time that I visited NRAO in Socorro. I could not have learned how to reduce and analyze VLA data from a better person. Thank you to Brenda Matthews for giving me access to the ALMA τ Ceti data, and letting me run with the modeling and the analysis. Thank you to Paul Kalas for initiating the ALMA Fomalhaut project. I have learned so much from your expertise. And, thank you to Meredith Hughes for beginning the 'Meredith Dynasty' that I have been proud to join.

Over the last few years, we have built up quite a 'Disk Group' at the CfA. In fact, we have gained so many members that we have had to move to a much larger conference room! Our Friday meetings are always entertaining, full of new criticisms of `CASA`. I am willing to bet that our group is singlehandedly responsible for the majority of `CASA` Helpdesk tickets. Thank you to all of the 'Disk Group' members past and present for friendship and helpful discussions, and a special thank you to Ilse Cleeves, Ian Czekala, Viviana Guzman, Jane Huang, Ryan Loomis, Charlie Qi, Luca Ricci, and Katherine Rosenfeld.

Of course all of the mentorship and hard work in the world, would not make graduate school run smoothly without the help of the department administrators who actually make things happen. I am grateful to all of the CfA computing and building staff for making my life easier over the last six years. I could not have managed several months of navigating the CfA on crutches without your kindness. And, a special thank you to Peg Herlihy, Muriel Hodges, and Robb Scholten.

I also want to thank my many friends and fellow graduate students for helping to maintain my mental sanity. I have truly enjoyed my time with all of the graduate students at Harvard. We have a wonderful community here that I believe is quite special. That being said, I want to especially call out Kate Alexander, Aaron Bray, Jason Dittmann, Courtney Dressing, Doug Ferrer, Kirit Karkare, Elisabeth Newton, Ana Maria Piso, Sukrit Ranjan, Laura Schaefer, Anjali Tripathi, Sarah Wellons, Lauren Woolsey, and all of the members of 'Scotch Hour' for making my day-to-day life at the CfA fun. And, than you to Amy Rosenthal, Kelly Brock, Meryl Federman, Alex Isakov, Tomo Lazovich, Kimberly Murdaugh, Kelly Perron, Ellen Putnam, and Susan Wang for making life *outside* of the CfA fun. Finally, thank you to Dawn Graninger for being the best officemate in existence. I am not sure how I would have survived this last year of graduate school without having you around to vent to, celebrate successes with, and share thesis formatting tips with.

Last, but in no way least, I want to thank my family for all of their love and support. My parents have been one of the most important influences on my life and my pursuit of a career in science. Thank you, Mom and Dad, for encouraging me in everything that I have done, even when it involved mummifying hotdogs in the kitchen (I hope those are finally all gone from the basement!). I would never be where I am today without your love and tireless support for my education. I will continue to appreciate your advice and insights moving forward in my career, and I will always try and 'Use my brain.' My fiancé, Jake Connors, has been an endless source of love and encouragement. I feel incredibly lucky that I met you at the beginning of graduate school, and that you have stuck through this long journey with me. Late nights and take-out food would be considerably less fun without someone

to share the experience with. Our adventures in the mountains have provided a much needed distraction from the daily grind of graduate school. I am proud to say that we will both have gotten a Ph.D. and climbed all 48 of the 4000-footers in New Hampshire when we leave Boston. How many people can say that?! Thank you for being my best friend, and always looking out for my mental and physical well-being.

In short, this thesis is a testament to all of the wonderful people in my life. Thank you for all of your collective support and encouragement!

For my family

1

Introduction

At least 20% of nearby main sequence stars are surrounded by disks of dusty material. In the currently accepted picture of these 'debris disks', planetesimals, similar to comets or asteroids in our own Solar System, are continually ground down through collisions. The resulting dust can be observed via scattered light at visible to near-infrared wavelengths or thermal emission at mid-infrared to millimeter wavelengths. Since the dust-producing planetesimals are expected to persist in stable regions like belts and resonances, the locations, morphologies, and physical properties of dust in these disks provide probes of planet formation and the subsequent dynamical evolution of planetary systems. Of key interest to the broader scientific community is the possibility to probe for wide-separation, Neptune-like planets in exoplanetary systems through the observable signatures they imprint on extrasolar debris disks.

New observational capabilities offer exciting opportunities to further the study of circumstellar disks, particularly debris disks, and their connection to planetary systems. For the past five years, the Atacama Large Millimeter/submillimeter Array

(ALMA) has more than doubled the number of debris disks that have been resolved at millimeter wavelengths with unprecedented resolution and sensitivity. In this thesis, we make use of these new observational capabilities to explore the debris disk phenomenon from several related angles. To shed light on the ongoing collisional processes within debris disks, we have used long wavelength observations to place the first constraints on the size distribution of grains in the disk, informing future theoretical and analytical work. This thesis also aims to enhance our understanding of the mechanisms that shape debris disk structure. To this end, we have used ALMA and other millimeter interferometers to resolve the structure of several notable, nearby debris disks around stars with spectral types ranging from A through M. These observations of individual systems hint at large-scale trends in disk structure and dynamics, and provide a starting point for future observations of a larger sample at both millimeter and complementary wavelengths.

This introductory chapter begins in Section 1.1 with an overview of circumstellar disk evolution from cloud collapse to the formation of mature planetary systems. In Sections 1.2 and 1.3, we discuss the properties of debris disks in our own Solar System and in extrasolar systems. Section 1.4 presents the current theoretical framework for understanding collisional processes in debris disks. Section 1.5 makes the case for why millimeter interferometry is critically important for studying the structure of debris disk systems. Finally, in Section 1.6, we outline the main questions that this thesis addresses and the work that has been done to answer those questions.

1.1 Circumstellar Disk Evolution

It is helpful to consider debris disks within the larger evolutionary sequence of circumstellar disks. The primary sites of star (and ultimately planet) formation are giant molecular cloud (GMC) complexes (Figure 1.1, top). These complexes can contain $> 10^4$ $M_\odot$ (e.g. Blitz 1993; McKee & Ostriker 2007) of gas and dust and are self-gravitating, partially supported by turbulence and/or internal magnetic pressure. These low density ($n_{H_2} \sim 10^2$ cm^{-2}) molecular clouds are inhomogeneous, exhibiting a hierarchical structure. Overdense regions within GMCs are termed 'clumps' with a characteristic density of $n_{H_2} \sim 10^2 - 10^4$ cm^{-2} (Williams et al. 2000). At smaller scales are gravitationally bound, dense 'cores' ($n_{H_2} \sim 10^4 - 10^6$ cm^{-2}) out of which individual (or multiple) stars form. In reality, the structure of molecular clouds is even more complex, broken into intricate filaments (e.g. Jackson et al. 2010; Ward-Thompson et al. 2010), in which the dense cores are embedded.

The eventual collapse of the dense cores signals the onset of star formation. The initial rotation of the collapsing core and the conservation of angular momentum naturally forms a disk surrounding the central protostar (Figure 1.1, right). In a typical system, the central protostar has a mass of $\sim 0.1 - 1.0$ $M_\odot$ and is surrounded by a toroidal disk with mass $0.01 - 0.1$ $M_\odot$. After collapse, the remaining envelope continues to fall onto the disk, and fuels accretion onto the protostar and a central jet. This phase of evolution is expected to last for $\sim 10^5 - 10^6$ years (e.g. Dunham et al. 2014, and references therein), after which the envelope dissipates leaving behind a pre-main sequence star and circumstellar disk.

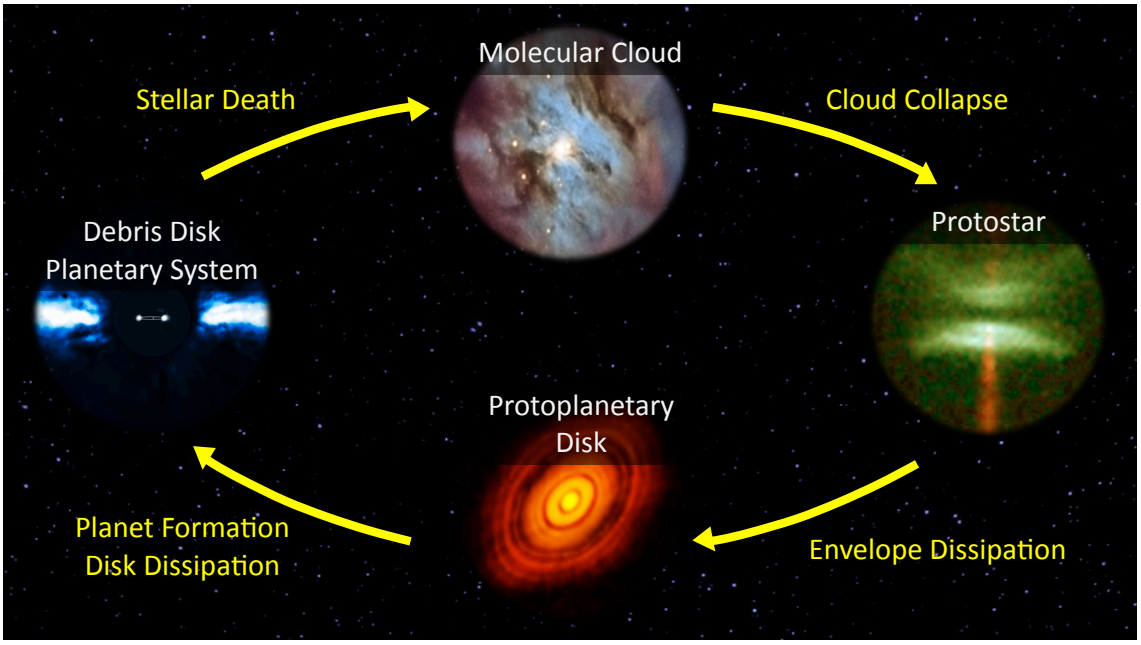

Figure 1.1: Illustration of the cycle of star formation and circumstellar disk evolution. Dense cores within a Giant Molecular Cloud complex *(top)* collapse to form a young protostar embedded in a surrounding envelope *(right)*. The envelope dissipates to leave a star and protoplanetary disk *(bottom)* from which planets form. After $\sim 1-10$ Myr, there is rapid clearing of disk material at all radii leaving behind a main sequence star, planetary system, and debris disk of remnant planetesimals *(left)*. When the star ultimately dies, it replenishes the interstellar medium with heavy elements that will become the building blocks for the next generation of stars and planets.

After the protostellar phase, the remaining 'protoplanetary disk' (Figure 1.1, bottom) retains about $1-10\%$ the mass of the central star in gas and dust, enough material to form giant planets. Indeed, for a Solar mass star, the disk contains enough material to form $\sim 10-100$ Jupiter-mass planets, if planet formation were 100-percent efficient. Protoplanetary disks evolve through a number of processes, including viscous transport, photoevaporation, grain growth, dust settling, and dynamical interactions with (sub)stellar and planetary-mass companions (e.g. Williams & Cieza 2011, and references therein). The amount of gas and small

grains in the disk decreases slowly at first, followed by a rapid clearing of material at all radii. For low and intermediate mass systems, the expected lifetime of the protoplanetary disk is $\sim 1 - 10$ Myr (e.g. Mamajek 2009), defining the timescale available for giant planet formation. This abrupt decrease in circumstellar disk mass at ~ 10 Myr is evident in Figure 1.2; older systems have disk masses several orders of magnitude less than younger systems.

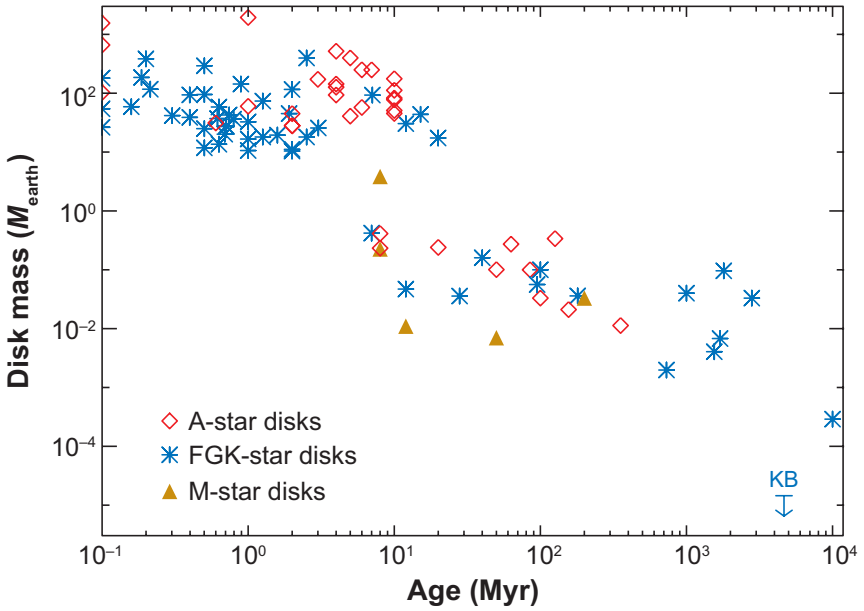

Figure 1.2: Evolution of circumstellar disk mass as derived from (sub)millimeter observations taken from Wyatt (2008). The population of protoplanetary disks is evident on the upper left with dust masses of ~ 100 $M_\oplus$, implying a total disk mass of > 30 $M_{\rm Jup}$ for a gas-to-dust ratio of 100. At ~ 10 Myr, there is a rapid decrease in disk mass of several orders of magnitude to the debris disks shown on the lower right. An upper limit on the dust mass of the Kuiper Belt of $< 10^{-5}$ $M_\oplus$ is included in the lower right corner (Moro-Martín & Malhotra 2003). According to the Nice model (e.g. Gomes et al. 2005), both the Asteroid and Kuiper Belts likely contained significantly more mass early in the Solar System's history, which was lost during the outward migration of the giant planets.

An intermediate stage of circumstellar disk evolution is defined where disks have

properties between protoplanetary and debris disks, exhibiting substantial clearings of gas and/or dust. These 'transition disks' were originally classified as objects with no excess emission (emission above the expected stellar flux) at wavelengths shorter than 10 μm and significant excesses longwards of 10 μm (e.g. Strom et al. 1989). The absence of a near-infrared excess was interpreted as a sign of clearing in the inner disk possibly due to early planet formation. In nearby star forming regions, $\sim 10-20\%$ of disks exhibit dips in their spectral energy distributions at near- to mid-infrared wavelengths (e.g. Currie & Kenyon 2009; Dahm & Carpenter 2009). However, these same systems show a range of physical properties including disk mass, accretion rate, and inner cavity size. This apparent variety suggests that a range of mechanisms is likely at play in the disk clearing phase.

The protoplanetary disk will disperse and accretion onto the central star will cease completely by the time the star reaches its main sequence phase. At this point, the main sequence star may be surrounded by any planets that successfully formed during the protoplanetary phase and a low-mass 'debris disk' (Figure 1.1, left). Debris disks are characterized by having dust masses of $< 0.10\ M_{\oplus}$ (see Figure 1.2) and little gas. The expected timescales to remove dust grains from a disk (through Poynting-Robertson drag, stellar winds, etc.) are shorter than the typical age of these systems. This implies that the remnant material must be second-generation rather than primordial, replenished through the collisional erosion of planetesimals, larger bodies similar to asteroids and comets in our own Solar System (see Section 1.4 for further discussion). Recent detections of CO gas in several debris disks (including the β Pictoris system, Dent et al. 2014) suggest that collisions between comet-like bodies may also generate observable amounts of gas. In addition, it is possible that

the formation of Pluto-sized bodies could continue on the inner edge of an extended planetesimal disk, initiating collisions that propagate outwards to radii of many tens of AU over Gyr timescales (Kenyon & Bromley 2002, 2008).

Finally, at the end of its main sequence lifetime, a dying Sun-like star will complete the cycle illustrated in Figure 1.1 by shedding its outer envelope and replenishing the interstellar medium (ISM) for the next generation of star formation. The evolution times of more massive (O and B-type) stars are comparable to or less than the age of the surrounding giant molecular cloud complex. As a result, these massive stars may interact with the cloud over their lifecycle in such a way (i.e. through shocks) that they trigger subsequent, sequential bursts of star formation (e.g. Elmegreen & Lada 1977).

1.2 Debris Disks in the Solar System

We know that our Solar System formed 4.6 billion years ago through a similar pathway as described in Section 1.1. However, the specifics of the Solar System's evolution are still hotly debated, particularly within the first Gyr when the planetary system was settling into its final configuration. Today, the Sun is surrounded not only by planets, but also by a large quantity of debris. These smaller bodies range in scale from submicron-sized dust to larger objects 1000's of km in size, and are concentrated into two debris disks, the Asteroid Belt between $2 - 3.5$ AU and the Kuiper Belt between $30 - 48$ AU. By studying the structure and composition of these two debris disks, we can find clues to the early evolution of the Solar System. In the future, observations of debris disks around other nearby main sequence stars

may help us better identify the role that planets have played in their dynamical evolution, and perhaps gain insights into the history of our own planetary system.

Recent observations have provided a number of constraints on the position, mass, size distribution, and even density of debris in the Solar System. The bulk of the main classical Kuiper Belt (Figure 1.3) appears radially confined between the 3:2 and 2:1 resonances with Neptune at 40 and 48 AU, respectively (e.g. Jewitt & Luu 2000; Hahn & Malhotra 2005; Bannister et al. 2015). Even Pluto, the largest known Kuiper Belt Object (KBO) is bound into the 3:2 resonance. The implied fractional width (defined as the width of the belt divided by its radial position) of the Kuiper Belt is only ~ 0.18, very narrow compared to observations of other systems. Both the Asteroid and Kuiper Belts are relatively 'mass poor.' Today, the main Asteroid Belt contains $\sim 5 \times 10^{-4}$ $M_\oplus$ of material (Bottke et al. 2005). The Kuiper Belt has a dust mass of only $\sim 10^{-5}$ $M_\oplus$ (see Figure 1.3, Moro-Martín & Malhotra 2003). Cratering records from the Moon and other planets provide important constraints on the typical sizes of debris in the Solar System (e.g. Halliday & Kleine 2006; Bottke et al. 2005; Morbidelli et al. 2008). The size distribution of KBOs is well determined for bodies larger than ~ 100 km (e.g. Gladman et al. 1998) to be a power law, $n(r) \propto r^{-4}$. For smaller KBOs (< 70 km in size) this power law flattens with an index of ~ -2.5 (Bernstein et al. 2004). This observed break is predicted theoretically for collisions between objects that are more like 'rubble piles' than solid rocks (Pan & Sari 2005). Indeed, observations of individual KBOs constrain their density to be close to 1 g cm^{-3}, indicative of low material strength for cosmochemically plausible rock to ice mass ratios (Jewitt & Sheppard 2002).

These observational constraints on the structure of the debris disks in the Solar

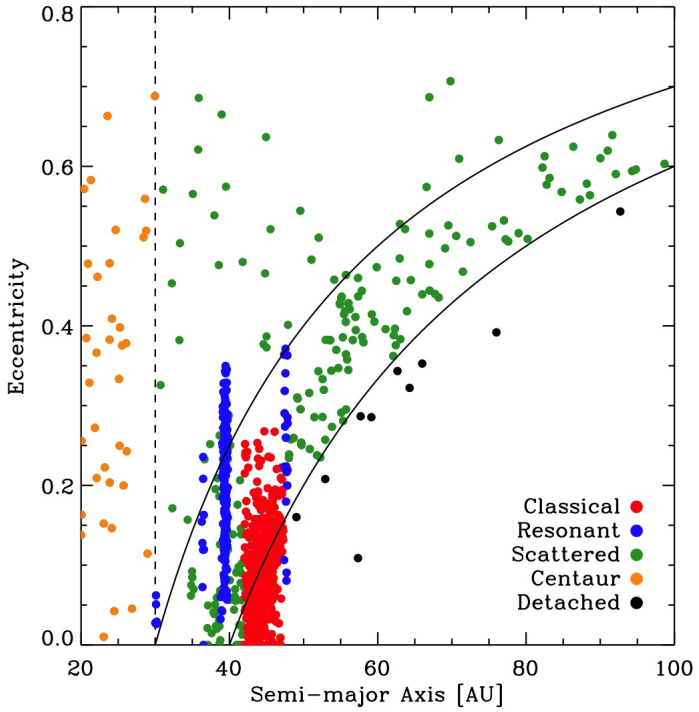

Figure 1.3: Observed distribution of Kuiper Belt Objects (KBOs) from David Jewitt (e.g. Jewitt & Luu 2000). The orbit of Neptune is indicated by the vertical dashed line. Objects in red are members of the main classical Kuiper Belt. Objects in blue are in resonances with Neptune. The two most populated bands of blue on either side of the classical belt correspond to the 2:1 and 3:2 resonances. Pluto is included in the population of 3:2 resonance objects.

System have informed our understanding of their past history and evolution. Both the Asteroid and Kuiper Belts likely contained significantly more mass early in the Solar System's history (Stern 1996; O'Brien et al. 2007, and references therein). Indeed, the current mass of the Kuiper Belt is several orders of magnitude below the masses of detected extrasolar debris disks (see Figure 1.2, Wyatt 2008). In the Nice model of the Solar System (Gomes et al. 2005; Morbidelli et al. 2005; Tsiganis et al. 2005), the outward migration of the giant planets from an initially compact configuration and the ensuing instability resulted in a significant depletion of mass

in the Kuiper Belt. After hundreds of Myrs of gradual migration, Jupiter and Saturn crossed their mutual 1:2 mean motion resonance, and Saturn was shifted outwards toward its current position. This relocation propelled Uranus and Neptune into more eccentric orbits, and as a result, ejected many planetesimals outwards, changing their orbits through exchange of angular momentum. As Neptune's orbit moved outwards, its mean motion resonances passed through the surrounding planetesimal disk and swept up objects to produce the concentrated main belt we see today. The history of the Solar System is also thought to have been punctuated by events that significantly altered the debris population, including collisions between protoplanets or asteroids (Nesvorný et al. 2003). For example, during the period of 'Late Heavy Bombardment,' an increased number of collisions between asteroids and protoplanets could have significantly changed the size distribution and composition of local debris belt bodies (Canup 2004).

1.3 Extrasolar Debris Disks

The first extrasolar debris disk was discovered by the *Infrared Astronomical Satellite* (*IRAS*) around Vega as infrared emission in excess of predictions for a stellar photosphere alone (Aumann et al. 1984). This excess emission was attributed to thermal emission from dust grains orbiting the star in a circumstellar disk. *IRAS* detected similar excesses around $\sim 15\%$ of main sequence stars (Aumann 1985). Subsequent infrared surveys have been conducted with both *Spitzer* and *Herschel*. The amount of dust in a debris disk is commonly quantified by the fractional luminosity, $f_d = L_{\rm dust}/L_{\rm star}$, calculated assuming that the disk is a pure or modified

blackbody. For typical debris disk systems, $f_d \sim 10^{-3} - 10^{-6}$, with a decrease towards older systems albeit with large dispersion (e.g. Hillenbrand et al. 2008; Moór et al. 2011). However, no previous infrared surveys with *Spitzer* or *Herschel* have reached the sensitivity needed to detect our own Kuiper Belt, $f_d \sim 10^{-7}$ (Vitense et al. 2012), so statistics are still somewhat incomplete. For Sun-like (F, G, and K-type stars), the *Herschel* DEBRIS and DUNES surveys determine debris disk occurrence rates of 17% and 20.2%, respectively (Matthews et al. 2014; Eiroa et al. 2013). The detection rate is higher for A stars with detection rates of 33% at 70 μm (Su et al. 2006) and 25% at 100 μm (Thureau et al. 2014). This apparent difference in detection rates for A through K spectral types is, however, likely an age effect (Su et al. 2006; Trilling et al. 2008). Few debris disks are known around M-type stars, perhaps because processes are more effective at removing grains from their surrounding disks. M stars have deep convective zones that produce strong coronal magnetic fields, which generate flares and stellar winds that could dominate grain removal processes (Plavchan et al. 2005). It is also possible that the lack of known M star debris disks is due to a selection effect; the current surveys are not sensitive to the same fractional luminosity towards M stars as towards earlier spectral type stars.

Since the original *IRAS* detection in 1984, significant advances in observational astronomy from optical to radio wavelengths have enabled resolved imaging of debris disk systems (e.g. Holland et al. 1998). Compared to measurements of only the spectral energy distributions (SEDs), resolved imaging of debris disks provides meaningful constraints on the structure of these disks. At optical to near-infrared wavelengths, scattered light highlights regions where small dust grains

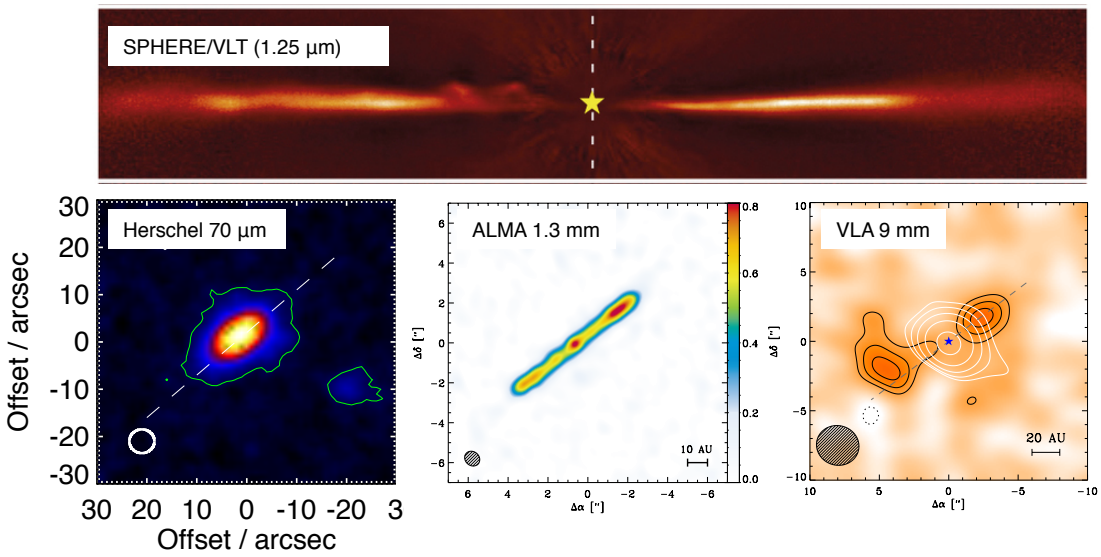

Figure 1.4: Resolved images of the AU Mic debris disk at near-infrared to radio wavelengths. *(top)* An image at 1.25 μm (J band) from SPHERE/VLT that shows five large-scale features in the southeast side of the disk at separations of $10-60$ AU moving outwards from the central star at speeds of $\sim 4-10$ km/s (Boccaletti et al. 2015). *(bottom, left)* A *Herschel* image of disk at 70 μm (Matthews et al. 2015), showing thermal emission from grains in the disk. *(bottom, middle)* A high resolution image at 1.3 mm from ALMA of the millimeter continuum emission from the disk, which traces larger grains that are less affected by stellar winds and radiation (MacGregor et al. 2013). *(bottom, right)* Emission from the disk (black contours) and star (white contours) at 9 mm as shown by the VLA (MacGregor et al. 2016b).

dominate, while longer wavelengths trace the population of larger grains. If a disk consists of multiple components, observations at different wavelengths can also probe components at different radial locations. Shorter wavelengths are ideal for detecting material closer to the star in warm Asteroid Belt analogues, while longer wavelengths trace cold Kuiper Belt analogues. With resolved observations at only one wavelength, we can constrain the radial location and width of a dust belt. Resolved imaging at multiple wavelengths can constrain the temperature structure of a disk, along with the distribution of grain sizes and their composition. Figure 1.4

illustrates the impact of multi-wavelength resolved imaging with four images of the AU Mic debris disk (23 ± 3 Myr, Mamajek & Bell 2014) at near-infrared to radio wavelengths. Each wavelength highlights different aspects of the system. Most notably, the top panel shows an image at 1.25 μm (J band) from SPHERE, the planet imaging instrument at the Very Large Telescope (VLT), which reveals five large-scale features in the southeast side of the disk at separations of $10-60$ AU that are moving outwards from the central star at speeds of $\sim 4-10$ km/s (Boccaletti et al. 2015). Proposed mechanisms for launching these 'waves' in the disk include resonances with planetary-mass objects, outflows from planets, and stellar activity, especially coronal mass ejections (CMEs). However, as of yet, no single explanation has been determined. The longer infrared, millimeter, and radio images (Matthews et al. 2015; MacGregor et al. 2013, 2016b) reveal the underlying structure of the disk (see discussion in Section 1.4 and 1.5) and significant emission from a stellar corona.

Resolved imaging has given us the first accurate measurements of the radial distribution of material in debris disks. Determinations from the spectral energy distribution (SED) alone are typically smaller due to the fact that dust grains are inefficient emiters ('gray bodies') and emit at a lower temperature than a blackbody would at the same distance from the central star (e.g. Booth et al. 2013). Many debris disks show evidence for a narrow 'birth ring' of planetesimals as the source of dusty material (see Section 1.4, e.g. Strubbe & Chiang 2006). However, a large population of debris disks are best fit by broad belt models. In the sample of nine *Herschel* resolved debris disks around A stars between $20-40$ pc, four systems are poorly fit by narrow ring models (Booth et al. 2013). Models of inner collisional depletion by Kennedy & Wyatt (2010) suggest that broad belts characterized by

rising surface density profiles may result in systems with ongoing planet formation. It could also be that some broad belts are actually made up of multiple distinct components unresolved by our current images. ALMA observations of the HD 107146 debris disk (Ricci et al. 2015a) revealed that the belt extends from 30 AU to 150 AU with a clear break at $\sim$ 70 AU. The HR 8799 system consists of both a warm inner debris disk and a cold outer disk (Su et al. 2009; Reidemeister et al. 2009) with four planets between them (Marois et al. 2008, 2010). Future resolved observations will shed further light on the apparent dichotomy of narrow and broad radial structures in debris disks.

1.4 Collisional Processes in Debris Disks

Since the dust lifetime for grains in a circumstellar disk is less than the age of the systems we observe, the dust must be continually replenished. The current theoretical model of debris disks hinges on a 'collisional cascade' in which large planetesimals leftover from the planet formation process collide with each other and grind down into smaller and smaller bodies. From an observational perspective, this collisional framework leads to testable theoretical predictions concerning the radial location and size distribution of bodies in the disk.

Both the AU Mic and β Pictoris debris disks exhibit similar midplane optical surface brightness profiles (the surface brightness of the disk as a function of radius). The inner regions of both disks have shallower slopes ($\sim r^{-1} - r^{-2}$), which steepen substantially in the outer disk ($\sim r^{-4} - r^{-5}$) near $\sim$ 35 AU and $\sim$ 100 AU for AU Mic and β Pictoris, respectively (Heap et al. 2000; Augereau et al. 2001; Krist

et al. 2005; Golimowski et al. 2006; Fitzgerald et al. 2007). Observations of these two systems led to the development of a unified framework for debris disks based on a narrow, localized belt of planetesimals, or 'birth ring,' that produces dust through a collisional cascade (Strubbe & Chiang 2006; Augereau & Beust 2006). Interior to the birth ring, small grains migrate inward and are removed from the disk by corpuscular and Poynting-Robertson (CPR) drag. Outside of the birth ring, small grains are blown out from the belt into an extended halo by stellar radiation and winds. Slightly larger grains are launched into eccentric orbits with the same periastron as the belt. The largest grains, which are minimally affected by stellar radiation/winds and drag forces, do not travel far from the belt of parent planetesimals before being ground down. Thus, grains are radially segregated in the disk according to their size, producing the characteristic scattered light profile. The confined ring of planetesimals predicted in this model is nicely analogous to the narrow Kuiper Belt in our own Solar System. One caveat, however, is that in order for such dynamics to prevail, the disk must be largely free of gas for the dust grains to not be affected by gas drag (Thébault & Augereau 2005).

Assuming conservation of mass, a steady-state collisional cascade leads to a power-law size distribution of colliding bodies of radius r within the disk, $N(r) \propto r^{1-q}$, or a combination of several such power laws with different indices for different sized grains. In this model, smaller 'bullets' shatter larger 'targets' through collisions. In essence, the total mass of bodies destroyed per unit time per logarithmic interval in radius must be size independent (Pan & Sari 2005; Pan & Schlichting 2012). Under these conditions,

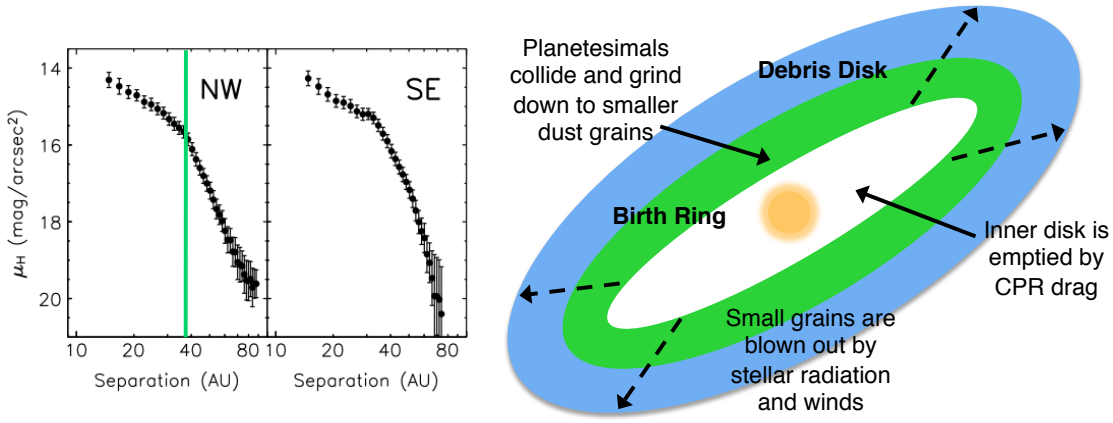

Figure 1.5: *(left)* The midplane optical surface brightness profiles of the AU Mic debris disk (Liu 2004). The break and subsequent steepening for the northwest profile beyond ~ 35 AU is indicated by the green vertical line. *(right)* A schematic of birth ring theory in the AU Mic debris disk as described by Strubbe & Chiang (2006) and Augereau & Beust (2006). Collisions between remnant planetesimals in a narrow birth ring produce smaller dust grains. Small grains within the birth ring are removed via corpuscular and Poynting-Robertson (CPR) drag. Outside of the birth ring, small grains are launched outwards by stellar winds and radiation forces. The largest grains are less affected by these forces and remain near their parent planetesimals until they are ground down through collisions.

$$\rho r^3 \times N(r) \times \frac{N(r_B(r))}{V} \times r^2 v_{\rm rel} = \text{constant}, \tag{1.1}$$

where ρ is the density of each body, $N(r)$ is the number of targets of size r, $r_B(r)$ is the size of the smallest bullet which can shatter a target of size r, V is the volume occupied by all of the bodies, and $v_{\rm rel}$ is the typical relative velocity of bullets and targets. In the simplest case, we assume that the velocity dispersion of the bodies and their distribution within the volume are independent of size. Then, by substituting $N(r) \propto r^{1-q}$, we can rewrite Equation 1.1 as

$$r^{6-q} \times r_B(r)^{1-q} = \text{constant}. \tag{1.2}$$

If we make further assumptions about the relation between the size of the bullet and the target, then Equation 1.1 dictates the slope of the grain size distribution, q.

The benchmark model of collisional cascades is presented by Dohnanyi (1969). Using laboratory experiments, Dohnanyi formulated a model of collisions in the Asteroid Belt, where bodies dominated by material strength have an isotropic velocity dispersion and collisions occur between bodies of roughly the same size, implying $r_B \propto r$. Incorporating these assumptions into the relation presented in Equation 1.2 yields

$$r^{6-q} \times r^{1-q} = r^{7-2q} = \text{constant}. \tag{1.3}$$

From Equation 1.3, we immediately recover Dohnanyi's classic result that $q = 7/2$ for a steady-state distribution.

We can alter the grain size distribution by relaxing the assumption that the bodies participating in the collisional cascade have a single velocity dispersion regardless of size (Pan & Schlichting 2012) as might be expected in a realistic disk with viscous stirring, dynamical friction, and collisional damping, or by relaxing the assumption that collisions between bodies are strength-dominated (Pan & Sari 2005). For small grains ($r < 1$ mm), non-gravitational forces further modify the size distribution. Grains smaller than some blowout size (~ 1 μm for Sun-like stars) are removed from the disk providing a natural cutoff to the size distribution (Wyatt

et al. 2011). In some models, this small-size cutoff produces waves superimposed on top of the power law grain size distribution (e.g. Campo Bagatin et al. 1994).

While many properties of collisional cascades can be obtained analytically, the accurate treatment of radiation pressure and drag forces often necessitates the use of numerical models. There are a number of numerical codes available that prioritize different aspects of the collisional cascade. N-body codes follow the trajectories of individual disk objects by numerically integrating their equations of motion and storing their instantaneous positions and velocities (e.g. Wyatt 2006; Krivov et al. 2009; Stark & Kuchner 2009; Kuchner & Stark 2010; Thébault 2012). These codes can handle an arbitrarily large array of forces, and are thus superior to other models for treating interactions with planets, gas within the disk, or the interstellar medium. Another approach is to use statistical methods that effectively replace particles with their distribution in an appropriate phase space (e.g. mass, distance, velocity) and solve equations that describe the gain and loss of objects through collisions and other physical processes at successive time steps (e.g. Kenyon & Bromley 2002, 2008; Krivov et al. 2006; Thébault & Augereau 2007; Löhne et al. 2012). Such codes are more accurate in handling collisions than N-body ones. There are also a number of hybrid codes that try to combine accurate treatments of both dynamics and collisions (e.g. Kral et al. 2013; Nesvold et al. 2013). As a whole, all of these models provide important information for the interpretation of observational results.

1.5 The Importance of Millimeter Interferometry

Radio astronomy began in 1933, when Karl Jansky detected radio emission from the Milky Way galaxy (Jansky 1933). During World War II, the development of radar and the techniques of phased arrays and antenna switching pushed the development of radio astronomy further. In 1946, Ryle & Vonberg (1946) made the first interferometric astronomical observations of the Sun using a two-element radio interferometer. Perhaps the most important step towards the modern technique of synthesis imaging came in 1962, with the realization that the Earth's rotation produces variation in the baseline lengths between a pair of antennas (Ryle 1962). The first instrument to make use of this technique was the Cambridge One-Mile Radio Telescope (Ryle et al. 1965). Following the success of this instrument, numerous radio interferometers began to make use of synthesis imaging techniques, notably including the Very Large Array (VLA) near Socorro, New Mexico (e.g. Thompson et al. 1980; Napier et al. 1983). In 2011, the VLA was upgraded to provide frequency coverage from 1 to 50 GHz, improved continuum sensitivity due to an expanded bandwidth, and a new modern correlator (e.g. Perley et al. 2011). Importantly for this thesis, the new Karl G. Jansky Very Large Array has enabled the detection of debris disks at centimeter wavelengths.

By the 1970s, both infrared and radio astronomy were making great advances, but the millimeter region of the spectrum was still unexplored. Synthesis imaging becomes more challenging at shorter millimeter wavelengths, since attenuation in the atmosphere is more significant at these wavelengths. Another large obstacle was the

lack of detectors that could respond to millimeter radiation with sufficient sensitivity for astronomical observations. The breakthrough came from Bell Labs with the development of superconducting-insulating-superconducting (SIS) devices (e.g. Wilson et al. 1970). These devices were the key to the subsequent development of heterodyne receivers for millimeter observations, and the first working example was placed on a telescope in Owens Valley in 1979 (e.g. Phillips & Woody 1982). Given these challenges, millimeter arrays were developed somewhat later during the 1980s and 1990s. Two early millimeter arrays were the Owens Valley Radio Observatory (OVRO) and the Berkeley-Illinois-Maryland Association (BIMA), which merged to form the Combined Array for Research in Millimeter-wave Astronomy (CARMA) in 2006 (e.g. Bock et al. 2006). Other notable arrays include the Nobeyama Millimeter Array completed in 1994 (e.g. Morita 1994), the Plateau de Bure Interferometer (PdBI) completed in the early 1990s (e.g. Guilloteau 1994), and the Submillimeter Array (SMA) on Mauna Kea, Hawaii completed in 2004 (e.g. Ho et al. 2004). Both the SMA and PdBI are currently being upgraded and expanded to meet the needs of new science cases. PdBI has been renamed the Northern Extended Millimeter Array (NOEMA), and is growing to include a total of twelve antennas (e.g. Chenu et al. 2016). The SMA has quadrupled the available bandwidth with the addition of the new SWARM correlator (e.g. Primiani et al. 2016), reducing the observing time required to reach the sensitivities needed for imaging faint, broad, debris belts by a factor of two.

In the last five years, the Atacama Large Millimeter/submillimeter Array (ALMA) has revolutionized millimeter interferometry (e.g. Wootten 2003). Still under construction, the full array will consist of 66 antennas, 54 of which are 12-m

in diameter. The remaining 12 antennas are slightly smaller with a diameter of 7-m and form the Atacama Compact Array (ACA) to provide shorter baselines. ALMA covers wavelengths from 0.3 mm to 3.6 mm (frequency coverage of 84 GHz to 950 GHz). Early Science began in 2011, and continues with the sixth proposal call in April 2017. ALMA has made numerous high impact science discoveries over the last five years, especially in the areas of circumstellar disk evolution and planet formation. These resolved images have revealed a wealth of detailed structure within circumstellar disks that may provide clues to the origin of planetary systems (e.g. ALMA Partnership et al. 2015; Andrews et al. 2016).

1.5.1 Millimeter Emission from Circumstellar Disks

Although circumstellar disks have been detected and resolved at wavelengths that range from optical to radio (see Section 1.3), observations at millimeter wavelengths offer a number of unique advantages. One such advantage is that the dust continuum emission from circumstellar disks at millimeter wavelengths is generally optically thin. Therefore, the observed emission traces the underlying surface density distribution of the disk. It should be noted that inferring a mass from millimeter flux measurements requires making some assumptions about the dust temperature and opacity. A typical assumption is that the dust opacity, κ_ν, is frequency-dependent with $\kappa_\nu = 10(\nu/10^{12}\ \mathrm{Hz})\ \mathrm{cm}^2\ \mathrm{g}^{-1}$ (Beckwith et al. 1990). However, this and other estimates depend strongly on the unknown grain size distribution in the disk. If the majority of mass in the disk is locked up in larger bodies, estimates of the total disk mass derived from millimeter measurements sensitive to smaller grains could

underestimate the total. Despite these complications, observations at millimeter wavelengths are the only reliable way to probe the surface density distribution in debris disks.

Observations at millimeter wavelengths are sensitive to not only thermal dust emission, but also to many rotational transitions of small molecules. In young protoplanetary disks, H_2 is thought to dominate the disk mass given the high elemental abundance of hydrogen. However, H_2 lacks a dipole moment and is therefore virtually unobservable except for a few measurements of infrared and ultraviolet lines (e.g. Beckwith et al. 1978; Brown et al. 1981). Fortunately, the next most abundant molecule, CO, is readily detectable at millimeter wavelengths. A few complications arise with observations of CO in protoplanetary disks, namely the high optical depth of many transitions that makes the observed flux density insensitive to density. In addition, when deriving a total gas mass from the CO flux density, we often assume a CO/H_2 abundance ratio comparable to that in the ISM ($\sim 10^{-4}$). Recent work (e.g. Miotello et al. 2016) suggests that a more complex analysis is required to accurately determine disk gas masses. Although protoplanetary disks have significantly higher gas content, there have been a number of recent detections of CO gas in debris disk systems (e.g. Hughes et al. 2008; Dent et al. 2014; Marino et al. 2016, Matrà et al. in prep.). The origin of gas in these older systems is still unclear. Is this material primoridial, persisting from the protoplanetary disk phase, or is it regenerated through collisions of icy, comet-like bodies? In systems such as β Pictoris (Dent et al. 2014) and 49 Ceti (Hughes et al. 2008), a secondary origin scenario is favored. However, the HD 21997 debris disk may have contributions from both primordial gas and secondary collisional material (Kóspál et al. 2013). Such

millimeter detections of CO gas in debris disks may prove critical in linking the primordial and debris stages of circumstellar disk evolution.

Millimeter wavelength observations are also ideally suited to test theoretical models of collisional processes in debris disks. A planetesimal birth ring, as described in Section 1.4, would remain hidden in optical and infrared images dominated by small grains that populate an extended halo (e.g. Su et al. 2005). To test the proposed birth ring framework of debris disks, we must turn to millimeter wavelengths. Observations at these longer wavelengths highlight thermal emission from larger grains that are less affected by stellar radiation and winds, and thus reliably trace the location of the dust-producing planetesimals (Wyatt 2006). The location of the break in the optical surface brightness profile marks the outer extent of the colliding planetesimals. Thus, this theory predicts that the radial location of the millimeter emission should match up with the position of this break as has been seen in the β Pictoris disk (Wilner et al. 2011).

1.5.2 Resolving Detailed Disk Structure

Currently, the discovery and characterization of exoplanet systems is a significant science driver for the broader scientific community. Although hundreds of planetary systems are now known, we still do not understand whether or not the architecture of the Solar System is typical. Indeed, we have yet to find another planetary system exhibiting a similar structure with inner rocky planets, outer giant planets, and both an inner warm and outer cold debris disk. Furthermore, the distributions of known exoplanet parameters are strongly affected by observational biases that are difficult

to disentangle from the true distributions. Both the transit and radial velocity (RV) techniques require long time baselines to detect planets at semi-major axes of greater than a few AU. While direct imaging is successful at detecting planets at large separations, it has difficulty in mature systems due to the low fluxes of planets after they lose much of their initial heat from formation (e.g. Spiegel & Burrows 2012).

The dust in debris disks is directly linked to the larger bodies in the system through collisions and gravitational perturbations. In particular, planets can imprint observable signatures on debris disks as dust is shepherded into long-lived belts and resonant concentrations. Thus, the resolved structure of debris disks offers a unique way to probe for wide-separation exoplanets that would otherwise remain undetectable. The perturbations a planet introduces in a debris disk can be divided into three components: secular, resonant, and scattering (Murray & Dermott 1999). Each of these perturbations can be linked to specific structures in the disk. Secular perturbations result from the long-term effect of a planet's gravity, causing disk evolution over tens of Myr before steady-state is reached. In the case of a single planet, the surrounding disk will typically align with the planet's orbit. If the planet's orbital plane is misaligned with the disk midplane, a warp is produced that propagates outwards from the disk centroid (e.g. Dawson et al. 2012). If a planet is on an eccentric orbit, it will cause the disk to become eccentric. We observe this eccentricity as an offset of the disk centroid or a brightness asymmetry between the two disk ansae (Wyatt et al. 1999). Resonant perturbations are produced at radial distances where the debris orbits the star an integer (p) number of times for every integer ($p + n$) number of planet orbits. The strongest resonance are usually first order ($n = 1$), although an infinite number of resonances are possible. It is thought

that planetary resonances may shape the inner edge of debris disks, and that there are planets hiding in the gaps observed in the debris (e.g. Faber & Quillen 2007). If a planet migrates outwards through a disk, much like Neptune swept through remnant planetesimals and shaped the Kuiper Belt in our own Solar System, it may sweep up material in its resonances producing a clumpy structure (e.g. Malhotra 1993). The observed clumpy structure could be used to pinpoint a planet's mass and location (e.g. Wyatt 2003; Chiang et al. 2009). Lastly, scattering processes involve a hyperbolic encounter between a planetesimal and a planet that imparts an impulsive change to the planetesimal's orbit. In the Solar System, comets are scattered inwards from the Kuiper Belt through interactions with the giant planets (Levison & Duncan 1997).

Structures indicative of planetary perturbations have been observed in a number of debris disk systems. In the well-known β Pictoris system, the presence of a giant planet was inferred from a warp in the disk structure and later confirmed through direct imaging (Mouillet et al. 1997; Lagrange et al. 2010). The Fomalhaut debris disk is significantly eccentric ($e \sim 0.12$), with a possible planet located on the inner edge of the disk (Kalas et al. 2005, 2008, 2013). Secular perturbations could also produce spiral structures within a disk. Resolved observations of the younger (~ 5 Myr) HD 141569 system reveal a tightly wound inner spiral that extends into two, more open spiral arms (Clampin et al. 2003). Greaves et al. (2005) report possible resonant clumps in the ϵ Eridani disk, although subsequent millimeter imaging does not confirm the significance of these features (MacGregor et al. 2015b). It is important to note, however, that the structure of debris disks can be shaped by other mechanisms including close encounters with other stars or interactions with

the interstellar medium, as has been discussed for the HD 15115 (Kalas et al. 2007; Rodigas et al. 2012), HD 32297 (Debes et al. 2009), and HD 61005 (Maness et al. 2009) systems.

With current millimeter interferometers, we can achieve spatial resolutions of a few arcseconds to tens of milli-arcseconds. At a distance of $\sim$ 100 pc (the average distance of the closest star forming regions), these spatial scales correspond to radial scales of hundreds to a few AU. Typical protoplanetary disks have radii of a few hundred AU (e.g. Andrews & Williams 2007), and typical debris disk radii range from $40 - 300$ AU (e.g. Pawellek et al. 2014). Given these expected radial scales, circumstellar disks are easily resolvable with the currently available instruments. Features produced by planets, such as clumps or gaps in a disk, are expected on much smaller scales, $<$ 10 AU. At 100 pc, a 10 AU feature in a disk would have a spatial scale of $\sim 0\farcs1$, challenging for many instruments, but achievable with ALMA. Although, adaptive optics instruments can achieve high resolution as well, the small grains visible at optical and near-infrared wavelengths do not reliably trace the underlying planetesimal distribution. Thus, millimeter interferometry provides us with the only means to probe small scale structures in debris disks produced through planetary interactions.

1.6 Overview of the Dissertation

In this thesis, we present new state-of-the-art observations at millimeter wavelengths using the Atacama Large Millimeter Array (ALMA), Submillimeter Array (SMA), Karl G. Jansky Very Large Array (VLA), and Australia Telescope Compact Array

(ATCA). While working with these data sets, we have developed a modeling framework (MacGregor et al. 2013) that employs Markov Chain Monte Carlo (MCMC) methods to fit simple parametric models directly to the observed millimeter visibilities. This MCMC approach allows us to efficiently characterize the multidimensional parameter space of these models and to determine the posterior probability distribution functions for all parameters. By combining observations and modeling, we have tried to answer three related questions concerning debris disks and planetary system evolution:

1. How are wide-separation, substellar companions formed?
2. What is the physical nature of the collisional process in debris disks?
3. Can the structure and morphology of debris disks provide probes of planet formation and subsequent dynamical evolution?

This work has yielded the first resolved images of notable debris disks at millimeter wavelengths, and complements other ground- and space-based observations by providing constraints on these systems with uniquely high angular resolution and wavelength coverage. Together these results provide a foundation to investigate the dynamical evolution of planetary systems through multi-wavelength observations of debris disks. Furthermore, nearby debris disks are the cornerstone templates for the interpretation of more distant, less accessible systems, and they will provide context for any statistical conclusions obtained from surveys of larger samples.

1.6.1 Formation of Wide-Separation, Substellar Companions

Direct imaging surveys for extrasolar planets are revealing a surprising population of low-mass ($< 40\ M_{\rm Jup}$) companions at wide separations (semi-major axis > 100 AU), which present serious challenges to standard models of both planet and binary star formation. Conventional 'core accretion' models struggle to form such massive objects at large semi-major axes (e.g. Lambrechts & Johansen 2012), while core fragmentation and gravitational instability are difficult to arrest at low masses (e.g. Boley et al. 2010). It is also possible that these objects formed closer in to their host stars and were subsequently scattered (or migrated) outwards through dynamical interactions with another close-in companion (e.g. Crida et al. 2009).

In Chapter 2, we present new constraints on the GQ Lup system (3 ± 2 Myr), one of the best characterized examples of a system with a directly imaged low-mass, wide-separation companion. To probe possible formation scenarios for GQ Lup, we obtained ALMA observations of 870 μm continuum and CO J$= 3 - 2$ line emission. These observations resolve a compact disk of dust and gas surrounding the primary star. While there is no detection of dust emission at the position of the companion, we place a stringent 3σ upper limit on the flux density of any circumplanetary disk associated with it of < 0.15 mJy, which implies an upper limit on the disk dust mass of $< 0.04\ M_{\oplus}$. Since models of *in situ* formation through core fragmentation or gravitational instability predict massive circumplanetary disks that persist for several Myrs, the non-detection of such a disk in the GQ Lup system disfavors these formation scenarios.

1.6.2 Probing Collisional Processes in Debris Disks

The spectral index of dust emission at long wavelengths encodes information on the grain size distribution in debris disks that can be used to constrain collisional models of planetesimals. As discussed in Section 1.4, the classical model of a steady-state collisional cascade assumes that the relative velocities and tensile strengths of the colliding bodies are independent of size, and leads to a power law size distribution, $dN(r)/dr \propto r^{-q}$ with index $q = 3.5$ (Dohnanyi 1969). New analytic and numerical studies that incorporate more realistic dynamics and material physics predict q values that range from $\sim 3.0 - 4.5$ (e.g. Pan & Sari 2005; Pan & Schlichting 2012).

Chapter 3 presents new observations of fifteen debris disks taken with both the VLA and ATCA at centimeter wavelengths. By pairing these data with available millimeter flux measurements from the literature, we robustly determine the millimeter spectral index of each disk, and thus the slope of the grain size distribution, providing an observational test of the theoretical collision models proposed previously. The analysis gives a weighted mean for the slope of the power law grain size distribution, $\langle q \rangle = 3.36 \pm 0.02$. We also find a tentative trend towards shallower grain size distributions for later (G–M) spectral type stars, indicating possible differences in the grain populations of debris disks around stars of different spectral types. These results provide the first observational constraints on the grain size distribution in a statistically significant sample of debris disks.

1.6.3 Resolving the Millimeter Structure of Debris Disks

The bulk radial structure of debris disks is generally well-explained by the presence of a localized belt of planetesimals, where smaller and smaller dust grains are produced through collisions and dispersed. However, many disks exhibit additional substructure such as brightness asymmetries, offsets, warps, and clumps that cannot be explained by the steady-state collisional models assumed in this framework, and suggest the influence of planetary mass bodies.

In this thesis, we present SMA and ALMA observations that resolve the structure of individual systems at millimeter wavelengths and constrain the mechanisms that shape debris disk structure. Observations at these wavelengths probe large grains, which are dynamically linked to the colliding bodies. By applying a consistent modeling framework to these observations, we have been able to place the first constraints on the position, width, surface density gradient, and asymmetries in the debris disks around the nearby stars AU Mic (Chapter 4), HD 15115 (Chapter 5), ϵ Eridani (Chapter 6), and τ Ceti (Chapter 7), all of which exhibit unique structures potentially linked to planetary systems. These systems form a growing sample of debris disks that exhibit rising radial surface density gradients, possibly indicative of the ongoing formation of Pluto-sized bodies near the inner edge of the disk (Kenyon & Bromley 2002). Both ϵ Eridani and τ Ceti, the two closest Sun-like stars with debris disks, are best characterized by broad belts of planetesimals (fractional width ≥ 0.3) in contrast to the narrow Kuiper Belt in our own Solar System (~ 0.18, Bannister et al. 2015).

In Chapter 8, we present ALMA mosaic observations of the Fomalhaut system,

which provide the first millimeter image of continuum dust emission from the complete outer debris disk with uniform sensitivity. Previous observations with the *Hubble Space Telescope* (*HST*) showed a narrow dust belt with a possible eccentric planet (Kalas et al. 2013). These new observations show that the disk is eccentric ($e = 0.12 \pm 0.01$), exhibiting 'apocenter glow,' excess emission seen at apocenter due to the higher surface density at this location in the disk (Pan et al. 2016). In order to characterize the disk structure from these observations, we develop a new analytic model that calculates orbital positions for particles in the disk given their eccentricity, semi-major axis, and other orbital parameters, providing independent constraints on each of these parameters in a MCMC framework.

Finally, we present ongoing work to conduct a comparative study of debris disk structure for a sample of the eight brightest debris disks around Sun-like (FGK) stars within 20 pc. We have assembled resolved millimeter observations using SMA or ALMA of all sources, and Chapter 9 shows the first images for the full sample. Although analysis and modeling are still ongoing, a range of structure is already evident with some disks exhibiting significant asymmetries.

These observations have also yielded surprising results regarding emission from the host stars, which are especially informative for studies of excess emission from unresolved Asteroid Belt analogues that could be confused with stellar emission. The ALMA image of AU Mic revealed a bright central point source, which subsequent modeling and VLA observations at centimeter wavelengths confirmed to be the result of a hot stellar corona (Cranmer et al. 2013; MacGregor et al. 2016b). A central point source was also detected in the ϵ Eridani and τ Ceti systems significantly in excess of the expected emission from a stellar photosphere, and characterized by a shallow

spectral index and high brightness temperature at long wavelengths. This emission is attributable to a stellar chromosphere, as has been noted for other Sun-like stars, including α Cen A and B (Liseau et al. 2015). In contrast, Fomalhaut, an A-type star, appears fainter at millimeter wavelengths than current photospheric models predict. In addition to chromopsheric emission, the long wavelength spectrum of A-type stars, like Fomalhaut, is further complicated by ionized stellar winds, which flatten the spectral slope at radio wavelengths (Aufdenberg et al. 2002).

2

ALMA Measurements of Circumstellar Material in the GQ Lup System

This thesis chapter originally appeared in the literature as

M. A. MacGregor, D. J. Wilner, I. Czekala, S. M. Andrews, Y. S. Dai, G. J. Herczeg, K. M. Kratter, A. L. Kraus, L. Ricci, L. Testi, 2017, Astrophysical Journal, Vol. 835, pp. 17–26

Abstract

We present ALMA observations of the GQ Lup system, a young Sun-like star with a substellar mass companion in a wide-separation orbit. These observations of 870 μm continuum and CO J=3–2 line emission with beam size $\sim 0\farcs3$ (~ 45 AU) resolve the disk of dust and gas surrounding the primary star, GQ Lup A, and provide deep

limits on any circumplanetary disk surrounding the companion, GQ Lup b. The circumprimary dust disk is compact with a FWHM of 59 ± 12 AU, while the gas has a larger extent with a characteristic radius of 46.5 ± 1.8 AU. By forward-modeling the velocity field of the circumprimary disk based on the CO emission, we constrain the mass of GQ Lup A to be $M_* = (1.03 \pm 0.05) * (d/156 \text{ pc}) \ M_\odot$, where d is a known distance, and determine that we view the disk at an inclination angle of $60\overset{\circ}{.}5 \pm 0\overset{\circ}{.}5$ and a position angle of $346^\circ \pm 1^\circ$. The 3σ upper limit on the 870 μm flux density of any circumplanetary disk associated with GQ Lup b of < 0.15 mJy implies an upper limit on the dust disk mass of $< 0.04 \ M_\oplus$ for standard assumptions about optically thin emission. We discuss proposed mechanisms for the formation of wide-separation substellar companions given the non-detection of circumplanetary disks around GQ Lup b and other similar systems.

2.1 Introduction

Direct imaging surveys for extrasolar planets are revealing a surprising population of low-mass companions at wide-separations (semi-major axis > 100 AU) (Chauvin et al. 2005; Luhman et al. 2006; Lafrenière et al. 2008; Ireland et al. 2011; Kraus et al. 2014; Bowler et al. 2015; Kraus et al. 2015). These substellar ($< 40 \ M_{\text{Jup}}$) companions present serious challenges to standard models of both planet and binary star formation (e.g. Debes & Sigurdsson 2006). Conventional "core accretion" models struggle to form such massive objects at large semi-major axes (Pollack et al. 1996; Lambrechts & Johansen 2012), while core fragmentation and gravitational instability are difficult to arrest at low masses and preferentially form more massive

objects (Bate et al. 2003; Kratter et al. 2010; Jiang et al. 2004; Boley et al. 2010). Another possibility is that these objects formed closer in to their host stars and were subsequently scattered (or migrated) outwards through dynamical interactions with another close in companion (Boss 2006; Crida et al. 2009).

The growing population of wide-separation companions offers a new window to explore the processes of giant planet assembly and the subsequent formation of moon systems. Several of these companions exhibit line emission, as well as infrared and ultraviolet excesses commonly associated with ongoing accretion from "circumplanetary" disks (Seifahrt et al. 2007; Schmidt et al. 2008; Bowler et al. 2011, 2014; Bailey et al. 2013; Zhou et al. 2014). There is also evidence for circumplanetary disks around planets at closer separations from photometric transit surveys (J1407, see Mamajek et al. 2012). Models of giant planet formation make testable predictions about the size, scale height, and mass distribution of these circumplanetary disks (e.g. Ayliffe & Bate 2009). Furthermore, the properties of these disks govern the composition and orbits of any moons that may form (Heller et al. 2014).

One of the most prominent and best characterized examples of a system with a directly imaged low-mass, wide-separation companion with evidence for a circumplanetary disk is GQ Lup. We present new observations of 870 μm continuum and CO J=3–2 line emission from the GQ Lup system made with the Atacama Large Millimeter/submillimeter Array (ALMA). These new ALMA observations place a stringent upper limit on the emission from any circumplanetary disk surrounding GQ Lup b, and they provide strong constraints on the geometry of the disk surrounding GQ Lup A. We introduce the GQ Lup system in Section 2.2. In Section 2.3, we present the ALMA observations. In Section 2.4, we describe the

analysis techniques and results for both continuum and line emission. In Section 2.5, we discuss the significance of the results on the circumprimary disk geometry, the limit on a circumplanetary disk, and implications for the formation mechanisms of wide-separation, substellar companions.

2.2 The GQ Lup System

The GQ Lup system is located in the 3 ± 2 Myr-old (Alcalá et al. 2014) Lupus I cloud (Tachihara et al. 1996) at a distance of 156 ± 50 pc (determined from parallax, see Neuhäuser et al. 2008). New parallax measurements from *Gaia* DR1 for stars in Lupus I, yield an average parallax of 6.4 ± 0.3 mas or 156.3 ± 7.3 pc (Lindegren et al. 2016), comparable to the earlier parallax measurements. The primary star, GQ Lup A, is a classical T Tauri star (spectral type K7V, Kharchenko & Roeser 2009), with a photospheric temperature of $\sim 4000 - 4300$ K (Pecaut & Mamajek 2013; Herczeg & Hillenbrand 2014; Donati et al. 2012). Seperuelo Duarte et al. (2008) estimate a stellar radius of 1.8 ± 0.3 $R_{\odot}$ and assume an effective temperature of 4060 K to determine a stellar luminosity of $0.8 \pm 0.3 L_{\odot}$. Although they adopt a much higher effective temperature of 4300 ± 50 K, Donati et al. (2012) obtain a comparable stellar radius of 1.7 ± 0.2 $R_{\odot}$. Previous estimates of the mass of GQ Lup A vary between 0.7 and 1.05 $M_{\odot}$, largely depending on the evolutionary models and effective temperatures used (Mugrauer & Neuhäuser 2005; Seperuelo Duarte et al. 2008; Donati et al. 2012). Adopting the higher effective temperature of 4300 K yields a mass of 1.05 ± 0.07 $M_{\odot}$, the upper value in this range (Donati et al. 2012). Additionally, GQ Lup A possesses strong mid- and far-infrared excesses, indicative

of a circumstellar disk (Hughes et al. 1994). Dai et al. (2010) marginally resolved 1.3 mm dust emission from the circumstellar disk using the Submillimeter Array (SMA) and determined an outer radius of < 75 AU.

The substellar companion, GQ Lup b, was discovered by Neuhäuser et al. (2005) using the *Hubble Space Telescope* (*HST*). By fitting to the broadband spectral energy distribution, Zhou et al. (2014) determine that the companion has a radius of 6.5 ± 2 $R_{\rm Jup}$, an effective temperature of 2050 ± 350 K, and a luminosity of $\log L_{\rm phot}/L_{\odot} = -2.25 \pm 0.24$. The mass of this companion is uncertain, with estimates ranging from $10 - 36$ $M_{\rm Jup}$ (Marois et al. 2007; Seifahrt et al. 2007; Neuhäuser et al. 2008; Lavigne et al. 2009). The projected separation of the companion from the primary star is $0\farcs7$ (Ginski et al. 2014), and recent work by Schwarz et al. (2016) favors orbits with high eccentricity and semi-major axes $100 - 185$ AU. Near-infrared spectroscopy by Seifahrt et al. (2007) showed Paβ line emission (equivalent width, EW $= -3.83 \pm 0.12$ Å), though subsequent observations by Lavigne et al. (2009) give a limit an order of magnitude lower for the same line (EW $= -0.46 \pm 0.08$ Å), possibly pointing to time variability of Paβ and ongoing disk accretion. Optical photometery using *HST* shows a significant blue excess that corresponds to an accretion rate $\sim 5 \times 10^{-10}$ $M_{\odot}$ yr^{-1} (Zhou et al. 2014).

2.3 Observations

The GQ Lup system was observed with ALMA in Band 7 (870 μm) in a one hour (total of $\sim$ 30 minutes on-source) Scheduling Block (SB) on 2015 June 14 with 41 operational antennas and on 2015 June 15 with 37 operational antennas, using

baselines that spanned 15 to 784 m. An additional one hour SB was executed on 2015 August 28 with 40 operational antennas, using baselines reaching to 1574 m. These observations are summarized in Table 2.1, including the dates, baseline lengths, weather conditions, and time on-source. Overall, the weather was very good (pwv $\lesssim$ 1.1 mm). The correlator was configured to optimize continuum sensitivity, while including both the ^{12}CO and ^{13}CO J=3–2 transitions at 345.79599 and 330.58797 GHz, respectively. The setup used four basebands, centered at 331, 333, 343, and 345 GHz, in two polarizations. The basebands with the targeted spectral lines, centered at 331 and 345 GHz, each have 3840 channels over a bandwidth of 1.875 GHz, while the other two basebands each have only 128 channels over a bandwidth of 2 GHz. The phase center for the June observations was specified at $\alpha = 15^{\rm h}49^{\rm m}12.082861$, $\delta = -35°39'05\farcs48071$ (J2000), and the phase center for the August observations was $\alpha = 15^{\rm h}49^{\rm m}12.082607$, $\delta = -35°39'05\farcs48550$. These phase centers correspond to the J2000 position of the star corrected for its proper motion of $(-15.1, -23.4)$ mas yr^{-1}. The field of view at the center frequency of 338 GHz is $\sim 18''$, set by the FWHM primary beam size of the 12-m diameter array antennas.

The raw datasets were delivered with calibration scripts provided by ALMA staff. We executed these scripts for each SB using the `CASA` package (version 4.5.0) to generate calibrated visibilities. Time-dependent gain variations due to atmospheric and instrumental effects were corrected using interleaved observations of the calibrator J1534-3526. Bandpass calibration was determined from observations of J1517-2422. The absolute flux calibration was derived from observations of Titan and Ceres, with a systematic uncertainty estimated at less than 10%. A single iteration of phase-only self-calibration was employed, after which the visibilities were

averaged into 30 second intervals. We generated both continuum and CO line images using the multi-frequency synthesis `CLEAN` algorithm in `CASA`. For spectral line imaging, the continuum level was subtracted from the spectral windows containing emission lines.

Table 2.1: ALMA Observations of GQ Lup

Observation Date	# of Antennas	Projected Baselines (m)	PWV (mm)	Time on Target (min)
2015 June 14	41	$16 - 784$	0.6	31.3
2015 June 15	37	$21 - 784$	0.4	31.1
2015 Aug 28	40	$15 - 1574$	1.1	35.0

2.4 Results and Analysis

2.4.1 Continuum Emission

Figure 2.1 (left panel) shows the ALMA 870 μm continuum emission. With robust = 0.5 weighting, the synthesized beam size is $0\farcs37 \times 0\farcs23$ (58×36 AU at 156 pc) with a position angle of $-87°$, and the rms noise level is 50 μJy/beam. This image reveals compact dust continuum emission around GQ Lup A (star symbol) and no evidence for emission at the position of GQ Lup b (diamond symbol). From this non-detection, we determine a 3σ upper limit on the flux density of any circumplanetary disk surrounding the secondary of < 0.15 mJy (assuming a point source). The right panel of Figure 2.1 shows the deprojected real visibilities averaged in bins of (u, v) distance, centered on GQ Lup A using the disk inclination and orientation determined by forward-modeling the CO emission (see Section 2.4.2 for

a detailed description). The profile shows a central peak and fall-off, but without the subsequent ringing that would be expected for a simple disk with a single radial power law surface brightness profile. A more complicated surface brightness profile (e.g. a broken power law, see Hogerheijde et al. 2016) is more consistent, but a proper radiative transfer calculation will be needed to determine the precise radial profiles of the disk surface density and temperature. The deprojected imaginary visibilities are consistent with zero, as is expected for a symmetric structure.

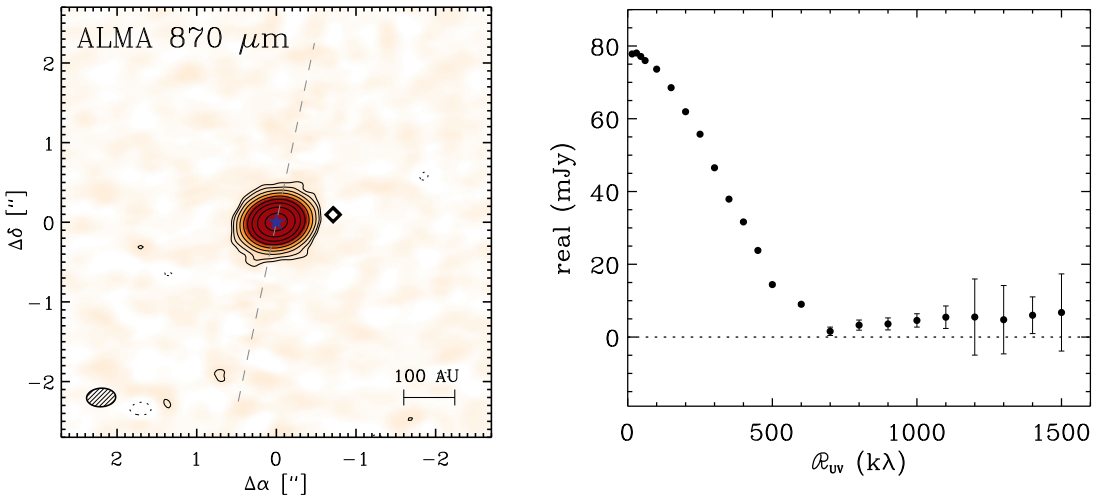

Figure 2.1: *(left)* ALMA image of the 870 μm continuum emission from GQ Lup. The contour levels are in steps of [3, 6, 12, 24, 48,...]×50 μJy, the rms noise level in the image. The star symbol marks the position of the primary star, GQ Lup A, and the diamond indicates the projected location of the secondary companion, GQ Lup b. The dashed gray line shows the position angle of the disk major axis determined by forward-modeling the CO emission and the dashed ellipse indicates the $0\farcs37 \times 0\farcs23$ (FWHM) synthesized beam size. *(right)* The deprojected real visibilities averaged in bins of (u, v) distance.

By fitting a simple two dimensional Gaussian to the continuum image, we obtain a total flux density for the circumprimary disk of 77.8 ± 0.2 mJy, consistent with previous interferometric and single dish millimeter flux measurements. Dai

et al. (2010) measure a flux density of 25 ± 3 mJy at 1.3 mm with the SMA. Nuernberger et al. (1997) measure a flux density of 38 ± 7 mJy at 1.25 mm with the SEST bolometer. If we extrapolate our ALMA measurement using a typical spectral index for T Tauri stars of 2.4 ± 0.5 (Andrews et al. 2013), we obtain a flux density at 1.3 mm of 29.7 ± 5.4 mJy, in good agreement with both previous flux density measurements within their uncertainties. Given this flux density, the GQ Lup circumstellar disk is brighter than $\sim 70\%$ of other Lupus sources with spectral types K4−M1 (Ansdell et al. 2016). The major axis FWHM of the continuum emission (deconvolved from the beam) is $0\farcs38 \pm 0\farcs07$. At a distance of 156 pc, this gives a characteristic size for the primary disk of 59 ± 12 AU, again comparable to the results of Dai et al. (2010), who derived an outer radius for the disk of $25 - 50$ AU ($\sim 50 - 100$ AU in diameter). Longer baseline observations with higher angular resolution are needed to better constrain the location and sharpness of the dust disk edges, and to probe for any substructure that might betray the presence of an additional inner companion in the system.

For optically thin emission, we can make a simple estimate of the total dust mass ($M_{\rm dust}$) for the circumprimary disk given the observed total flux density (Hildebrand 1983):

$$M_{\rm dust} = \frac{F_\nu D^2}{\kappa_\nu B_\nu(T_{\rm dust})}. \tag{2.1}$$

Here, $B_\nu(T_{\rm dust})$ is the Planck function at the dust temperature, $T_{\rm dust}$, and κ_ν is the dust opacity. For consistency with Bowler et al. (2015) and Ansdell et al. (2016), we adopt the frequency-dependent dust opacity $\kappa_\nu = 10(\nu/10^{12}\ {\rm Hz})\ {\rm cm^2\ g^{-1}}$ from

Beckwith et al. (1990). At 870 μm, the dust opacity is $\kappa_\nu = 3.4$ cm^2 g^{-1}. To estimate the dust temperature, we use the dust temperature-stellar luminosity relationship of Andrews et al. (2013): $T_{\rm dust} = 25(L/L_\odot)^{1/4}$. For GQ Lup A, this relation yields $T_{\rm dust} = 24 \pm 8$ K. The resulting dust mass is 15.10 ± 0.04 $M_\oplus$.

Similarly, we can use the 3σ upper limit on the flux density of a circumplanetary disk around the companion GQ Lup b to place an upper limit on the potential dust mass. Given its low luminosity, we assume that heating of a circumplanetary disk around GQ Lup b is dominated by the primary star, GQ Lup A, rather than by the companion itself. If we assume that the orbit of GQ Lup b and the circumprimary disk are coplanar, the radiative equilibrium temperature at the position of GQ Lup b (~ 220 AU, see Section 2.5.1 for discussion), is 18 ± 2 K. Taking this value as a representative dust temperature for our analysis, the resulting 3σ upper limit on the dust mass is $M_{\rm dust} < 0.04$ $M_\oplus$. For a gas-to-dust ratio of 100, this implies a total circumplanetary disk mass of $M_{\rm tot} < 4$ $M_\oplus$ or $< 0.04 - 0.13\%$ the mass of the companion itself (for companion masses of $10 - 36$ $M_{\rm Jup}$). This estimate of the disk dust mass is sensitive to both the assumed dust opacity, κ_ν, and the characteristic dust temperature, $T_{\rm dust}$. van der Plas et al. (2016) derive a temperature-luminosity relationship for spectral types M5 and later (assuming different prescriptions for disk flaring and opacity than Andrews et al. 2013): $T_{\rm dust} = 22(L/L_\odot)^{0.16}$. Given a luminosity of ~ 0.006 $L_\odot$ for GQ Lup b, this relationship implies a dust temperature of ~ 10 K. If we take $T_{\rm dust} = 10$ K, instead, then $M_{\rm dust} < 0.14$ $M_\oplus$ and $M_{\rm tot} < 14$ $M_\oplus$. Even for this low temperature the total disk mass is $\lesssim 0.1 - 0.3\%$ of the companion mass. Any possible viscous heating of the disk (e.g. Isella et al. 2014) is neglected here because of the low measured accretion rate, $\sim 5 \times 10^{-10}$ $M_\odot$ yr^{-1} ~ 0.5 $M_{\rm Jup}$ Myr^{-1}.

If we take the measured accretion rate together with a disk mass of $\lesssim 4-14\ M_{\oplus}$ for the circumplanetary disk, this yields an expected lifetime of $\sim 2\times10^4 - 1\times10^5$ years, shorter than the age of the GQ Lup system of ~ 2 Myr. The total dust mass of the circumplanetary disk also places constraints on the possibility of moon formation around the companion. In our own Solar System, the total mass of the moons of Jupiter, Saturn, and Uranus are all $\sim 10^{-4}$ the mass of their host planet (Canup & Ward 2006). The dust content of the GQ Lup b disk is at least a factor of six lower than this moon-planet mass ratio, making it difficult to form gas giant moons. However, in the model of Canup & Ward (2006) satellites form in a circumplanetary disk during the final stages of growth of the host planet, so we cannot rule out the future formation of rocky moons.

If we assume optically thick dust emission for the circumplanetary disk, then we can derive an upper limit on its size. In this limit, the intensity, I_ν, is approximately $B_\nu(T_{\rm dust})$. Thus,

$$R_{\rm dust} = \sqrt{\frac{F_\nu D^2}{\pi B_\nu(T_{\rm dust})}}. \tag{2.2}$$

Given the upper limit of $F_\nu < 0.15$ mJy and a dust temperature of 18 K, $R_{\rm dust}$ must be < 1.1 AU. For comparison, the Hill radius of GQ Lup b assuming a semi-major axis of ~ 100 AU and an eccentricity of ~ 0.2 is $R_{\rm Hill} \sim 12-19$ AU (for companion masses between $10-40\ M_{\rm Jup}$). Thus, this small disk size may be compatible with numerical simulations of circumplanetary accretion disks that are thick, dense, and truncated at a few tenths of the Hill radius ($R \sim 0.3-0.4 R_{\rm Hill}$) by the gravity of the central star (e.g. Ayliffe & Bate 2009; Martin & Lubow 2011; Szulágyi et al. 2016).

2.4.2 ^{12}CO and ^{13}CO Emission

Figure 2.2 shows the velocity-integrated intensity ($0^{\rm th}$ moment) overlaid as contours on the intensity-weighted velocity ($1^{\rm st}$ moment) for both the ^{12}CO and ^{13}CO emission (left and right panels, respectively). Both maps show a clear pattern of Keplerian rotation, seen more explicitly in the channel maps shown in Figure 2.3 (top: ^{12}CO, bottom: ^{13}CO). Only the central 11 channels are shown for each line, where emission is clearly resolved at $> 3\sigma$. For the ^{12}CO image, the typical rms in a given channel is 11 mJy/beam higher due to calibration issues in the spectral window containing ^{12}CO for two of the scheduling blocks that were dealt with by ALMA staff. The integrated and peak intensity are 14.5 Jy km s^{-1} and 1.43 Jy/beam (130σ), respectively. For the ^{13}CO image, the typical rms noise is 6.5 mJy/beam. The integrated and peak intensity are 1.76 Jy km s^{-1} and 0.35 Jy/beam (54σ), respectively. The systemic velocity in the LSRK frame is 3.00 ± 0.01 km s^{-1}, and corresponds to -2.88 ± 0.01 km s^{-1} in the barycentric frame. Schwarz et al. (2016) recently derived a comparable systemic velocity for the primary of -2.8 ± 0.2 km s^{-1} from near infrared observations using the CRIRES instrument on the VLT.

The CO emission morphology does not show any indication of truncation of the circumprimary gas disk due to the companion, GQ Lup b. Both the ^{12}CO and ^{13}CO emission appear largely symmetric in their spatial distribution across the disk major axis (position angle = 346°). There is an indentation and compact $> 6\sigma$ emission peak visible northwest of the star in the ^{12}CO moment and channel maps with velocities between 2 and 3 km s^{-1}. Extended interstellar molecular cloud material was seen by van Kempen et al. (2007) in single dish ^{12}CO emission towards GQ Lup

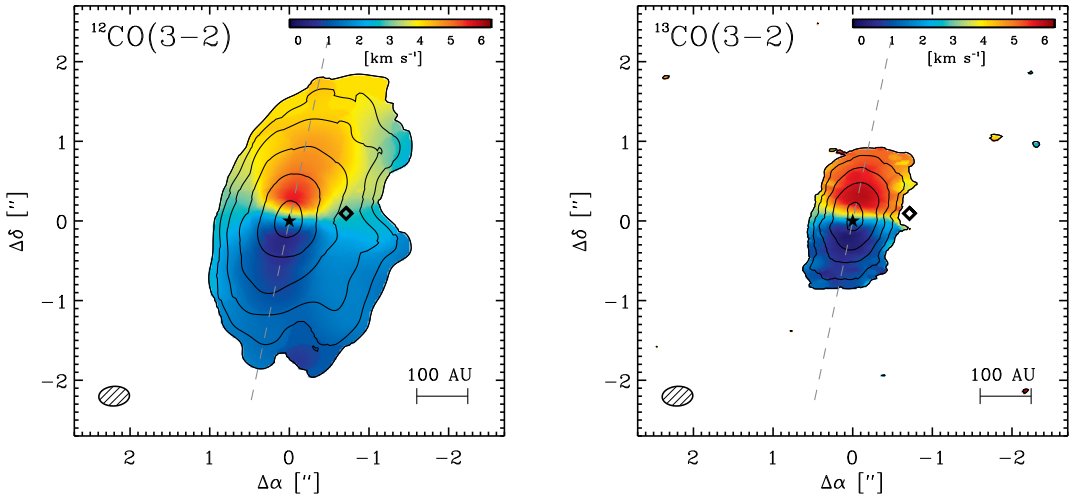

Figure 2.2: *(left)* The ^{12}CO J=3–2 moment maps for the GQ Lup A circumstellar disk. The zeroth moment (velocity-integrated intensity) map is indicated by contours in steps of [3, 6, 12, 24, 48,...]×11 mJy km s^{-1} beam^{-1}, the rms noise level in the image. The first moment (intensity-weighted velocity) is shown in color with a scale bar for reference. *(right)* The ^{13}CO J=3–2 moment maps for the GQ Lup disk. The zeroth moment map is overlaid with contours in steps of [3, 6, 12, 24, 48,...]×6.5 mJy km s^{-1} beam^{-1}, the rms noise level in the image. Again, the first moment is shown in color with a scale bar for reference. In both panels, the star symbol marks the position of the primary star and the diamond indicates the projected location of the secondary companion. The dashed gray line shows the position angle, $PA = 346°$, of the disk major axis determined from modeling and the dashed ellipse indicates the $0\farcs37 \times 0\farcs23$ (FWHM) synthesized beam size.

with $v_{\rm LSRK} \sim 4 - 5$ km s^{-1}. Although the velocities of the observed structure and the extended interstellar component do not match exactly, it is plausible that the ^{12}CO ALMA images of the circumprimary disk are affected by contamination from ambient cloud emission.

In order to determine a dynamical mass for GQ Lup A and to characterize the gas disk geometrical properties, we forward-model the ^{12}CO and ^{13}CO molecular line

emission using the `DiskJockey` package[1] (Czekala et al. 2015). We adopt a simple parametric model of disk structure, which uses a self-similar surface density profile (Lynden-Bell & Pringle 1974) described by a characteristic radius, r_c, and total gas mass, $M_{\rm gas}$:

$$\Sigma = \Sigma_c \left(\frac{r}{r_c}\right)^{-1} \exp\left[-\left(\frac{r}{r_c}\right)^2\right]. \tag{2.3}$$

Here, Σ_c is a normalization given by $e \times \Sigma(r_c)$, $M_{\rm gas} = X_{\rm CO}\Sigma_c(2\pi r_c^2)$, and $X_{\rm CO}$ is the fractional abundance of CO (assumed to be constant throughout the disk). The disk is assumed to be vertically isothermal and in hydrostatic equilibrium, with a radial power law index, q, and a normalization at 10 AU, T_{10}:

$$T = T_{10}\left(\frac{r}{10\ {\rm AU}}\right)^{-q}. \tag{2.4}$$

The velocity field is assumed to be Keplerian with systemic velocity, $v_{\rm sys}$, and is dominated by the stellar mass, M_*. Non-thermal (turbulent) line broadening is denoted by a constant velocity width, ξ. We also include two offsets in both RA and DEC, $\Delta\alpha$ and $\Delta\delta$, respectively. The posterior probability of the model parameters is evaluated in the following manner: (1) sky-images of a given disk structure are generated using the `RADMC-3D` radiative transfer program (Dullemond 2012), Fourier transformed, and sampled at the (u, v) locations corresponding to the ALMA baselines, and (2) the model visibilities are then evaluated using a χ^2 likelihood function which incorporates the statistical weights on each visibility measurement.

[1]Open source and available at `https://github.com/iancze/DiskJockey` under an MIT license.

This generative model allows us to fully explore the uncertainties in each parameter as well as determine the one dimensional marginalized probability distribution on stellar mass. Although more sophisticated models of disk structure are desirable, this simple model has been proven to yield accurate stellar masses, as confirmed by comparison with measurements of circumbinary disks around spectroscopic binaries (Rosenfeld et al. 2012; Czekala et al. 2015, 2016). Further details of the modeling framework can be found in Czekala et al. (2015).

Table 2.2: ^{12}CO and ^{13}CO Model Parameters

Parameter	Description	^{12}CO Best-fit	^{13}CO Best-fit
M_*	Stellar mass ($M_\odot$)	0.93 ± 0.15	1.03 ± 0.15
i	Disk inclination (°)	60.3 ± 0.4	60.5 ± 0.5
PA	Disk position angle (°)	346 ± 1	346 ± 1
r_c	Characteristic radius (AU)	97.6 ± 3.7	46.5 ± 1.8
T_{10}	Temperature at 10 AU (K)	85.5 ± 2.5	50.6 ± 2.4
q	Temperature power law index	0.43 ± 0.02	0.38 ± 0.04
$\log M_{\rm gas}$	Gas mass ($\log M_\odot$)	-4.72 ± 0.03	-3.67 ± 0.05
ξ	Nonthermal line width (km/s)	0.72 ± 0.02	0.55 ± 0.02
$v_{\rm sys}$	Systemic velocity (km/s)	3.00 ± 0.01	3.00 ± 0.01
$\Delta\alpha$	RA offset ($''$)	0.07 ± 0.01	0.06 ± 0.01
$\Delta\delta$	DEC offset ($''$)	0.11 ± 0.01	0.10 ± 0.01

The best-fit parameter values and their 68% uncertainties are listed in Table 2.2. Figure 2.3 shows the channel maps for the data (top), best-fit model imaged like the data (middle), and resulting residuals (bottom) for both the ^{12}CO (top grouping) and ^{13}CO (bottom grouping) emission. The results for both lines are consistent, although the ^{12}CO fits may be biased by the cloud contamination evident in the residuals (see channels with velocities between $1 - 4$ km s^{-1}). As a result, we focus on the best-fit parameters from the ^{13}CO modeling.

The models imply a stellar mass, M_*, for GQ Lup A of 1.03 ± 0.15 $M_\odot$. The quoted uncertainty on the mass includes the significant uncertainty in the distance ($\pm$50 pc) added in quadrature. At a known distance, d, the constraint on the stellar mass can be recast as $M_* = (1.03 \pm 0.05) * (d/156 \text{ pc})$ $M_\odot$, where the formal uncertainty on M_* is $\sim 5\%$ including systematic uncertainties estimated from more complex models (e.g. vertical structure, see Rosenfeld et al. 2013). Previous estimates of the stellar mass of GQ Lup A from the literature are mostly lower than our determination, ranging between 0.7 and 1.05 $M_\odot$ (see discussion in Section 2.2, Mugrauer & Neuhäuser 2005; Seperuelo Duarte et al. 2008; Donati et al. 2012). The discrepancy in mass estimates results largely from differences in stellar evolutionary models and uncertainty in the effective temperature. Given this result and previous work (Czekala et al. 2015, 2016; Rosenfeld et al. 2013), ALMA can play a substantial role in precisely measuring the masses of large samples of young stars, providing constraints on evolutionary models. Much work has been done to determine allowable orbits for the companion, GQ Lup b, all of which assume a stellar mass of 0.7 $M_\odot$ (Ginski et al. 2014; Pearce et al. 2015; Schwarz et al. 2016). Pearce et al. (2015) define a criteria for a bound orbit, $B < 1$, where $B \propto (M/M_\odot)^{-1}$. This new determination of the stellar mass of GQ Lup A may prove relevant for constraining allowable orbits of the secondary.

The characteristic radius and total gas mass for the best-fit model to the ^{13}CO emission are 46.5 ± 1.8 AU and $\log M_{\rm gas}/M_\odot = -3.67 \pm 0.05$, respectively. We also compare our ^{12}CO and ^{13}CO integrated line intensities to the model grids of Williams & Best (2014), which predict a gas mass between $10^{-4} - 10^{-3}$ $M_\odot$, consistent with our modeling results. By combining this gas mass with the total

dust mass determination from Section 2.4.1, we can calculate the gas-to-dust ratio for the circumstellar disk around GQ Lup A to be 4.7 ± 0.5. This result is well below ISM gas-to-dust ratios, but is comparable to measurements made by Ansdell et al. (2016) for circumstellar disks around other T Tauri stars in Lupus with similar stellar masses. In fact, nearly all of the detected Lupus disks are inferred to have gas-to-dust ratios well below 100. A significant caveat to our derived gas mass is that it depends inversely on the CO/H_2 abundance ratio, which we assume to be ISM-like $\sim 10^{-4}$. Furthermore, recent work by Miotello et al. (2016) suggests that a more complex analysis is required to accurately determine disk gas masses.

2.5 Discussion

We have performed interferometric observations of the GQ Lup system at 870 μm with ALMA and detected both continuum and ^{12}CO and ^{13}CO J=3–2 line emission. The continuum image reveals compact dust emission surrounding the primary star, but no emission at the position of the secondary companion. We place a robust 3σ upper limit on the flux of a circumplanetary disk surrounding the companion of < 0.15 mJy. We use the Keplerian velocity field as determined by the line emission data to estimate the mass of the primary star, $M_* = (1.03 \pm 0.05) * (d/156 \text{ pc})\ M_\odot$, and the geometry of the circumprimary disk. We now use this new information to discuss the geometry of the circumprimary disk and implications for formation scenarios of massive companions on wide orbits.

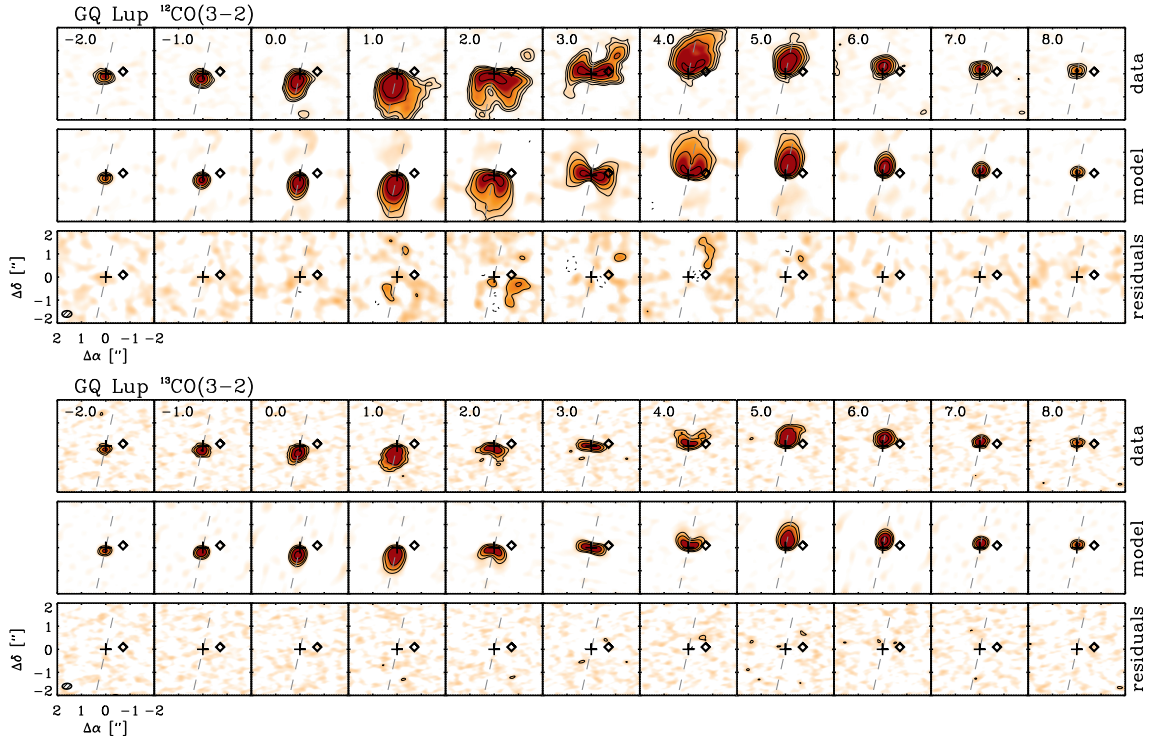

Figure 2.3: Channel maps (top row), the best-fit model (model row), and the imaged residuals (bottom row) for both the ^{12}CO (top) and ^{13}CO (bottom) J=3–2 emission for GQ Lup. Contours for all panels are in steps of $[3, 6, 12, 24, 48, ...]\times$ the rms noise level in the image, with an rms of 11 mJy/beam and 6.5 mJy/beam for the ^{12}CO and ^{13}CO images, respectively. The ellipse in the lower left corner of both bottom leftmost panels indicates the $0\farcs37 \times 0\farcs23$ (FWHM) synthesized beam size. Each channel is 1 km/s wide with the LSR velocities labeled in the upper left corner of each panel.

2.5.1 Circumprimary Disk Geometry

The CO emission models place tight constraints on the geometry of the circumprimary disk through the inclination and position angle. For the ^{13}CO emission, the best-fit inclination is $i = 60\fdg5 \pm 0\fdg5$ and position angle is $PA = 346° \pm 1°$. There are discrepancies in the literature over the inclination angles of the stellar rotation axis and circumprimary disk for the GQ Lup system. Broeg et al. (2007) combine photometric rotation period monitoring with a previous measurement of $v\sin i$ from

HARPS (Guenther et al. 2005) to determine the inclination of the star's rotational axis to be $i = 27° \pm 5°$, much lower than the inclination of the circumstellar disk. In contrast, Seperuelo Duarte et al. (2008) derive a higher inclination of $53° \pm 18°$ from spectrophotometric data taken with the 1.52 m ESO telescope in La Silla. Using high resolution VLT/CRIRES spectra of CO emission from GQ Lup, Pontoppidan et al. (2011) find a best-fit disk inclination of $65° \pm 10°$. Our analysis agrees with these later determinations of the disk inclination and suggests that the disk inclination is significantly higher than previously estimated for the star.

Assuming that the orbit of GQ Lup b is also coplanar with the circumprimary disk implies that the current physical separation of GQ Lup b could be as large as ~ 220 AU. Schwarz et al. (2016) and Ginski et al. (2014) (assuming a stellar mass of 0.7 $M_{\odot}$) propose three families of orbital solutions for GQ Lup b: 1) semi-major axis ~ 100 AU, $i \sim 57°$, eccentricity ~ 0.15, 2) semi-major axis < 185 AU, $28° < i < 63°$, eccentricity 0.2 to 0.75, and 3) semi-major axis > 300 AU, $52° < i < 63°$, eccentricity > 0.8. More specifically, they note that orbits with lower eccentricities between $0.1 - 0.4$ have high inclinations between $48° - 63°$. Given the apparent discrepancy between these high inclinations and the assumed low inclination of the circumstellar disk ($i \sim 27°$), Schwarz et al. (2016) and Ginski et al. (2014) suggest that GQ Lup b was likely scattered to its current position since *in situ* formation would result in a low eccentricity orbit near the plane of the circumstellar disk. Our new robust measurement of the circumstellar disk inclination relieves some of this tension and does not exclude an *in situ* formation, since an inclination of $60.^{\circ}5 \pm 0.^{\circ}5$ is well within the range determined for low eccentricity orbits.

2.5.2 Comparison to Other Young Substellar Objects

The 3σ dust mass upper limit we obtain for GQ Lup b is lower than previous circumplanetary disk mass constraints obtained with ALMA. Bowler et al. (2015) observed GSC 6214-210, a $5-10$ Myr-old system with a ~ 15 $M_{\rm Jup}$ companion at a separation of ~ 320 AU and did not detect dust emission surrounding either the primary or secondary; they place an upper limit on the circumplanetary dust mass of < 0.15 $M_{\oplus}$ or $< 0.3\%$ of the companion mass. However, a non-detection of millimeter dust emission around both the primary and the secondary is consistent with the results of a large survey of the TW Hya association, which found dust masses for similar late spectral type objects of $\lesssim 10^{-2}$ $M_{\oplus}$ (Rodriguez et al. 2015). In older systems like these, it is possible that the effects of grain growth and drift have depleted the disks of grains that are emissive at millimeter wavelengths. In contrast, ALMA observations of the younger, 2 Myr-old FW Tau system (Kraus et al. 2015) detected significant dust emission surrounding the < 40 $M_{\rm Jup}$ companion at ~ 330 AU (Caceres et al. 2015), implying a circumplanetary dust mass of $1-2$ $M_{\oplus}$. However, the spectral energy distribution, especially at near-infrared wavelengths, suggests that FW Tau C is degenerate between a planetary mass object and a very low mass star or brown dwarf (spectral type M5−M8) with an edge-on disk (Bowler et al. 2014). Figure 2.4 compares our ALMA constraint on the dust luminosity of a circumplanetary disk around GQ Lup b to the previous constraints on FW Tau C from Kraus et al. (2015). Also included in Figure 2.4 are previous (sub)millimeter measurements for sources with spectral types M5 and later from surveys of the young (~ 2 Myr-old) Lupus, Taurus, and ρ Ophiucus star-forming

regions (Ansdell et al. 2016; Andrews et al. 2013; Ricci et al. 2014; Testi et al. 2016). All of the dust luminosities were calculated from measurements of the 890 μm flux density. To construct this plot, we assumed the mean distance for each star forming region to be the following: 156 ± 50 pc (Lupus I, II, IV, Neuhäuser et al. 2008), 200 ± 50 pc (Lupus III Comerón 2008), 140 ± 20 pc (Taurus, Torres et al. 2012), and 135 ± 8 pc (ρ Ophiucus, Mamajek 2008). The ALMA limit for GQ Lup b is nearly an order of magnitude lower than the detections from these other large surveys. This wide spread in dust luminosity for similar spectral type objects shows that there is a wide range of evolutionary outcomes for circumstellar disks at these young ages.

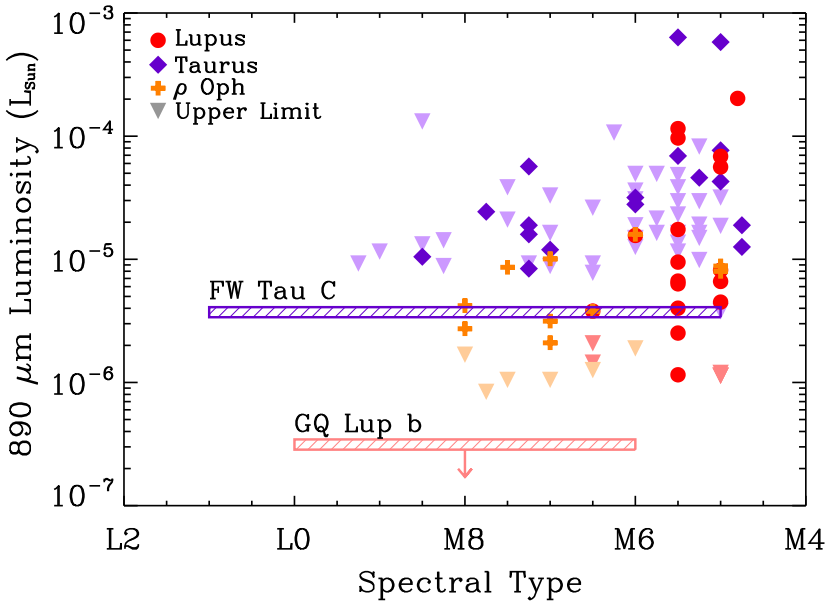

Figure 2.4: (Sub)millimeter dust luminosities as a function of spectral type for the young ($\sim$ 2 Myr-old) Lupus (red circles, Ansdell et al. 2016), Taurus (purple diamonds, Andrews et al. 2013; Ricci et al. 2014), and ρ Ophiucus (orange crosses, Testi et al. 2016) star forming regions. The upside down triangles indicate 3σ upper limits. Our upper limit for GQ Lup b is nearly an order of magnitude lower than the previous ALMA measurement of a circumplanetary disk surrounding FW Tau C (Kraus et al. 2015).

2.5.3 Implications for Formation Scenarios

The growing sample of systems with deep millimeter observations and corresponding limits on circumplanetary disk masses allows us to speculate on proposed formation mechanisms of such systems (Debes & Sigurdsson 2006; Dai et al. 2010). One possibility is that these wide-separation substellar companions formed *in situ* through core fragmentation or gravitational instability. However, models predict that companions formed through these mechanisms should be surrounded by massive circumplanetary disks that persist over several Myrs by accreting material from the disk of the parent star (Stamatellos & Herczeg 2015; Vorobyov & Basu 2010; Boley 2009). Another possibility is that these substellar companions formed much closer in to the primary star and were later scattered outward through dynamical interactions with another massive body (Boss 2006; Crida et al. 2009; Schneider et al. 2009). Such chaotic events are likely to disrupt or destroy any circumplanetary disk surrounding the companion, since the closest approach is $<< R_{\rm Hill}$. However, a recent survey by Bryan et al. (2016) of eight wide separation planetary mass companions ruled out the presence of $< 7\ M_{\rm Jup}$ inner companions in these systems at separations of $15 - 50$ AU, suggesting that scattering may not be a dominant mechanism for the formation of wide separation companions. It is also possible that such systems formed through the standard binary fragmentation route (Fisher 2004; Offner et al. 2010; Bate 2012), where turbulent fragmentation and orbit evolution can result in wide-separation, unequal mass binary systems.

While the null detection of a circumplanetary disk around GQ Lup b ($M_{\rm dust} < 0.04\ M_{\oplus}$) argues against *in situ* formation, its orbital parameters are

still consistent with such a model. Indeed, the models of Ginski et al. (2014) and Schwarz et al. (2016) do not exclude low eccentricity orbits as would be expected for a planet-like formation within a larger protoplanetary disk. The morphology of the GQ Lup A disk points against a scattering origin for the companion. There is no observational evidence for a sharp inner edge or cavity indicative of an additional companion in the system that may have scattered GQ Lup b out to its current position. Observations with higher angular resolution are needed to probe for any substructure in the circumprimary disk that would signify the influence of an additional companion, or features that may have resulted from a previous scattering event.

Schwarz et al. (2016) measure the projected rotational velocity of GQ Lup b to be $5.3^{+0.9}_{-1.0}$ km s^{-1}, making it a slow rotator compared to the giant planets in the Solar System and the recent measurement of β Pictoris b (Snellen et al. 2014). Objects formed through gravitational instability or core fragmentation seem to follow a spin-mass trend, where higher mass objects rotate faster than lower mass objects. The unusually slow spin of GQ Lup b could point to a different formation scenario, but, as Schwarz et al. (2016) point out, GQ Lup b is still quite young and will likely spin up over time, making its slow spin less discrepant.

2.6 Conclusions

We present new ALMA observations of 870 μm dust continuum and CO J=3–2 line emission from the GQ Lup system. These observations resolve the circumstellar disk surrounding GQ Lup A, and provide a deep upper limit on any emission from a

circumplanetary disk surrounding GQ Lup b. The main results are as follows.

1. The circumprimary disk appears compact with a FWHM of 59 ± 12 AU. Given the total flux density and assuming optically thin emission, we determine a total dust mass of $M_{\rm dust} = 15.10 \pm 0.04\ M_{\oplus}$.

2. There is no indication that the circumprimary disk traced by ^{12}CO and ^{13}CO emission is truncated or affected by the presence of the companion, GQ Lup b. The characteristic radius of the ^{13}CO emission is 46.5 ± 1.8 AU, more extended than the dust disk. By forward-modeling the Keplerian velocity field, we robustly constrain both the mass of the primary star, $M_* = (1.03 \pm 0.05) * (d/156\ {\rm pc})\ M_{\odot}$, and the geometry of the circumprimary disk, $i = 60\overset{\circ}{.}5 \pm 0\overset{\circ}{.}5$ and $PA = 346^{\circ} \pm 1^{\circ}$. An inclination of $i = 60^{\circ}$ is significantly higher than previous estimates of $20 - 30^{\circ}$. If the companion orbit is coplanar with the circumprimary disk, then this high inclination implies that the current physical separation of the secondary is ~ 220 AU.

3. We determine a robust 3σ upper limit on the flux density of any circumplanetary disk surrounding GQ Lup b of < 0.15 mJy. If we assume optically thin emission, then this implies an upper limit on the dust mass of $M_{\rm dust} < 0.04\ M_{\oplus}$. This limit is an order of magnitude lower than previous ALMA measurements for circumstellar disks around M5 and later sources of similar ages (~ 2 Myr). In the optically thick limit, we can instead derive an upper limit on the radius of the circumplanetary disk of $R_{\rm dust} < 1.1$ AU.

4. Since models of *in situ* formation of wide-separation, substellar companions through core fragmentation or gravitational instability predict massive

circumplanetary disks that persist for several Myrs, the lack of detections of such massive disks disfavors these formation scenarios.

Millimeter observations of additional systems with young substellar companions are needed to characterize the disk properties and to assess whether or not the features of the GQ Lup system are typical of the whole population. In addition, higher angular resolution is needed to probe for any substructure in circumprimary disks, like GQ Lup, that could indicate the presence of additional companions involved in dynamical evolution.

Acknowledgments

M.A.M acknowledges support from a National Science Foundation Graduate Research Fellowship (DGE1144152) and from NRAO Student Observing Support. This paper makes use of the following ALMA data: ADS/JAO.ALMA #2013.1.00374.S. ALMA is a partnership of ESO (representing its member states), NSF (USA) and NINS (Japan), together with NRC (Canada) and NSC and ASIAA (Taiwan) and KASI (Republic of Korea), in cooperation with the Republic of Chile. The Joint ALMA Observatory is operated by ESO, AUI/NRAO and NAOJ. The National Radio Astronomy Observatory is a facility of the National Science Foundation operated under cooperative agreement by Associated Universities, Inc. This work has also made use of data from the European Space Agency (ESA) mission *Gaia* (`http://www.cosmos.esa.int/gaia`), processed by the *Gaia* Data Processing and Analysis Consortium (DPAC,

http://www.cosmos.esa.int/web/gaia/dpac/consortium). Funding for the DPAC has been provided by national institutions, in particular the institutions participating in the *Gaia* Multilateral Agreement.

3

Constraints on Planetesimal Collision Models in Debris Disks

This thesis chapter originally appeared in the literature as

M. A. MacGregor, D. J. Wilner, C. Chandler, L. Ricci, S. T. Maddison,

S. R. Cranmer, S. M. Andrews, A. M. Hughes, A. Steele, 2016,

Astrophysical Journal, Vol. 823, pp. 79–92

Abstract

Observations of debris disks offer a window into the physical and dynamical properties of planetesimals in extrasolar systems through the size distribution of dust grains. In particular, the millimeter spectral index of thermal dust emission encodes information on the grain size distribution. We have made new VLA observations of a sample of seven nearby debris disks at 9 mm, with 3″ resolution and ~ 5 μJy/beam rms. We combine these with archival ATCA observations of eight additional debris

disks observed at 7 mm, together with up-to-date observations of all disks at (sub)millimeter wavelengths from the literature to place tight constraints on the millimeter spectral indices and thus grain size distributions. The analysis gives a weighted mean for the slope of the power law grain size distribution, $n(a) \propto a^{-q}$, of $\langle q \rangle = 3.36 \pm 0.02$, with a possible trend of decreasing q for later spectral type stars. We compare our results to a range of theoretical models of collisional cascades, from the standard self-similar, steady-state size distribution ($q = 3.5$) to solutions that incorporate more realistic physics such as alternative velocity distributions and material strengths, the possibility of a cutoff at small dust sizes from radiation pressure, as well as results from detailed dynamical calculations of specific disks. Such effects can lead to size distributions consistent with the data, and plausibly the observed scatter in spectral indices. For the AU Mic system, the VLA observations show clear evidence of a highly variable stellar emission component; this stellar activity obviates the need to invoke the presence of an asteroid belt to explain the previously reported compact millimeter source in this system.

3.1 Introduction

Debris disks represent the end stage of protoplanetary disk evolution. As such, they provide essential information on the processes of planet formation and circumstellar disk dispersion (see reviews by Backman & Paresce 1993; Wyatt 2008; Matthews et al. 2014). The small dust grains detected at optical through centimeter wavelengths are thought to be produced by the collisional erosion of larger bodies, analogous to comets or Kuiper Belt Objects, commonly referred to as planetesimals.

These kilometer-sized remnants of planet formation are effectively invisible around other stars, but emission from the dusty debris produced in ongoing collisions offers a unique window into their physical properties and dynamics. In particular, the spectral index of dust emission at millimeter to radio wavelengths encodes information on the grain size distribution within disks that can be used to constrain collisional models of planetesimals (Ricci et al. 2012, 2015b).

The dominant mechanism responsible for stirring the planetesimals within debris disks to incite collisions remains controversial. Stirring could be triggered by the ongoing formation of Pluto-sized bodies within the disk (Kenyon & Bromley 2002, 2008) or by the dynamical effects of fully formed planets (Mustill & Wyatt 2009). In either case, the reference model for dust production is the steady-state collisional cascade first formulated by Dohnanyi (1969). This model assumes that the relative velocities and tensile strengths of the colliding bodies are independent of size, and leads to a power law size distribution, $n(a) \propto a^{-q}$ with index $q = 3.5$. However, the fragmentation process in debris disks could be more complex. Recent analytic and numerical studies relax some of the restrictive assumptions of the reference model, and incorporate more realistic dynamics and material physics. Including a size-dependent velocity distribution predicts a steeper distribution, $q \sim 4$ (Pan & Schlichting 2012; Gáspár et al. 2012), while decreasing the tensile strength of the colliding bodies predicts a shallower distribution, $q \sim 3$ (Pan & Sari 2005).

We present observations of seven debris disks at 9 mm using the Karl G. Jansky Very Large Array (VLA) of the National Radio Astronomy Observatory. These long wavelength observations probe emission from the largest accessible dust grains in the disks. When combined with (sub)millimeter data, these observations provide

a long lever arm in wavelength that mitigates the impact of absolute calibration uncertainties on spectral index determinations. In addition, the spectral slopes at these long wavelengths are relatively insensitive to the effects of temperature, given typical debris belts at 10's of K. We combine this sample with observations of eight additional debris disks with the Australia Telescope Compact Array (ATCA) at 7 mm. By pairing these long wavelength measurements with previous observations at shorter (sub)millimeter wavelengths, we can determine the spectral index of the dust emission and thus the grain size power law index q for the combined sample of fifteen debris disks. We compare our results with predictions from existing collisional cascade models and explore the effects of material strengths, velocity distributions, and small-size cutoffs on the steady-state grain size distribution.

In Section 3.2 we present the VLA sample of debris disks. Sections 3.3 and 3.4 discuss the VLA observations, analysis, and results. In Section 3.5, we describe how we determine the slope of the grain size distribution, q, and we present the results for the combined VLA and ATCA sample of debris disks. In Section 3.6, we compare our results to predictions from collisional cascade models and discuss results from analytical modeling of a steady-state grain population. In Section 3.7, we summarize the main conclusions of this study.

3.2 VLA Sample

We selected a sample of seven debris disks to observe with the VLA at 9 mm to measure spectral indices and constrain the slope of the grain size distribution, q. The sample was assembled based on the following criteria:

1) accessible source declinations, $\delta > -35°$, 2) evidence in the literature for strong millimeter/submillimeter emission ($F_{0.85\text{mm}} \gtrsim 8$ mJy), and 3) small enough angular extent to obtain reliable total flux measurements using the most compact array configurations. Table 3.1 lists the source positions and stellar properties, and a brief discussion of each target follows. All of these disks have been studied extensively at other wavelengths and have well sampled spectral energy distributions (SEDs) through the far-infrared. In addition, most of these disks have interferometric data that resolve their millimeter emission structure, either from the Submillimeter Array (SMA) or the Atacama Large Millimeter/submillimeter Array (ALMA).

3.2.1 HD 377

HD 377 is a G2V star at a distance of 39.1 ± 2 pc (van Leeuwen 2007) with an estimated age of $\sim$ 150 Myr (Geers et al. 2012). Spectral energy distribution modeling indicates the presence of dust between 3 and 150 AU (Roccatagliata et al. 2009) and results in a two temperature component fit with a warmer inner belt at $T_{\text{dust}} \approx 130$ K and a colder outer belt at $T_{\text{dust}} \approx 50$ K (Morales et al. 2011; Panić et al. 2013). Choquet et al. (2015) recently detected HD 377 in reprocessed archival *Hubble Space Telescope* (*HST*) scattered light images. The disk was resolved at 870 μm with the SMA, revealing a symmetric belt of emission centered at $\sim$ 47 AU with a width of $\sim$ 32 AU (Steele et al. 2016). Greaves et al. (2012) did not detect the disk at $7.5 - 11.5$ mm with the Green Bank Telescope (GBT), but the noise level of 14 μJy/beam gave a 2σ upper limit on the disk flux of < 28 μJy. No gas has been detected in the system (Geers et al. 2012). Searches with VLT/NACO have not

Table 3.1: Debris Disk Sample Characteristics

Source	α (J2000)	δ (J2000)	SpT	L_* ($L_\odot$)	D[a] (pc)	Age (Myr)	PA[b] (°)	Disk gas?
HD 377	00 08 25.8	+06 37 00.5	G2	1.0	30	150	47	N
49 Ceti	01 34 37.8	−15 40 34.9	A1	20.	59	40	101	Y
HD 15115	02 26 16.3	+06 17 33.1	F2	3.3	45	21	279	N
HD 61005	07 35 47.5	−32 12 14.0	G8	0.5	35	40	70	N
HD 104860	12 04 33.7	+66 20 11.7	F8	1.4	48	140	1	N
HD 141569	15 49 57.8	−03 55 16.2	B9.5	21.	116	5	356	Y
AU Mic	20 45 09.8	−31 20 31.8	M1	0.1	10	21	128	N
q^1 Eri	01 42 29.3	−53 44 27.0	F9	1.2	17	4800	55	N
ϵ Eri	03 32 54.9	−09 27 29.4	K2	0.3	3	400–800	0	N
β Pic	05 47 17.1	−51 03 59.4	A6	8.7	19	21	32	Y
HD 95086	10 57 03.0	−68 40 02.5	A8	8.6	90	17	15	N
HD 107146	12 19 06.5	+16 32 53.9	G2	1.0	29	80–200	148	N
AK Sco	16 54 44.8	−36 53 18.6	F5	3.0	142	18	49	Y
HD 181327	19 22 58.9	−54 32 17.0	F6	3.3	51	12	107	N
Fomalhaut	22 57 39.0	−29 37 20.1	A4	16.	7	440	156	N

[a] All distances measured by van Leeuwen (2007)

[b] Position angle measured east of north to the disk major axis

References for stellar and disk properties: HD 377, Geers et al. (2012), Choquet et al. (2015); 49 Ceti, Torres et al. (2008), Hughes et al. (2008); HD 15115, Binks & Jeffries (2014), Kalas et al. (2007); HD 61005, Desidera et al. (2011), Hines et al. (2007); HD 104860, Steele et al. (2016); HD 141569, Weinberger et al. (2000), White et al. (2016b); AU Mic, Binks & Jeffries (2014), MacGregor et al. (2013); q^1 Eri, Butler et al. (2006), Liseau et al. (2008), Liseau et al. (2010); ϵ Eri, Mamajek (2008), Greaves et al. (2014); β Pic, Binks & Jeffries (2014), Dent et al. (2014), Heap et al. (2000); HD 95086, Meshkat et al. (2013), Su et al. (2015); HD 107146, Wichmann et al. (2003), Ardila et al. (2004); AK Sco, Pecaut et al. (2012), Czekala et al. (2015); HD 181327, Nordström et al. (2004), Schneider et al. (2006); Fomalhaut, Mamajek (2012), Kalas et al. (2005)

revealed the presence of any gas giant planets with masses between 3 and 7 $M_{\rm Jup}$ and separations of $20-50$ AU (Apai et al. 2008).

3.2.2 49 Ceti

49 Ceti is an A1V star at a distance of 59 ± 1 pc (van Leeuwen 2007) and a member of the Argus Association, indicating an age of ~ 40 Myr (Torres et al. 2008). The dust disk was resolved at 70 μm with *Herschel/PACS* (Roberge et al. 2013). SED modeling indicates that this disk has two distinct components, a cold ($T_{\rm dust} = 62 \pm 1$ K) outer disk extending from 40 to 200 AU and a warmer ($T_{\rm dust} = 175 \pm 3$ K) inner belt within 40 AU (Wahhaj et al. 2007; Hughes et al. 2008; Roberge et al. 2013). New ALMA observations at 850 μm are consistent with this picture and are best-fit by an inner belt of small dust grains between $\sim 4-60$ AU and an outer belt of larger grains between $\sim 60-300$ AU (Hughes et al. in prep).

In addition to the dust disk, 49 Ceti is notable for exhibiting substantial CO emission (Zuckerman et al. 1995; Dent et al. 2005; Hughes et al. 2008). Resolved (SMA) observations of CO emission in the 49 Ceti system reveal that the inner disk is devoid of gas, while the outer belt contains 0.02 ± 0.01 $M_\oplus$ of gas (Hughes et al. 2008). *Herschel* spectroscopy indicates that this gas cannot be primordial, and may instead be secondary material coming from the destruction of comet-like ices (Roberge et al. 2013).

3.2.3 HD 15115

HD 15115 ("the blue needle") is an F2V star at 45 ± 1 pc (van Leeuwen 2007) whose space motions suggest membership in the 21 ± 4 Myr-old (Binks & Jeffries 2014) β Pictoris moving group (Moór et al. 2011). An infrared excess suggesting orbiting dust was noted in *IRAS* observations (Silverstone 2000). Subsequent scattered light imaging from *HST* and other telescopes have resolved an asymmetric, edge-on circumstellar disk (Kalas et al. 2007; Debes et al. 2008; Rodigas et al. 2012; Mazoyer et al. 2014; Schneider et al. 2014). Observations of 850 μm emission using the James Clerk Maxwell Telescope/SCUBA-2 suggested the presence of a reservoir of large dust grains in the disk, with low temperature ($T_{\rm dust} = 56 \pm 9$ K). Observations at 1.3 mm with the SMA resolve a belt of emission at $\sim$ 110 AU with a width of $\sim$ 43 AU (MacGregor et al. 2015a). In addition, the millimeter emission shows a $\sim 3\sigma$ feature aligned with the asymmetric western extension of the scattered light disk. If real, this additional feature indicates that the distribution of larger grains in the disk may be asymmetric as well.

3.2.4 HD 61005

HD 61005 ("the moth") is a G8V star at a distance of 35 ± 1 pc (van Leeuwen 2007). An argument has been made for membership in the Argus Association, suggesting an age of $\sim$ 40 Myr (Desidera et al. 2011). The presence of dust was originally inferred from a significant *Spitzer* infrared excess (Carpenter et al. 2005), and follow-up *HST* images revealed a remarkable swept-back disk in scattered light

that extends from $\lesssim 10$ to 240 AU (Hines et al. 2007; Maness et al. 2009). The SED is best fit by a belt with $T_{\rm dust} \approx 80$ K at ~ 90 AU. The disk was resolved at 1.3 mm with the SMA, and the continuum emission is fit by a narrow belt ($\Delta R/R = 0.05$) at ~ 70 AU (Ricarte et al. 2013; Steele et al. 2016). There is no indication that the dramatic scattered light asymmetry persists at millimeter wavelengths. Given the wavelength-dependent nature of the belt morphology, it is possible that the observed swept-back features result from interactions with the interstellar medium, which would be expected to affect only smaller grains (Maness et al. 2009).

3.2.5 HD 104860

HD 104860 is an F8 zero age main sequence star ($\sim$ 140 Myr) at a distance of 48 ± 2 pc (van Leeuwen 2007). The SED is well fit by a single temperature component at a radius of 105 AU and $T_{\rm dust} = 33 \pm 3$ K (Najita & Williams 2005; Roccatagliata et al. 2009; Pawellek et al. 2014). The disk was resolved at 70, 100, and 160 μm with *Herschel* (Morales et al. 2013), and these observations are best fit by including a second warm, less massive dust belt at ~ 5 AU with $T_{\rm dust} \approx 190$ K. SMA observations at 1.3 mm reveal an axisymmetric, broad belt at ~ 110 AU with a width of ~ 100 AU (Steele et al. 2016). GBT observations at $7.5 - 11.5$ mm (Greaves et al. 2012) placed a 2σ upper limit on the disk flux of < 24 μJy. No gas has been detected in the system (Najita & Williams 2005).

3.2.6 HD 141569

The HD 141569 system consists of HD 141569A, a young ~ 5 Myr-old B9.5V star at 116 ± 8 pc (van Leeuwen 2007), and a pair of low mass comoving companions with spectral types M2 and M4 located $\sim 7\farcs5$ away (Weinberger et al. 2000). Despite its young age, the star is surrounded by a highly evolved late-stage transition or early debris disk. The morphology of this disk is complex. Scattered light and near-infrared imaging reveal asymmetric spiral structures between $\sim 175 - 210$ AU and $\sim 300 - 400$ AU (Weinberger et al. 2000; Mouillet et al. 2001; Clampin et al. 2003; Biller et al. 2015). While this outer spiral structure is truncated at 175 AU, there is an additional inner debris belt between 10 and 50 AU (White et al. 2016b) with a dust temperature of $T_{\rm dust} \approx 80$ K determined from SED modeling (Nilsson et al. 2010).

In addition to dust, this system contains between 20 and 460 $M_\oplus$ of gas (Zuckerman et al. 1995; Thi et al. 2014). Most of this gas is associated with the outer part of the disk and distributed non-uniformly in two ring-like structures at ~ 90 and 250 AU (Dent et al. 2005). However, near-infrared observations indicate that there is additional CO gas distributed between 10 and 50 AU, commensurate with the inner debris system (Brittain & Rettig 2002; Goto et al. 2006). Recent SMA and CARMA observations at 870 μm and 2.8 mm, respectively, resolve the gas disk (Flaherty et al. 2016) and reveal a large inner hole in the CO gas distribution interior to ~ 29 AU and an outer edge at ~ 224 AU, interior to the previously imaged scattered light rings. Additionally, these observations yield $T_{\rm gas} \sim 27$ K, lower than the dust temperature.

3.2.7 AU Mic

AU Mic is a nearby (9.91 ± 0.10 pc; van Leeuwen 2007) M1V star in the β Pictoris moving group, suggesting an age of 23 ± 3 Myr (Mamajek & Bell 2014). The star is surrounded by a nearly edge-on circumstellar disk extending to a radius of at least 210 AU, discovered in coronographic images of scattered starlight (Kalas et al. 2004). ALMA Cycle 0 observations at 1.3 mm revealed (1) an outer belt with an emission profile that rises with radius out to 40 AU and (2) a newly recognized central peak that remained unresolved (MacGregor et al. 2013). The outer dust belt shows no evidence of asymmetries and is characterized by a dust temperature of $T_{\rm dust} \approx 25$ K. The central peak is ~ 6 times brighter than the expected stellar photosphere, indicating an additional emission process in the inner region of the system, either a warm ($T_{\rm dust} \approx 75$ K) planetesimal belt or a hot stellar chromosphere or corona (Cranmer et al. 2013; Schüppler et al. 2015). AU Mic is also well known to be a rich source of stellar flaring activity, notably at X-ray (Mitra-Kraev et al. 2005; Schneider & Schmitt 2010) and ultraviolet (Robinson et al. 2001) wavelengths.

3.3 VLA Observations

VLA observations for six of the seven sources in the sample were carried out between June and August 2014 at a wavelength of 9 mm (Ka band). Two 120-minute scheduling blocks (SBs) were observed in the D configuration (baseline lengths 0.04 to 1.03 km) for all disks except HD 141569, where only one SB was executed. HD 61005 was observed in the DnC configuration (with north-south baselines to

2.11 km, for its southern declination). We observed AU Mic, the seventh source, in June and July 2013 with two 105-minute SBs in the D configuration and one 105-minute SB in the C configuration (baseline lengths 0.05 to 3.38 km). Table 3.2 summarizes the essentials of these observations, including the observation dates, array configurations, number of antennas, baseline lengths, weather conditions, on-source time, and the gain calibrators used. Overall, the weather conditions were very good for these summer observations (rms of $< 6^\circ$ measured with the Atmospheric Phase Interferometer at 11.7 GHz). The total bandwidth available for all observations was 8 GHz, split into 4×2 GHz basebands centered at 30, 32, 34, and 36 GHz. The characteristic rms for these observations was ~ 5 μJy/beam and the typical natural weight beam FWHM was $\sim 3''$.

The data from each track were calibrated separately using the `CASA` software package. The passband shape was calibrated using available bright sources, mainly J0319+4130, J0609-1542, J1256-0547, and J1924-2914. Observations of 3C48 and 3C286 during each track were used to derive the absolute flux scale, with an estimated accuracy of $< 10\%$. Imaging and deconvolution were performed with the `CLEAN` task in `CASA` (version 4.3.1).

3.4 Results of the VLA Observations

Figure 3.1 shows the VLA 9 mm images for the six detected debris disks in the sample. HD 377 was undetected. For the detected disks, the peak signal-to-noise ratio achieved ranges between $\sim 4\sigma$ (HD 15115 and HD 104860) and $\sim 16\sigma$ (HD 141569).

Table 3.2: VLA Observations

Source	Obs. Date	Config.	Ant.	Baseline Lengths (km)	API[a] rms (°)	On-source Time (min)	Gain Calibrator(s)
HD 377	2014 Jul 3	D	27	0.04 – 1.31	6.6	64.8	J0011+0823
	2014 Jul 10	D	26	0.04 – 1.31	5.6	62.1	
49 Ceti	2014 Jul 13	D	27	0.04 – 1.31	5.8	63.3	J0132−1654
	2014 Jul 14	D	25	0.04 – 1.31	3.4	66.4	
HD 15115	2014 Jul 8	D	26	0.04 – 1.31	3.0	65.7	J0224+0659
	2014 Jul 11	D	26	0.04 – 1.31	3.1	65.6	
HD 61005	2014 Sep 19	DnC	27	0.04 – 2.11	1.5	62.0	J0747−3310
	2014 Sep 20	DnC	27	0.04 – 2.11	3.3	62.2	
HD 104860	2014 Aug 30	D	27	0.04 – 1.31	5.3	61.4	J1220+7105
	2014 Aug 30	D	27	0.04 – 1.31	4.6	61.2	
HD 141569	2014 Jun 6	D	25	0.04 – 1.31	4.0	61.5	J1557−0001
AU Mic	2013 May 9	DnC	27	0.04 – 2.11	4.1	49.7	J2101−2933
	2013 May 11	DnC	27	0.04 – 2.11	2.8	49.9	
	2013 Jun 21	C	27	0.05 – 3.38	1.3	50.0	

[a] Measure of the tropospheric contribution to the interferometric phase determined by the Atmospheric Phase Interferometer (API), an interferometer comprised of two 1.5-m antennas separated by 300 m, observing an 11.7 GHz beacon from a geostationary satellite.

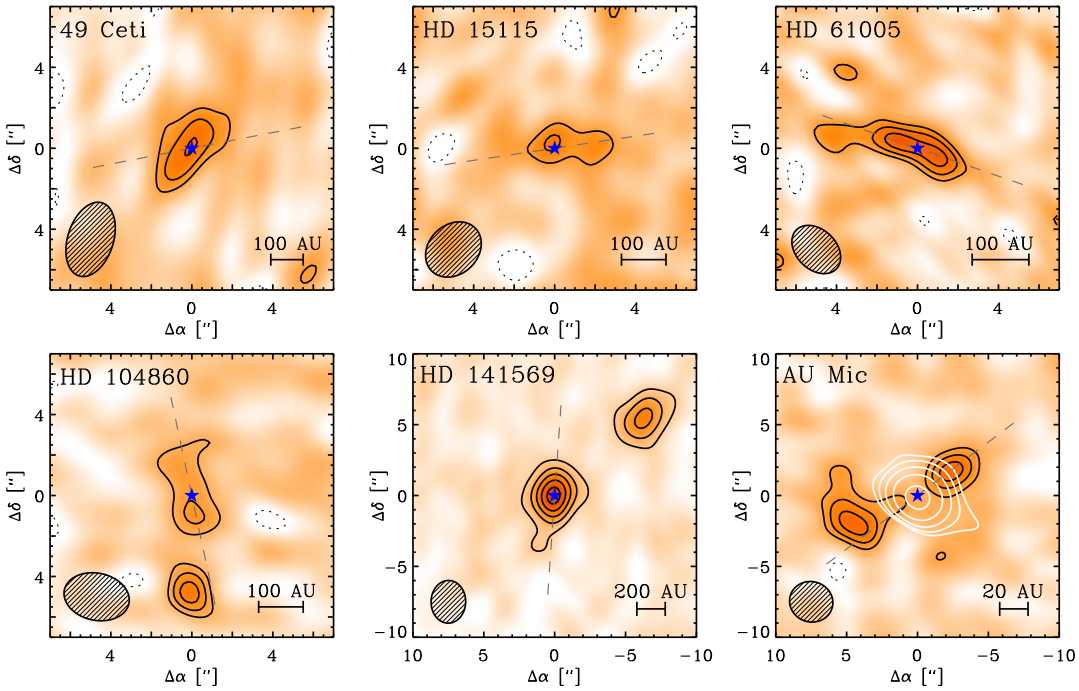

Figure 3.1: Images of the 9 mm continuum emission from the six debris disks detected in the VLA sample. Contour levels are in steps of $[2, 3, 4, 6]$ × rms for all images, except HD 141569 (lower center) where contours are in steps of 3 × rms (characteristic rms $\sim$ 5 μJy). The white contours in the AU Mic image (lower right) mark the subtracted stellar component in steps of $[10, 20, 40, 80, 160]$ × rms. The ellipse in each lower left corner indicates the synthesized beam size. The star symbol marks the position of the stellar photosphere. The dashed gray line indicates the position angle of the disk determined from previous optical, near-infrared, or millimeter imaging and listed in Table 3.1.

The 49 Ceti and HD 141569 disks are unresolved by these observations. The HD 15115, HD 61005, and HD 104860 disks are all marginally resolved, appearing extended in the direction of their position angles as determined from previous optical, near-infrared, and millimeter imaging. Indeed, the HD 15115 disk shows a hint (at a $\sim 2\sigma$ level) of the same asymmetric western extension seen in previous optical and millimeter imaging (MacGregor et al. 2015a). For all five of these disks, the total flux density was determined by integrating the surface brightness over

the area showing continuum emission at $\gtrsim 2\sigma$ above the background rms in the image. The total uncertainty on the 9 mm flux density was taken to be the rms noise measured for the image added in quadrature with the 10% uncertainty in the absolute flux calibration. For HD 377, we obtain a 3σ upper limit on the total disk flux density. Table 3.3 lists the synthesized beam size and position angle, the measured 9 mm flux density, and the rms for all of the sources in the sample.

Table 3.3: Results of the VLA Observations

Source	Beam Size[a] ($''$)	Beam P.A.[b] (deg.)	$F_{9\mathrm{mm}}$ (μJy)	rms Noise (μJy/beam)
HD 377	2.8×2.4	21.2	< 13.1	4.4
49 Ceti	3.8×2.6	339.6	25.1	5.5
HD 15115	3.0×2.4	314.0	12.8	4.1
HD 61005	2.6×2.0	45.6	57.3	8.6
HD 104860	3.1×2.3	75.6	14.0	3.5
HD 141569	3.0×2.4	338.6	85.0	5.1
AU Mic	3.1×2.8	41.0	> 60.8	5.2

[a] Beam size determined with natural weighting
[b] Beam position angle measured from east of north

AU Mic is the only disk that is well resolved in the sample. The C configuration affords high angular resolution (beam size $< 1''$, corresponding to < 10 AU at the distance of AU Mic) relative to the extent of the disk. This high resolution allows us to separate emission from the the central star and the disk. The star is very active at radio wavelengths, flaring on timescales shorter than the scheduling blocks. We were able to isolate the disk emission by subtracting a time-dependent point source model from the data to account for the stellar emission. In doing this, we could not avoid subtracting out some disk emission co-located with the star. We estimated the

total flux density as for the other disks in the sample. However, the result obtained should be considered a lower limit to the disk emission. A detailed account of the stellar emission observed in the AU Mic system is included in Appendix A.

3.5 Determining the Slope of the Grain Size Distribution q

We adopt the method of Ricci et al. (2012, 2015b) who used ATCA observations at 7 mm to constrain the millimeter grain size distribution of six debris disks. Since the thermal dust emission from debris disks is optically thin, the flux density is given by $F_\nu \propto B_\nu(T_{\rm dust})\kappa_\nu M_{\rm dust}/D^2$, where $B_\nu(T_{\rm dust})$ is the Planck function at the dust temperature $T_{\rm dust}$, $\kappa_\nu \propto \nu^\beta$ is the dust opacity, expressed as a power law at long wavelengths, $M_{\rm dust}$ is the total dust mass in the disk, and D is the distance. Draine (2006) derived a relation between β, the dust opacity power law index, and q, the grain size distribution parameter: $\beta = (q-3)\beta_s$, where, β_s is the dust opacity spectral index of small (i.e. much smaller than the observing wavelength) particles. For size distributions that follow a power law with $3 < q < 4$ from blow-out grain sizes (on the order of $\sim \mu$m) to larger planetesimals ($\sim 1 - 100$ km), $\beta_s = 1.8 \pm 0.2$, consistent with observations of both diffuse and dense interstellar clouds. It should be noted, that given the restrictive assumption of $3 < q < 4$, this relation could prove inaccurate for any disks that have a size distribution index outside of this range. Additionally, for dust compositions with large fractions of amorphous carbons or ices, values of β_s can drop to ~ 1.4 (e.g. 'cel800' produced by

the pyrolysis of cellulose at 800° C in Draine 2006), resulting in higher q values for a given β. For a representative case, where $\beta = 0.5$, $q = 3.28$ and 3.36 for $\beta_s = 1.8$ and 1.4, respectively. The change in q due to a change in β_s is ~ 0.08 in this case, comparable to the uncertainties on q derived by our analysis. Since we do not expect this effect to be large, and given our limited knowledge of the grain compositions in the debris disks in our sample, we assume $\beta_s = 1.8$ for the purposes of our analysis. This relation between β and q has been found to be very accurate for different dust models considered in the literature to interpret the millimeter wavelength emission of young circumstellar disks (see e.g. D'Alessio et al. 2001; Ricci et al. 2010b,a).

For debris disks around solar-type and earlier stars, the dust is typically warm enough ($k_B T_{\rm dust} >> h\nu$) for the Planck function at long wavelengths to reduce to the Rayleigh-Jeans approximation $B_\nu(T_{\rm dust}) \propto \nu^2$. A more accurate expression can be obtained by approximating the Planck function as a power law $B_\nu(T_{\rm dust}) \propto \nu^{\alpha_{\rm Pl}}$, where $\alpha_{\rm Pl} = \alpha_{\rm Pl}(T_{\rm dust}) \lesssim 2$ (and $= 2$ in the Rayleigh-Jeans limit). Given two frequencies, the spectral index $\alpha_{\rm Pl}$ of the Planck function between ν_1 and ν_2 can be expressed as

$$\alpha_{\rm Pl} = \left| \frac{\log(B_{\nu_1}/B_{\nu_2})}{\log(\nu_1/\nu_2)} \right| \tag{3.1}$$

Substituting the Taylor expansion of B_ν to second order yields the following approximation for the spectral index:

$$\alpha_{\rm Pl} \approx 2 + \frac{\log\left(\frac{2k_B T_{\rm dust} - h\nu_1}{2k_B T_{\rm dust} - h\nu_2}\right)}{\log(\nu_1/\nu_2)} \tag{3.2}$$

For our purposes, the spectral index of the Planck function can be approximated by the Rayleigh-Jeans solution with a correction that depends on the dust temperature $T_{\rm dust}$ and observing frequencies used to determine the millimeter spectral index.

Observationally, the flux density of debris disks at millimeter and centimeter wavelengths can be described by a simple power law $F_\nu \propto \nu^{\alpha_{\rm mm}}$, where $\alpha_{\rm mm} = |\log(F_{\nu_1}/F_{\nu_2})/\log(\nu_1/\nu_2)|$.

Combining these relationships provides a simple expression for the slope of the grain size distribution, q as a function of $\alpha_{\rm mm}$, $\alpha_{\rm Pl}$, and β_s:

$$q = \frac{\alpha_{\rm mm} - \alpha_{\rm Pl}}{\beta_s} + 3 \tag{3.3}$$

Thus, by measuring the millimeter spectral index, $\alpha_{\rm mm}$, and by inferring $\alpha_{\rm Pl}$ from the dust temperature for each disk, we can determine the slope of the grain size distribution, q.

3.5.1 Estimated q Values for the Complete Sample

We complement the VLA 9 mm observations of the seven debris disks with ATCA 7 mm observations of eight additional debris disks (system characteristics listed in Table 3.1) analyzed in previous papers. Results for Fomalhaut were presented by Ricci et al. (2012), and results for q^1 Eri, β Pic, HD 95086, HD 107146, and HD 181327 were presented by Ricci et al. (2015b). For HD 181327 and HD 95086, we have recalculated spectral indices given newly available ALMA measurements. For q^1 Eri, we have recalculated the spectral index using the flux measurement at

870 μm from APEX (Liseau et al. 2008), to be closer to the Rayleigh-Jeans regime for a more accurate determination of the spectral slope. Su et al. (2015) suggest that previous flux measurements of HD 95086 are likely contaminated by emission from the extragalactic background. Any such background galaxies are included within the ATCA beam and not resolved from the disk. Given this situation, which may well apply to other sources, we simply use the total flux density within the beam in the analysis. The ϵ Eridani debris disk, which was not detected at 7 mm with ATCA (MacGregor et al. 2015b), provides an upper limit on the spectral index in combination with resolved observations at 1.3 mm from the SMA. We have also included archival ATCA observations of AK Sco, a $\sim$ 18 Myr-old binary system with a massive ($\sim 5 - 10\ M_{\rm Jup}$) circumbinary disk of gas and dust (Czekala et al. 2015). Given its age, there is some debate as to whether this system is a long-lived disk of primordial origin or a second-generation debris disk. We choose to include it in the sample to examine the effects gas might have on collisional cascade properties (see Section 3.5.2). We used the `uvfit` routine in Miriad to fit a point source model to the ATCA 7 mm AK Sco visibilities and obtained a total flux density of $F_{7\rm mm} = 430.0 \pm 18.2$ μJy. Figure 3.2 shows images of the 7 mm continuum emission from the debris disks detected by ATCA (excluding Fomalhaut).

Table 3.4 lists a previously reported flux density of each disk in the sample at a given (sub)millimeter wavelength, and we use these values combined with the VLA 9 mm and ATCA 7 mm fluxes to determine a millimeter spectral index, $\alpha_{\rm mm}$. Eight of the disks in the sample have flux measurements from ALMA data available. For the remaining seven disks, we used flux measurements from the SMA, JCMT/SCUBA, and APEX as available. The reported uncertainties for these

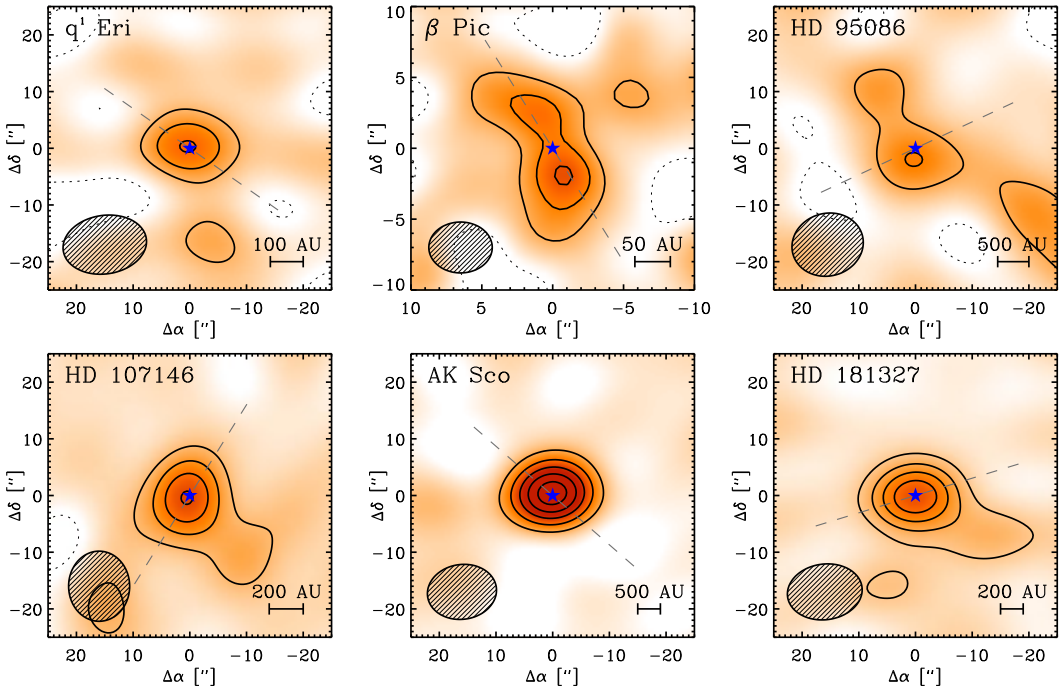

Figure 3.2: Images of the 7 mm continuum emission from six debris disks detected in the ATCA sample. Contour levels are in steps of 2 × rms for all images, except AK Sco (lower center) where contours are in steps of 4 × rms (characteristic rms $\sim$ 14 μJy). The ellipse in each lower left corner indicates the synthesized beam size. The star symbol marks the position of the stellar photosphere. The dashed gray line indicates the position angle of the disk determined from previous optical, near-infrared, or millimeter imaging and listed in Table 3.1.

(sub)millimeter flux measurements include a 10% uncertainty in the absolute flux density calibration added in quadrature to the statistical uncertainties. Table 3.4 also presents the dust temperature ($T_{\rm dust}$), the spectral index of the Planck function ($\alpha_{\rm Pl}$), and the slope of the grain size distribution (q) derived using Equation 3.3. For all of the disks, the dust temperature was inferred by assuming radiative equilibrium with the central star: $T_{\rm dust} = (L_*/16\pi\sigma R_{\rm dust}^2)^{1/4}$. Here, we used established stellar properties to determine L_* and resolved (sub)millimeter imaging to estimate a characteristic radius for the dust, $R_{\rm dust}$. The uncertainties on $R_{\rm dust}$ and $T_{\rm dust}$

are conservatively estimated to be 20% and 10%, respectively. Given $T_{\rm dust}$ and the two frequencies used to measure $\alpha_{\rm mm}$, we determined $\alpha_{\rm Pl}$ for each disk using the relationship derived in Equation 3.2. The final uncertainty on q results from propagating the errors on $\alpha_{\rm mm}$, $\alpha_{\rm Pl}$, and β_S.

For the complete sample, q values range from 2.84 (HD 141569) to 3.64 (HD 104860). The weighted mean of these q values is $\langle q \rangle = 3.36 \pm 0.02$. This result is consistent with previous work by Ricci et al. (2015), which presented results for five of the debris disks included in this larger sample and obtained a weighted mean of $\langle q \rangle = 3.42 \pm 0.03$.

3.5.2 Trends in q with Stellar and Disk Properties

With this larger sample, we can not only determine a weighted mean value of q, but begin to look for trends with stellar and system characteristics. The stars in the sample span a wide range of ages ($5 - 4800$ Myr) and spectral types (A−M). Table 3.1 lists the characteristics of the stars in the full sample, including age, spectral type, luminosity, distance, and whether or not gas has been detected in the disk.

We first consider trends with stellar properties, namely age and spectral type. There does not seem to be any correlation between system age and grain size distribution. For disks with estimated ages < 100 Myr (49 Ceti, HD 15115, HD 61005, HD 141569, AU Mic, β Pic, HD 95086, Ak Sco, and HD 181327), the weighted mean is $\langle q \rangle = 3.36 \pm 0.02$. Disks with estimated ages > 100 Myr (HD 377, HD 104860, q^1 Eri, ϵ Eri, HD 107146, and Fomalhaut) have a weighted mean of

Table 3.4: Grain Size Distribution Slopes (q)

Source	(Sub)mm λ (mm)	(Sub)mm Instr.	$F_{\rm mm}$ (mJy)	Ref.[a]	$\alpha_{\rm mm}$	$R^{\rm b}_{\rm dust}$ (AU)	Ref.[a]	$T^{\rm c}_{\rm dust}$ (K)	$\alpha_{\rm Pl}$	q
HD 377	0.87	SMA	3.5 ± 1.0	1	> 2.39	50	1	44	1.92 ± 0.02	> 3.26
49 Ceti	0.85	ALMA	17 ± 3	2	2.76 ± 0.11	120	2	55	1.94 ± 0.01	3.46 ± 0.08
HD 15115	1.3	SMA	2.6 ± 0.6	3	2.75 ± 0.15	110	15	45	1.92 ± 0.02	3.46 ± 0.10
HD 61005	1.3	SMA	7.2 ± 0.3	4	2.49 ± 0.08	70	4	30	1.91 ± 0.03	3.32 ± 0.06
HD 104860	1.3	SMA	4.4 ± 1.1	1	3.08 ± 0.23	110	1	28	$1.90^{+0.02}_{-0.04}$	3.64 ± 0.15
HD 141569	0.87	ALMA	3.78 ± 0.45	5	1.63 ± 0.06	30	5	109	1.97 ± 0.02	2.84 ± 0.05
AU Mic	1.3	ALMA	7.14 ± 0.15	6	< 2.46	20	6	25	$1.90^{+0.03}_{-0.07}$	< 3.31
q^1 Eri	0.87	APEX	39.4 ± 4.1	7	2.94 ± 0.10	85	7	33	$1.88^{+0.02}_{-0.04}$	3.59 ± 0.08
ϵ Eri	1.3	SMA	17.2 ± 5.0	8	> 2.39	64	8	27	$1.89^{+0.03}_{-0.06}$	> 3.28
β Pic	0.87	ALMA	60 ± 6	9	2.81 ± 0.10	85	9	52	1.93 ± 0.01	3.49 ± 0.08
HD 95086	1.3	ALMA	3.1 ± 0.18	10	2.37 ± 0.15	90	16	50	1.93 ± 0.01	3.24 ± 0.10
HD 107146	1.25	ALMA	12.5 ± 1.3	11	2.55 ± 0.11	60	11	30	$1.90^{+0.05}_{-0.02}$	3.36 ± 0.07
AK Sco	1.3	ALMA	32.65 ± 0.07	12	2.62 ± 0.03	14	12	95	1.97 ± 0.01	3.36 ± 0.04
HD 181327	1.3	ALMA	7.5 ± 0.1	13	2.38 ± 0.05	90	17	60	1.94 ± 0.01	3.24 ± 0.05
Fomalhaut	0.85	SCUBA	97.0 ± 5.0	14	2.70 ± 0.17	135	18	48	1.91 ± 0.02	3.44 ± 0.11

[a] References: 1) Steele et al. (2016), 2) Hughes et al. (in prep), 3) MacGregor et al. (2015a), 4) Ricarte et al. (2013), 5) White et al. (2016b), 6) MacGregor et al. (2013), 7) Liseau et al. (2008), 8) MacGregor et al. (2015b), 9) Dent et al. (2014), 10) Su et al. (2016, in prep), 11) Ricci et al. (2015a), 12) Czekala et al. (2015), 13) Marino et al. (2016), 14) Ricci et al. (2012), 15) MacGregor et al. (2015a), 16) Su et al. (2015), 17) Stark et al. (2014), 18) Boley et al. (2012)

[b] Uncertainty on $R_{\rm dust}$ assumed to be 20%

[c] Uncertainty on $T_{\rm dust}$ assumed to be 10%

$\langle q \rangle = 3.35 \pm 0.02$, consistent with the other subsample within the uncertainties. A Kolmogorov-Smirnov (K-S) test gives a 85% probability that these two subsamples are drawn from the same distribution. However, we notice a tentative trend with spectral type. If we arbitrarily choose to separate the sample into two groups by spectral type, then the weighted mean is $\langle q \rangle = 3.40 \pm 0.02$ for stars with spectral types A−F (49 Ceti, HD 15115, HD 61005, HD104860, HD 141569, q^1 Eri, β Pic, HD 95086, AK Sco, and HD 181327) and $\langle q \rangle = 3.30 \pm 0.03$ for spectral types G−M (HD 377, HD 61005, AU Mic, ϵ Eridani, and HD 107146). Given the uncertainties, these two subsamples differ in q by $\sim 3\sigma$. The clear outlier in the sample is HD 141569, with a q value of 2.84 ± 0.03 (discussed in Section 3.6.4). If we exclude this source from the sample, the weighted mean for A−F stars is $\langle q \rangle = 3.45 \pm 0.02$, different from the other subsample by $\sim 5\sigma$. A Spearman's rank correlation measure of statistical dependence between two variables indicates that this trend is significant at 96% confidence. A K-S test gives a probability of only 15% that these two subsamples are drawn from the same distribution. Given the small number statistics (there are noticeably fewer late type stars in the sample), we cannot draw any firm conclusions. However, this is suggestive that stars with later spectral types may exhibit shallower grain size distributions. Interestingly, Pawellek et al. (2014) also note a trend of increasing q values for more luminous stars, determined from mid- to far-infrared observations probing smaller grain sizes.

It is also plausible that characteristics of the disks themselves, regardless of stellar properties, might affect the grain size distribution. Four of the disks in the sample have robust detections of gas: 49 Ceti, HD 141569, β Pic, and AK Sco. For these disks with gas, $\langle q \rangle = 3.33 \pm 0.03$ including HD 141569, and $\langle q \rangle = 3.42 \pm 0.03$

omitting HD 141569, neither value differing from the mean of the full sample by $> 3\sigma$. The K-S probability for these two subsamples is 92%. However, since there are only four disks with detections of gas in the sample, observations of more debris disks are needed to address the effect of disk gas on grain size distribution.

3.6 Discussion

We have performed interferometric observations of a sample of seven debris disks at 9 mm with the VLA and supplemented them with observations of eight debris disks observed with ATCA at 7 mm. By combining these long wavelength flux densities with previous (sub)millimeter measurements, we have determined a millimeter spectral index and inferred the slope of the grain size distribution, q. The weighted mean of the q values in the complete sample is $\langle q \rangle = 3.36 \pm 0.02$.

We now compare these new results for the full sample to theoretical models of collisional cascades. In particular, we consider the effects of incorporating alternative velocity distributions (Section 3.6.1), material strengths (Section 3.6.2), and radiation pressure blowout (Section 3.6.3) on the resulting grain size distributions in debris disks.

3.6.1 Comparison to Collisional Models

The reference model for dust production in debris disks is the steady-state catastrophic collisional cascade. In this model, smaller 'bullets' shatter larger 'targets' through collisions. Assuming conservation of mass, this shattering recipe

leads to a power law size distribution of colliding bodies with radius a within the disk, $n(a) \propto a^{-q}$. A detailed description of the analytic treatment of collisional cascades can be found in Pan & Sari (2005) and Pan & Schlichting (2012).

The benchmark model of collisional cascades is presented by Dohnanyi (1969). Using laboratory experiments, Dohnanyi formulated a model of collisions in the Asteroid Belt, where bodies dominated by material strength have an isotropic velocity dispersion and collisions occur between bodies of roughly the same size. Given these assumptions, Dohnanyi obtains the classic result of $q = 7/2$ in steady-state.

If the assumption that the bodies participating in the collisional cascade have a single velocity dispersion regardless of size is relaxed, then steeper grain size distributions can be produced. Pan & Schlichting (2012) extend the Dohnanyi (1969) formulation of collisional cascades by accounting for viscous stirring, dynamical friction, and collisional damping in addition to the mass conservation requirement already discussed. For collisions between equal-sized, strength-dominated bodies, accounting for a size-dependent velocity distribution where velocity decreases with decreasing particle size yields $3.64 \leq q \leq 4$. If, instead, the velocity *increases* with decreasing particle size, then shallower size distributions are produced. This scenario makes sense for particles close to the blowout size, where radiation pressure strongly affects the particles' velocities. Given a population of grains with velocity function $v \propto a^p$ and material strength parameterized by $Q_D^* \propto a^\gamma$, Pan & Schlichting (2012) give a simple formulation for q as a function of γ and p: $q = \frac{21+\gamma-2p}{6+\gamma-2p}$. For small grains ($a \lesssim 1$ mm) strongly affected by radiation pressure, the collision velocities are expected to be proportional to the radiation-pressure induced eccentricities and

$p \approx -1$. For strength-dominated particles, $0 \geq \gamma > -1/2$. Given a representative value of $\gamma = -0.3$, this formulation yields $q = 2.95$. For the somewhat larger (sub)millimeter particles probed by our observations, it is plausible to expect q values somewhere between this estimation and Dohnanyi's $q = 3.5$.

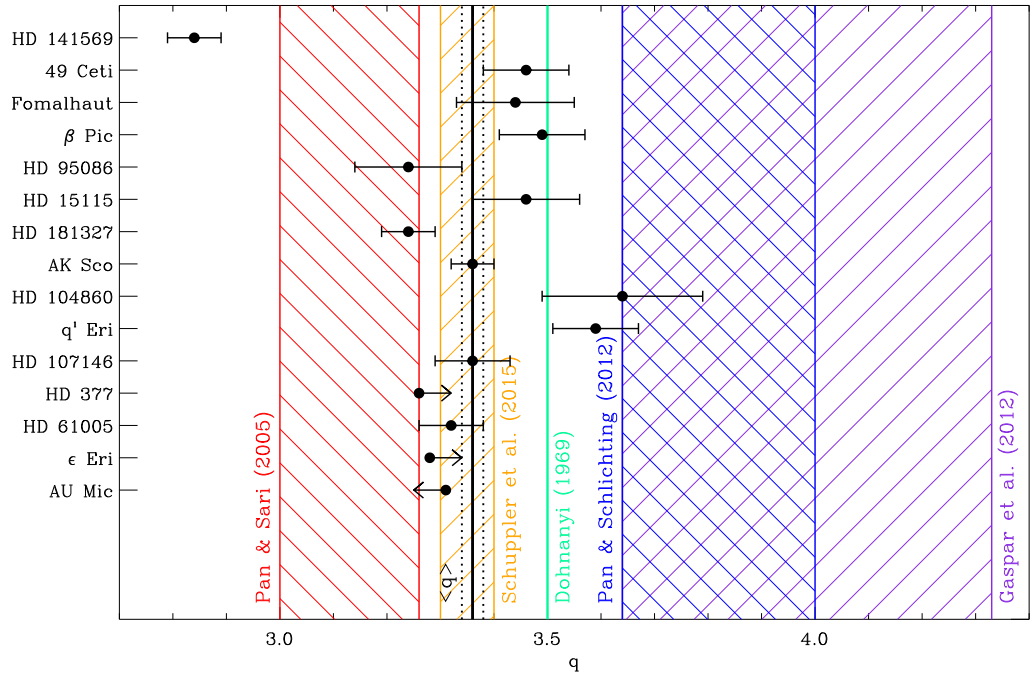

Figure 3.3: Distribution of power law index q values for the full sample of debris disks together with model predictions. Black data points indicate the values for the individual disks in the sample, with the weighted mean and uncertainty, $q = 3.36 \pm 0.02$, shown by the solid and dotted black lines, respectively. Stars have been ordered by luminosity from top to bottom (see Table 3.1 for specific luminosity values). The solid lines and dashed regions indicate different model predictions: (red) 'rubble pile' planetesimals not dominated by material strength (Pan & Sari 2005), (orange) results of the ACE numerical model for AU Mic (Schüppler et al. 2015), (green) the classic Dohnanyi (1969) result, (purple) numerical results of Gáspár et al. (2012), and (blue) incorporating a size-dependent velocity distribution (Pan & Schlichting 2012).

A number of other numerical models incorporate more realistic physics in order to model the grain size distributions in debris disks. Gáspár et al. (2012) explored

the evolution of collisional cascades in debris disks using numerical models. They varied a total of 21 variables in their models describing the geometry of the system, the strength of the colliding bodies, and the outcome of collisions. In steady-state, these calculations yield a range of $q \approx 3.64 - 4.33$. Löhne et al. (2012) use the ACE (Analysis of Collisional Evolution, see e.g. Krivov et al. 2013) code, which takes into account grain material strength, mutual gravity, and the relative orientation of the orbits of colliding particles, to model the size distribution for HD 207129. Schüppler et al. (2014) and Schüppler et al. (2015) use the same numerical code to model the size distributions of HIP 17439 and AU Mic, respectively. For grain sizes between 10 μm and 1 mm, these models yield q values between 3.3 and 3.4 for all three systems. Additionally, Thébault & Wu (2008) suggest that the grain size distribution should depend on the degree of dynamical excitation of the dust-producing planetesimals. In disks with parent bodies in low-eccentricity, low-inclination orbits, the resulting size distribution should be flatter than classical collisional cascade models. Pawellek & Krivov (2015) use the ACE code to examine this prediction and obtain $q \sim 3$ for grains of size $a = \frac{a_{\rm bl}}{2e}$, where $a_{\rm bl}$ is the blowout size and e is the mean eccentricity of parent bodies. For larger grains, $100 < a < 1000$ μm, the slope is closer to $\sim 3.3 - 3.4$.

Figure 3.3 shows the distribution of q values from the fifteen debris disks in the sample along with the steady-state model predictions of Dohnanyi (1969), Pan & Sari (2005), Schüppler et al. (2015), Gáspár et al. (2012), and Pan & Schlichting (2012). The weighted mean of the sample, $\langle q \rangle = 3.36 \pm 0.02$, is comparable to the classic Dohnanyi (1969) solution of $q = 3.5$, but still differs formally by $\sim 7\sigma$. Models of specific debris disk systems using the ACE numerical code (e.g. Löhne

et al. 2012; Schüppler et al. 2014, 2015) yield q values between $\sim 3.3 - 3.4$, lower than classical collisional cascade models and comparable to the weighted mean of our sample. Gáspár et al. (2012) obtain some q values from their models that are comparable to the observed mean value, but only by increasing the scaling of the strength regime, S, to $>> 10^8$ erg/g, in excess of the fiducial value of 3.5×10^7 erg/g (Benz & Asphaug 1999). All of the models from Pan & Schlichting (2012) that incorporate a size-dependent velocity distribution where velocity decreases with decreasing particle size yield q values greatly in excess of the observed q values for all of the individual disks in our sample. However, the velocities in the grain size range of interest could instead increase with decreasing particle size due to radiation pressure. As is shown above, such a velocity distribution could reproduce q values comparable to our results.

We can also explore the effect of additional parameters on the grain size distribution, namely the strength of the colliding bodies and deviations from a strict power law introduced by a small-size cutoff due to radiation pressure. This is done in the following two sections.

3.6.2 Varying the Strength of Colliding Bodies

Models of collisions between rubble pile grains can predict q values comparable to our results. However, it is unclear if these parameters are realistic for the colliding grains probed by our millimeter observations of debris disks. The idea of collisions between strengthless rubble piles was proposed to explain observations of comets and Kuiper Belt Objects (KBOs), which are on the order of several kilometers in

size (Asphaug & Benz 1996; Jewitt & Sheppard 2002). Our observations probe millimeter to centimeter sized grains, which are typically assumed to be rocky and strength dominated. Analytical and numerical calculations indicate that bodies do not become gravity-dominated until they are larger than ~ 1 km (Wyatt et al. 2011). Furthermore, laboratory experiments show that the strength of small rocky particles does not vary significantly with particle size, scaling as $a^{-0.4}$ (Housen & Holsapple 1999). However, one could imagine that millimeter and centimeter sized grains might be more similar to loose conglomerates than rocky pebbles, and thus might exhibit strength scaling laws more similar to large rubble piles. In fact, measurements of the optical polarization of the AU Mic debris disk taken with *HST/ACS* suggest that the grains in the disk are highly porous ($91 - 94\%$), more like 'bird nests' (Graham et al. 2007).

To produce the models discussed in Section 3.6.1, we require that the bodies participating in the collisional cascade are strength-dominated. If the colliding bodies are more like 'rubble piles,' held together by gravity instead of material strength, we can replace the destruction criterion that collisions occur between bodies of the same size with the requirement that the kinetic energy of the bullet be equal to the gravitational energy of the target. Pan & Sari (2005) derive a range of q values $3.0 \leq q \leq 3.26$ for such a collisional population, lower than the steady-state collisional cascade predictions of Dohnanyi (1969).

3.6.3 Wavy Distributions Produced by a Small-Size Cutoff

Grains within a debris disk are continually subject to radiation pressure from the central star. Large grains are less affected by this radiation pressure and remain in bound orbits, while smaller grains are placed in hyperbolic orbits. A 'blowout' size, $a_{\rm bl}$, can be defined as the grain size for which the force due to radiation pressure ($F_{\rm rad}$) is half the force from gravity ($F_{\rm g}$) and $F_{\rm rad}/F_{\rm g} \gtrsim 0.5$. For grains smaller than this blowout size, bound orbits are impossible and grains are removed from the disk.

Dohnanyi (1969) did not include a small-size cutoff in his theoretical framework to account for the removal of grains smaller than the blowout size. Including such a cutoff superimposes waves or ripples on the predicted power law distribution. The lack of grains smaller than $a_{\rm bl}$, causes the equilibrium number of blowout-sized grains to be enhanced. In turn, this results in an enhanced destruction rate of grains with sizes typically destroyed by blowout-sized grains. Consequentially, the absence of these grains produces a higher equilibrium number of grains that would have been destroyed by them. This ripple effect propagates upwards through the grain size distribution. Previous numerical simulations have produced and discussed this wavy pattern (Campo Bagatin et al. 1994; Thébault et al. 2003; Krivov et al. 2006; Wyatt et al. 2011). The wavelength and amplitude of these waves depends strongly on the collisional velocities and properties of the colliding bodies.

A realistic debris disk, however, is not expected to have a sharp cutoff at small grain sizes. Krivov et al. (2006) note that dispersion in densities and fragmentation energies within an inhomogeneous grain population will likely weaken or smear any waves produced in the size distribution. Additionally, including erosive or cratering

collisions has a clear impact on the grain size distributions (Thébault & Augereau 2007; Kenyon & Bromley 2016), washing out ripples at grain sizes much above the blowout size.

Within the analysis of this paper, we have assumed that the size distribution of particles within a debris disk is a power law, $n(a) \propto a^{-q}$. Given the wavy size distributions predicted by some numerical models, however, it is plausible that the power law size distribution we measure between millimeter and centimeter wavelengths does not reflect the full distribution from micron to kilometer sizes. In order to explore the effect of ripples on the measured grain size distribution further, we have replicated with small modifications the numerical model presented by Wyatt et al. (2011) and implemented analytically by Kenyon & Bromley (2016). The details of the model are described first, and the results and implications follow. This simple model provides a useful illustration of how possible modulations in the grain size distribution would be reflected in the observed opacity spectrum. However, the results should not be over interpreted, given the range of effects that may damp such modulations in more realistic systems.

A Steady-State Model with a Small-Size Cutoff

We define a population of planetesimals divided into N bins spaced logarithmically in size, where the mass and size of the kth bin are m_k and a_k, respectively. The largest bin is defined to be $k = 1$ and size decreases with increasing k such that $a_{k+1}/a_k = 1 - \delta$, with $\delta = 0.01$. The size of the smallest bin is defined as the blowout size, $a_{\rm bl}$, and the size of the largest bin is fixed at 10^4 m. Like Wyatt et al. (2011), we

assume a steady-state where the mass loss rate per logarithmic bin is constant and the mass in each bin is defined as $m_k = C/R_k^c$, where C is some arbitrary constant and R_k^c is the collision rate in bin k. The discrete form of the collision rate can be expressed as

$$R_k^c = \sum_{i=1}^{i_{ck}} \frac{3m_i}{2\rho\pi a_i^3}(a_k + a_i)^2 P_{ik}, \tag{3.4}$$

where ρ is the particle density, P_{ik} is the intrinsic collision probability between particle i and k defined as $\pi v_{\rm rel}/V$, $v_{\rm rel}$ is the relative collision velocity, and V is the total volume through which the planetesimals are moving. The smallest impactors that can catastrophically destroy particles of size a_k have size $X_c a_k$, where $X_c = (2Q_D^*/v_{\rm rel}^2)^{1/3}$ and Q_D^* is the collision energy required to eject half the mass from a pair of colliding bodies.

Using this formalism, the mass in each bin can be solved for analytically, beginning with the smallest bin, $k = N$. Since there are no smaller impactors available, only bodies of size a_N are involved in the collisional cascade. Thus, R_K^c can be solved for simply:

$$R_N^c = \left(\frac{6P_{NN}}{\rho\pi a_N}\right) \times m_N = A_N m_N \tag{3.5}$$

The mass in bin N is then $\sqrt{C/A_N}$. Next, we can consider bin $N-1$. In this bin, the summation in Equation 3.4 has two terms:

$$R_k^c = A_{k+1} m_{k+1} + A_k m_k \tag{3.6}$$

Since we already determined the mass in bin N, we know the first term $A_{k+1}m_{k+1} = B_k$. We can then simplify Equation 3.6 to $R_k^c = B_k + m_k A_k$. The mass in bin $N-1$ is then found by solving a quadratic equation:

$$m_k^2 A_k + m_k B_k - C = 0 \tag{3.7}$$

Moving up to bins of larger size, R_k^c always contains two terms, a sum over all collisions with smaller particles and $m_k A_k$ for the current bin. Thus, the mass in each bin is found simply by solving Equation 3.7 for every bin. In this formulation, the shape of the steady-state distribution is independent of the total mass.

Once we have determined the steady-state number of grains in each bin, we calculate grain opacities to determine whether the resulting wavy number distribution translates to an observable effect. We assume the same grain compositions as Ricci et al. (2010b) that contain 7% silicates, 21% carbon, and 42% water ice by volume, and have 30% porosity. The details of these assumptions are not important to demonstrate the resulting effect on the opacities. For each size bin, we use the Mie scattering code implemented by Dullemond & Dominik (2004) for use in RADMC, a code for dust continuum radiative transfer. The output of this code is an opacity spectrum for each individual grain size in our model. To determine the ensemble opacity at each wavelength, we then calculate a mass-weighted average over all grain sizes given the steady-state size distribution.

The final result of this procedure is the ensemble opacity of a given population of grains as a function of wavelength. For our observations, we measure flux density at two wavelengths in order to determine the millimeter spectral index, $\alpha_{\rm mm}$. If the dust

opacity is a simple power law, ν^{β}, we can infer $\beta = \alpha_{\rm mm} - 2$ from our observations so long as the disk emission is optically thin and in the Rayleigh-Jeans regime. Given the final ensemble opacity spectrum from our models, we can determine the power law index, β, between any two wavelengths we might observe at. By computing β for a range of models and wavelengths corresponding to the observations presented in this study, we can examine the scatter in β (and thus q) we might expect due to waves produced by a small-size cutoff in the grain size distribution.

Variations in Spectral Indices Due to Waves in Grain Size Distributions

To determine the expected scatter in the observed millimeter-centimeter spectral index from waves superimposed on the power law grain size distribution, we considered three free parameters in our model: $a_{\rm bl}$, $v_{\rm rel}$, and Q_D^*. For debris disks, $v_{\rm rel} \gtrsim 1$ km s^{-1} (Krivov 2007); we calculated models for a range of 1 to 6 km s^{-1}. We considered both constant $Q_D^* = Q_s$ and a power law dependence on grain size, $Q_D^* = Q_s r^{\beta_s}$. For rocky objects dominated by material strength, $Q_s = 6 \times 10^3$ J kg^{-1} and $\beta_s = -0.40$ (Benz & Asphaug 1999). The blowout size, $a_{\rm bl}$ is expected to vary between $\sim 1 - 10$ μm for the disks in the sample.

Figure 3.4 shows the resulting size distribution (left panel) and ensemble opacity as a function of wavelength (right panel) for two example models with blowout size, $a_{\rm bl}$, of 1 μm and 10 μm. For both models, we fixed $v_{\rm rel} = 5$ km s^{-1} and $Q_D^* = 6 \times 10^3$ J kg^{-1}. The waves produced in the size distribution by the changing blowout size are seen as muted features in the dust opacity curves. For these two models, blowout sizes of 1 and 10 μm produce dust opacity power law indices of $\beta = 0.63$ and 0.88,

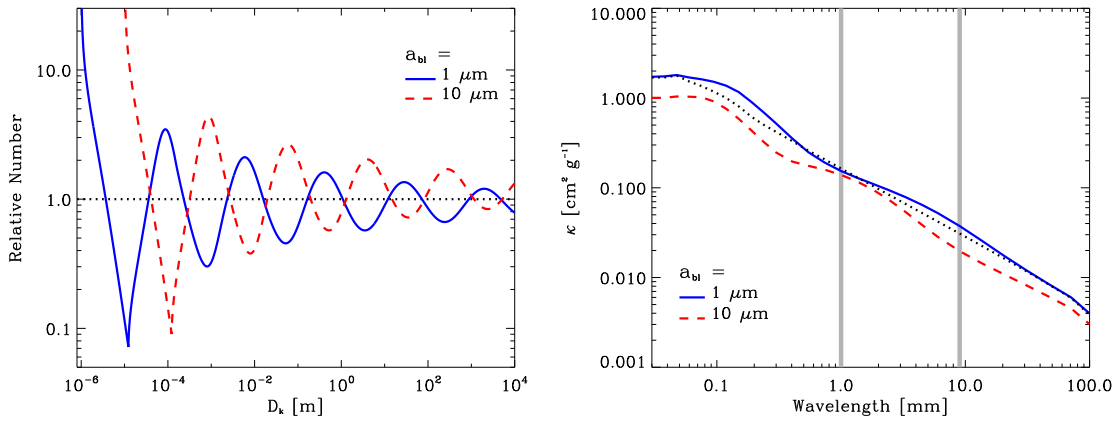

Figure 3.4: *(left)* Comparison of the relative size distribution, $n(a)/n(a)_{\rm pl}$, for a steady-state collisional cascade with a blowout size $a_{\rm bl}$ of 1 μm (blue solid line) and 10 μm (red dashed line). For both models, we have divided the analytic number distribution, $n(a)$, by the expectation for a power law distribution, $n(a)_{\rm pl} \propto a^{-3.5}$, to show the waves introduced by the small-size cutoff more clearly. The expected power law size distribution, $n(a)_{\rm pl}$, is indicated by the dotted black line. For all models, we assume $Q_D^* = 6 \times 10^3$ J kg^{-1} and $v_{\rm rel} = 5$ km s^{-1}. *(right)* The resulting ensemble opacity as a function of wavelength for a 1 μm blowout size (blue solid line) and a 10 μm blowout size (red dashed line). Again, the dotted black line indicates the expected ensemble opacity for the power law size distribution with no waves. The gray lines indicate the wavelengths of our (sub)millimeter and VLA observations used to determine the millimeter spectral index, $\alpha_{\rm mm}$.

respectively. For lower relative velocities ($v_{\rm rel} \sim 1$ km s^{-1}) the waves are damped at long millimeter and centimeter wavelengths and the change in β is negligible. For the full range of free parameters we explored, the resulting values of β ranged from 0.5 to 1.1, comparable to the spread in our complete sample of debris disks, $-0.20 \lesssim \beta \lesssim 1.15$. This is not a definitive explanation for the trend we see in spectral index as a function of stellar type, but it suggests that the waves produced by introducing a cutoff at small grain sizes could introduce observable scatter in the values of β, and thus q, similar to that seen in the measured spectral indices. It is also possible that grain porosity could change with particle size and create

damped resonances as a function of wavelength that might produce structure in the opacity spectrum and result in low values of β. Recent work suggests that K−M (and possibly G) stars do not exhibit a blowout limit for plausible dust compositions (e.g. Reidemeister et al. 2011; Vitense et al. 2012; Schüppler et al. 2015). The lack of a sharp size cutoff for such stars could further damp any waves in the grain size distribution, possibly contributing to the inferred shallower size distribution for these late-type stars.

3.6.4 Stellar Emission Components

A potential source of bias is our implicit assumption that all of the emission we detect at long wavelengths comes from the dusty debris. If the measured flux densities at long wavelengths include emission from any additional mechanisms, then we will underestimate the true millimeter spectral index and thus the size distribution power law index, q. As discussed in Appendix A, the AU Mic system exhibits significant emission from stellar activity at both 1.3 and 9 mm that can be explained by models of a hot stellar corona or chromosphere. Given this stellar activity, the presence of an asteroid belt (MacGregor et al. 2013; Schüppler et al. 2015) is no longer needed to explain the previously reported compact millimeter emission. In this system, we were able to distinguish the excess stellar emission from the disk and subtract it using a time-dependent model. Only three other systems are well enough resolved by the centimeter observations to address this issue, β Pic, ϵ Eridani, and Fomalhaut. Indeed, while the ϵ Eridani debris disk is not detected at centimeter wavelengths, the central star exhibits excess emission attributable to a

hot chromosphere (MacGregor et al. 2015b). The Fomalhaut system shows a central peak at 7 mm distinct from the cold, outer debris belt whose origin is unclear (Ricci et al. 2012). In the eleven unresolved systems in the sample, we cannot separate disk dust emission from any stellar contamination, if present.

The clear outlier in the sample is HD 141569, with a q value of 2.84 ± 0.03, well-below the weighted mean of our complete sample and the classic Dohnanyi prediction. In order to increase this q-value to 3.50, as predicted by Dohnanyi (1969), more than 90% of the emission measured at 9 mm would have to come from contamination from a stellar component, vastly in excess of the expected photospheric flux at these long wavelengths. However, a contribution from an active stellar chromosphere or corona cannot be ruled out. While this system has been imaged with ALMA at 870 μm, it remains unresolved (White et al. 2016b), so we have no constraints on the millimeter or centimeter stellar emission. The HD 141569 disk is the youngest source in the sample with an age of $\sim$ 5 Myr and contains a significant amount of gas. Furthermore, HD 141569 has two nearby M dwarf companions (Weinberger et al. 2000) with their own associated radio emission (see Figure 3.1). It is possible that one or all of these system characteristics contributes to the low q value measured, or that the central region of the disk is optically thick at these wavelengths. For example, gas drag and other transport mechanisms (Poynting-Robertson or stellar wind drag) would tend to flatten the size distribution of affected grains. Wyatt et al. (2011) show that the resulting q value is $\alpha_r - 1$, where α_r is the slope of the redistribution function or the mass distribution of fragments produced in collisions. Given $\alpha_r = 4$, the expected q value for a system with gas drag would be ~ 3, much flatter than the classic Dohnanyi prediction of $q = 3.5$ and

more comparable to the result for HD 141569.

In order to conclusively determine if the flux measurement of HD 141569 or any of the other unresolved disks in the sample are contaminated by coronal or chromospheric emission, observations at millimeter and centimeter wavelengths with higher angular resolution are needed. A growing number of nearby solar type stars, including α Cen A and B (Liseau et al. 2015) and ϵ Eridani (MacGregor et al. 2015b), have all been seen to exhibit excess emission at long wavelengths attributable to a hot chromosphere. However, except for AU Mic, none of the other debris disks in our sample that have been resolved with ALMA show any evidence for an additional strong stellar emission component.

3.7 Conclusions

We present new VLA observations at 9 mm of a sample of seven debris disks. Using the best available flux measurements at (sub)millimeter wavelengths, we place tight constraints on the millimeter/centimeter spectral indices. We combine these with archival ATCA observations at 7 mm of an additional eight debris disks building on the work of Ricci et al. (2015a) and Ricci et al. (2012) to infer the dust grain size distribution power law index, q.

1. For the full sample, the weighted mean for the slope of the power law grain distribution is $\langle q \rangle = 3.36 \pm 0.02$, with a range of 2.84 to 3.64. This result is closest to the prediction of $q = 3.50$ in the classical model of a collisional cascade presented by Dohnanyi (1969) and to recent numerical results by Löhne

et al. (2012), Schüppler et al. (2014), and Schüppler et al. (2015) for specific debris disk systems. The models of Pan & Schlichting (2012) that incorporate size-dependent velocity distributions where velocity decreases with decreasing particle size produce significantly steeper size distributions. Numerical models by Gáspár et al. (2012) yield some q values consistent with these results, but only by increasing the scaling of the strength curve in excess of fiducial values. Shallower size distributions can be produced by models that allow for a velocity distribution where velocity increases with decreasing particle size or models that consider colliding bodies not dominated by material strength.

2. Although limited by small number statistics, the observations suggest a trend in q as a function of stellar type. The weighted mean for stars with spectral types A−F is 3.45 ± 0.02 and 3.30 ± 0.03 for spectral types G−M. We see no evidence for trends in q as a function of system age or gas abundance in the disk.

3. Introducing a cutoff in the grain size distribution at small sizes due to radiation pressure can superimpose waves on the power law grain distribution. We examine a range of analytic models varying the blowout size ($a_{\rm bl}$), the relative collision velocity ($v_{\rm rel}$), and the collision energy (Q_D^*). Changing the blowout size from 1 μm (typical for K and M stars) to 10 μm (for A and B stars) produces measurable waves in the grain size distribution and the resulting dust opacity. For a reasonable range of parameter values, the waves produced vary the inferred dust opacity power law index β between 0.5 and 1.1, a spread in values comparable to the scatter in the observations. In realistic debris disk systems, however, inhomogeneities in densities and fragmentation energies

likely weaken or smear these modulations.

4. The VLA observations of the AU Mic system show significant and variable emission from stellar activity at centimeter wavelengths on timescales from minutes to months. Given this new evidence, the asteroid belt posited by MacGregor et al. (2013) is not needed to explain any aspects of the observed millimeter emission. High angular resolution at centimeter wavelengths allows us to distinguish this stellar emission from the dust disk emission. However, the vast majority of debris disks in the sample have not been resolved at centimeter wavelengths. Given this, we are unable to separate disk dust emission from any stellar contamination (or extragalactic background contamination), if present, for these systems. Higher resolution observations at millimeter and centimeter wavelengths are needed to place better constraints on the contribution of stellar activity to the total flux measurements.

These VLA and ATCA observations provide the longest wavelength flux measurements of these fifteen debris disk systems to date. But, observations at centimeter wavelengths of new systems are needed to continue to grow the sample and place better constraints on any trends in the grain size distribution with stellar or disk properties.

Acknowledgments

M.A.M acknowledges support from a National Science Foundation Graduate Research Fellowship (DGE1144152). The National Radio Astronomy Observatory is

a facility of the National Science Foundation operated under cooperative agreement by Associated Universities, Inc. The Australia Telescope Compact Array is part of the Australia Telescope National Facility which is funded by the Australian Government for operation as a National Facility managed by CSIRO. We thank Margaret Pan, Hilke Schlichting, and Scott Kenyon for helpful conversations. We thank Meredith Hughes, Kate Su, David Rodriguez, Sebastián Marino, Aaron Boley, and Jacob White for providing data prior to publication. We also thank the anonymous referee for a careful and thoughtful review.

4

Millimeter Emission Structure in the First ALMA Image of the AU Mic Debris Disk

This thesis chapter originally appeared in the literature as

M. A. MacGregor, D. J. Wilner, K. A. Rosenfeld, S. M. Andrews, B. Matthews, A. M. Hughes, M. Booth, E. Chiang, J. R. Graham, P. Kalas, G. Kennedy, B. Sibthorpe, 2013, Astrophysical Journal Letters, Vol. 762, pp. L21–L25

Abstract

We present 1.3 millimeter ALMA Cycle 0 observations of the edge-on debris disk around the nearby, ∼10 Myr-old, M-type star AU Mic. These observations obtain 0.″6 (6 AU) resolution and reveal two distinct emission components: (1) the previously

known dust belt that extends to a radius of 40 AU, and (2) a newly recognized central peak that remains unresolved. The cold dust belt of mass $\sim 1\ M_{\rm Moon}$ is resolved in the radial direction with a rising emission profile that peaks sharply at the location of the outer edge of the "birth ring" of planetesimals hypothesized to explain the midplane scattered light gradients. No significant asymmetries are discerned in the structure or position of this dust belt. The central peak identified in the ALMA image is ~ 6 times brighter than the stellar photosphere, which indicates an additional emission process in the inner regions of the system. Emission from a stellar corona or activity may contribute, but the observations show no signs of temporal variations characteristic of radio-wave flares. We suggest that this central component may be dominated by dust emission from an inner planetesimal belt of mass $\sim 0.01\ M_{\rm Moon}$, consistent with a lack of emission shortward of 25 μm and a location $\lesssim$3 AU from the star. Future millimeter observations can test this assertion, as an inner dust belt should be readily separated from the central star at higher angular resolution.

4.1 Introduction

Debris disks are created by the collisional erosion of planetesimals, the building blocks of planetary systems. These collisions continuously generate dust grains with a range of sizes that are detected with astronomical measurements from optical to radio wavelengths. Resolved observations of nearby debris disks are instrumental in advancing our understanding of these systems. At a distance of 9.91 ± 0.10 pc (van Leeuwen 2007), the M1 star AU Mic hosts one of the closest and best studied

debris disks. The detection of submillimeter emission (Liu et al. 2004) from this 23 ± 3 Myr-old system (Mamajek & Bell 2014) in the β Pic moving group (Zuckerman 2001) was followed quickly by the discovery of an edge-on disk seen in scattered starlight (Kalas et al. 2004). Subsequent work has characterized the scattered light in great detail, exploiting its proximity to constrain its radial and vertical structure (Liu 2004; Krist et al. 2005; Metchev et al. 2005; Graham et al. 2007; Fitzgerald et al. 2007).

Observations of dust emission at (sub)millimeter wavelengths provide important, complementary information about debris disk structures. Unlike the small grains probed at optical and near-infrared wavelengths that react strongly to stellar radiation and wind forces, the large grains that dominate the millimeter-wave emission have dynamics more like the parent planetesimals. As a result, long-wavelength images trace best the location and distribution of the larger colliding bodies (Wyatt 2006), and potentially also the signatures of planets that interact with them (Ertel et al. 2012). These size-dependent dust dynamics manifest beautifully in the edge-on AU Mic disk. Resolved millimeter-wave observations show an emission belt within the extended optical disk that peaks near a radius of 35 AU, where the midplane scattered light profile steepens dramatically (Wilner et al. 2012). These features are elegantly explained by the presence of a "birth ring" of planetesimals at that location, where small grains released in a collisional cascade are launched into an extended halo (Strubbe & Chiang 2006; Augereau & Beust 2006).

With the advent of the Atacama Large Millimeter Array (ALMA), the millimeter emission in nearby debris disks can be imaged in much greater detail (e.g., Boley et al. 2012). In this *Letter*, we present new, sub-arcsecond resolution

ALMA Cycle 0 observations of AU Mic at $\lambda = 1.3$ mm. The ALMA data provide substantially improved constraints on the locations of colliding planetesimals in the AU Mic disk and help shed light on the processes that may be shaping the planetesimal distribution. They also reveal a previously unknown, centrally located emission feature.

4.2 Observations

AU Mic was observed by ALMA with its Band 6 receivers over four 2 hour-long "scheduling blocks" (SBs) in 2012 April and June. Table 4.1 summarizes the observations. The 16-20 operational 12-m antennas were arranged to span baseline lengths of 21–402 m (corresponding to a maximum resolution of $\sim 0\farcs6$). The correlator was configured to optimize continuum sensitivity, processing two polarizations in four 2 GHz-wide basebands, each with 128 spectral channels, centered at 226, 228, 242, and 244 GHz. In each SB, we interleaved observations of AU Mic (pointing center $\alpha = 20^{\rm h}45^{\rm m}09\fs34$, $\delta = -31°20'24\farcs09$, J2000, within $1''$ of the star position at all epochs) with the nearby quasar J2101−295.

Table 4.1: ALMA Cycle 0 Observations of AU Mic

ID	Date (UT)	Antennas	PWV (mm)
SB-1	2012 Apr 23 07:30 – 09:26	17	1.7
SB-2	2012 Apr 23 09:39 – 11:03	16	1.7
SB-3	2012 Apr 24 09:09 – 11:19	18	3.0
SB-4	2012 Jun 16 05:48 – 08:02	20	0.7

The data from each SB were calibrated independently within the `CASA` software

package. After applying system temperature measurements and phase corrections from the water vapor radiometers, the data were flagged and averaged into 6.048 second integrations. A calibration of the spectral response of the system was determined from observations of J1924−292, and complex gain variations induced by atmospheric and instrumental effects were corrected using observations of J2101−295. The absolute flux calibration was derived from observations of Neptune: a mean calibration was applied to all basebands, with a systematic uncertainty of ∼10% (see Section 4.3.3). To generate an image at the mean frequency, 235 GHz (1.28 mm), we Fourier inverted the calibrated visibilities with natural weighting and performed a multi-frequency synthesis deconvolution with the `CLEAN` algorithm. The visibilities were further reduced by spectrally averaging over the central 112 channels in each baseband and re-weighted by the observed scatter.

4.3 Results and Analysis

4.3.1 Image of 1.3 mm Dust Continuum Emission

Figure 4.1 shows an image of the $\lambda = 1.3$ mm emission from SB-4 (with the most antennas and best weather conditions), with synthesized beam $0\farcs80 \times 0\farcs69$ (8×7 AU), p.a. 49°, and rms of 30 μJy beam^{-1}. An image constructed from all 4 SBs is consistent but noisier, which we attribute to systematic calibration issues resulting from the poorer weather conditions of the earlier observations. The emission is confined to a narrow band with aspect ratio >10:1, with an orientation consistent with the scattered light disk. The emission is not resolved in the direction

perpendicular to the elongation. There are clear peaks near both extrema and in the middle of the structure (detected at all four epochs). The emission is marginally brighter at the northwest end than the southeast end, and shows small undulations along its length, though none of these variations are significant. We interpret the observed structure as a superposition of two components: (1) the nearly edge-on dust belt with limb-brightened ansae, and (2) a new, distinct, and compact feature located at the center of the belt.

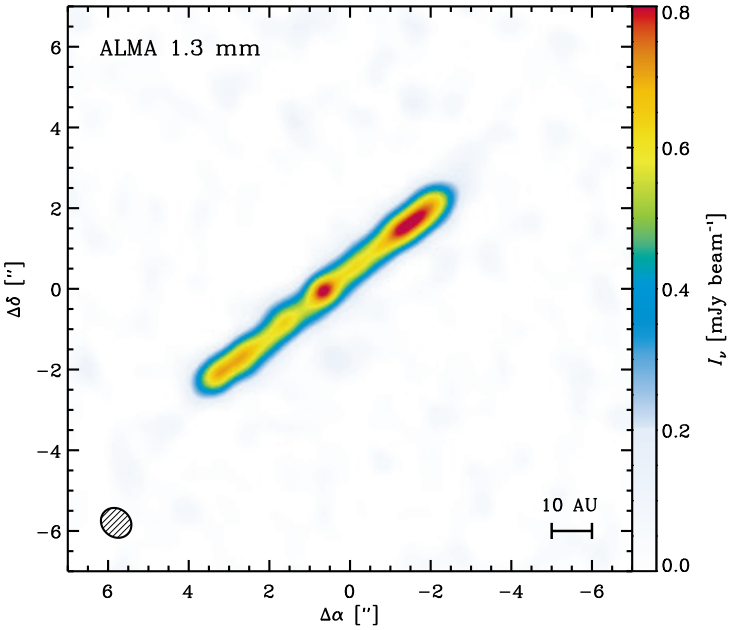

Figure 4.1: ALMA image of the 1.3 mm continuum emission from AU Mic. The ellipse in the lower left corner represents the $0\farcs80 \times 0\farcs69$ (8×7 AU) synthesized beam.

4.3.2 Modeling Formalism

Building on the phenomenological methodology of Wilner et al. (2011, 2012) to analyze resolved millimeter emission from debris disks, we construct a parametric

model to quantify the observed properties of the AU Mic emission. We consider two model components: a vertically thin, axisymmetric "outer" belt, and an additional source to account for the central peak. The belt component is informed by models of the scattered light that show the disk midplane within 50 AU is remarkably straight, $\lesssim$0.°5 from edge-on, and thin (FWHM $\sim$0.″3). We assume the belt is viewed at an inclination of 89.°5. The belt is characterized as an annulus with (unprojected) radial intensity $I_\nu(r) \propto r^x$ for $r_i < r < r_o$, with a normalization defined by $F_{\rm belt} = \int I_\nu \, d\Omega$, a center determined by offsets (relative to the pointing center) $\{\Delta\alpha, \Delta\delta\}$, and an orientation described by a position angle (PA). We treat the central component as a circular Gaussian with mean $\Delta r_{\rm cen}$, variance $\sigma^2_{\rm cen}$ (half width at half maximum $\mathcal{R}_{\rm cen} = \sqrt{2 \ln 2}\ \sigma_{\rm cen}$), and flux density $F_{\rm cen}$. The mean $\Delta r_{\rm cen}$ is defined as a radial shift from the belt center *in the plane of the belt*. We also include power-law spectral scalings between the 4 basebands for each component, denoted $\alpha_{\rm belt}$ and $\alpha_{\rm cen}$, where $F_\nu \propto \nu^\alpha$.

For a given parameter set, we compute four synthetic visibility sets sampled at the same spatial frequencies observed by ALMA, corresponding to the spectrally averaged basebands (at 226, 228, 242, and 244 GHz). By fitting the visibility data directly, we are not sensitive to the non-linear effects of deconvolution, and take advantage of the full range of available spatial frequencies. The fit quality is quantified by a likelihood metric, $\mathcal{L}$, determined from the χ^2 values summed over the real and imaginary components at all spatial frequencies ($\ln \mathcal{L} = -\chi^2/2$). A Markov Chain Monte Carlo (MCMC) approach was utilized to characterize the multi-dimensional parameter space of this model and determine the posterior probability distribution functions for each parameter. We used the affine-invariant

ensemble sampler proposed by Goodman & Weare (2010), in a locally-modified version of the parallelized implementation described by Foreman-Mackey et al. (2012), to compute likelihood values for $\sim 10^6$ MCMC trials. Uniform priors were assumed for all parameters, with bounds imposed to ensure that the model was well-defined: $\{F_{\rm belt},\, F_{\rm cen},\, \sigma^2_{\rm cen}\} \geq 0$, and $0 \leq r_i < r_o$.

4.3.3 Results of Model Fits

The best-fit parameter values and their 68% uncertainties determined from the marginalized posterior probability distributions are listed in Table 4.2. The data and best-fit model are compared in the image plane in Figure 4.2; there are no significant residuals. The best-fit model has a reduced $\chi^2 = 1.37$ (905,920 independent datapoints, 12 free parameters). The modeling procedure was performed on each SB individually and the full dataset (all 4 SBs together). The results were entirely consistent, although the parameter uncertainties were notably smaller from the superior SB-4 dataset alone, and we focus on those results.

Most parameters are determined with high precision. We find good agreement of the outer belt parameters $\{F_{\rm belt},\, r_i,\, r_o\}$ with the less well-constrained fits of Wilner et al. (2012), and on the disk PA from measurements of scattered starlight (e.g., Krist et al. 2005). We measure a flat spectrum for the outer belt ($\alpha_{\rm belt} \approx 0$) across the 4 basebands, which corresponds to the *difference* between the spectral slopes of AU Mic and Neptune ($\alpha_{\rm Neptune} \approx 2.1$), consistent with data from 350 μm to 1.3 mm (Wilner et al. 2012).

The central emission peak is detected with high confidence at $F_{\rm cen} = 320$ μJy

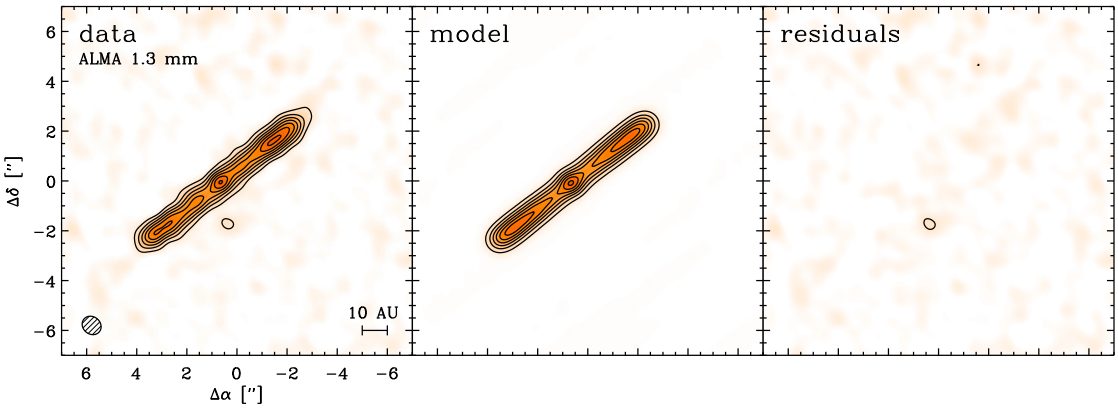

Figure 4.2: *(left)* The observed 1.3 mm emission from AU Mic, *(center)* the best-fit model (see §4.3.3), and *(right)* the imaged residuals. Contours are drawn at 4σ (120 μJy beam^{-1}) intervals.

Table 4.2: Model Parameters

Parameter	Description	Best-Fit	68% Confidence Interval
$F_{\rm belt}$	Belt flux density (mJy)	7.14	+0.12, -0.25
x	Belt radial power law index	2.32	+0.21, -0.31
r_i	Belt inner radius (AU)	8.8	+11.0, -1.0
r_o	Belt outer radius (AU)	40.3	+0.4, -0.4
PA	Belt position angle (°)	128.41	+0.12, -0.13
$\alpha_{\rm belt}$	Belt spectral index	-0.15	+0.40, -0.58
$F_{\rm cen}$	Gaussian flux density (mJy)	0.32	+0.06, -0.06
$\Delta r_{\rm cen}$	Gaussian offset (AU)	0.71	+0.35, -0.51
$\sigma^2_{\rm cen}$	Gaussian variance (AU^2)	$\leq$5.9	(3 σ limit)
$\alpha_{\rm cen}$	Gaussian spectral index	-0.35	+2.1, -4.5
$\Delta\alpha$	R.A. offset of belt center ($''$)	0.61	+0.02, -0.02
$\Delta\delta$	Dec. offset of belt center ($''$)	-0.03	+0.02, -0.02

($> 10\sigma$ brighter than the outer belt at that location). It is unresolved, with $\mathcal{R}_{\rm cen} \leq 3.0$ AU (3σ), and positionally coincident with the outer belt center: $\Delta r_{\rm cen} \leq 1.9$ AU (3σ). Regarding the outer belt, the most notable result is that the models strongly favor rising emission profiles with large, positive gradients: $x \approx 2.3 \pm 0.3$. Models with the standard assumption of $x < 0$ produce significant residuals, under-predicting the intensities at $\pm$1-2$''$ from the belt center. Because of the steep increase in the emission profile, there is only a weak constraint on the inner edge of the outer belt. The best-fit r_i deviates from 0 at the $\sim 2\sigma$ level: the 3σ limit is $r_i \leq 21$ AU.

4.4 Discussion

We have presented new, sub-arcsecond resolution ALMA observations of 1.3 mm emission from the AU Mic debris disk and analyzed the data with a simple parametric model. This emission is resolved into two distinct components: (1) an edge-on outer belt with an emission profile that *rises* with radius out to 40 AU, and (2) an unresolved peak at the center of the outer belt. This distribution is more complex than the single, narrow ring often assumed for debris disks. However, it has some similarities to other nearby resolved systems, like ϵ Eridani (Backman et al. 2009) or HR 8799 (Su et al. 2009), that show an inner component inferred from excess infrared emission, separate from an extended and colder outer belt.

4.4.1 The Central Emission Peak

The stellar photosphere is much fainter than the central peak noted in Figure 4.1. A NextGen stellar model (Hauschildt et al. 1999) with $T_{\rm eff} = 3720$ K, $L_* = 0.11$ $L_\odot$, and $M_* = 0.6$ $M_\odot$ (e.g., Metchev et al. 2005; Chen et al. 2005) that matches the AU Mic photometry from 0.4–25 μm contributes only $F_* = 52$ μJy at 1.3 mm, $\sim$6$\times$ fainter than observed. However, AU Mic is an active star that exhibits radio-wave bursts. In quiescence, observations find $<$120 μJy at 3.6 cm (White et al. 1994), and the contribution at 1.3 mm from hot coronal plasma seen in X-rays is unlikely to be significant (though better spectral constraints are desirable, see Leto et al. 2000). Flares are detected from AU Mic at $\sim$200–1200 μJy at 6 cm (Bower et al. 2009), but this non-thermal emission is much weaker at 1.3 mm. While the unknown variability makes any extrapolation to 1.3 mm problematic, the temporal properties of the ALMA emission provide additional information. Radio-wave flares have fast decay times, of order an hour (Kundu et al. 1987); but, the mm-wave peak persists at a consistent intensity in all four ALMA observations, within uncertainties that are typically $2-3\times$ larger than for SB-4, spanning timescales from 1 hour (within SB-4) to 2 months (SB-1 to SB-4). Unfortunately, the spectral index ($\alpha_{\rm cen}$) constraints are not good enough to be diagnostic. We suspect that stellar emission is too weak and too ephemeral to be responsible for the 1.3 mm peak, but the available data does not allow for a firm determination of its contribution.

Alternatively, the central emission peak could be produced by dust in a distinct (unresolved) planetesimal belt located close to the star. In Section 4.3.3, we constrained the extent of this peak to $\mathcal{R}_{\rm cen} \leq 3$ AU (3σ), inside the inner working

angle ($0\farcs8 \approx 8$ AU) of all previous high resolution imaging of scattered light (Krist et al. 2005; Fitzgerald et al. 2007). Rough models of the spectral energy distribution (SED) from the ALMA central peak can help assess the feasibility that it originates in an inner dust belt. In this context, the most salient feature of the AU Mic SED is the absence of emission excess at $\lambda \leq 25$ μm (e.g., Liu et al. 2004; Chen et al. 2005). We assume the central peak represents the combined emission from the star and dust, such that $F_{\rm dust} = F_{\rm cen} - F_* \approx 0.25$ mJy at 1.3 mm. Optically thin dust emission at a temperature, T, has $F_{\rm dust} \approx \kappa_\nu B_\nu(T) M_{\rm dust}/D^2$, where κ_ν is the opacity spectrum, B_ν the Planck function, $M_{\rm dust}$ the mass, and $D = 9.91$ pc. For a given dust population characterized by κ_ν, we computed the maximum T (and minimum $M_{\rm dust}$) consistent with both the observed millimeter flux density and the infrared SED. We calculated various κ_ν for dust with the Weingartner & Draine (2001) "astrosilicate" composition and a power-law size distribution $n(a) \propto a^{-3.5}$ between $a_{\rm min} = 0.2$ μm (the blow-out size; Strubbe & Chiang 2006) and $a_{\rm max}$ values from 1 μm to 1 cm. For $a_{\rm max} \leq 100$ μm, models of the central peak over-predict the observed 60-70 μm emission if $T > 35$ K. However, larger grains with $a_{\rm max} \geq 1$ mm at temperatures up to $T \approx 75$ K can be accommodated without producing an excess at $\lambda \leq 25$ μm. These maximum T values are comparable to the expected dust temperatures a few AU from the star, compatible with the emission size constraints ($\mathcal{R}_{\rm cen}$). The corresponding minimum $M_{\rm dust}$ is $\sim 9 \times 10^{23}$ g, about 1% of the lunar mass. These calculations show that the central emission peak is consistent with a cool dust belt located $\lesssim$3 AU from the central star, with a total mass comparable to the asteroid belt in our Solar System. If this interpretation is correct, then ALMA observations at higher resolution can determine its properties. Interestingly, the

temperature of this putative inner belt is colder than the $\sim$ 190 K found to apply systematically to inner belts around F5–K0 stars by Morales et al. (2011).

4.4.2 The Outer Dust Belt

Our modeling of the ALMA data locates the far edge of the outer emission belt with high precision, $r_o = 40$ AU, which matches closely the outer edge of the hypothesized "birth ring" of colliding planetesimals. This analysis does not define the shape of the edge below the $\sim$ 6 AU resolution limit, but the truncation is reminiscent of the outer edge of the classical Kuiper Belt (47 ± 1 AU; Trujillo & Brown 2001). The origins of such sharp edges remain unclear: they could be from dynamical interactions (Ida et al. 2000; Boley et al. 2012), or they may simply represent the initial conditions, where planetesimal formation was efficient and successful in the primordial disk. Adopting the opacity used in Section 4.4.1 ($\kappa_\nu = 2.7$ cm^2 g^{-1}), and assuming $T \approx 25$ K (for 35-45 AU), the dust mass of this outer belt is 7×10^{25} g (consistent with previous estimates; Liu et al. 2004), $\sim$100$\times$ more massive than the hypothesized inner belt; the Kuiper Belt and asteroid belt have a similar mass ratio.

The mm-wave emission morphologies of cold belts of dusty debris reflect the dynamical processes that shape the underlying planetesimal distributions. For AU Mic, our modeling suggests that its outer emission belt can be described by an increasing emission profile with a positive radial power-law index $x \approx 2.3 \pm 0.3$. If we assume the emitting dust is in radiative equilibrium with a temperature profile $T \propto r^{-0.5}$, this implies a rising surface density profile, $\Sigma \propto r^{2.8}$, strongly peaked near 40 AU. A broad parent body ring with constant surface density would produce a

radial intensity profile with $x \approx -0.5$, a value ruled out with high confidence ($> 5\sigma$). A rising behavior is predicted for "self-stirred" disks with ongoing planet formation (Kenyon & Bromley 2002); in particular, the models of Kennedy & Wyatt (2010) suggest $\Sigma \propto r^{7/3}$. However, the timescale required to assemble Pluto-sized bodies at ∼40 AU to initiate a collisional cascade around a low-mass star like AU Mic is much longer than its ∼10 Myr age (Kenyon & Bromley 2008). Moreover, this scenario does not naturally accommodate the presence of a separate, interior planetesimal belt. Of course, the still modest resolution of the data is compatible with more complex scenarios, such as multiple closely-spaced belts of different brightnesses that mimic a smooth gradient. Scattered light observations of the AU Mic disk show asymmetries on both large and small scales, with several peaks and depressions projected against the broad ansae in Figure 4.1, at radii beyond the millimeter undulations (features A–E; see Fitzgerald et al. 2007). With such a steep emission gradient in this outer belt, the data do not strongly constrain its width, or the location of its inner edge. Our modeling indicates substantial emission from mm-sized grains interior to 40 AU, in the ∼20–40 AU zone inferred to be highly depleted of μm-sized grains from polarized scattered light (Graham et al. 2007).

The ALMA data show no clear evidence for asymmetries or substructure that would signal planet-disk interactions. The hints of modulating millimeter brightness along the belt in Figure 4.1 are insignificant in the residuals from subtracting a symmetric parametric model (see Figure 4.2). This rules out substructure brighter than 90 μJy beam^{-1} (3σ), corresponding to dust clumps $\gtrsim 1\%$ of the lunar mass (for the dust properties adopted above). Those limits argue against over-densities of dust-producing planetesimals trapped in mean motion resonances (Kuchner &

Holman 2003), as might arise from the outward migration of planets (Wyatt 2003). Given the young age of the system, the broad and smooth character of the outer belt in the AU Mic disk may resemble the Kuiper Belt prior to the epoch of Neptune's migration (Malhotra 1995). It is interesting that none of the claims of millimeter emission clumps in debris disks have survived scrutiny at higher sensitivity (Piétu et al. 2011; Hughes et al. 2011, 2012). It may be that any such features are effectively erased by collisions (Kuchner & Stark 2010). We also find no significant centroid offset between the outer belt and central peak, as might result from the secular perturbations of a planet in an eccentric orbit (Wyatt et al. 1999). The limit on the displacement, $\Delta r_{\rm cen} < 1.9$ AU (3σ), corresponds approximately to a limit on ae, where a is the semi-major axis and e is the eccentricity. This limit can still accommodate a wide-orbit planet with modest eccentricity, similar to Uranus. Such a planet could be responsible for stirring the disk to 40 AU in $\sim$10 Myr (e.g. for $a = 30$ AU and $e = 0.05$, see eqn. 15 of Mustill & Wyatt 2009). Limits from high contrast direct imaging admit Saturn-mass planets at these separations (Delorme et al. 2012).

4.4.3 Concluding Remarks

The basic architecture of the AU Mic debris disk appears remarkably similar to the Solar System, with a potential analog to the asteroid belt at a few AU, and a colder, more massive, and apparently truncated counterpart of the Kuiper Belt extending to 40 AU. Future observations are needed to determine if stellar processes could be responsible for emission attributed to the asteroid belt, and to determine if the Solar

System analogy extends to include a planetary system like our own.

Acknowledgments

M.A.M. thanks NRAO for Student Observing Support funds. A.M.H. is supported by a fellowship from the Miller Institute for Basic Research in Science. M.B. is funded through a Space Science Enhancement Program grant from the Canadian Space Agency and an NSERC Discovery Accelerator Supplement. E.C. acknowledges NSF grant AST-0909210. P.K. and J.R.G. acknowledge support from NSF Award 0909188 and NASA Award NNX11AD21G This paper makes use of the following ALMA data: ADS/JAO.ALMA#2011.0.00142.S. ALMA is a partnership of ESO (representing its member states), NSF (USA) and NINS (Japan), together with NRC (Canada) and NSC and ASIAA (Taiwan), in cooperation with the Republic of Chile. The Joint ALMA Observatory is operated by ESO, AUI/NRAO and NAOJ. The National Radio Astronomy Observatory is a facility of the National Science Foundation operated under cooperative agreement by Associated Universities, Inc.

5

Resolved Millimeter Emission from the HD 15115 Debris Disk

This thesis chapter originally appeared in the literature as

M. A. MacGregor, D. J. Wilner, S. M. Andrews, A. M. Hughes, 2015,

Astrophysical Journal, Vol. 801, pp. 59–66

Abstract

We have used the Submillimeter Array (SMA) to make 1.3 millimeter observations of the debris disk surrounding HD 15115, an F-type star with a putative membership in the β Pictoris moving group. This nearly edge-on debris disk shows an extreme asymmetry in optical scattered light, with an extent almost two times larger to the west of the star than to the east (originally dubbed the "Blue Needle"). The SMA observations reveal resolved emission that we model as a circumstellar belt of thermal dust emission. This belt extends to a radius of $\sim$ 110 AU, coincident with the break

in the scattered light profile convincingly seen on the western side of the disk. This outer edge location is consistent with the presence of an underlying population of dust-producing planetesimals undergoing a collisional cascade, as hypothesized in "birth ring" theory. In addition, the millimeter emission shows a $\sim 3\sigma$ feature aligned with the asymmetric western extension of the scattered light disk. If this millimeter extension is real, then mechanisms for asymmetry that affect only small grains, such as interactions with interstellar gas, are disfavored. This tentative feature might be explained by secular perturbations to grain orbits introduced by neutral gas drag, as previously invoked to explain asymmetric morphologies of other, similar debris disks.

5.1 Introduction

Nearly a hundred dusty debris disks around nearby stars have been spatially resolved at one or more wavelengths (Matthews et al. 2014). The bulk radial structure of these disks is generally well explained by the presence of a localized belt of planetesimals, or "birth ring," where smaller and smaller dust grains are produced in a catastrophic collisional cascade and dispersed (Strubbe & Chiang 2006; Augereau & Beust 2006). However, many disks exhibit additional substructure such as brightness asymmetries, offsets, warps, and clumps that cannot be explained by the steady-state collisional models assumed in this framework. Numerous mechanisms have been proposed to explain morphologies that depart from axial symmetry, including interactions with interstellar gas, planetary resonances, and stellar flybys (Debes et al. 2009; Maness et al. 2009, 2008; Kalas et al. 2007, and references therein). Still, most of these

structures have been detected only at optical and infrared wavelengths, probing a population of small grains that react strongly to stellar radiation and winds. Additional observational constraints, particularly at millimeter wavelengths, are needed to access larger grains with dynamics more similar to the parent colliding bodies, to solidify our understanding of the mechanisms that shape debris disk structure.

HD 15115 is an F2V star at 45 ± 1 pc (van Leeuwen 2007) whose space motions suggest membership in the young β Pictoris moving group (Moór et al. 2011), which includes the well-studied β Pic and AU Mic debris disks. Although the case for membership in this group is not ironclad (see Debes et al. 2008), recent estimates suggest an age of 23 ± 3 Myr for these stars (Mamajek & Bell 2014). An infrared excess from HD 15115 indicating orbiting dust was first noted from *IRAS* observations (Silverstone 2000). Subsequent scattered light imaging from *HST*, Keck, LBT, and Gemini have resolved a remarkable edge-on circumstellar disk (Kalas et al. 2007; Debes et al. 2008; Rodigas et al. 2012; Schneider et al. 2014; Mazoyer et al. 2014). This disk shows an extreme asymmetry in optical scattered light (Kalas et al. 2007): the east side of the disk extends to $\sim 7''$ (315 AU), while the west side reaches $> 12''$ (> 550 AU). Moreover, there are indications that this asymmetry has roots at smaller scales. As described by Debes et al. (2008), the optical surface brightness drops steadily on the east side from $\sim 1''$ (< 45 AU), while the western side appears to flatten interior to $\sim 2''$ (~ 90 AU). In "birth ring" theory, this flattening corresponds to the outer edge of the planetesimal belt where smaller grains are created in collisions and are subsequently launched by stellar forces into wider bound and unbound orbits. The presence of a ring structure is

supported by a subtle concavity visible in scattered light to the north of the star (Schneider et al. 2014), and this brighter side of a ring becomes clear in recent high contrast images (Mazoyer et al. 2014).

A 3σ detection of 850 μm continuum emission from the HD 15115 system using the James Clerk Maxwell Telescope/SCUBA suggested the presence of a reservoir of large dust grains in the disk, with low temperature ($T_d = 62$ K) and low mass (~ 0.047 $M_\oplus$) indicative of debris (Williams & Andrews 2006). Subsequent mapping observations with SCUBA-2 obtained a consistent but higher flux density (8.5 ± 1.2 mJy vs. 4.9 ± 1.6 mJy) and did not resolve any structure with a $14''$ (FWHM) beam (Panić et al. 2013). In light of the asymmetric morphology of the HD 15115 disk seen in scattered light, we have used the Submillimeter Array (SMA)[1] to resolve the millimeter emission from the disk, aimed at tracing the distribution of underlying planetesimals. These observations reveal a planetesimal belt together with tentative evidence for an asymmetric extension of millimeter emission to the west, coincident with the extended feature seen in optical scattered light. We quantify the detected millimeter structure and discuss the plausibility of proposed mechanisms for the asymmetry.

[1]The Submillimeter Array is a joint project between the Smithsonian Astrophysical Observatory and the Academica Sinica Institue of Astronomy and Astrophysics and is funded by the Smithsonian Institution and the Academica Sinica.

5.2 Observations

We observed HD 15115 in fall 2013 with the SMA (Ho et al. 2004) on Mauna Kea, Hawaii at a wavelength of 1.3 mm using both the compact and extended configurations of the array. Table 5.1 summarizes the essentials of these observations, including the dates, baseline lengths, and atmospheric opacity. With the extended baselines, these observations probe angular scales down to $\lesssim 1''$. While typically only six (or fewer) of the eight array antennas were available during the five tracks, the weather conditions were generally very good for observations at this wavelength. The total bandwidth available was 8 GHz derived from two sidebands spanning ± 4 to 8 GHz from the local oscillator (LO) frequency. The phase center was located at $\alpha = 02^{\rm h}26^{\rm m}16\overset{\rm s}{.}24$, $\delta = +06°17'33\overset{''}{.}19$ (J2000), corresponding to the position of the star uncorrected for its proper motion of (86.31,-49.97) mas yr^{-1} (van Leeuwen 2007). The $\sim 54''$ (FWHM) field of view is set by the primary beam size of the 6-m diameter array antennas.

The data from each track were calibrated independently using the IDL-based MIR software package. Time-dependent complex gains were determined using observations of two nearby quasars, J0224+069 ($0\overset{\circ}{.}8$ away) and J0238+166 ($10\overset{\circ}{.}8$ away), interleaved with observations of HD 15115 in a 12 minute cycle for the extended tracks and a 16 minute cycle for the compact tracks. The passband shape was calibrated using available bright sources, mainly 3C84 or 3C454.3. Observations of Uranus during each track were used to derive the absolute flux scale with an estimated accuracy of $\sim 10\%$. Imaging and deconvolution were performed with

standard routines in the Miriad software package. A variety of visibility weighting schemes were used to explore compromises in imaging between higher angular resolution and better surface brightness sensitivity.

Table 5.1: Submillimeter Array Observations of HD 15115

Obs. Date	Array Config.	# of Antennas	Baseline Lengths (m)	LO Freq. (GHz)	HA Range	225 GHz Opacity[a]
2013 Sep 15	Ext.	6	25 – 174	225.5	$-4.2, 3.3$	0.08
2013 Oct 19	Ext.	5	20 – 182	235.5	$-3.8, 4.9$	0.28
2013 Nov 18	Ext.	6	23 – 174	225.5	$-2.3, 3.1$	0.10
2013 Dec 10	Com.	6	8 – 53	225.5	$-1.3, 3.7$	0.20
2013 Dec 12	Com.	6	6 – 53	224.9	$-4.5, 4.8$	0.11

[a] Characteristic value for the track measured at the nearby Caltech Submillimeter Observatory

5.3 Results and Analysis

5.3.1 1.3 mm Dust Continuum Emission

Figure 5.1 shows a contour image of the 1.3 millimeter emission overlaid on a *Hubble Space Telescope*/Advanced Camera for Surveys coronographic image of optical scattered light (F606W filter) from Kalas et al. (2007). The synthesized beam size for this 1.3 millimeter image, obtained with natural weighting, is $3\farcs0 \times 2\farcs1$ (135×95 AU), position angle 73°. The rms noise is 0.30 mJy beam^{-1}, and the peak signal-to-noise ratio is about 5. The red star symbol indicates the stellar position, corrected for proper motion, i.e. offset from the phase center by $(1\farcs3, -0\farcs7)$. This position coincides very closely with the emission peak, well within the combined

uncertainties of the absolute astrometry and modest signal-to-noise. The image reveals a narrow band of 1.3 millimeter continuum emission that extends from the east-southeast to west-northwest, aligned closely with the optical scattered light disk orientation. The western extent of the millimeter emission appears to be greater than the eastern extent, although the significance of this elongation is not high.

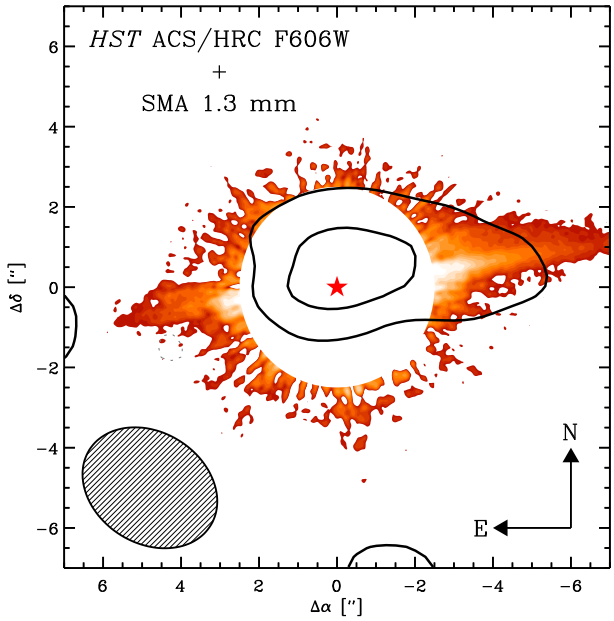

Figure 5.1: SMA image of the 1.3 millimeter continuum emission from HD 15115, overlaid on an image of optical scattered light from the *Hubble Space Telescope* (Kalas et al. 2007). The contour levels are in steps of 2×0.3 mJy, the rms noise level. The ellipse in the lower left corner indicates the $3\farcs0 \times 2\farcs1$ (FWHM) synthesized beam size. The star symbol marks the position of the stellar photosphere, corrected for proper motion.

5.3.2 Disk Modeling

In order to characterize the millimeter emission from HD 15115, we used the procedure described by MacGregor et al. (2013) that employs Markov Chain Monte

Carlo (MCMC) methods to fit a simple parametric model to the observed visibilities. We assume that the emission arises from a geometrically thin, axisymmetric belt characterized by a surface brightness profile of the form $I_\nu(r) \propto r^x$ for $R_{\rm in} < r < R_{\rm out}$. The belt emission normalization is defined by a total flux density $F_{\rm belt} = \int I_\nu d\Omega$, and the belt center is given by offsets relative to the pointing center $\{\Delta\alpha, \Delta\delta\}$. The various scattered light observations show that the disk is nearly edge-on to the line of sight. For our models, we adopt an inclination angle of 87° and an orientation on the sky described by a position angle of $278\overset{\circ}{.}5 \pm 0\overset{\circ}{.}5$ (Kalas et al. 2007). Small variations in these values have no material impact on the results. This initial model does not attempt to account for any asymmetric structure in the emission. To address the western extension, we also made models that included an unresolved source with flux density, $F_{\rm res}$, and position, Δr, defined as an offset from the belt center along the position angle of the disk major axis.

For a given parameter set, we compute synthetic visibilities corresponding to the SMA observations and compare directly to the data with a χ^2 value (the sum of real and imaginary components over all spatial frequencies). By fitting the visibility data directly, we are not sensitive to the non-linear effects of deconvolution, and take full advantage of the complete range of spatial frequencies sampled by the observations. We assumed uniform priors for all parameters, with reasonable bounds imposed to ensure that the model was well-defined: $F_{\rm belt} \geq 0$ and $0 \leq R_{\rm in} < R_{\rm out}$. In addition, we constrained the two parameters $\{\Delta\alpha, \Delta\delta\}$ that describe the belt center to be within $0\overset{''}{.}5$ of the offsets predicted from the stellar proper motion; this generously accomodates the uncertainties in the proper motion and the absolute astrometry of the observations. The fit quality is characterized by a likelihood metric, $\mathcal{L}$,

determined from the χ^2 values ($\ln\mathcal{L} = -\chi^2/2$). We make use of the affine-invariant ensemble MCMC sampler proposed by Goodman & Weare (2010) and implemented effectively in `Python` by Foreman-Mackey et al. (2013). With this MCMC approach, we can characterize efficiently the multidimensional parameter space of this simple model and determine posterior probability distribution functions for each parameter by marginalizing over all other parameters in turn.

5.3.3 Results of Model Fits

Figure 5.2 shows the output of $\sim 10^4$ MCMC trials and Table 5.2 lists the best-fit model parameter values and their 68% uncertainties determined from the marginalized posterior probability distributions for the full model (axisymmetric belt plus western extension). Figure 5.3 shows comparisons between the data and the best-fit models in the image plane, including the imaged residuals in the rightmost panels. The simple symmetric disk model in the upper panels of Figure 5.3 reproduces the bulk of the millimeter emission well, but the residual image shows a $\sim 3\sigma$ feature coincident with the western extension of the scattered light along the disk axis, and this model yielded a reduced $\chi^2 = 3.67$ (153,032 independent data points, 6 free parameters). The departure from unity reflects the poor fit of the model, in part due to the presence of the residual western emission. By including additional parameters in the model that account for this residual feature ($F_{\rm res}$ and Δr), the model fit was more satisfactory, as can be seen in the lower panels of Figure 5.3, with reduced $\chi^2 = 1.88$.

The total flux density of the best fit model is constrained to be $F_{\rm belt} =$

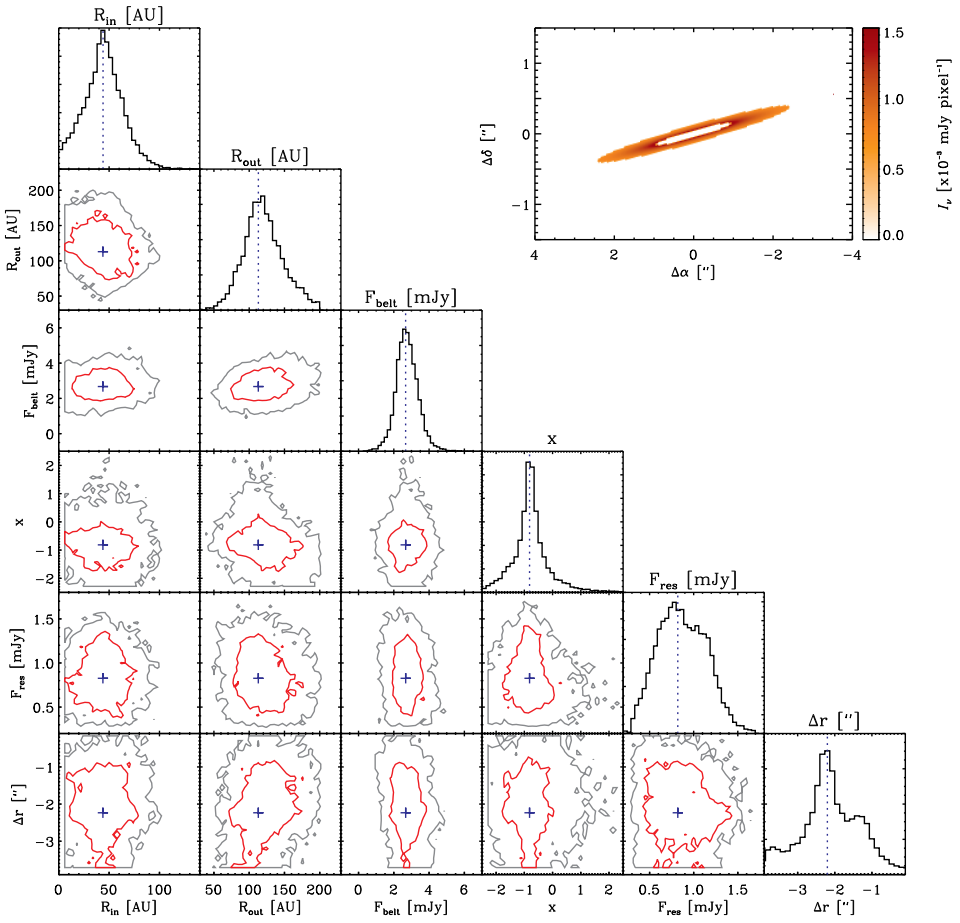

Figure 5.2: A sample of the output from a run of $\sim 10^4$ MCMC trials for the 6 best-fit model belt parameters ($R_{\rm in}$, $R_{\rm out}$, $F_{\rm belt}$, x, $F_{\rm res}$, and Δr). The diagonal panels show the 1D histogram for each parameter marginalized over all other parameters considered in the model. For each parameter, the peak of each histogram is taken to be the best-fit value. The remaining panels show contour plots of the 1σ (red) and 2σ (gray) regions for each pair of parameters, with the blue crosses marking the best-fit values. The inset panel in the upper right shows the resulting best-fit model at full resolution, pixel scale $\sim 0\farcs02$ (0.9 AU). The 1σ and 2σ regions are determined by assuming normally distributed errors, where the probability that a measurement has a distance less than a from the mean value is given by erf $\left(\frac{a}{\sigma\sqrt{2}}\right)$.

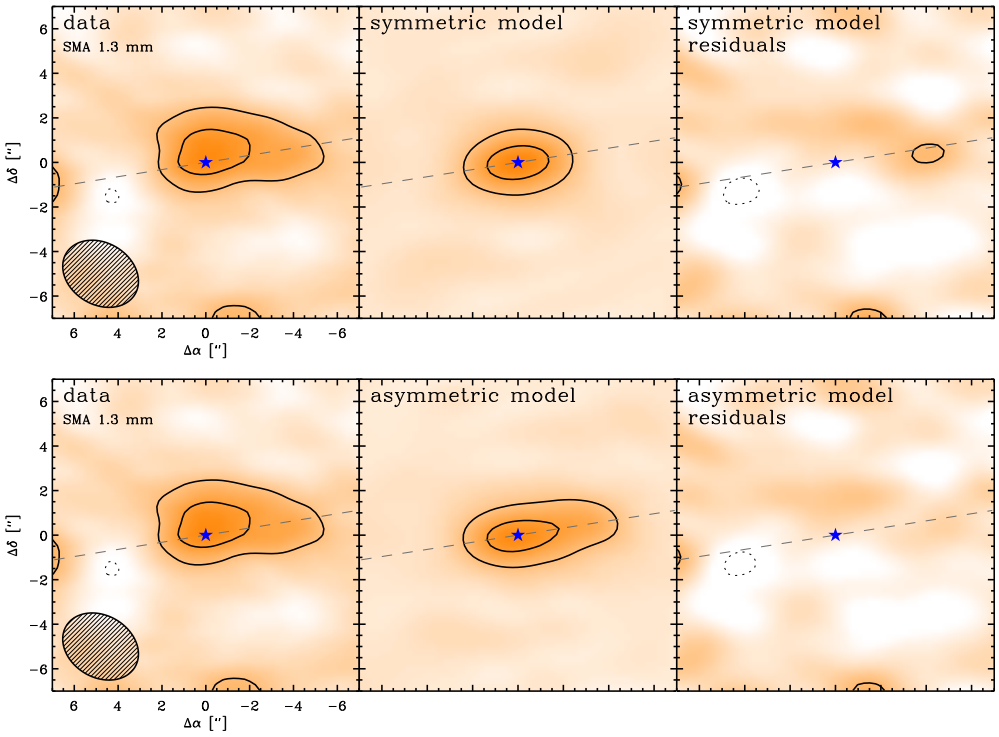

Figure 5.3: *(upper): (left)* The 1.3 millimeter continuum emission from HD 15115 observed with the SMA, as in Figure 5.1, *(center)* image of the best-fit azimuthally symmetric disk model (see Section 5.3 for a description of the modeling formalism and results), and *(right)* the imaged residuals from the symmetric model, showing a 3σ feature on the western side of the disk. *(lower): (left)* the SMA image, *(center)* image of the best-fit asymmetric model, and *(right)* the imaged residuals from the asymmetric model, which do not show any remaining significant features. The contour levels are at 2σ (0.6 mJy beam^{-1}) intervals in all panels.

$2.6^{+0.5}_{-0.8}$ mJy. If we extrapolate the available submillimeter measurements in the literature using the typical spectral index of ~ 2.65 for debris disks at these wavelengths (Gáspár et al. 2012), we find close agreement with the SMA value. In particular, extrapolating the SCUBA-2 observation of Panić et al. (2013) to 1.3 mm gives 2.8 ± 0.4 mJy, while the older SCUBA observation of Williams & Andrews (2006) gives 1.6 ± 0.5 mJy. Given this consistency, it seems likely that the SMA observations detect the full disk emission and do not miss any significant, more

extended, millimeter flux.

Table 5.2: Model Parameters

Parameter	Description	Best-Fit	68% Confidence Interval
$F_{\rm belt}$	Belt flux density (mJy)	2.56	$+0.50, -0.83$
$R_{\rm in}$	Belt inner radius (AU)	43.4	$+28.3, -28.3$
$R_{\rm out}$	Belt outer radius (AU)	113.	$+30.6, -21.8$
x	Belt radial power law index	-0.75	$+1.37, -0.87$
$F_{\rm res}$	Point source flux (mJy)	0.84	$+0.16, -0.12$
Δr	Point source offset ($''$)	-3.55	$+0.45, -0.12$
$\Delta\alpha$	R.A. offset of belt center ($''$)	1.26	$+0.07, -0.05$
$\Delta\delta$	Decl. offset of belt center ($''$)	-0.78	$+0.09, -0.05$

The location of the outer edge of the modelled millimeter emission belt, $R_{\rm out} = 110^{+31}_{-22}$ AU, can be compared to expectations based on the scattered light radial surface brightness profile and "birth ring" theory. The *HST* imaging of HD 15115 by Debes et al. (2008) shows that the scattered light profile steepens on the western side of the disk, falling as $r^{-3.56\pm0.06}$ beyond $1\farcs8$ (81 AU). The ground based scattered light observations of Rodigas et al. (2012) show a similar break in the western surface brightness profile near $\sim 1.8 - 2''$ ($\sim 80 - 90$ AU). The model fit to the outer edge of the millimeter belt is consistent with both of these determinations, within the substantial uncertainties. However, in the context of theory, it remains unclear why the eastern side of the scattered light disk shows no clear break in surface brightness slope.

The observations of Rodigas et al. (2012) additionally show a drop in the scattered light surface brightness of the disk's western side *interior* to $1''$ (45 AU), presumably marking the inner edge of the belt. The higher contrast images of Schneider et al. (2014) and Mazoyer et al. (2014) confirm this feature and suggest at

least a partial clearing within this radius. Analysis of the spectral energy distribution of the system by Moór et al. (2011) yields a best-fit model with an inner warm component and an outer cold ring at a minimum radius of 42 ± 2 AU. Both of these determinations of the inner disk edge match the (poorly constrained) best-fit inner radius of the millimeter belt, $R_{\rm in} = 43 \pm 28$ AU.

Despite the modest signal-to-noise ratio of the millimeter observations, this model fitting exercise yields constraints on the inner and outer radii of the millimeter emission belt that are consistent with previous observations and compatible with the "birth ring" model of debris disks.

Not surprisingly, given the limits of the resolution and sensitivity of the SMA data, model fitting does not provide a strong constraint on the power-law gradient of the millimeter radial emission profile, $x = -0.75^{+1.37}_{-0.87}$. The well known degeneracy between the emission gradient, x, and disk outer radius, $R_{\rm out}$, (e.g. Mundy et al. 1996) is apparent in Figure 5.2 as a slope introduced in the lower contours resulting from that pair of model parameters. For very negative values of x, the contours spread to span a wide range of potential outer radii, as the width and extent of the emission belt become difficult to constrain due to the low brightness in the outer regions. Similarly, the inner radius of the disk is poorly constrained for positive gradients. If we assume that the emitting dust is in radiative equilibrium with stellar heating, leading to a temperature gradient described by $T \propto r^{-0.5}$, then taking the best fit exponent at face value implies a relatively shallow surface density profile, $\Sigma \propto r^{-0.25}$ (albeit with large uncertainty).

5.4 Discussion

Millimeter imaging of HD 15115, like its suspected sister stars in the β Pictoris moving group, β Pic (Wilner et al. 2011) and AU Mic (Wilner et al. 2012; MacGregor et al. 2013), shows a resolved belt of emission with outer edge coincident with a previously observed break in scattered light, consistent with an underlying "birth ring" of colliding planetesimals. For all of these stars, resolved multi-wavelength datasets suggest planetesimal collisions within a belt produce grains with a spectrum of sizes, and the effects of size-dependent dust dynamics produce the compact millimeter emission and an extended scattered light halo. HD 181327, a fourth member of the β Pictoris moving group, also shows a belt of cold dust seen in *Herschel* PACS 70 μm and ATCA 3.2 mm images (Lebreton et al. 2012), though higher resolution millimeter images are still needed to determine its underlying structure.

The detection of a $\sim 3\sigma$ residual along the western extent of the HD 15115 disk, aligned with the asymmetry seen in scattered light from small grains, provides tantalizing evidence that the distribution of larger grains in this system may be asymmetric as well. Similar asymmetric debris disk morphologies in scattered light have been observed in other highly inclined systems where the geometry favors detection, notably HD 32297 (Currie et al. 2012b; Debes et al. 2009; Boccaletti et al. 2012) and HD 61005 (Hines et al. 2007; Maness et al. 2009), as well as β Pic (Kalas & Jewitt 1995). While all of these disks show unique morphological details, similar physical mechanisms may be responsible for the overall shaping of the asymmetric

appearance of the debris. However, it is unclear if the asymmetries can be clearly traced back to the dust-producing parent bodies. The constraints from millimeter observations so far fail to provide a consistent picture. HD 32297 was observed at 1.3 millimeters in the early days of CARMA (Maness et al. 2008), and the millimeter image shows a hint of asymmetry, albeit at low signal-to-noise. On the other hand, SMA 1.3 millimeter observations of HD 61005 (Ricarte et al. 2013) provide no evidence that the millimeter grains are present in the spectacular swept-back wings seen in scattered light.

The most common mechanisms invoked to explain the scattered light asymmetries in these highly inclined debris disks involve interactions with the local interstellar medium (ISM). Ram pressure from interstellar gas can remove bound and unbound grains from a disk directly, or by inducing outflows of disk gas that entrain the grains (Maness et al. 2009; Debes et al. 2009). Additionally, neutral gas can introduce secular perturbations to the orbits of bound grains, producing significant effects on disk morphology on orbital timescales (Maness et al. 2009). Alternatively planets within the system can have dust-trapping resonances that create clumpy, wavelength-dependent grain distributions (Wyatt 2006). Looking outside of the system entirely, external perturbation by a close stellar flyby can also shape the distribution of disk grains (Kalas et al. 2007). An increase in the dust grain scattering cross section or a local density enhancement could produce a local increase of collisions (Mazoyer et al. 2014). Finally, azimuthal asymmetries could be generated through the "photoelectric instability" effect, if the disk has a high enough total dust to gas mass ratio (Lyra & Kuchner 2013). Each of these mechanisms affects different sized grains preferentially and works under specific

physical conditions. In the following, we examine the plausibility of each of these mechanisms for creating asymmetric structures in the HD 15115 disk and similar systems.

5.4.1 Interactions with the ISM

Because the proper motion of HD 15115 is nearly parallel to the disk major axis, Debes et al. (2009) suggest that the dominant disk asymmetry in scattered light arises from an ongoing interaction with the local ISM. In this picture, the eastern side of the disk plows head first into the ISM, causing that side to become truncated, while small grains are blown out to the west. Motivated by the swept back morphologies of HD 32297, HD 15115, and HD 61005, Debes et al. (2009) construct a model for a disk interacting with the gaseous ISM, based on the gas drag felt by meteorites entering the Earth's atmosphere. This results in a scaling law for the radial distance ($R_{\rm deflect}$) at which unbound grains are significantly perturbed from their original circumstellar orbits:

$$R_{\rm deflect} = 286 \left(\frac{1.67 \times 10^{-22} \text{ g cm}^{-3}}{\rho_{\rm gas}} \right)^{\frac{1}{2}} \left(\frac{20 \text{ km s}^{-1}}{v_{\rm rel}} \right) \left(\frac{L_\star}{L_\odot} \right)^{\frac{1}{2}} \text{ AU}, \qquad (5.1)$$

where $\rho_{\rm gas}$ is the ISM gas density and $v_{\rm rel}$ is the relative cloud-disk velocity. By applying the definition of β, the ratio of the force of radiation pressure to the gravitational force exerted by the star, Equation (1) can be recast into a scaling relation for the ISM gas density ($n_{\rm gas}$) and disk relative velocity ($v_{\rm rel}$) needed to perturb unbound grains from their orbits. Assuming perfectly absorbing spherical

grains (Burns et al. 1979)

$$\beta = 0.574 \left(\frac{L_\star}{L_\odot}\right)\left(\frac{M_\star}{M_\odot}\right)^{-1}\left(\frac{1\ \mathrm{g\ cm^{-3}}}{\rho_{\mathrm{dust}}}\right)\left(\frac{1\ \mu\mathrm{m}}{r_{\mathrm{dust}}}\right), \tag{5.2}$$

which yields the relation

$$\left(\frac{n_{\mathrm{gas}}}{200\ \mathrm{cm^{-3}}}\right)\left(\frac{v_{\mathrm{rel}}}{30\ \mathrm{km\ s^{-1}}}\right)^2 \gtrsim 0.6262\left(\frac{M_\star}{0.95\ M_\odot}\right)\left(\frac{a_{\mathrm{dust}}}{0.1\ \mu\mathrm{m}}\right) \times \left(\frac{\rho_{\mathrm{dust}}}{2\ \mathrm{g\ cm^{-3}}}\right)\left(\frac{70\ \mathrm{AU}}{r}\right)^2. \tag{5.3}$$

Interpreting *HST* images of HD 61005, Maness et al. (2009) discuss a second model for ISM interaction in which an interstellar gas cloud removes both bound and unbound grains from a disk due to ram pressure stripping. In this scenario, the drag force on a grain must be comparable to or exceed the gravitational force binding the grain to the star. For the bound case, Maness et al. (2009) show that this leads to the following scaling relation for the cloud density (n_{gas}) and the relative cloud-disk velocity (again v_{rel})

$$\left(\frac{n_{\mathrm{gas}}}{200\ \mathrm{cm^{-3}}}\right)\left(\frac{v_{\mathrm{rel}}}{30\ \mathrm{km\ s^{-1}}}\right)^2 \gtrsim \left(\frac{M_\star}{0.95\ M_\odot}\right)\left(\frac{a_{\mathrm{dust}}}{0.1\ \mu\mathrm{m}}\right) \times \left(\frac{\rho_{\mathrm{dust}}}{2\ \mathrm{g\ cm^{-3}}}\right)\left(\frac{70\ \mathrm{AU}}{r}\right)^2. \tag{5.4}$$

A similar relation is obtained for the unbound case with an additional constant factor accounting for the relative distance traveled by a grain parallel and perpendicular to the disk midplane. Although formulated somewhat differently from Debes et al.

(2009), the resulting expression is functionally identical with the exception of a constant factor (compare equations 5.3 and 5.4).

While ram pressure stripping of disk grains by the ISM seems like an attractive explanation for the asymmetry seen in systems like HD 15115, Marzari & Thébault (2011) use numerical modeling to show that even grains just above the disk blow-out size ($1 - 10$ μm) are minimally affected by ISM interactions and are lost from the disk before they acquire any significant inclination. The millimeter grains, with much smaller values of β, should feel little to no effect from ISM gas. Thus, this argument has difficulty explaining an asymmetry in the millimeter disk emission. Moreover, Maness et al. (2009) point out that the ISM densities required are characteristic of cold clouds ($n \sim 50$ cm^{-3}, $T \sim 20$ K) that occupy only a very small volumetric filling factor within the Local Bubble.

Maness et al. (2009) also propose that disk *gas* could undergo ram pressure stripping by the ISM, and disk grains are consequently swept away when they become entrained in this outflowing gas. In this scenario, sufficient disk gas is required and the grains must be entrained effectively, neither of which is assured. However, measurements of the NA I doublet towards HD 15115 by Redfield (2007) indicate that the column density for this disk is ~ 5 times greater than towards β Pic; he estimates that the upper limit on the total gas mass in the circumstellar disk is ~ 0.3 $M_{\oplus}$.

In order for direct ram pressure stripping of disk grains to occur, the force of the ISM on the grains must be comparable to the stellar gravitational force. Yet, Maness et al. (2009) propose that in the case where this condition is not met, neutral gas

can still affect disk morphology over timescales of $\sim 10^3 - 10^4$ years by introducing secular perturbations to the orbits of bound grains. A similar mechanism has been proposed as the removal mechanism for dust from our Solar System at $20 - 100$ AU (Scherer 2000). Like drag from the Solar wind, neutral gas drag involves the transfer of momentum from incident gas particles to grain surfaces. However, unlike the Solar wind, interstellar gas drag tends to increase grain eccentricities and semi-major axes, and can eventually unbind grains from the system. The normalcy of the interstellar densities, velocities, and cloud sizes required by this neutral gas drag model make it a promising mechanism for producing the structures in this family of asymmetrical debris disks. Furthermore, the presence of detectable gas in the disk lends additional credibility to the argument that neutral gas drag may play a role in shaping the disk morphology.

5.4.2 Interactions with Other Perturbers

An alternative mechanism to ISM interactions that can produce disk asymmetries involves planet induced resonances. Parent planetesimals locked in resonance with orbiting planets can produce large grains that stay in resonance, or, if collisions are unimportant, grains can drift into resonances due to Poynting-Robertson drag (Krivov et al. 2007). Wyatt (2006) predict that in the former case, an asymmetry can be present at short and long wavelengths, but absent at intermediate wavelengths. In this model, the large grains that dominate millimeter emission trace the parent planetesimals and thus exhibit the same clumpy, resonant distribution. The small grains dominant at short wavelengths are preferentially created in the high-density

resonant clumps and expelled from the system on short timescales. The mid-sized grains traced by intermediate wavelengths remain bound, but fall out of resonance due to radiation pressure and are scattered into an axisymmetric distribution. Maness et al. (2008) invoke this prediction to explain the multi-wavelength observations of HD 32297, which appears asymmetric at both optical and millimeter wavelengths, but symmetric in the mid-infrared. A similar picture may be hinted at in the case of HD 15115. The scattered light observations are clearly asymmetric, and the SMA observations suggest a potential millimeter asymmetry. However, observations at $3 - 5$ μm show a symmetric disk morphology (Rodigas et al. 2012). Detailed dynamical models of these systems are needed to draw firm conclusions about this speculation.

Global disk asymmetries could also be produced by a single or periodic stellar flyby, as proposed to explain the large scale scattered light asymmetry of the β Pic debris disk (Kalas & Jewitt 1995; Kalas et al. 2001). Kalas et al. (2007) point out that the β Pic moving group member, HIP 12545, nearby in the sky to HD 15115 (3.°9, Moór et al. 2006), could be involved in a past interaction, as these two stars show identical proper motion, galactic space motion, and heliocentric distance within the measured uncertainties. Morever, the present location of HIP 12545 is in the direction of the truncated eastern side of the HD 15115 disk, as in the simulations of (Larwood & Kalas 2001) flyby interactions. However, there are no indications other than this circumstantial evidence for any interaction. Furthermore, the membership of HD 15115 in the β Pic moving group has been called into question. Moór et al. (2006) used kinematic arguments to propose this group membership. The recent Bayesian analysis by Malo et al. (2013) suggests a higher probability of membership

in the Columba Association. A better understanding of the group membership and age of HD 15115 certainly would be helpful in unraveling the origins of the debris disk morphology.

5.4.3 Interactions within Disk Material

Gemini Near-Infrared Coronographic Imager (NICI) data in the H and Ks bands (Mazoyer et al. 2014) resolved the HD 15115 disk and detected ansae on both sides at a radius of 1.99″ ($\sim$ 90 AU). These new observations indicate a ring-like shape with an inner cavity that appears symmetric, in contrast with the east-west brightness asymmetry seen in other images. If the inner ring is truly symmetric, an alternative or additional mechanism for the observed brightness asymmetry is possible. Mazoyer et al. (2014) suggest that both a local increase in the dust grain scattering cross section and/or a local density enhancement of small grains could lead toward an increase in collisions at the location of the western brightness peak. A similar explanation was recently invoked to explain the millimeter emission clump seen in ALMA observations of the β Pictoris disk (Dent et al. 2014).

We can crudely estimate the mass of small grains needed to account *entirely* for the tentative excess millimeter emission on the western side of the disk. Optically thin dust emission at a temperature, $T_{\rm dust}$, has flux $F_{\rm dust} \approx \kappa_\nu B_\nu(T_{\rm dust}) M_{\rm dust}/D^2$, where κ_ν is the dust opacity, B_ν is the Planck function, $M_{\rm dust}$ is the dust mass, and $D = 45$ pc. We estimate a characteristic temperature for dust in this excess feature of $\sim$ 30 K, using its approximate radial location ($\sim$ 160 AU) and assuming radiative equilibrium of starlight with blackbody grains (Backman & Paresce 1993). To

estimate an appropriate dust opacity, we assume that the grain size distribution is described by a power-law between 0.1 μm and some maximum size $a_{\rm max}$, $n(a) \propto a^q$. For grains with composition volume fractions of 0.07, 0.21, 0.42, and 0.30 for silicate, carbon, ice, and vacuum, respectively, Ricci et al. (2010b) calculate dust opacities as a function of $a_{\rm max}$. (Note, the results are not very sensitive to other reasonable assumptions about composition.) Adopting a typical power-law exponent $q = -3.5$, and maximum grain size $a_{\rm max} = 0.1$ millimeter, models yield a dust opacity, $\kappa_\nu \sim 3$ cm^2 g^{-1}. Given these assumptions, the mass of small grains required to account for the excess millimeter flux is $\sim 1 \times 10^{26}$ g, or ~ 1.4 times the lunar mass. As this large mass indicates, a very significant collision would be required for small grains to account entirely for the western millimeter emission feature. Furthermore, such a collisional feature is transient and can persist for only a small fraction of the system age (Jackson et al. 2014).

Lyra & Kuchner (2013) discuss an additional mechanism by which disk gas can generate azimuthal asymmetries through the "photoelectric instability" effect. In this scenario, a dense region of dust heats the gas through photoelectric heating and creates a local pressure maximum, which in turn attracts additional dust. The resulting instability could lead to the development of rings, spirals, or other structures within the disk. Lyra & Kuchner (2013) suggest that this effect will occur in disks with a total disk dust to gas mass ratio, $\epsilon \sim 1$. In the case of HD 15115, estimates of the total dust and gas mass in the disk suggest that $\epsilon > 0.16$, in the regime where this mechanism could work. However, without further analysis, it is unclear whether the level of azimuthal asymmetries produced would be large enough to account for these new observations.

In short, there is still no clear consensus as to which of these mechanisms is responsible for shaping the debris around HD 15115 and other, similar systems (notably HD 61005 and HD 32297). Each mechanism affects different sized grains preferentially and operates under specific physical conditions. Improved constraints on the detailed morphologies of these systems are required to reach definitive conclusions.

5.5 Conclusions

We present SMA 1.3 mm observations that resolve the emission from the HD 15115 debris disk, the first at such a long wavelength. The bulk of the millimeter emission is described well by a symmetric belt, consistent with the presence of a "birth ring" of collisional planetesimals indicated by previous observations of scattered light. The SMA observations also show a $\sim 3\sigma$ residual feature coincident with the western extension of the scattered light along the disk major axis. If real, this additional feature hints that the distribution of larger grains may be asymmetric as well.

There is no consensus concerning the physical mechanism or mechanisms responsible for the scattered light asymmetries in HD 15115 and other, similar debris disks. Ram pressure from surrounding interstellar gas can strip both bound and unbound grains, or induce outflows of disk gas that entrain grains. However, the tentative millimeter emission asymmetry disfavors any process that affects only small grains. An alternative mechanism invokes neutral gas in the disk that introduces secular perturbations to grain orbits, producing significant effects on disk morphology on orbital timescales (Maness et al. 2009). The presence of atomic

gas towards HD 15115 suggests that this idea should be explored more thoroughly. Interactions with perturbers are another possibility. Dust-trapping resonances from orbiting planets may be able to explain the observed wavelength-dependent structure. Future observations of HD 15115 at higher angular resolution and sensitivity with the Atacama Large Millimeter/submillimeter Array are needed to resolve the detailed morphology of the millimeter emission and to address the processes responsible for shaping this remarkable debris disk.

Acknowledgments

We thank Paul Kalas for providing the *Hubble Space Telescope* image in Figure 5.1. M.A.M acknowledges support from a National Science Foundation Graduate Research Fellowship (DGE1144152). We thank Katherine Rosenfeld, Til Birnstiel and John Debes for helpful conversations.

6

The Epsilon Eridani System Resolved by Millimeter Interferometry

This thesis chapter originally appeared in the literature as

M. A. MacGregor, D. J. Wilner, S. M Andrews, J.-F. Lestrade, S. Maddison, 2015, Astrophysical Journal, Vol. 809, pp. 47–57

Abstract

We present observations of ϵ Eridani from the Submillimeter Array (SMA) at 1.3 millimeters and from the Australia Telescope Compact Array (ATCA) at 7 millimeters that reach an angular resolution of $\sim 4''$ (13 AU). These first millimeter interferometer observations of ϵ Eridani, which hosts the closest debris disk to the Sun, reveal two distinct emission components: (1) the well-known outer dust

belt, which, although patchy, is clearly resolved in the radial direction, and (2) an unresolved source coincident with the position of the star. We use direct model-fitting of the millimeter visibilities to constrain the basic properties of these two components. A simple Gaussian shape for the outer belt fit to the SMA data results in a radial location of $64.4^{+2.4}_{-3.0}$ AU and FWHM of $20.2^{+6.0}_{-8.2}$ AU (fractional width $\Delta R/R = 0.3$). Similar results are obtained taking a power law radial emission profile for the belt, though the power law index cannot be usefully constrained. Within the noise obtained (0.2 mJy beam^{-1}), these data are consistent with an axisymmetric belt model and show no significant azimuthal structure that might be introduced by unseen planets in the system. These data also limit any stellocentric offset of the belt to < 9 AU, which disfavors the presence of giant planets on highly eccentric (> 0.1) and wide (10's of AU) orbits. The flux density of the unresolved central component exceeds predictions for the stellar photosphere at these long wavelengths, by a marginally significant amount at 1.3 millimeters but by a factor of a few at 7 millimeters (with brightness temperature 13000 ± 1600 K for a source size of the optical stellar radius). We attribute this excess emission to ionized plasma from a stellar corona or chromosphere.

6.1 Introduction

Debris disks, composed of planetesimals remaining after planet formation and circumstellar disk dispersion, represent the end-stage of protoplanetary disk evolution (see reviews by Backman & Paresce 1993; Wyatt 2008; Matthews et al. 2014). While these remnant planetesimals cannot be observed directly, they are

ground down through ongoing collisions into smaller and smaller dust grains that scatter starlight and produce detectable thermal emission. Observations of this dusty debris at millimeter wavelengths are especially critical to our understanding of the most readily accessible systems. The large grains that dominate emission at these long wavelengths do not travel far from their origin and therefore reliably trace the underlying planetesimals distribution, unlike the small grains that are rapidly removed by stellar radiation and winds (Wyatt 2006). Since planets, if present, will inevitably perturb the dust-producing planetesimals, the millimeter emission morphology encodes information on the architecture and dynamical evolution of these systems. For example, the outward migration of a planet can confine planetesimals in a belt between its resonances (Hahn & Malhotra 2005), or trap planetesimals into mean motion resonances outside its orbit (Kuchner & Holman 2003; Wyatt 2003; Deller & Maddison 2005). A planet can also sculpt out sharp edges in a belt (Quillen 2006; Chiang et al. 2009), or force planetesimals onto eccentric or inclined orbits (Wyatt et al. 1999).

At a distance of only 3.22 pc (van Leeuwen 2007), the $400 - 800$ Myr-old (Mamajek 2008) main-sequence K2 star ϵ Eridani hosts the closest debris disk to the Sun, originally identified through the detection of far-infrared emission by *IRAS* (Aumann 1985). Pioneering observations with JCMT/SCUBA resolved a nearly face-on belt of emission at 850 μm, peaking at 60 AU (18″) radius, with several brightness enhancements or clumps (Greaves et al. 1998). Analysis by Greaves et al. (2005) of JCMT images spanning 5 years offered tentative evidence that some of these clumps are stationary, and so likely background galaxies, while others appear to be co-moving with the star, and so are likely associated with the disk.

Subsequent single-dish observations from 250 to 1200 μm have confirmed the basic belt morphology, but not all of the low significance asymmetries (Schütz et al. 2004; Backman et al. 2009; Greaves et al. 2014; Lestrade & Thilliez 2015). A warmer dust component, reaching to several AU from the star, can be explained in modeling the spectral energy distribution by an additional dust belt (Backman et al. 2009; Greaves et al. 2014), or by inward transport from the outer belt (Reidemeister et al. 2011). In addition, precision radial velocity observations suggest the presence of a Jupiter-mass planet with semi-major axis of 3.4 AU (1″) (Hatzes et al. 2000), although the reality of this planet signal remains controversial (Anglada-Escudé & Butler 2012). Because ϵ Eridani is so nearby, it is a key template for understanding debris disk phenomena around Sun-like stars, and detailed study of its debris disk provides essential context for the interpretation of more distant, less accessible systems.

We present observations of ϵ Eridani at 1.3 mm and at 7 mm, using the Submillimeter Array (SMA) and the Australia Telescope Compact Array (ATCA), respectively, using the most compact, lowest angular resolution ($4'' - 10''$) configurations of these telescopes. While even higher resolution may be desirable, these interferometric observations are conservatively tuned to provide a first look at structures below the resolution of previous single dish observations. For these arrays at these wavelengths, the primary beam field of view encompasses the entire emission region from the outer debris belt, enabling efficient observations of the full disk with a single pointing. Section 6.2 describes these observations of the ϵ Eridani system. Section 6.3 describes the modeling procedure and the results. Section 6.4 discusses the implications of the model fits for the outer dust belt properties, azimuthal

asymmetries, and the nature of an inner component of excess millimeter emission.

6.2 Observations

6.2.1 Submillimeter Array

We observed ϵ Eridani in July, August and November 2014 with the SMA (Ho et al. 2004) on Mauna Kea, Hawaii at a wavelength of 1.3 mm in the subcompact configuration. Table 6.1 summarizes the essentials of these observations, including the dates, baseline lengths, and atmospheric opacity. Six tracks were obtained, all with 7 operational antennas in the array. The weather conditions were very good for observations at this wavelength (225 GHz opacities from 0.07 to 0.12). The total bandwidth available was 8 GHz consisting of two sidebands of 4 GHz width spanning ± 4 to 8 GHz from the local oscillator (LO) frequency of 225.5 GHz (217.5 − 221.5 GHz and 229.5 − 233.5 GHz). The phase center was located at $\alpha = 03^{\rm h}32^{\rm m}54\overset{\rm s}{.}9024$, $\delta = -09°27'29\overset{''}{.}4486$ (J2000), corresponding to the position of the star corrected for its proper motion of (-975.17,19.49) mas yr^{-1} (van Leeuwen 2007) as of July 1, 2014 . At the LO frequency, the field of view is $\sim 52''$, set by the primary beam size of the 6-m diameter array antennas.

The data from each track were calibrated independently using the IDL-based MIR software package. Time-dependent complex gains were determined from observations of two nearby quasars, J0339-017 ($7\overset{\circ}{.}9$ away) and J0423-013 ($14\overset{\circ}{.}9$ away), interleaved with observations of ϵ Eridani in a 16 minute cycle. The passband shape was calibrated using available bright sources, mainly 3C84 or 3C454.3.

Observations of Uranus or Callisto during each track were used to derive the absolute flux scale with an estimated accuracy of $\sim 10\%$. Imaging and deconvolution were performed with the `CLEAN` task in the `CASA` software package. A variety of visibility weighting schemes were used to explore compromises in imaging between higher angular resolution and better surface brightness sensitivity. With natural weighting, the beam size is $6\farcs0 \times 5\farcs5$ (19×18 AU) and the rms noise level is 0.17 mJy beam^{-1}. The longest baselines in the dataset probe size scales of $\sim 4''$ (13 AU).

Table 6.1: Submillimeter Array Observations of ϵ Eridani

Obs. Date	Array Config.	Projected Baselines (m)	HA Range	225 GHz Opacity[a]
2014 July 28	Subcompact	$6 - 35$	$-3.6, 3.3$	0.09
2014 July 29	Subcompact	$6 - 35$	$-3.7, 2.8$	0.07
2014 July 30	Subcompact	$6 - 35$	$-3.5, 7.1$	0.08
2014 Aug 5	Subcompact	$6 - 35$	$-3.5, 2.2$	0.12
2014 Nov 19	Subcompact	$6 - 56$	$-3.6, 4.3$	0.07

[a] Characteristic value for the track measured at the nearby Caltech Submillimeter Observatory. The LO frequency for all observations was 225.5 GHz.

6.2.2 Australia Telescope Compact Array

We observed ϵ Eridani in late June and early August 2014 with the ATCA, located near Narrabri, NSW, at a wavelength of 7 mm using the compact H75 and H168 configurations of the array. Table 6.2 summarizes the essentials of these observations. Four tracks were obtained in each of the two antenna configurations, all with 6 operational antennas. The winter weather provided good atmospheric phase stability for this ATCA high frequency band (rms path typically < 150 microns from the

seeing monitor), especially for the short baselines of interest, except for the last track in the H168 configuration (2014 July 28), which proved to be unusable due to high winds and relatively poor seeing. Data from the stationary sixth antenna of the array, located ~ 6 km from the others, was discarded, given the large gap from the rest of the antennas and less stable phase on the much longer baselines. The bandwidth provided by the Compact Array Broadband Backend was 8 GHz, with 2 GHz wide bands centered at 43 GHz and at 45 GHz, in two polarizations (Wilson et al. 2011). The phase center was identical to the contemporaneous SMA observations. The field of view is $\sim 70''$, set by the primary beam size of the 22-m diameter array antennas.

Table 6.2: Australia Telescope Compact Array Observations of ϵ Eridani

Obse. Date	Array Config.	Projected Baselines (m)	HA Range	Seeing rms (microns)[a]
2014 June 25	H168	$36 - 180$	$-3.6, 3.6$	150
2014 June 26	H168	$36 - 180$	$-3.6, 3.6$	60
2014 June 27	H168	$31 - 180$	$-4.0, 3.6$	70
2014 June 28	H168	$31 - 180$	$-4.1, 0.0$	250
2014 Aug 2	H75	$22 - 84$	$-4.7, 3.9$	80
2014 Aug 3	H75	$22 - 84$	$-4.4, 4.0$	80
2014 Aug 4	H75	$22 - 84$	$-4.6, 4.0$	150
2014 Aug 5	H75	$22 - 84$	$-3.8, 4.0$	130

[a] Characteristic value for the track measured by the ATCA seeing monitor, an interferometer on a 230 m east-west baseline that tracks the 30.48 GHz beacon on the geostationary communications satellite, OPTUS-B3, at an elevation of 60°. (Middelberg et al. 2006). The LO frequency for all observations was 44 GHz.

The data from the seven usable tracks were calibrated independently using the Miriad software package. Time-dependent complex gains were determined using the

nearby quasar 0336-019 (7.°8 away), interleaved with observations of ϵ Eridani in a 12 minute cycle. The passband shape was calibrated using the available bright sources 1921-293 or 0537-441. Observations of 1934-638 and Uranus during each track were used to derive the absolute flux scale. Comparison of the derived fluxes for 0336-019 for each of the seven nights shows a maximum difference of 6%, and we conservatively estimate the flux scale accuracy is better than 10%. Imaging and deconvolution were performed with the standard routines `invert`, `CLEAN`, and `restor` in the Miriad software package.

6.3 Results and Analysis

6.3.1 Continuum Emission

Figure 6.1 shows an SMA 1.3 mm image and ATCA 7 mm image of ϵ Eridani, together with the *Herschel/SPIRE* 250 μm image extracted from the Herschel Science Archive for reference (Greaves et al. 2014). For the 1.3 mm image, the synthesized beam size, obtained with natural weighting and a modest taper to improve surface brightness sensitivity is $9.''2 \times 8.''7$ (30×28 AU), position angle 68°. The rms noise is 0.20 mJy beam^{-1}. This image reveals emission from a compact central source at the stellar position ($\sim 7\sigma$) together with patchy emission from the nearly face-on belt of cold dust located $\sim 18''$ from the star. For the 7 mm image, the synthesized beam size obtained with natural weighting is $9.''2 \times 7.''0$ (30×23 AU), position angle 83°. The rms noise is 7 μJy beam^{-1}. A central peak is clearly detected ($\sim 10\sigma$). Unlike the 1.3 mm image, the 7 mm image shows little sign of

emission from the outer dust belt. In both images, the position of the central peak is consistent with the predicted stellar position, within the uncertainty dictated by the synthesized beam size, θ, and the signal-to-noise ratio, SNR of $\sim 0.5\theta/SNR \approx 0\farcs6$ (see Reid et al. 1988).

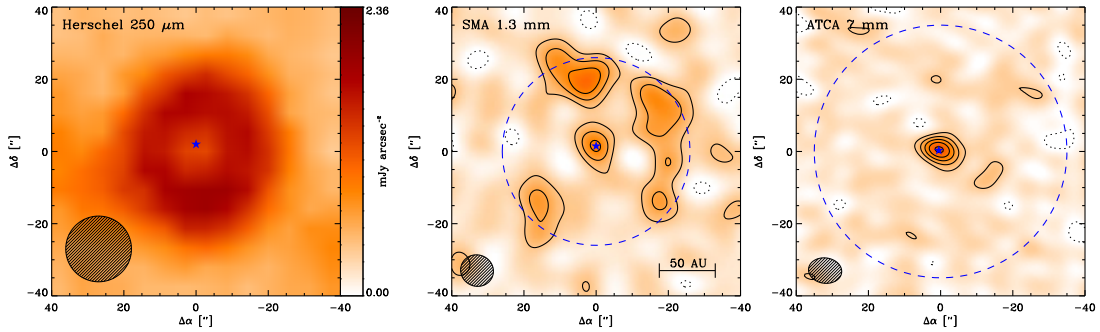

Figure 6.1: *(left) Herschel/SPIRE* 250 μm image of ϵ Eridani, from the Herschel Science Archive (see also Greaves et al. 2014). The ellipse in the lower left indicates the $\sim 19''$ beam size. *(center)* SMA image of the 1.3 millimeter continuum emission from ϵ Eridani. The contour levels are in steps of 2×0.2 mJy, the rms noise level. The ellipse in the lower left corner indicates the $9\farcs2 \times 8\farcs7$ (FWHM) synthesized beam size. The dashed blue circle indicates the $\sim 52''$ SMA primary beam (FWHM) at the LO frequency (225.5 GHz). *(right)* ATCA image of the 7 millimeter continuum emission from ϵ Eridani. The contour levels are in steps of 2×7 μJy, the rms noise level. The ellipse in the lower left corner indicates the $9\farcs2 \times 7\farcs0$ (FWHM) synthesized beam size. The dashed blue circle indicates the $\sim 70''$ ATCA primary beam (FWHM) at 44 GHz. In all three panels, the star symbol marks the position of the stellar photosphere, corrected for proper motion. For the center and right panels, the stellar position is: $\alpha = 03^{\rm h}32^{\rm m}54\fs9024$, $\delta = -09°27'29\farcs4486$ (J2000).

6.3.2 Emission Modeling Procedure

To characterize the 1.3 mm emission from ϵ Eridani, we used the procedure described by MacGregor et al. (2013, 2015a) that employs a Markov Chain Monte Carlo (MCMC) method to fit simple parametric models to the observed visibilities. We

fit the visibility data directly both to avoid the non-linear effects of deconvolution and to take advantage of the full range of spatial frequencies in the observations that are not necessarily represented well in the images. We assume that the emission arises from a geometrically thin, axisymmetric belt, where we consider two different parametric shapes for the surface brightness profile, $I_\nu(r)$: (1) an annulus with $R_{\rm in} < r < R_{\rm out}$ and power law slope, $I_\nu(r) \propto r^x$, and (2) a Gaussian, $I_\nu(r) \propto \exp[-((r - R_{\rm cen})/\sqrt{2}\sigma)^2]$, where $R_{\rm cen}$ is the position of the belt, σ is the width, and the FWHM $= \Delta R = 2\sqrt{2\ln(2)} \times \sigma$. The limited signal-to-noise of the dataset precludes exploring more complicated, but physically plausible, surface brightness shapes, such as multiple rings or a broken power law. The belt emission normalization is defined by a total flux density, $F_{\rm belt} = \int I_\nu d\Omega$, and the belt center is given by offsets relative to the pointing center $\{\Delta\alpha, \Delta\delta\}$. The central peak coincident with the stellar position is described by a point source with total flux, $F_{\rm cen}$, and the offsets of this point source relative to the belt center are given by two additional parameters $\{\Delta\alpha_{\rm star}, \Delta\delta_{\rm star}\}$. The previous imaging observations show that the belt is viewed close to face-on ($i = 30°$, Greaves et al. 2014). We fit the SMA data directly for an inclination angle, i, and also an orientation on the sky described by a position angle, PA, east of north.

The ϵ Eridani disk spans a large angle on the sky, approaching (or possibly exceeding) the half power field of view of the SMA. As a result, the primary beam response has the potential to affect the properties derived for the outer regions of the millimeter emission belt. To account for this in the analysis, we multiply each belt model by an accurate, frequency-dependent beam model, normalized to unity at the beam center. Appendix B provides a detailed discussion of the SMA primary

beam shape. For ATCA, with its larger field of view at the observed wavelength, the effects of the primary beam shape are much less important, and a simple Gaussian provides an adequate description.

For each set of model parameters, we use the Miriad `uvmodel` task to compute two synthetic visibility sets sampled at the same spatial frequencies as our SMA observations, corresponding to the two spectrally averaged sidebands (218.9 and 230.9 GHz). The fit quality is characterized by a likelihood metric, $\mathcal{L}$, determined from the χ^2 values computed using the real and imaginary components at all spatial frequencies ($\ln\mathcal{L} = -\chi^2/2$). This modeling scheme is implemented using the affine-invariant ensemble MCMC sampler proposed by Goodman & Weare (2010) and realized in `Python` by Foreman-Mackey et al. (2013). A MCMC approach allows us to more effectively characterize the multidimensional parameter space of this model and to determine the posterior probability distribution functions for each parameter. We assumed uniform priors for all parameters, with reasonable bounds imposed to ensure that the model was well-defined: $F_{\rm belt} \geq 0$ and $0 \leq R_{\rm in} < R_{\rm out}$. In addition, we constrained the four offset parameters $\{\Delta\alpha, \Delta\delta, \Delta\alpha_{\rm star}, \Delta\delta_{\rm star}\}$ that describe the belt center and stellar position to be within $5''$ of the offsets predicted from the stellar proper motion; this constraint very generously accommodates the uncertainties in the proper motion and the absolute astrometry of the observations.

For the ATCA 7 mm observations, where the ϵ Eridani emission belt is not visible in the image, we simplified the model substantially. We fix all of the model parameters to the best-fit values from the analysis of the SMA data, except the total belt flux ($F_{\rm belt}$), the total flux for the central peak ($F_{\rm cen}$), and two position offsets $\{\Delta\alpha, \Delta\delta\}$. In essence, we fix the *shape* of the emission structure to that

found from analysis of the SMA data, and we determine the 7 mm fluxes for the central component and for the belt component, allowing for the possibility of a small positional shift between the SMA and ATCA datasets. We do not constrain $F_{\rm belt}$ to be positive as for the SMA observations

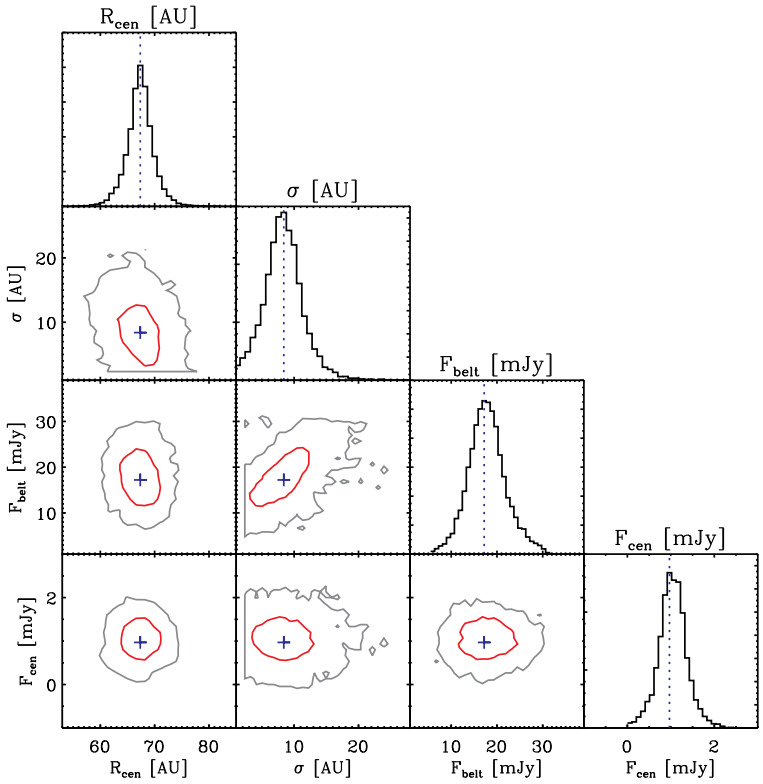

Figure 6.2: A sample of the output from a run of $\sim 10^4$ MCMC trials for the 4 best-fit Gaussian belt geometry parameters ($R_{\rm cen}$, σ, $F_{\rm belt}$, and $F_{\rm cen}$). The diagonal panels show the 1D histogram for each parameter marginalized over all other parameters considered in the model. For each parameter, the peak of each histogram is taken to be the best-fit value. The remaining panels show contour plots of the 1σ (red) and 2σ (gray) regions for each pair of parameters, with the blue crosses marking the best-fit values.

6.3.3 Results of Model Fits

Table 6.3 lists the resulting best-fit parameter values and their 68% uncertainties determined from the marginalized posterior probability distributions for both the power law and Gaussian belt models fit to the SMA 1.3 mm data. Figure 6.2 shows a sample of the output for the main Gaussian belt parameters, including the marginalized posterior probability distributions. The 1σ and 2σ regions are determined by assuming normally distributed errors, where the probability that a measurement has a distance less than a from the mean value is given by $\mathrm{erf}\left(\frac{a}{\sigma\sqrt{2}}\right)$. Both of these functional forms provide good fits to the observed visibilities, with reduced χ^2 values of about 1.4 (59,924 independent data points, 11 and 10 free parameters for the power law and Gaussian models, respectively) for each. Figure 6.3 shows the best-fit models of the 1.3 mm data in the image plane, at the full resolution of the models, and imaged like the SMA data, both without noise and with the noise level obtained by the observations, which results in patchy outer belt emission very similar to the SMA image in Figure 6.1. The imaged residuals are also shown in Figure 6.3, and these are mostly noise (see Section 6.4.1 for further discussion of the residuals from these axisymmetric models).

A useful way of visualizing the interferometric data and model fits is through the deprojected visibility function, which takes advantage of (near) axisymmetry to reduce the dimensionality (Lay et al. 1997). In particular, the real part of the complex visibilities are averaged in concentric annuli of deprojected (u, v) distance, $\mathcal{R}_{uv}$, from the center of the emission structure. Figure 6.4 shows this view of the SMA 1.3 mm data together with the best-fit power law and Gaussian belt models.

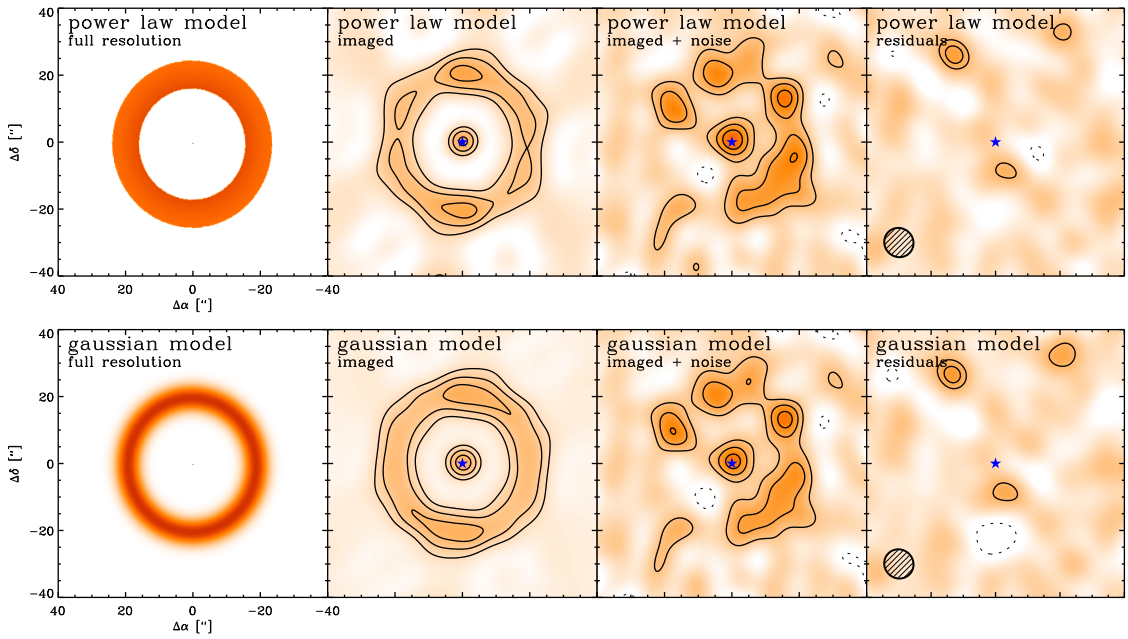

Figure 6.3: Images of the best-fit models to the SMA 1.3 mm emission. *(Upper): (left)* the best-fit power law disk model at full resolution, pixel scale $\sim 0\farcs2$ (0.8) AU, and *(center, left)* image of the best-fit power law disk model with no noise, *(center, right)* the best-fit power law disk model with simulated noise, and *(right)* the imaged residuals from the power law disk model, made using the same imaging parameters as in Figure 6.1. *(Lower): (left)* the best-fit Gaussian disk model at full resolution, and *(center, left)* image of the best-fit Gaussian disk model, *(center, right)* image with simulated noise of the best-fit Gaussian disk model, and *(right)* the imaged residuals from the Gaussian disk model, again made using the same imaging parameters as in Figure 6.1. The contour levels are at 0.4 mJy beam^{-1} (2σ) intervals in all panels. The ellipse in the lower left corner of the residual images indicates the $9\farcs2 \times 7\farcs0$ (FWHM) synthesized beam size.

Table 6.3: SMA Model Parameters

Param.	Description	Power Law Best-Fit	Gaussian Best-Fit
$F_{\rm belt}$	Belt flux density (mJy)	$16.9(+3.9, -5.6)$	$17.2(+5.1, -4.5)$
$F_{\rm cen}$	Central source flux (mJy)	$1.08(+0.19, -0.41)$	$1.06(+0.34, -0.34)$
$R_{\rm in}$	Belt inner radius (AU)	$53.4(+6.1, -5.0)$	–
$R_{\rm out}$	Belt outer radius (AU)	$80.2(+3.0, -7.1)$	–
x	Radial power law index	$1.92(+0.18, -2.94)$	–
$R_{\rm cen}$	Belt center radius (AU)	–	$64.4(+2.4, -3.0)$
σ	Belt width (AU)	–	$8.55(+2.54, -3.46)$
i	Belt inclination (°)	$17.9(+10.2, -15.3)$	$17.3(+14.2, -14.2)$
PA	Belt position angle (°)	$3.42(+23.3, -23.4)$	$1.66(+6.70, -6.70)$
$\Delta\alpha$	R.A. offset belt center (″)	$0.01(+0.65, -1.03)$	$0.02(+0.80, -0.80)$
$\Delta\delta$	Decl. offset belt center (″)	$1.63(+0.86, -0.86)$	$1.63(+0.70, -1.01)$
$\Delta\alpha_{\rm star}$	R.A. offset star (″)	$-1.18(+0.65, -1.40)$	$-1.22(+0.87, -1.26)$
$\Delta\delta_{\rm star}$	Decl. offset star (″)	$0.11(+0.90, -1.29)$	$0.11(+1.10, -1.10)$

Table 6.4: ATCA Model Parameters

Param.	Description	Best-Fit
$F_{\rm belt}$	Belt flux density (μJy)	$110.(+65., -117.)$
$F_{\rm cen}$	Central source flux (μJy)	$66.1(+6.9, -10.5)$
$\Delta\alpha$	R.A. offset belt center (″)	$-0.87(+0.72, -0.87)$
$\Delta\delta$	Decl. offset belt center (″)	$0.38(+0.86, -0.62)$

The result is a function with a zero-crossing null and several subsequent oscillations. Although these SMA observations are missing the short (u, v) spacings needed to sample the peak of the visibility function, the overall shape matches nicely that expected for a narrow annulus of emission, plus a small and constant positive offset contribution from an unresolved central source. Figure 6.4 also shows the single dish flux measurements at the zero-spacing of the deprojected visibility function (with small offsets from zero for clarity). It is remarkable that the simple axisymmetric belt models of the SMA data appear to provide a very good estimate of the total flux, despite the lack of shorter baseline data. This consistency provides indirect support for the basic model of the emission distribution.

Table 6.4 lists the best-fit parameter values from the modeling and their 68% uncertainties for the 7 mm data. This model again provides a good fit to the data, with reduced $\chi^2 = 1.32$ (151,976 independent data points, 4 free parameters). We note that the best-fit belt flux at 7 mm is positive, albeit with low statistical significance; this positive value suggests the presence of emission below the detection threshold in individual beams in the image. The position offsets between the ATCA and SMA data are small, consistent with zero.

6.4 Discussion

We have performed interferometric observations of the ϵ Eridani system at 1.3 mm and 7 mm with the SMA and the ATCA, respectively, with baselines that sample to $\sim 4''$ (13 AU) resolution. The 1.3 mm image reveals emission from a resolved outer dust belt located $\sim 18''$ (60 AU) from the star, and a compact source coincident

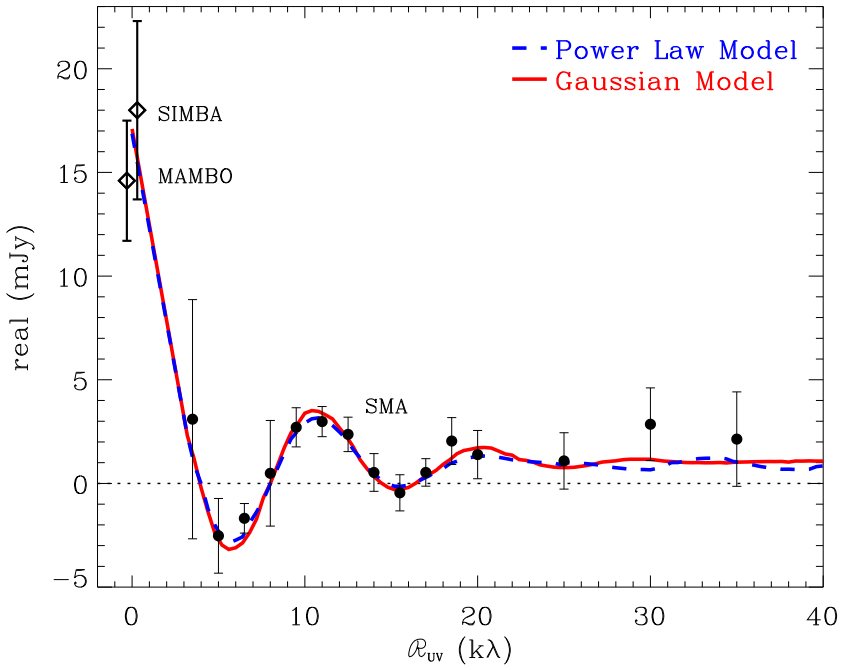

Figure 6.4: The real part of the SMA 1.3 mm visibilities averaged in bins of deprojected (u,v) distance from the disk center, compared to the best-fit power law (dashed blue) and Gaussian (solid red) disk models plus a central point-source. The single dish MAMBO-2/IRAM (Lestrade & Thilliez 2015) and SIMBA fluxes (Schütz et al. 2004) extrapolated from 1.2 mm to 1.3 mm are plotted at $\mathcal{R}_{uv} = 0$ kλ (slightly offset from zero, for clarity).

with the stellar position. The 7 mm image shows only a central peak, detected with greater significance than in the 1.3 mm image. We modeled the visibility data assuming two emission components, an outer belt with a power law or Gaussian radial surface brightness profile, and a central point source. Both functional forms provide good fits to the 1.3 mm data, and we used the best-fit emission shape parameters to obtain constraints on the component flux densities from the 7 mm data. We now use the new information about these emission components to discuss implications for the debris disk and to compare to claims derived from previous millimeter and submillimeter observations with lower angular resolution.

6.4.1 Outer Belt

Several basic properties of the outer emission belt are strongly constrained by the SMA 1.3 mm observations, including its flux, radial location and width, viewing geometry, and departures from axisymmetry. These new constraints bear on the possible presence of unseen planets in the system.

Belt Flux

The total flux density of the best-fit power law and Gaussian models, is constrained to be $F_{\rm belt} = 16.9^{+3.9}_{-5.6}$ mJy and $17.2^{+5.1}_{-4.5}$ mJy, respectively. These values are consistent with each other, within the uncertainties. They are also consistent with previous single-dish mapping measurements in this atmospheric window, accounting for minor differences in effective wavelength due to the broadband nature of bolometer detectors. Lestrade & Thilliez (2015) obtained a total flux density of 17.3 ± 3.5 mJy using MAMBO-2 on the IRAM 30-m telescope and Schütz et al. (2004) measured a total flux density of 21.4 ± 5.1 mJy using SIMBA with the SEST 15-m telescope. If we extrapolate these measurements using the spectral index of ~ 2.14 derived for ϵ Eridani at submillimeter wavelengths (Gáspár et al. 2012), we find close agreement with the values obtained from the SMA analysis. In particular, extrapolating the IRAM/MAMBO-2 observation to 1.3 mm gives 14.6 ± 2.9 mJy, while the older SIMBA observation gives 18.0 ± 4.3 mJy (see Figure 6.4).

Belt Location and Width

For the best-fit power law model, the outer radius of the millimeter emission belt is determined to be $R_{\rm out} = 80.2^{+3.0}_{-7.1}$ AU. Previous imaging studies of ϵ Eridani provide estimates of the outer radius between $70 - 90$ AU, in good agreement with this determination (Greaves et al. 1998, 2005, 2014; Backman et al. 2009). Additionally, we constrain the inner radius of the power law model, $R_{\rm in} = 53.4^{+6.1}_{-5.0}$ AU. This value agrees most closely with analysis of 160 μm *Herschel* observations by Greaves et al. (2014), which also suggest an inner radius of the outer belt of ~ 54 AU. Other single-dish observations indicated that the belt extends further inward towards the star, $R_{\rm in} = 35 - 40$ AU (Greaves et al. 1998, 2005; Backman et al. 2009). The model fits to the SMA 1.3 mm data do not support such a wide belt with an inner radius so close to the star.

The best-fit Gaussian model is characterized by a radial location, $R_{\rm cen} = 64.4^{+2.4}_{-3.0}$ AU, and a width, $\sigma = 8.55^{+2.54}_{-3.46}$ AU, or FWHM $= \Delta R = 2\sqrt{2\ln(2)} \times \sigma = 20.2^{+6.0}_{-8.2}$ AU. These parameters are most directly comparable to the belt parameters derived by Lestrade & Thilliez (2015) using IRAM/MAMBO-2 observations at 1.2 mm with a telescope FWHM beam size of $10\farcs7$; they fit a Gaussian shape to the disk emission radial profile and obtain a central radius $R_{\rm cen} = 57 \pm 1.3$ AU, FWHM $= 12'' \pm 1''$, and infer $8 \leq \Delta R \leq 22$ AU. This central radius is slightly smaller than that derived from the SMA data, but plausibly consistent within the mutual uncertainties. Since the lower limit on the width is narrower than implied by the fit to the SMA data at the 68% confidence interval, we examine this potential discrepancy more closely.

The effect of changing the belt location ($R_{\rm cen}$) and width (σ) is dramatic on the null locations in the deprojected visibility function. We expressed our Gaussian model using a surface brightness profile of the form $I_\nu(r) = A \times \exp[-((r - R_{\rm cen})/\sqrt{2}\sigma)^2]$. The Fourier transform of a radially symmetric function like this can be expressed by a Hankel transform:

$$F(\rho) = 2\pi A \int_0^\infty I_\nu(r) J_0(\rho r) r dr, \tag{6.1}$$

where, $\rho = 2\pi\sqrt{u^2 + v^2} = 2\pi\mathcal{R}_{uv}$. For a Gaussian ring, there is an exact solution to this integral involving an infinite series of hypergeometric functions that can be evaluated numerically to find the exact locations of the visibility nulls. Fortunately, there is also an approximate solution to the Hankel transform using a generalized shift operator (described in Baddour 2009) that yields the values of the null locations to within 1% of the exact solution,

$$F(\rho) = 2\pi A\sigma^2 \times \exp[-(\rho\sqrt{2}\sigma)^2/4] \times J_0(\rho R_{\rm cen}), \tag{6.2}$$

From this simple expression, we can see immediately that for a fixed belt width, decreasing the belt radius (inward towards the star) moves the zero-crossing null locations towards larger $\mathcal{R}_{uv}$. For a fixed belt location, decreasing the belt width moves the zero-crossing null locations towards slightly smaller $\mathcal{R}_{uv}$ (and increases the amplitude of subsequent oscillations). The best-fit Gaussian model to the SMA data, $R_{\rm cen} = 64$ AU, $\sigma = 8.6$ AU yields nulls at $\mathcal{R}_{uv} \approx 4$, 8, and 14 k$\lambda$. By comparison, a Gaussian model with $R_{\rm cen} = 57$ AU and $\Delta R = 8$ AU ($\sigma \sim 4$ AU), at the lower limit of width suggested by Lestrade & Thilliez (2015), results in nulls at $\mathcal{R}_{uv} \approx 5$, 9, and

16 kλ, which are significantly offset from the data. The differences between these fit results may stem from the oversimplified assumption of a strict Gaussian shape for the emission, perhaps exacerbated by deconvolution of the synthesized beam resulting from the shift-and-add procedure used to restore the MAMBO map from the chopped observations of the ϵ Eridani field.

The presence of planets can affect the widths of planetesimal belts, through dynamical interactions. Given the best-fit Gaussian belt parameters, we can constrain the fractional belt width of the ϵ Eridani debris disk to $\Delta R/R = 0.31^{+0.09}_{-0.13}$. This fractional width lies within the range of $0.1 \leq \Delta R/R \leq 0.4$ obtained by Lestrade & Thilliez (2015). For comparison, the classical Kuiper Belt in our Solar System appears radially confined between 40 and 48 AU ($\Delta R/R \sim 0.18$), filling the region between the 3:2 and 2:1 resonances with Neptune, likely the result of its outward migration (Hahn & Malhotra 2005). A narrow ring of millimeter emission in the Fomalhaut debris disk (FWHM $\sim$ 16 AU and $\Delta R/R \sim 0.1$) has been attributed to confinement by shepherding planets orbiting inside and outside the ring (Boley et al. 2012). The best-fit value of the fractional width of the ϵ Eridani belt is wider than the Fomalhaut belt and the classical Kuiper Belt, but not as wide as the belt surrounding the Sun-like star HD 107146, which also shows hints of a more complex radial structure (Ricci et al. 2015a).

The SMA 1.3 mm data do not place any strong constraints on the sharpness of the belt edges. This is evidenced by the comparable fit quality for both the sharp-edged power law and smoother Gaussian surface density profiles. Sharp edges in the underlying planetesimal distribution might be expected from planetary interactions, as regions within chaotic zone boundaries are rapidly cleared. For

example, the sharp inner edge of the Fomalhaut debris disk seen in scattered light has long suggested sculpting by a planet (Quillen 2006; Chiang et al. 2009). In contrast, "self-stirred" debris disks are not expected to show sharp edges. In these models, the formation of Pluto-sized bodies initiate collisions that propagate outward to radii of several tens of AU over Gyr timescales (Kenyon & Bromley 2008). This process tends to produce a radially extended planetesimal belt, with an outwardly increasing gradient. The specific models of Kennedy & Wyatt (2010) predict an $r^{7/3}$ profile for the belt optical depth. Given the limits of the resolution and sensitivity of the SMA data, model fitting does not provide a strong constraint on the power law gradient of the belt emission, $x = 1.92^{+0.18}_{-2.94}$. However, if we take this best-fit exponent at face value and assume that the emitting dust is in radiative equilibrium with stellar heating, which gives a temperature gradient close to $T \propto r^{-0.5}$, then this value implies a rising surface density profile, $\Sigma \propto r^{2.4}$ (with large uncertainty). This is similar to the rising surface density profile, $\Sigma \propto r^{2.8}$ found from millimeter observations of the AU Mic debris disk (MacGregor et al. 2013), as well as the rising surface density towards the outer edge of the HD 107146 debris disk (Ricci et al. 2015a). Since the surface density of protoplanetary accretion disks decreases with radius, this small but growing sample of debris disks with rising gradients may point to support for self-stirred models of collisional excitation.

Belt Viewing Geometry

In addition to the belt parameters, the data place constraints on the disk viewing geometry through the inclination and position angle parameters. The position angles from both the power law and Gaussian belt models are consistent with $PA = 0°$,

as previous observations have found (Lestrade & Thilliez 2015). The inclinations determined from the SMA models are $i = 17.^{\circ}9^{+10.2}_{-15.3}$ (power law) and $i = 17.^{\circ}3^{+14.2}_{-14.2}$ (Gaussian), lower than but consistent with claims of $i \approx 25^{\circ}$ from analysis of most other far-infrared and submillimeter images (Greaves et al. 1998, 2005; Lestrade & Thilliez 2015). Greaves et al. (2014) fit a flat ring model to *Herschel* 160 μm data and obtain a higher inclination value, $i = 30^{\circ} \pm 5^{\circ}$, still compatible with the fits to the SMA 1.3 mm data within the uncertainties. However, this difference could be a sign of background confusion affecting the inferences from the far-infrared images, or perhaps a wavelength dependence of this parameter due to the emission sampling different grain size populations. To assess whether or not such a higher inclination could affect the other belt parameters in the SMA analysis, we fixed $i = 30^{\circ}$ and re-ran the MCMC model fitting procedure; the best-fit parameters are hardly changed ($< 3\%$).

Limits on Belt Stellocentric Offset

The model fits show no significant centroid offset between the belt and central component, as might result from the secular perturbations of a planet in an eccentric orbit interior to the belt. For planet induced eccentricities, the displacement of the belt centroid from the star should be $\sim ae$, where a is the semi-major axis of the belt and e is the forced eccentricity (e.g. Chiang et al. 2009). Our modeling allows us to place a robust 3σ upper limit on the displacement, $\Delta r_{\rm cen} \lesssim 2.''7 = 8.7$ AU. Based on a possible far-infrared north-south flux asymmetry attributed to pericenter glow (enhanced emission at periapse), Greaves et al. (2014) raise the possibility of an additional planet in the ϵ Eridani system with semi-major axis within the outer belt

$a = 16 - 54$ AU and eccentricity $e \approx 0.03 - 0.3$. Given the constraint on the centroid offset from the SMA data, the presence of a giant planet on a wide orbit of several 10's of AU with a large eccentricity, $e \gtrsim 0.1$ is disfavored. This is in accord with direct imaging constraints at infrared wavelengths that preclude planets of about 1 Jupiter mass beyond 30 AU (Janson et al. 2015). However, the effects of a Uranus or Neptune-like planet with lower orbital eccentricity is still easily accommodated within the limits.

Limits on Belt Azimuthal Structure

The azimuthal structure of the ϵ Eridani debris disk has been the subject of much debate. The first JCMT/SCUBA 850 μm image of the disk showed a non-uniform brightness distribution with several peaks of modest signal-to-noise ratio (Greaves et al. 1998). Follow-up JCMT/SCUBA observations from up to 5 years later suggested that three of the peaks in the original image appear to move with the stellar proper motion, and in fact showed tentative evidence of counterclockwise rotation of $\sim 1^\circ$ yr^{-1} (Greaves et al. 2005). Several other peaks did not appear to move with the star and were presumed to be background features. Lestrade & Thilliez (2015) claim from IRAM/MAMBO-2 observations that the disk shows a similar azimuthal structure, with four peaks, in the northeast, southeast, southwest, and northwest. However, *CSO* observations at 350 μm did not confirm the same peaks (Backman et al. 2009), and *Herschel* observations at 250 μm (albeit at lower resolution) show a relatively smooth emission distribution, with the southern end $\sim 10\%$ brighter than the northern end (Greaves et al. 2014).

The interest in determining the robustness of the ϵ Eridani clump structure stems from the suggestion that the outward migration of a planet could trap planetesimals outside of its orbit in mean motion resonances. A variety of numerical simulations show that the pattern of clumps observed in a disk depends on the planet mass and the resonances involved (e.g. Kuchner & Holman 2003; Wyatt 2003; Deller & Maddison 2005). Thus, the emission morphology of a debris belt can be diagnostic of the presence of a planet and its migration history. However, other numerical simulations suggest that all azimuthal asymmetries should be effectively erased by collisions within debris disks as dense as ϵ Eridani (Kuchner & Stark 2010), which would imply that any clumps are spurious, or perhaps background sources. Background sources seem particularly problematic to the east of ϵ Eridani in wide field *Herschel* submillimeter images, which likely contributed to confusion at earlier epochs when the disk was superimposed on them.

The SMA 1.3 mm data probes structure at higher angular resolution than the previous single dish observations. Moreover, the interferometer naturally provides spatial filtering that serves to highlight the presence of any compact emission peaks. After removing azimuthally symmetric models from the SMA data, any significant azimuthal structure should be readily apparent in the imaged residuals. Figure 6.5 shows the azimuthal profile of the residual image obtained after subtracting the best-fit Gaussian belt model from the data. Each point represents the mean brightness calculated in a small annular sector with opening angle of 10° and radial range of 10″ to 30″. Uncertainties are the image rms noise divided by the square root of the number of beams in each sector. The only potentially significant feature is a peak at 20°, which is visible at the $\sim 4\sigma$ level in the residual images of Figure 6.3

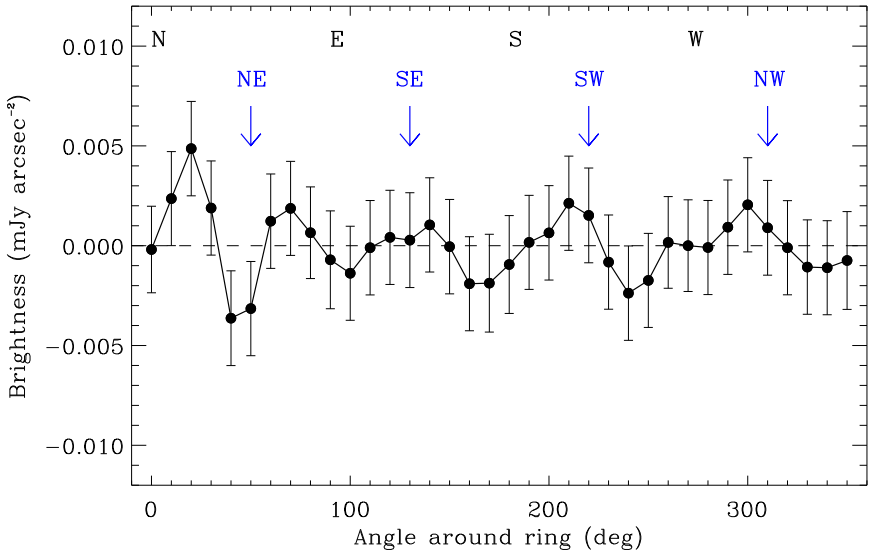

Figure 6.5: Azimuthal profile of the residual emission after subtracting our best-fit Gaussian model from the 1.3 mm continuum emission. The four clumps discussed by Greaves et al. (2005) and Lestrade & Thilliez (2015) are marked by the blue arrows.

(right panels). The locations of the previously claimed four clumps (Greaves et al. 2005; Lestrade & Thilliez 2015) are marked with arrows in Figure 6.5. While the azimuthal profile of the imaged residuals shows roughly four low significance peaks, these are not aligned well with the previously claimed clumps, and the separations cannot be readily attributed to the previously claimed rotation. However, the signal-to-noise of these residuals is still lacking. The signature of the four clumps discussed in Lestrade & Thilliez (2015), if they do exist, have been weakened in the fitting procedure by using an azimuthally uniform ring as the model. A more definitive statement about low level clumps will require high resolution observations with higher sensitivity.

The imaginary part of the visibilities is very sensitive to the presence of asymmetries in the emission structure. Indeed, the effect of the marginally

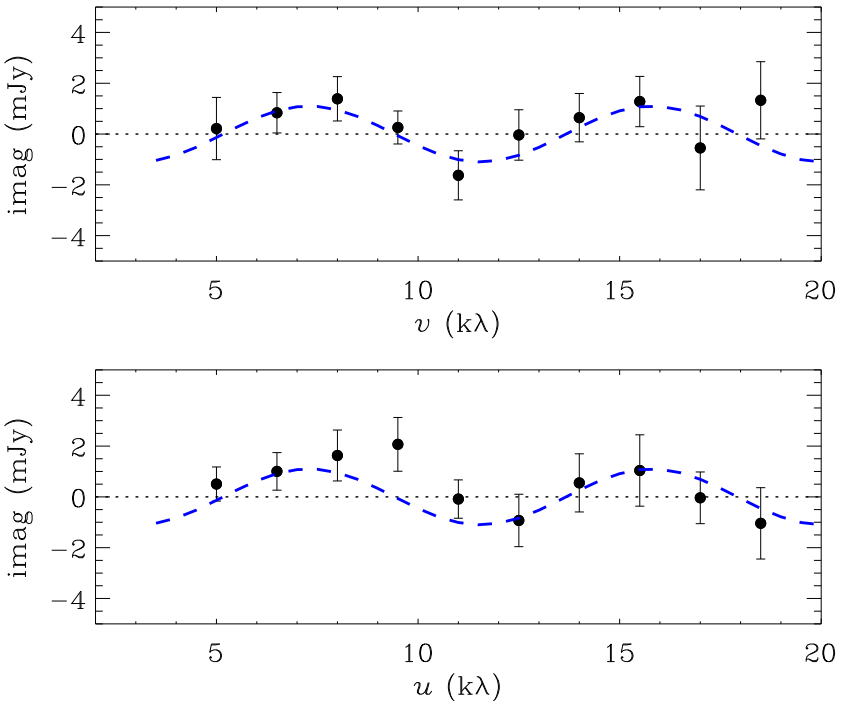

Figure 6.6: Complex visibilities of the 1.3 mm emission binned along the v-axis *(top)* and the u-axis *(bottom)*. Model visibilities generated by inserting a 1 mJy point source at the position of the 4σ peak seen in the residual map are shown by the blue dashed lines.

significant peak in the residual images is apparent. Figure 6.6 shows the imaginary part of the visibilities binned along the u-axis and along the v-axis of the Fourier plane. For a symmetric structure, the imaginary part of the visibilities should be zero; however, both of these views show hints of a low amplitude, sinusoidal oscillation. This structure in the visibilities arises naturally from a single, offset emission peak. The Fourier transform of a point source with amplitude, A, offset from the center of the image in the u and v directions by x_0 and y_0, respectively, is given by $G(u, v) = A \times \exp[-2\pi(x_0 u + y_0 v)]$ (making use of the shift theorem, whereby a shift in the position of a function by an amount x_0 corresponds to a phase change in its Fourier transform by $\exp(i2\pi x_0 u)$, e.g. Isella et al. 2013); the

imaginary part of this expression is $\mathcal{I}(G(u,v)) = A \times \sin[2\pi(x_0 u + y_0 v)]$. That is, a point source offset from $(0,0)$ introduces a simple sinusoidal oscillation in the imaginary part of the visibilities. As shown in Figure 6.6, if we insert a 1 mJy point source at the location of the 4σ peak in the residual image ($x_0 \approx 15''$, $y_0 \approx 25''$) into the visibilities, the resulting imaginary visibility curve matches very well the shape and scale of the residuals. Thus, this single residual feature can account for most of the structure in the imaginary visibilities, or most of the detected asymmetry. This feature does not match up with any of the clumps previously identified in single dish images. Also, it is positioned clockwise from the northeast feature, which is not consistent with the counterclockwise rotation suggested by Greaves et al. (2005). The exact nature of this marginally significant peak is uncertain. If it is a background galaxy, then the proper motion of the star will move the debris disk away from it, and this should become evident in interferometric observations at future epochs. An extragalactic source should also appear compact at the arcsecond level. Recent deep ALMA surveys (Hodge et al. 2013; Karim et al. 2013) have built up statistics describing the number counts of submillimeter galaxies expected in a given field of view. At 1.3 mm, the expected number of sources with flux ≥ 1 mJy expected in the $52''$ primary beam of the SMA is $0.41^{+0.25}_{-0.15}$ (Ono et al. 2014). Hence the presence of a background submillimeter galaxy in the image at this flux level is not a rare event. Verification and characterization of any asymmetric structure in the millimeter emission from the belt requires observations with higher resolution and sensitivity.

Belt Spectral Index

The long wavelength spectral index of the continuum belt emission reflects the underlying dust opacities and provides a constraint on the size distribution of the emitting grains in the debris disk (Ricci et al. 2012), which can be related to collisional models.

For optically thin dust emission, the flux density is given by $F_\nu \propto B_\nu(T_{\rm dust})\kappa_\nu M_{\rm dust}/D^2$, where $B_\nu(T_{\rm dust})$ is the Planck function at the dust temperature $T_{\rm dust}$, $\kappa_\nu \propto \nu^\beta$ is the dust opacity, expressed as a power law at these long wavelengths, $M_{\rm dust}$ is the dust mass, and D is the distance. At long millimeter wavelengths, for sufficiently high temperatures, the Planck function reduces to the Rayleigh-Jeans approximation $B_\nu(T_{\rm dust}) \propto \nu^{\alpha_{\rm Pl}}$ with $\alpha_{\rm Pl} = 2$. Thus, $\alpha_{\rm mm} \approx \alpha_{\rm Pl} + \beta$, where $\alpha_{\rm mm}$ is the millimeter spectral index. Draine (2006) derived a relation between β, the dust opacity power law index, and q, the grain size distribution parameter: $\beta \approx (q-3)\beta_s$, where $\beta_s = 1.8 \pm 0.2$ is the dust opacity spectral index in the small particle limit for interstellar grain materials, valid for $3 < q < 4$ and size distributions that follow a power law over a broad enough interval. Combining these relationships provides a simple expression for the slope of the grain size distribution, q, as a function of $\alpha_{\rm mm}$, $\alpha_{\rm Pl}$, and β_s: $q = (\alpha_{\rm mm} - \alpha_{\rm Pl})/\beta_s + 3$.

For ϵ Eridani, the fit to the ATCA 7 mm data places an upper limit on the belt flux density of $F_{\rm belt} < 310$ μJy (3σ). Combining this 7 mm limit with the SMA 1.3 mm measurement provides a long lever arm in wavelength that largely overcomes systematic uncertainties and constrains the millimeter spectral index, $\alpha_{\rm mm} > 2.39$. This limit on the spectral index results in a limit on the grain size distribution

power-law index $q > 3.22$.

The derived limit on the grain size distribution power-law index is consistent with the classical prediction of $q = 3.5$ for a steady-state collisional cascade (Dohnanyi 1969). Ricci et al. (2012) obtained a similar result from analysis of the millimeter spectrum of the Fomalhaut debris disk, $q = 3.48 \pm 0.14$. This standard collisional cascade assumes that collisions in the disk occur between bodies of identical tensile strength and velocity dispersion, regardless of size. Pan & Schlichting (2012) revisited the theory by relaxing the assumption of a single velocity dispersion and solving self-consistently for a size-dependent velocity distribution in steady-state. This more complex analysis yields steeper size distributions, with $q \approx 4$. Since the ϵ Eridani spectral index is only a lower limit, a steeper grain size distribution cannot be ruled out. We note that the best-fit value for the 7 mm flux density ($F_{\rm belt} = 110$ μJy) yields $q = 3.55 \pm 0.36$, still shallower than predicted by models with size-dependent velocity dispersions. This result, and the more robust measurement for Fomalhaut, do not support the steeper size distributions predicted by the collisional models with velocity distribution variations. But spectral indices need to be determined for a much larger sample of debris disks to draw a definitive conclusion.

6.4.2 Central Component

A central source is clearly detected in the SMA 1.3 mm image and ATCA 7 mm image, coincident with the position of the star at the time of observation. The source size is below the resolution limit of these observations, most clearly evidenced

by the lack of fall off at long baselines in Figure 6.4. The 1.3 mm flux density of this source is $F_{\rm cen} = 1.08^{+0.19}_{-0.41}$ mJy. Lestrade & Thilliez (2015) report a similar value in MAMBO-2/IRAM 1.2 mm data, detecting a central source with flux density 1.2 ± 0.3 mJy. These measurements are only marginally compatible with expectations for the stellar photosphere at these long wavelengths. The effective temperature of ϵ Eridani is $T_{\rm eff} = 5039 \pm 126$ K (Baines & Armstrong 2012), and a Kurucz stellar atmosphere model (see Backman et al. 2009) predicts a 1.3 mm flux density of 0.53 mJy (with 2% uncertainty). The ATCA 7 mm flux density of this same central source is $F_{\rm cen} = 66.1^{+6.9}_{-10.5}$ μJy, substantially in excess of the stellar photoshere model flux prediction of 18 μJy. The central source persists at a consistent intensity in all of the 8 days of ATCA observations, showing no significant variability. The mean flux density is 66.5 ± 9.5 μJy and 65.9 ± 7.0 μJy for the June and August observations, respectively.

In principle, the central 1.3 mm excess emission could be explained by thermal dust emission from a warm inner belt. This small 1.3 mm excess, together with *Spitzer* 24 μm and *Herschel* 70 and 160 μm inner excesses, are consistent with emission from a $70 - 100$ K blackbody, similar to previous inferences by Backman et al. (2009) and Greaves et al. (2014) from the infrared spectrum alone. For reasonable grain sizes, this blackbody emission corresponds to a (very narrow) inner dust belt at $2 - 10$ AU, consistent with the size constraint from the SMA observations. However, this same blackbody model produces negligible emission at 7 mm. While previous infrared measurements indicate that there is clearly some warm dust present in the system (unresolved in our observations), no inner dust belt scenario can also match the substantial 7 mm excess from the ATCA observations.

We consider it likely that the unresolved excess emission from the central source arises from an additional *stellar* component, either an ionized corona or chromosphere. The absence of variability on the month to month timescale suggests a thermal origin. In particular, the millimeter wavelength emission from ϵ Eridani is reminiscent of the nearby solar-type stars α Cen A and B (spectral types G2V and K2V) recently reported by Liseau et al. (2015) and attributed to heated plasma, similar to the Sun's chromosphere. Following Liseau et al. (2013), we calculate the Planck brightness temperature for ϵ Eridani at 1.3 mm and 7 mm, assuming the photospheric radius of the star is sufficiently similar at optical and radio wavelengths to introduce negligible errors. Optical interferometry of ϵ Eridani gives a precise measure of the stellar radius, $R_{\rm phot} = 0.74 \pm 0.01\ R_{\odot}$ (Baines & Armstrong 2012). At 1.3 mm, this radius and the excess emission implies $T_{\rm B} = 7800 \pm 1400$ K, somewhat higher than the optical effective temperature. At 7 mm, however, $T_{\rm B} = 13000 \pm 1600$ K, very much in excess of the photospheric prediction. Indeed, the ϵ Eridani emission follows the same trend with increasing wavelength as found for α Cen A and B from ALMA observations. Liseau et al. (2015) measure spectral indices between 0.87 mm and 3.1 mm of 1.62 and 1.61 for α Cen A and B, respectively. From the SMA and ATCA data, the spectral index of the central component of ϵ Eridani between 1.3 mm and 7 mm is very similar, 1.65 ± 0.23 (where we have added in quadrature the $\sim 10\%$ flux scale uncertainties at both wavelengths with the 1σ errors from model fits). The stellar spectrum clearly starts to deviate strongly from a simple optically thick photosphere with a Rayleigh-Jeans spectral index of 2.0, and the contrast between the photosphere and the putative chromosphere increases at longer wavelengths. While observations of ϵ Eridani at

centimeter wavelengths have so far provided only upper limits, < 80 μJy at 3.6 cm (Gudel 1992) and < 105 μJy at 6 cm (Bower et al. 2009), much more sensitive observations are now possible with the upgraded Karl G. Jansky Very Large Array (VLA), and this would be useful to help constrain the plasma properties.

6.5 Conclusions

We present SMA 1.3 mm and ATCA 7 mm observations of ϵ Eridani, the first millimeter interferometric observations of this nearby debris disk system, probing to 4″ (13 AU) scales. These observations resolve the outer dust emission belt surrounding the star, and they reveal a compact emission source coincident with the stellar position. We use MCMC techniques to fit models of the emission structure directly to the visibility data in order to constrain the properties of the two components. The main results are:

1. The outer belt is located precisely and resolved radially. Gaussian and power law emission profiles each fit the SMA 1.3 mm data comparably well. For the best-fit Gaussian model, the belt radial location is $R_{\rm cen} = 64.4^{+2.4}_{-3.0}$ AU and FWHM $= 20.2^{+6.0}_{-8.2}$ AU, corresponding to a fractional belt width $\Delta R/R = 0.31^{+0.09}_{-0.13}$. This width is at the high end of inferences from previous single dish millimeter observations, and wider than the classical Kuiper Belt in our Solar System.

2. The outer belt shows no evidence for significant azimuthal structure that might be attributed to gravitational sculpting by planets. After subtracting

a symmetric model from the SMA 1.3 mm data, imaging shows only one low significance peak, and its location does not correspond to any clumps identified in previous millimeter and submillimeter observations of ϵ Eridani. The presence of this feature is consistent with source counts for the extraglactic background in the field of view. In addition, the SMA 1.3 mm data constrains any centroid offset of the belt from the star to < 9 AU, which limits the presence of giant planet perturbers on wide and eccentric orbits in the system.

3. A central source coincident with the star is clearly detected in both the SMA 1.3 mm image and the ATCA 7 mm image, and the flux densities of this source exceed extrapolations from shorter wavelengths for the stellar photosphere. While the excess is marginal at 1.3 mm, it is highly significant– about a factor of three– at 7 mm. The stellar spectrum clearly departs from an optically thick photosphere at these long wavelengths, with spectral index 1.65 ± 0.23 between 1.3 mm and 7 mm. This spectrum cannot be explained by an inner warm dust belt and plausibly results from heated plasma in a stellar chromosphere, by analogy with the Sun and α Cen. The high brightness temperature at 7 mm of 13000 ± 1600 K for a source of stellar size lends additional credence to this conclusion.

4. Combining the SMA 1.3 mm measurement of the belt flux density with the ATCA 7 mm upper limit constrains the spectral index of the emission, $\alpha_{\rm mm} > 2.39$. For conventional assumptions about the dust grains, this spectral index corresponds to a limit on the slope of the power law grain size distribution in the belt, $q > 3.22$, consistent with the classical prediction of $q = 3.5$ for a self-similar steady-state collisional cascade. This slope is also

consistent with the steeper distributions predicted by collisional models that allow for size-dependent velocities and strengths.

These SMA and ATCA millimeter wavelength observations provide the highest resolution view of the outer dust belt surrounding ϵ Eridani at the longest wavelengths to date. But deeper observations are still needed to measure radial gradients in the debris disk and to reveal substructure due to planets, if present, in order to further constrain scenarios for the evolution of planetesimals surrounding this very nearby star.

Acknowledgments

M.A.M acknowledges support from a National Science Foundation Graduate Research Fellowship (DGE1144152) and from the Swinburne Centre for Astrophysics & Supercomputing. D.J.W. thanks the Swinburne Visiting Researcher Scheme. S.T.M. acknowledges the support of the visiting professorship scheme from the Université Claude Bernard Lyon 1. The Submillimeter Array is a joint project between the Smithsonian Astrophysical Observatory and the Academia Sinica Institute of Astronomy and Astrophysics and is funded by the Smithsonian Institution and the Academia Sinica. We thank Mark Gurwell and Scott Paine for discussions about the Submillimeter Array primary beam shape.

7

ALMA Observations of the Debris Disk of Solar Analogue Tau Ceti

This thesis chapter originally appeared in the literature as

M. A. MacGregor, S. M. Lawler, D. J. Wilner, B. C. Matthews, G. M. Kennedy, M. Booth, J. Di Francesco, 2016, Astrophysical Journal, Vol. 828, pp. 113–120

Abstract

We present 1.3 mm observations of the Sun-like star τ Ceti with the Atacama Large Millimeter/submillimeter Array (ALMA) that probe angular scales of $\sim 1''$ (4 AU). This first interferometric image of the τ Ceti system, which hosts both a debris disk and possible multiplanet system, shows emission from a nearly face-on belt of cold

dust with a position angle of 90° surrounding an unresolved central source at the stellar position. To characterize this emission structure, we fit parametric models to the millimeter visibilities. The resulting best-fit model yields an inner belt edge of $6.2^{+9.8}_{-4.6}$ AU, consistent with inferences from lower resolution, far-infrared *Herschel* observations. While the limited data at sufficiently short baselines preclude us from placing stronger constraints on the belt properties and its relation to the proposed five planet system, the observations do provide a strong lower limit on the fractional width of the belt, $\Delta R/R > 0.75$ with 99% confidence. This fractional width is more similar to broad disks such as HD 107146 than narrow belts such as the Kuiper Belt and Fomalhaut. The unresolved central source has a higher flux density than the predicted flux of the stellar photosphere at 1.3 mm. Given previous measurements of an excess by a factor of ~ 2 at 8.7 mm, this emission is likely due to a hot stellar chromosphere.

7.1 Introduction

The 5.8 Gyr-old (Mamajek 2008) main-sequence G8.5V star τ Ceti is the second closest (3.65 pc, van Leeuwen 2007) solar-type star reported to harbor both a tentative planetary system and a debris disk (after ϵ Eridani, e.g. Greaves et al. 1998; Hatzes et al. 2000). The τ Ceti debris disk was first identified as an infrared excess by *IRAS* (Aumann 1985) and confirmed by ISO (Habing et al. 2001). Greaves et al. (2004) marginally resolved 850 μm emission from the system with the James Clerk Maxwell Telescope (JCMT)/SCUBA, revealing a massive (1.2 $M_\oplus$) disk extending to 55 AU from the star. Recent *Herschel* observations at 70, 160, and

250 μm resolve the disk well and are best fit by a broad dust belt with an inner edge between $1 - 10$ AU and an outer edge at ~ 55 AU (Lawler et al. 2014). Due to its proximity and similarity to our Sun in age and spectral type, τ Ceti has been the object of numerous searches for planets using the radial velocity technique (e.g. Pepe et al. 2011), most of which have proved unsuccessful. Using extensive modeling and Bayesian analysis of radial velocity data from the High Accuracy Radial Velocity Planet Searcher (HARPS) spectrograph (Mayor et al. 2003; Pepe et al. 2011), the Anglo-Australian Planet Search (AAPS) on the Anglo Australian Telescope (AAT), and the High Resolution Echelle Spectrograph (HIRES) on the Keck telescope (Vogt et al. 1994), Tuomi et al. (2013) report evidence for a tightly-packed five planet system. This purported planetary system consists of five super-Earths with masses of $4.0 - 13.2$ $M_\oplus$ (for orbits co-planar with the disk), semi-major axes ranging over $0.105 - 1.35$ AU, and small eccentricities, $e \sim 0 - 0.2$. The veracity of these planet candidates, however, remains controversial. Tuomi et al. (2013) acknowledge that the detected signals could also result from a combination of instrumental bias and stellar activity, although no further evidence is given to support these alternative interpretations. Also of note is the sub-Solar metallicity of τ Ceti, [Fe/H] $= -0.55 \pm 0.05$ dex (Pavlenko et al. 2012), which makes it an interesting target for exoplanet searches due to the observed higher frequency of low-mass planets around low-metallicity stars (Jenkins et al. 2013).

We present interferometric observations of the τ Ceti system at 1.3 mm using the Atacama Large Millimeter/submillimeter Array (ALMA). Millimeter imaging of this debris disk opens a unique window on the location and morphology of the underlying population of dust-producing planetesimals orbiting the star. While these

large, kilometer-sized bodies cannot be detected directly, millimeter observations probe emission from the large dust grains produced through collisions that are not rapidly redistributed by stellar radiation and winds (Wyatt 2006). These new ALMA observations provide limits on the disk location and width, which bear on the proposed planetary system within the disk. In Section 7.2, we present the ALMA observations of the τ Ceti system. In Section 7.3, we describe the analysis technique and disk model results. In Section 7.4, we discuss the significance of the best-fit model parameters for the dust belt inner edge, width, proposed planetary system, and the origin of a bright, unresolved central emission source.

7.2 Observations

The τ Ceti system was observed using Band 6 (1.3 mm) in December 2014 with the ALMA 12-m array. We obtained one scheduling block (SB) in good weather (PWV = 1.76 mm) with 34 antennas, with the longest baselines sampling to $1''$ (4 AU) resolution. These observations were complemented by two SBs taken with the Atacama Compact Array (ACA) in July 2014 to provide shorter baselines and sensitivity to emission at larger scales. For these ACA SBs, 11 operational antennas were available. The observation dates, baseline lengths, and total time on-source are summarized in Table 7.1. For maximum continuum sensitivity, the correlator was configured to process two polarizations in four 2 GHz-wide basebands centered at 226, 228, 242, and 244 GHz, each with 256 spectral channels. For the July SBs, the phase center was $\alpha = 01^{\rm h}44^{\rm m}02.348$, $\delta = -15°56'02''.509$ (J2000, ICRS reference frame). The phase center for the December SB was $\alpha = 01^{\rm h}44^{\rm m}02.299$,

$\delta = -15°56'02\farcs154$ (J2000, ICRS reference frame). Both phase centers were chosen to be the position of τ Ceti at the time of the observations given its proper motion of $(-1721.05, 854.16)$ mas yr^{-1} (van Leeuwen 2007). The field of view is $\sim 26''$, given by the FWHM size of the primary beam of the ALMA 12-m antennas at the mean frequency of 234 GHz.

The data from all three SBs were calibrated separately using the `CASA` software package (version 4.2.2). We corrected for time-dependent complex gain variations using interleaved observations of the calibrator J0132-1654. Observations of J0137-2430 were used to determine the spectral response of the system. The absolute flux calibration scale was derived from observations of Neptune, and a mean calibration was applied to all four basebands, with a systematic uncertainty of $\sim 10\%$ (see Butler 2012, for a complete discussion of flux density models of Solar System bodies).

To generate a first image at the mean frequency, 234 GHz (1.3 mm), we Fourier inverted the calibrated visibilities with natural weighting and a multi-frequency synthesis with the `CLEAN` algorithm. To improve surface brightness sensitivity, we included a modest taper using the `uvtaper` parameter in `CLEAN`, which controls the radial weighting of visibilities in the (u, v)-plane through the multiplication of the visibilities by the Fourier transform of a circular Gaussian (on-sky FWHM $= 6''$). With the added taper, however, it became difficult to resolve the outer disk and the central stellar emission. For clarity, we chose to image the disk and the star separately. We isolate the disk emission by subtracting a point source model from these data using the `CASA` task `uvsub` to account for the stellar emission. To isolate the stellar component, we image with `CLEAN` and no taper, only including

baselines longer than 40 kλ, where we expect the star to dominate the emission (see Section 7.3). We choose to account for the primary beam in our modeling (see Section 7.3.2) and thus do not apply a primary beam correction to any of these images.

Table 7.1: ALMA Observations of τ Ceti

Obs. Date	Array	# of Antennas	Projected Baselines (m)	Time on Target (min)
2014 Jul 7	ACA	11	$9-50$	5.8
2014 Jul 16	ACA	11	$9-50$	33.9
2014 Dec 15	12-m	34	$15-350$	41.4

7.3 Results and Analysis

7.3.1 Continuum Emission

Figure 7.1 shows an ALMA 1.3 mm image of the τ Ceti disk made with the central star subtracted (middle panel) along with an image including only baselines longer than 40 kλ showing emission from the star and not the disk (right panel). The *Herschel/PACS* 70 μm star-subtracted image (left panel) is shown for reference (Lawler et al. 2014). The natural weight rms noise is 30 μJy and 180 μJy for the 12-m and ACA observations, respectively. For the image showing only the stellar emission, the natural weight rms is higher, 35 μJy, since we exclude some baselines. The belt is not detected in the ACA observations given the low signal-to-noise ratio, and we only consider the 12-m data for imaging and modeling (see Section 7.3.2). For the 1.3 mm image of the star, the synthesized beam with natural weighting is

$1\farcs9 \times 1\farcs0$ (7×4 AU), and position angle $= -87°$. To improve surface brightness sensitivity, the image of the disk makes use of a modest taper and has a synthesized beam size of $6\farcs5 \times 6\farcs1$ (24×22 AU), and position angle $= 55°$.

These 1.3 mm images reveal (1) patchy emission ($\sim 6\sigma$) from a nearly face-on (low inclination) dust disk, and (2) a bright (23σ), unresolved central peak coincident with the expected stellar position. The disk is located $\sim 12''$ (~ 44 AU) from the star with a position angle of $\sim 90°$ (E of N). Reid et al. (1988) quantify the position uncertainty, σ of a point source given the signal-to-noise ratio, S/N, and the synthesized beam size, θ: $\sigma \sim 0.5\theta/(S/N) \approx 0\farcs14$, for our observations. The position of the observed central source is coincident with the expected stellar position within this uncertainty.

7.3.2 Emission Modeling Procedure

We make use of the modeling scheme described in MacGregor et al. (2013, 2015b). In this approach, we construct parametric models of the 1.3 mm disk emission and then compute corresponding model visibilities using a python implementation[1] of the Miriad `uvmodel` task (Loomis et al. in prep). To determine the best-fit parameter values and their uncertainties, we employ the `emcee` Markov Chain Monte Carlo (MCMC) package (Foreman-Mackey et al. 2013). This affine-invariant ensemble sampler for MCMC, enables us to accurately sample the posterior probability

[1]The code used to perform this part of the analysis is publicly available at `https://github.com/AstroChem/vis_sample` or in the Anaconda Cloud at `https://anaconda.org/rloomis/vis_sample`

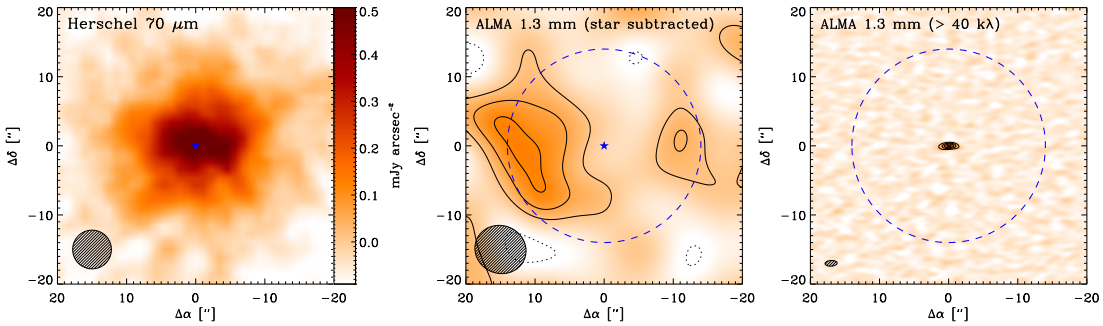

Figure 7.1: *(left) Herschel/PACS* map of the 70 μm emission from the τ Ceti debris disk with the stellar contribution subtracted (see Lawler et al. 2014). The *Herschel* 5.″6 beam size is shown by the ellipse in the lower left corner. *(center)* The τ Ceti debris disk imaged by ALMA at 1.3 mm with contours in steps of 2σ, where σ is the rms noise level in the image $\sim$ 30 μJy. To isolate the disk emission, a point source model has been subtracted to account for the central stellar emission. Using natural weighting along with a 6″ Gaussian taper, the resulting FWHM synthesized beam size is 6.″5 $\times$ 6.″1. *(right)* ALMA image of the 1.3 mm continuum emission for baselines longer than 40 kλ showing only the central point source with contours in steps of 5σ. Imaging with natural weighting and no taper yields a FWHM synthesized beam size of 1.″9 $\times$ 1.″0. The position of the stellar photosphere is indicated in the left two panels by the blue star symbol. The primary beam of the ALMA antennas at 1.3 mm (FWHM $\sim$ 26″) is shown by the dashed blue circle in the right two panels.

functions of all model parameters with minimal fine-tuning. Due to the much higher rms noise of the ACA data, we choose to only fit models to the visibilities from the full 12-m ALMA array.

We model the millimeter emission of the τ Ceti debris disk as an axisymmetric, geometrically thin belt with an inner radius, $R_{\rm in}$, an outer radius, $R_{\rm out}$, and a radial surface brightness distribution described by a simple power law, $I_\nu \propto r^{\gamma-0.5}$. Here, γ describes the power law in radial surface density, $\Sigma \propto r^\gamma$, and temperature is assumed to follow a power law, $T \propto r^{-0.5}$, approximating radiative equilibrium for blackbody grains. To first order, the dust temperature also depends on the

grain opacity, $T \propto r^{-2/(4+\beta)}$, where β is the power law index of the grain opacity as a function of frequency, $\kappa_\nu \propto \nu^\beta$. Gáspár et al. (2012) measure $\beta = 0.58$, from observations of debris disks, which implies a temperature power law index of ~ -0.44. Thus, the expected change in the temperature profile due to β is much smaller than the uncertainty in our resulting model fits and we choose to ignore this effect. Furthermore, the surface density and temperature profiles are degenerate, so we assume a blackbody profile and fit only for γ.

We constrain the outer disk radius using previous JCMT/SCUBA observations (Greaves et al. 2004), since the parent body disk may have a different size relative to the smaller grains imaged with *Herschel*. While Greaves et al. (2004) suggested that the disk was highly inclined, the *Herschel* image (Figure 7.1, left panel) indicates that it is closer to face-on. The SCUBA image is therefore marginally resolved at best, so we take their derived disk radius of 55 AU as an upper limit on $R_{\rm out}$ and allow the inner radius, $R_{\rm in}$, to vary. We fit for the surface density radial power law index, γ, within a range of -4 to 4. The unresolved central peak seen in images is modeled by a central point source with flux, $F_{\rm cen}$. We do not fit for any relative offsets of the belt center, point source position, and phase center. Models of the *Herschel* images derive an inclination of $i = 35^\circ \pm 10^\circ$ and position angle, $PA = 105^\circ \pm 10^\circ$ (Lawler et al. 2014), and we assume that the millimeter belt emission is described by the same geometry. For all parameters, we assume uniform priors and require that the model be physically plausible: $F_{\rm cen} \geq 0$, and $0 \leq R_{\rm in} < R_{\rm out} \leq 55$ AU.

A total flux density, $F_{\rm belt} = \int I_\nu d\Omega$, provides the normalization for the belt emission. Using SCUBA on the JCMT, Greaves et al. (2004) obtain a total flux density at 850 μm for the disk of 5.8 ± 0.6 mJy, including both the

central star and likely contamination from background sources. Recent SCUBA-2 observations at 850 μm yield a total flux density of 4.5 ± 0.9 mJy, including a contribution from the star of ~ 1 mJy (Holland et al., in prep.). An extrapolation of this measurement using the typical spectral index of 2.58 for debris disks at (sub)millimeter wavelengths (Gáspár et al. 2012), yields an expected flux density of the disk at 1.3 mm of 1.2 ± 0.2 mJy. This more robust single-dish flux measurement allows us to constrain the total flux density of our models with a Gaussian prior, 0.6 mJy $\leq F_{\rm belt} \leq$ 1.6 mJy, accounting for uncertainty in both the single-dish 850 μm flux measurement and the extrapolation to 1.3 mm.

The angular scale of the τ Ceti debris disk is $\sim 25''$ in diameter. At 1.3 mm, the half power field of view of the 12-m ALMA antennas is comparable, FWHM$\sim 26''$. Given this, we must account for the effect of the primary beam response on our model parameters. To do this, we model the ALMA primary beam as a Gaussian normalized to unity at the beam center and multiply each parametric disk model by this Gaussian beam model. Since we account for the effect of the primary beam in our modeling scheme, we choose not to apply a primary beam correction to the images shown in Figure 7.1 (right panels).

7.3.3 Results of Model Fits

Modeling the ALMA 1.3 mm visibilities yields a final best-fit model with a reduced χ^2 value of 1.1. Table 7.2 lists the best-fit values for each of the 5 free parameters along with their corresponding 1σ (68%) uncertainties. The 1D (diagonal panels) and 2D (off-diagonal panels) projections of the posterior probability distributions

for all parameters except the total belt flux, $F_{\rm belt}$, are shown in Figure 7.2. A full resolution image of this best-fit model (with a flat surface density profile, $\gamma = 0$, and the central star excluded) is shown in the leftmost panel of Figure 7.3. The same model convolved with the $\sim 6''$ ALMA synthesized beam and imaged like the observations in Figure 7.1 is shown in the next two panels both without (left) and with (right) simulated random noise with an rms of 30 μJy. Including the simulated noise results in a patchy image with emission structure similar to the ALMA 1.3 mm image shown in Figure 7.1. In both the ALMA and model images, the most significant peaks of emission are consistent with the expectation for a slightly inclined disk with PA near 90°. The rightmost panel of Figure 7.3 shows the residuals resulting from subtracting this best-fit model from the observed visibilities, again imaged with the same parameters. No significant features are evident.

Table 7.2: ALMA Model Parameters

Parameter	Description	Best-Fit	68% Confidence Interval
$R_{\rm in}$	Belt inner radius (AU)	6.2	$+9.8, -4.6$
$R_{\rm out}$	Belt outer radius (AU)	52.	$+3., -8.$
$F_{\rm belt}$	Belt flux density (mJy)	1.0	$+0.6, -0.4$
$F_{\rm cen}$	Central source flux (mJy)	0.69	$+0.02, -0.04$
γ	Surface density power law index	-0.3	$+1.9, -1.3$

The best-fit total belt flux density is $F_{\rm belt} = 1.0^{+0.6}_{-0.4}$ mJy, constrained by the Gaussian prior taken from previous single dish flux measurements. Lawler et al. (2014) note that the SCUBA and SCUBA-2 flux densities are higher than expected given an extrapolation from the *Herschel* flux density measurements. This difference suggests that these earlier observations could be contaminated by the extragalactic background or that the disk could have an additional warm component. Given

the limits in sensitivity of our ALMA data, the total flux density we measure is consistent with both the *Herschel* and SCUBA/SCUBA-2 values and we cannot distinguish between these two scenarios.

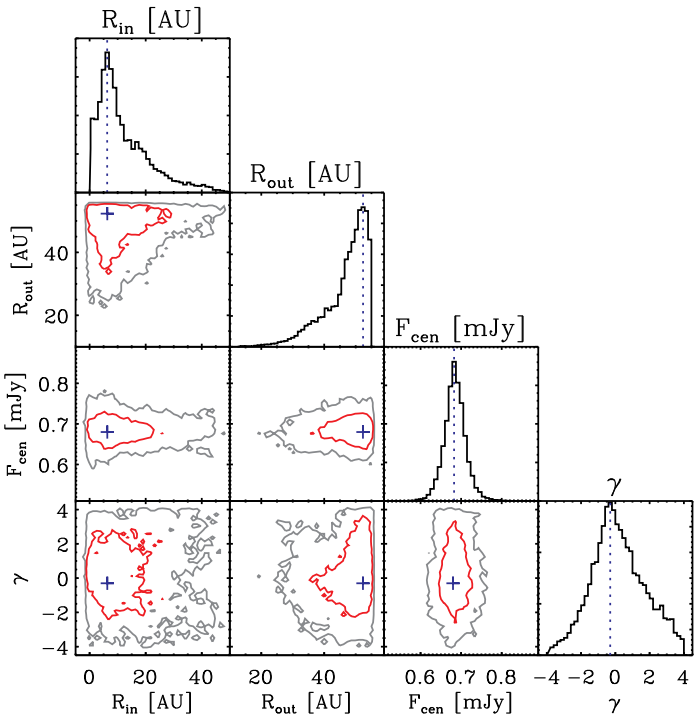

Figure 7.2: The 1D (diagonal panels) and 2D (off-diagonal panels) projections of the posterior probability distributions for the best-fit model parameters ($R_{\rm in}$, $R_{\rm out}$, $F_{\rm cen}$, and γ) resulting from $\sim 10^4$ MCMC trials. For a given parameter, the 1D distribution is determined by marginalizing over all other model parameters. The best-fit parameter value is indicated by the vertical blue dashed line. The 2D joint probability distributions show the 1σ (red) and 2σ (gray) regions for all parameter pairs, with the best-fit parameter values marked by the blue cross symbol.

Not surprisingly, given the sensitivity limits of the ALMA data, model fitting does not provide a strong constraint on the power law index of the surface density

radial profile, $\gamma = -0.3^{+1.9}_{-1.3}$. With large uncertainty, this result implies a shallow surface density profile. In addition, we see a clear degeneracy between the surface density gradient, γ, and the disk outer radius, $R_{\rm out}$ (e.g. Mundy et al. 1996). For very negative values of γ, the outer regions of the resulting belt model have low surface brightness, making it difficult to constrain the position of the outer edge. Thus, the contours shown in Figure 7.2 for that pair of parameters exhibit a slope, spreading out to span a wide range of possible outer radii for increasingly negative values of γ.

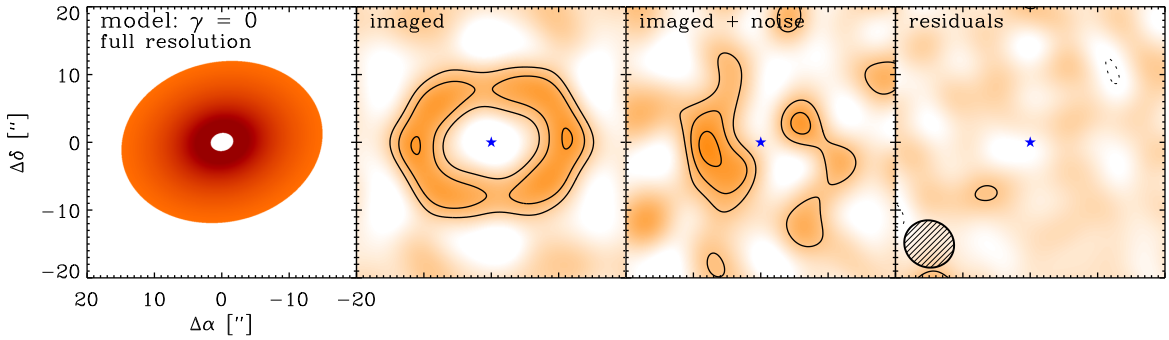

Figure 7.3: *(left)* A full resolution (pixel scale $\sim 0\farcs05 \sim 0.2$ AU) image of the best-fit model to the 1.3 mm ALMA continuum emission. For simplicity, we have chosen a flat surface density profile with $\gamma = 0$ and excluded the central stellar component. *(center left)* The same best-fit model convolved with the $\sim 6''$ ALMA synthesized beam and imaged as in Figure 7.1, but with no noise added. *(center right)* The convolved best-fit model (same as shown in center left) with added simulated random noise at the same level as the ALMA 1.3 mm image, rms ~ 30 μJy. *(right)* The residuals of the full best-fit model including the star and imaged with the same parameters as in Figure 7.1. The ellipse in the lower left corner shows the $6\farcs5 \times 6\farcs1$ (FWHM) synthesized beam size.

Another helpful way to visualize and compare the ALMA observations and the best-fit model is by deprojecting the real and imaginary visibilities based on the inclination, i, and position angles, PA, of the disk major axis, as is shown in Figure 7.4 (see Lay et al. 1997, for a detailed description of deprojection). Essentially,

the coordinates for each visibility point are defined by a distance from the origin of the (u, v) plane, $\mathcal{R} = \sqrt{u^2 + v^2}$. To change to a deprojected, rotated coordinate system, we define an angle $\phi = \frac{\pi}{2} - PA$, where PA is the position angle of the disk measured east of north. The new coordinates are defined as $u' = u\ \cos\phi + v\ \sin\phi$ and $v' = (-u\ \sin\phi + v\ \cos\phi)\ \cos i$, where i is the inclination angle of the disk. Then, the new deprojected (u, v) distance is $\mathcal{R}_{uv} = \sqrt{u'^2 + v'^2}$. Assuming that the disk is axisymmetric, we average the visibilities azimuthally in annuli of $\mathcal{R}_{uv}$. For our ALMA τ Ceti observations, the real part of the deprojected visibilities is reasonably consistent with the prediction for a broad belt of emission, showing a central peak and several oscillations of decreasing amplitude. The constant offset from zero is the visibility signature of the unresolved central peak we see clearly in the images. The imaginary visibilities are essentially zero, indicating that there is no asymmetric structure in the disk, which is consistent with the absence of any significant residuals in Figure 7.3 (rightmost panel). Note that we are lacking (u, v) coverage on baselines shorter than $\lesssim 20$ kλ, the region of the visibility curve with the most structure.

7.4 Discussion

We have obtained ALMA 1.3 mm observations of the τ Ceti system using both the ACA and the full 12-m array with baselines corresponding to scales of $1''$ (4 AU). The resulting image shows emission from an outer dust disk located $\sim 12''$ (~ 44 AU) from the star surrounding an unresolved central peak. We fit parametric models to the millimeter visibilities, which included two components: (1) an outer disk with a radial surface density profile described by a power law with index γ, and (2) a

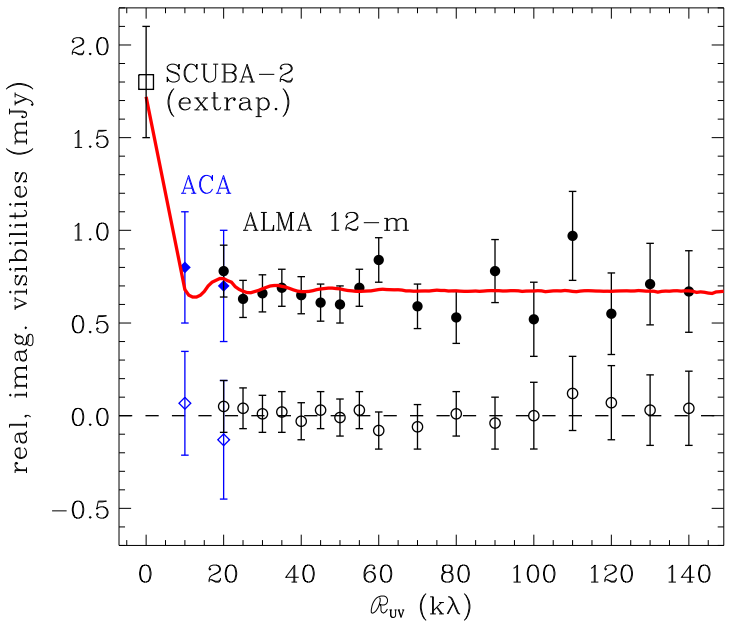

Figure 7.4: The deprojected real (filled symbols) and imaginary (open symbols) visibilities for the ACA (blue diamonds) and 12-m array (black circles), compared to the best-fit belt model (red solid line). The single dish SCUBA-2 flux (Holland et al., in prep.) extrapolated from 850 μm to 1.3 mm is also plotted at $\mathcal{R}_{uv} = 0$ kλ.

point source at the stellar position. In the context of our simple model, this analysis provides tentative constraints on the location of the disk inner edge and the width of the disk. We now compare the model fits to previous *Herschel* observations and discuss implications for the geometry of the proposed inner planetary system located within the dust belt.

7.4.1 Location of the Disk Inner Edge and Belt Width

Our best-fit model yields an inner radius for the disk of $6.2^{+9.8}_{-4.6}$ AU, consistent with the analysis of *Herschel* observations that constrained the inner edge of the disk to be between 1 and 10 AU from the star (Lawler et al. 2014). For comparison, the

planetary system proposed by Tuomi et al. (2013) consists of five super-Earths in a tightly-packed configuration with semi-major axes ranging over $0.105 - 1.35$ AU. Given the uncertainties on $R_{\rm in}$ from our best-fit model, the disk could extend well into this inner planetary system ($R_{\rm in} < 1$ AU) or end far beyond the outermost planet ($R_{\rm in} > 2$ AU). None of the proposed planets have large enough orbital radius or mass to cause significant perturbations or clear the disk beyond 3 AU (within the range of $R_{\rm in}$ allowed by our models). Lawler et al. (2014) use numerical simulations to show that the system would be stable with an additional Neptune-mass planet on an orbit of $5 - 10$ AU, the largest mass planet at such separations that cannot be ruled out by the radial velocity data.

The belt position and width are strongly constrained by the location of the first null in the deprojected real visibilities (see Figure 7.4, MacGregor et al. 2015b). Although we obtained some ACA data, the integration time was short, and the resulting sensitivity (rms ~ 180 μJy) at short baselines (< 20 kλ) was insufficient to discriminate between disk models with inner radii of $1 - 10$ AU, the parameter space with significant implications for the proposed planetary system. New observations with shorter baselines are needed to better determine the location of the dust belt, as well as its radial surface density gradient. To demonstrate the contribution that such observations would make to our analysis, we carried out simulations of ALMA ACA observations (rms 60 μJy, using 10 antennas in the Cycle 4 setup) at 1.3 mm for a model with our best-fit $R_{\rm in} = 6.2$ AU and $\gamma = -1, 0, +1$, and a model with $R_{\rm in} = 20$ AU and $\gamma = 0$, all consistent with the ALMA observations presented here. Figure 7.5 (left panel) shows the real component of the expected complex visibilities for all four models, along with our current ACA observations. The center

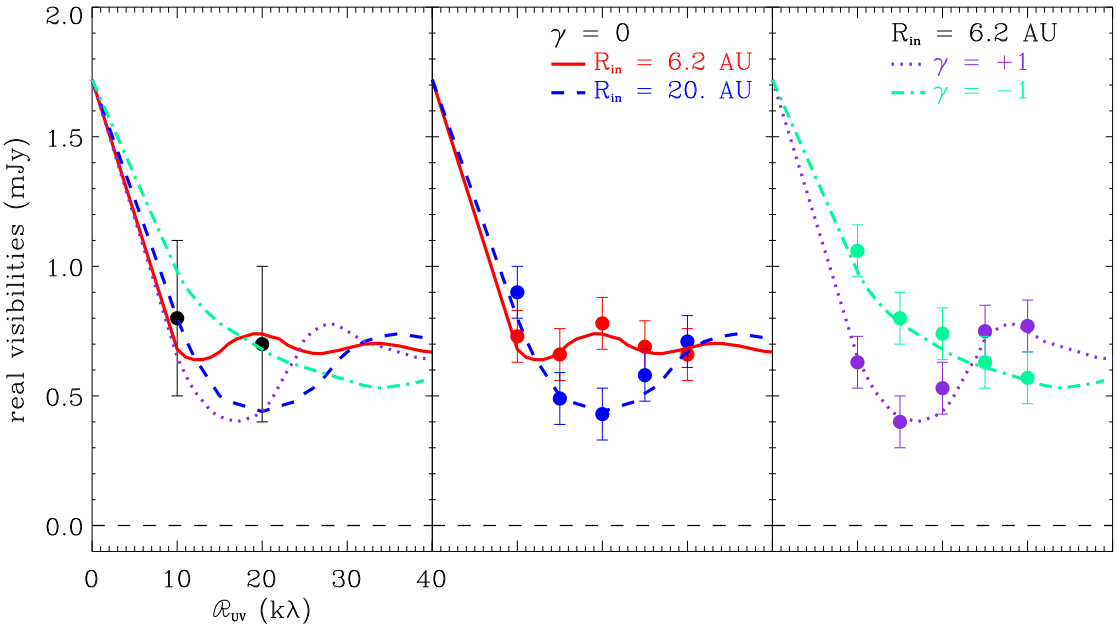

Figure 7.5: *(left)* The deprojected real component of the expected complex visibilities for belt models with our best-fit $R_{\rm in} = 6.2$ AU and $\gamma = -1, 0, +1$ (dot-dash green line, solid red line, and dotted purple line, respectively), and a model with $R_{\rm in} = 20$ AU and $\gamma = 0$ (dashed blue line). The real visibilities from our ACA observations presented here are shown by the black points and are consistent with all four models. *(center)* The real visibilities of simulated ACA 1.3 mm emission for models with $\gamma = 0$ and $R_{\rm in} = 6.2$ and 20 AU (red and blue points, respectively). With 10 antennas and 10 hours on source, these models are easily distinguishable. *(right)* The real visibilities of simulated ACA 1.3 mm emission for models with $R_{\rm in} = 6.2$ AU and $\gamma = +1$ and -1 (purple and green points, respectively). Again, these profiles are clearly different in shape, with the zero-crossing null locations shifted by > 10 kλ.

and right panels show the real part of simulated ACA visibilities for all four belt models compared to the expected theoretical visibility curves. These profiles are clearly different in shape, with the zero-crossing locations shifted by > 10 kλ and the amplitude of the oscillations differing by more than a factor of 2.

Although the ALMA observations allow for broad disk models that extend in toward the central star, they are not consistent with a narrow ring model located far

from the star. The contours for the inner and outer radius in Figure 7.2 show the absence of any models with large $R_{\rm in}$ and small $R_{\rm out}$, indicating that the disk must be broad. Indeed, we can place a strong upper limit, $R_{\rm in} < 25$ AU with 99% (3σ) confidence. Given the values of $R_{\rm in}$ and $R_{\rm out}$ from our best-fit model, the fractional width of the τ Ceti disk is $\Delta R/R = 1.6^{+0.3}_{-0.6}$. If we assume that the outer belt edge at millimeter wavelengths aligns with the edge found at far-infrared wavelengths ($R_{\rm out} = 55$ AU), we can place a lower limit on the belt width, $\Delta R > 30$ AU. At 99% confidence, $\Delta R/R > 0.75$. For comparison, our Solar System's classical Kuiper Belt has a fractional width of $\Delta R/R \sim 0.18$ (e.g. Hahn & Malhotra 2005; Bannister et al. 2015), significantly more narrow. In fact, the Kuiper Belt appears to be confined between Neptune's 3:2 and 2:1 resonances. Similarly, the Fomalhaut debris disk appears narrow with $\Delta R/R \sim 0.1$, possibly attributable to planets orbiting both interior to and exterior to the ring (Boley et al. 2012). In contrast, recent ALMA observations of the HD 107146 debris disk (Ricci et al. 2015a) indicate that its belt extends from 30 AU to 150 AU ($\Delta R/R \sim 1.3$), with a break at $\sim$ 70AU. The ϵ Eridani debris disk also appears to be somewhat broader with a fractional width determined from resolved SMA observations of $\Delta R/R = 0.3$ (MacGregor et al. 2015b). The fractional width of the τ Ceti belt is substantially larger than both the classical Kuiper Belt and Fomalhaut. However, the τ Ceti belt is comparable in width to the HD 107146 disk, suggesting that it might also have a more complicated radial structure, which we are unable to resolve with these observations.

Kalas et al. (2006) discuss the implications of the observed diversity in debris disk structures in the context of scattered light observations. For a narrow belt structure, both the inner and outer edges of the disk must be maintained by

gravitational perturbers such as stellar or substellar companions, or be confined by mean-motion resonances with an interior planet as is the case for our own Kuiper Belt. Without any such confinement mechanism for the outer disk edge, and since more massive planets have been ruled out around τ Ceti at distances approaching ~ 10 AU (Lawler et al. 2014), the expected structure is indeed a wide belt.

7.4.2 Central Component

In addition to the extended emission from an outer belt, the ALMA 1.3 mm image shows a bright, unresolved point source (see the constant positive offset on long baselines in Figure 7.4) at the expected position of the star with a flux density of $0.69^{+0.02}_{-0.05}$ mJy. For a G8.5V star with an effective temperature of 5344 ± 50 K, an extrapolation of a PHOENIX stellar atmosphere model (Husser et al. 2013) predicts a 1.3 mm flux density of 0.60 mJy (with 5% uncertainty). Thus, the flux density of this central source is marginally higher than the expectation for the stellar photosphere at this millimeter wavelength. We note, however, that an extrapolation of the mid-infrared flux of the star, as measured by WISE at 22 μm (Wright et al. 2010) and AKARI at 9 and 18 μm (Ishihara et al. 2010), yields a prediction for the flux of the stellar photosphere at 1.3 mm of ~ 0.5 mJy, substantially lower than the measured 1.3 mm flux density. Our ALMA measurement is complemented by previous observations by Villadsen et al. (2014) with the Karl G. Jansky Very Large Array (VLA) at 34.5 GHz (8.7 mm) and 15.0 GHz (2.0 cm). At 8.7 mm, the measured flux density is 25.3 ± 3.9 μJy, significantly higher than the predicted photospheric flux density of 14 μJy. While the star is not detected at 2.0 cm, a

robust 99% confidence upper limit is determined of < 11.7 μJy (model photospheric prediction of 2.5 μJy).

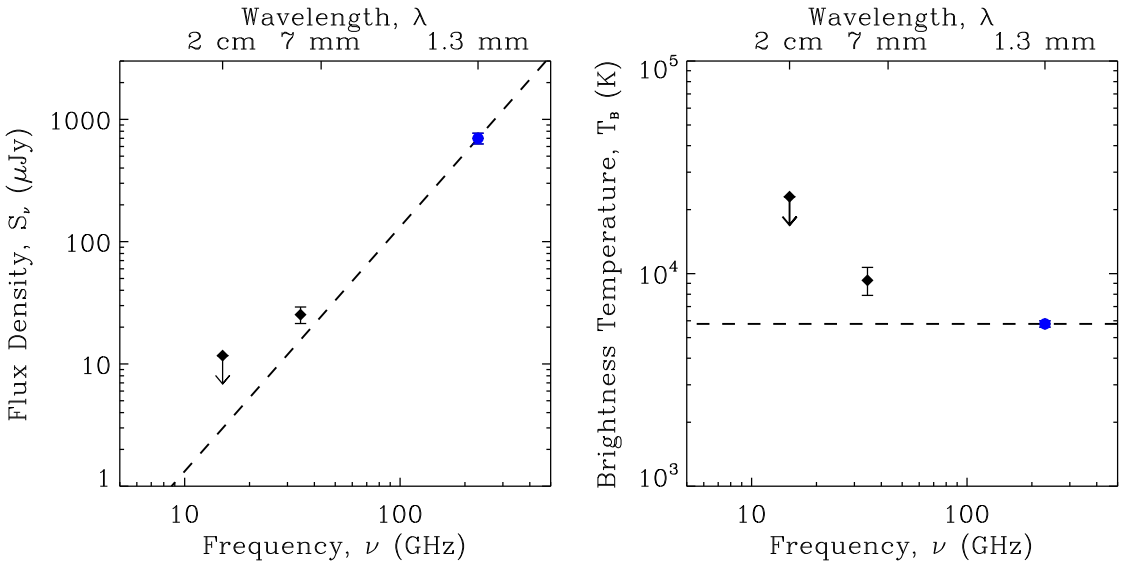

Figure 7.6: *(left)* Flux density spectrum of τ Ceti from ALMA and VLA observations. The dashed line indicates the expected spectral index of 2.0 for a classical photosphere. *(right)* Brightness temperature spectrum calculated assuming the photospheric radius of the star. For both plots, our ALMA measurements are shown as blue circles and the VLA measurements (Villadsen et al. 2014) are shown as black diamonds. Detections are indicated by points with 1σ error bars. The 99% upper confidence limit at 2.0 cm is indicated by the downwards arrow. Again, the dashed line indicates the expected brightness temperature for a classic photosphere with the brightness temperature determined from our 1.3 mm ALMA measurement.

As Villadsen et al. (2014) discuss, the observed unresolved emission from τ Ceti at both millimeter and centimeter wavelengths plausibly arises from a hot stellar chromosphere. Similar excess emission at long wavelengths has been noted for several neighboring Sun-like stars, including α Cen A and B (spectral types G2V and K2V, respectively) observed with ALMA by Liseau et al. (2015) and ϵ Eridani (spectral type K2V) observed with the Submillimeter Array (SMA) and Australia Telescope Compact Array (ATCA) by MacGregor et al. (2015b). We combine our

new ALMA 1.3 mm flux density with the previous VLA 8.7 mm measurement and 2 cm upper limit, and determine the Planck brightness temperature at all three wavelengths (following Liseau et al. 2013). Figure 7.6 shows the resulting ALMA and VLA constraints on both the flux density and the brightness temperature spectra of τ Ceti. We assume that the photospheric radius is comparable at optical and millimeter/centimeter wavelengths, and adopt a value of $0.793 \pm 0.004\ R_{\odot}$, obtained from interferometric measurements using the FLUOR instrument on the CHARA array (di Folco et al. 2007). At 1.3 mm this analysis yields $T_B = 5,800 \pm 200$ K, modestly hotter than the effective temperature of 5344 ± 50 K. However, at longer wavelengths, the brightness temperature diverges significantly from the photospheric prediction with $T_B = 9,300 \pm 1400$ K and $< 23,000$ K at 8.7 mm and 2 cm, respectively.

Additionally, the spectral index at long wavelengths of the central emission from τ Ceti shows the same deviation from an optically thick photosphere (spectral index of ~ 2) as is seen for α Cen A and B and ϵ Eridani. Between 1.3 and 8.7 mm, the spectral index of the central peak in our observations of τ Ceti is 1.74 ± 0.15 (with the $\sim 10\%$ uncertainty in the flux scale and the 1σ modeling errors added in quadrature). For comparison, the measured spectral indices between 0.87 and 3.2 mm are 1.62 and 1.61 for α Cen A and B, respectively (Liseau et al. 2015).

7.5 Conclusions

We observed the τ Ceti debris disk with ALMA at 1.3 mm with baselines that probe $1''$ (4 AU) scales. These are the first observations of this nearby system with

a millimeter interferometer and reveal somewhat patchy emission from a dust disk surrounding an unresolved central emission peak. In order to characterize these two emission components, we fit simple parametric models directly to the visibility data within an MCMC framework.

Our best-fit model yields an inner belt edge of $6.2^{+9.8}_{-4.6}$ AU, consistent with the analysis of previous far-infrared *Herschel* observations. Given the relatively low sensitivity at short baselines in the ALMA observations, we are unable to place a tighter constraint on the inner edge and its position relative to the proposed five planet system. These data, however, provide a strong lower limit on the fractional width of the belt, $\Delta R/R > 0.75$ with 99% confidence. This result implies that the τ Ceti debris disk is broad, much wider than the classical Kuiper Belt in our Solar System and more comparable to the HD 107146 debris disk (Ricci et al. 2015a).

The bright central peak at the stellar position has a flux density of $F_{1.3\mathrm{mm}} = 0.69^{+0.02}_{-0.05}$ mJy, somewhat higher than the predicted flux of the stellar photosphere at 1.3 mm. At longer centimeter wavelengths, this excess is more significant, increasing to $\sim 2\times$ the photospheric prediction in VLA observations at 8.7 mm (Villadsen et al. 2014). The spectral index between these two measurements is 1.74 ± 0.15, shallower than the expectation for an optically thick photosphere. Given the high brightness temperatures at both 1.3 and 8.7 mm, this excess emission is likely due to a hot stellar chromosphere. Similar spectra have been observed for other nearby Sun-like stars, e.g. α Cen A/B and ϵ Eridani.

These first ALMA observations of the τ Ceti system allow us to probe the structure of the debris disk with higher resolution than previous work. However,

higher sensitivity observations at shorter baselines are still needed to constrain the location of the inner edge of the dust belt more precisely. If the disk extends in towards the star, within the orbit of the outermost proposed planet, this provides strong evidence against the posited five planet system. However, if the disk inner edge is located well outside the proposed planetary system, an additional massive planet on a wide orbit may be required to clear out the central hole in the belt. Additional observations with the ACA could provide the necessary sensitivity to determine the position of the inner disk edge and its implications for an interior planetary system.

Acknowledgments

This paper makes use of the following ALMA data: ADS/JAO.ALMA#2013.1.00588.S. ALMA is a partnership of ESO (representing its member states), NSF (USA) and NINS (Japan), together with NRC (Canada) and NSC and ASIAA (Taiwan) and KASI (Republic of Korea), in cooperation with the Republic of Chile. The Joint ALMA Observatory is operated by ESO, AUI/NRAO and NAOJ. The National Radio Astronomy Observatory is a facility of the National Science Foundation operated under cooperative agreement by Associated Universities, Inc. M.A.M acknowledges support from a National Science Foundation Graduate Research Fellowship (DGE1144152). S.M.L. gratefully acknowledges support from the NRC Canada Plaskett Fellowship. B.C.M. acknowledges support from a Natural Science and Engineering Research Council (NSERC) Discovery Accelerator Supplement grant. G.M.K. is supported by the Royal Society as a Royal Society University

Research Fellow. M.B. acknowledges support from a FONDECYT Postdoctral Fellowship, project no. 3140479 and the Millennium Science Initiative (Chilean Ministry of Economy), through grant RC130007.

8

A Complete ALMA Map of the Fomalhaut Debris Disk

This thesis chapter originally appeared in the literature as

M. A. MacGregor, L. Matrà, P. Kalas, D. J. Wilner, M. Pan, G. M. Kennedy, M. C. Wyatt, G. Duchene, A. M. Hughes, G. H. Rieke, M. Clampin, M. P. Fitzgerald, J. R. Graham, W. S. Holland, O. Panić, A. Shannon, K. Su, 2017, accepted to Astrophysical Journal

Abstract

We present ALMA mosaic observations at 1.3 mm (223 GHz) of the Fomalhaut system with a sensitivity of 14 μJy/beam. These observations provide the first millimeter map of the continuum dust emission from the complete outer debris disk with uniform sensitivity, enabling the first conclusive detection of apocenter glow. We adopt a MCMC modeling approach that accounts for the eccentric orbital

parameters of a collection of particles within the disk. The outer belt is radially confined with an inner edge of 136.3 ± 0.9 AU and width of 13.5 ± 1.8 AU. We determine a best-fit eccentricity of 0.12 ± 0.01. Assuming a size distribution power law index of $q = 3.46 \pm 0.09$, we constrain the dust absorptivity power law index β to be $0.9 < \beta < 1.5$. The geometry of the disk is robustly constrained with inclination $65\overset{\circ}{.}6 \pm 0\overset{\circ}{.}3$, position angle $337\overset{\circ}{.}9 \pm 0\overset{\circ}{.}3$, and argument of periastron $22\overset{\circ}{.}5 \pm 4\overset{\circ}{.}3$. Our observations do not confirm any of the azimuthal features found in previous imaging studies of the disk with *HST*, SCUBA, and ALMA. However, we cannot rule out structures ≤ 10 AU in size or which only affect smaller grains. The central star is clearly detected with a flux density of 0.75 ± 0.02 mJy, significantly lower than predicted by current photospheric models. We discuss the implications of these observations for the directly imaged Fomalhaut b and the inner dust belt detected at infrared wavelengths.

8.1 Introduction

The proximity of Fomalhaut (7.66 ± 0.04 pc, van Leeuwen 2007) has resulted in its debris disk being one of the best-studied. With an age of ~ 440 Myr (Mamajek 2012), Fomalhaut is at a stage when significant dynamical activity can still occur, as indicated by the period of Late Heavy Bombardment in our own Solar System, an epoch that has important implications for the final architecture of the planetary system. The outer debris disk is located at ~ 140 AU, and has been resolved at a range of wavelengths spanning from optical to radio (Holland et al. 1998; Kalas et al. 2005, 2008, 2013; Acke et al. 2012; Ricci et al. 2012; Boley et al. 2012; White

et al. 2016a). In addition to the cold ($\sim$ 50 K) outer belt, the system has a warm ($\sim$ 150 K), unresolved inner component detected as excess emission at infrared wavelengths with both *Spitzer* and *Herschel* (Stapelfeldt et al. 2004; Su et al. 2013). Su et al. (2016) placed limits on the radial location of this inner belt between $\sim 8-15$ AU with a non-detection from the Atacama Large Millimeter/submillimeter Array (ALMA). Direct imaging has also revealed the presence of a very low mass object, Fomalhaut b, near the outer disk and with a highly eccentric orbit (Kalas et al. 2008, 2013). Given its unique characteristics and architecture, the Fomalhaut system is a Rosetta stone for understanding the interaction between planetary systems and debris disks studying which will enhance our physical understanding of more distant planetary systems.

Dusty debris disks, like the Fomalhaut system, are produced from the continual collisional erosion of larger planetesimals, similar to asteroids or comets. The resulting dust is shaped by the larger bodies or planets in the system through collisions and gravitational perturbations, imprinting observable signatures in the structure of the disk. For example, an interior planet on an eccentric orbit can impose a forced eccentricity on the dust particles in the disk (Wyatt et al. 1999). Such a planet could also sculpt a sharp interior edge (Quillen 2006; Chiang et al. 2009). The outward migration of a planet can radially confine the belt between resonances (Hahn & Malhotra 2005), similar to Neptune in our own Solar System, or trap dust into mean motion resonance outside its orbit (Kuchner & Holman 2003; Wyatt 2003; Deller & Maddison 2005). Observations at millimeter wavelengths offer an advantage for probing these planetary-induced structures, since the large grains that emit predominantly at these wavelengths are not significantly perturbed by

radiation forces and better trace the location of the larger planetesimals. Previous resolved images have revealed that the Fomalhaut debris disk is both radially confined and significantly eccentric. However, there has yet to be a complete map of the disk structure at millimeter wavelengths, necessary to probe for azimuthal disk structure that might stem from planetary interactions.

Here, we present new mosaic observations with the Atacama Large Millimeter/submillimeter Array (ALMA) of the Fomalhaut debris disk, which build the first complete millimeter map of the system at the current epoch. By mapping the outer belt with uniform sensitivity, we are able to place constraints on the azimuthal structure of the belt and make the first robust observational detection of apocenter glow. In Section 8.2 we present the new ALMA observations. In Section 8.3 we discuss the structure of the continuum emission (8.3.1), our modeling approach (8.3.2), and the results of our modeling (8.3.3). In Section 8.4, we discuss the significance of the results in the context of apocenter glow (8.4.1), the structure and geometry of the disk (8.4.2), implications for the directly imaged Fomalhaut b (8.4.3), and constraints on the emission of the central star (8.4.4). Section 8.5 presents our conclusions.

8.2 Observations

We observed the Fomalhaut system with ALMA in Band 6 (1.3 mm, 223 GHz). To map the entire outer dust belt, we constructed a seven pointing mosaic covering the star and the disk circumference. The phase center for the central pointing was $\alpha = 22^{\rm h}57^{\rm m}39.449$, $\delta = -29°37'22''.687$ (J2000), corresponding to the position of the

star corrected for its proper motion (328.95, -164.67) mas yr^{-1}. One pointing was positioned on each of the disk ansae, and the remaining four pointings were spaced evenly on either side of the ring. All of these seven pointings were observed within a single 45 minute scheduling block (SB), which was executed four times on 2015 December 29-30 with 38 antennas in the array and an average precipitable water vapor (pwv) of ~ 0.75 mm. An additional three executions were carried out on 14 January 2016 with $44 - 46$ antennas in the array and pwv ~ 2.4 mm. Table 8.1 summarizes these observations including the dates, baseline lengths, weather conditions, and time on-source. The two-week difference between observations produces a negligible pointing difference due to proper motion compared with the natural weight beam size, which we ignore.

Table 8.1: ALMA Observations of Fomalhaut

Observation Date	# of Antennas	Projected Baselines (m)	PWV (mm)	Time on Target (min)
2015 Dec 29	38	$15.1 - 310.2$	0.76	41.9
	38	$15.1 - 310.2$	0.65	41.9
	38	$15.1 - 310.2$	0.83	30.7
2015 Dec 30	38	$15.1 - 310.2$	1.1	26.6
2016 Jan 14	46	$15.1 - 331.0$	2.3	41.9
	46	$15.1 - 331.0$	2.4	41.9
	44	$15.1 - 312.7$	2.7	41.9

The correlator set-up for these observations was designed to optimize the continuum sensitivity, while also covering the ^{12}CO J $= 2 - 1$ transition at 230.538 GHz. To achieve this, four basebands were centered at 213.98, 215.98, 229.59, and 231.48 GHz, in two polarizations. The baseband covering the ^{12}CO spectral line included 3840 channels over a bandwidth of 1.875 GHz with a velocity

resolution of 1.27 km/s. The remaining three continuum basebands included only 128 channels with a total bandwidth of 2 GHz each.

The raw datasets were processed by ALMA staff using the `CASA` software package (version 4.5.2). The absolute flux calibration was determined from observations of Pallas, J2357-5311, and J2258-275, with a systematic uncertainty of $< 10\%$. Observations of J2258-2758 were also used to determine the bandpass calibration and to account for time-dependent gain variations. To reduce the size of the dataset, the visibilities were averaged into 30 second intervals. We generated continuum images using the multi-frequency synthesis `CLEAN` algorithm in `CASA`, and correct for the telescope primary beam. In Band 6, the primary beam of the ALMA 12-m antennas has FWHM$\sim 26''$. The imaging of the ^{12}CO data is described in Matrà et al. (2017).

8.3 Results and Analysis

8.3.1 Continuum Emission

Figure 8.1 (left panel) shows the primary beam corrected ALMA 1.3 mm continuum image of Fomalhaut. With natural weighting, the rms noise level is 14 μJy/beam and the synthesized beam size is $1\farcs56 \times 1\farcs15$ (12×9 AU at 7.7 pc) with a position angle of $-87°$. The right panel of Figure 8.1 shows the ALMA 1.3 mm image overlaid as contours on a *Hubble Space Telescope* (*HST*) STIS coronographic image of optical scattered light (Kalas et al. 2013). The millimeter continuum emission structure appears to match well with the narrow belt structure observed in the previous *HST*

image. Overall, the new ALMA image shows emission from three components: (1) a narrow, eccentric ring (30σ), (2) an unresolved central point source at the stellar position (54σ), and (3) an unresolved point source on the eastern side of the disk (10σ). Most strikingly, we note a significant flux difference between the apocenter (NW) and pericenter (SE) sides of the disk of ~ 65 μJy ($> 5\sigma$), which we attribute to 'apocenter glow,' a result of the disk's eccentricity (Pan et al. 2016, see Section 8.4.1 for further discussion).

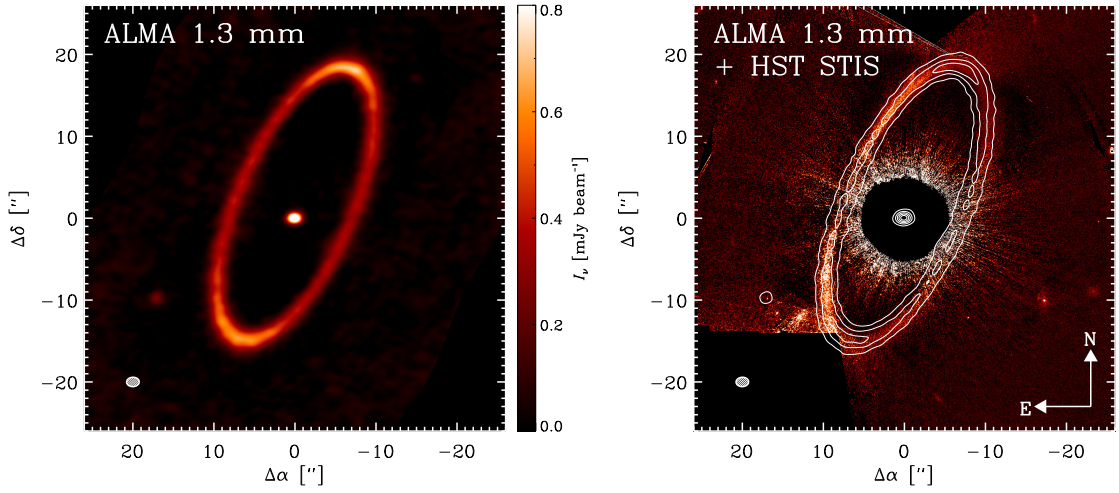

Figure 8.1: *(left)* ALMA image of the 1.3 mm continuum emission from Fomalhaut. The dashed white ellipse in the lower left corner shows the natural weight beam size of $1\farcs56 \times 1\farcs15$. The rms noise is 14 μJy/beam. *(right)* The ALMA continuum image overlaid as contours (white) on the *HST* STIS image from Kalas et al. (2013). Contour levels are in steps of $[5, 15, 25, 35, 45, 55]\times$ the rms noise.

We attribute the unresolved point source in the southeast quadrant to a background galaxy. The total flux density for this source is 0.150 ± 0.014 mJy, determined by fitting a point source model to the visibilities using the `uvmodelfit` task in `CASA`. Recent deep ALMA surveys have built up statistics on the number of faint background sources expected in a given field of view (Hatsukade et al. 2013;

Carniani et al. 2015). Given these (sub)millimeter source counts, the number of sources with flux density of > 0.15 mJy expected within our field of view is $2.6^{+5.7}_{-1.9}$. The measured position of this point source is $\alpha = 22^{\rm h}57^{\rm m}40.766$, $\delta = -29°37'32''.309$ (J2000). This region has been imaged with *HST*/STIS in the optical (GO-13726; PI Kalas) where the nearest background source is $0''.68$ west and $0''.03$ north of the ALMA position. Given that the ALMA beam radius is $\sim 0''.78$ along Right Ascension, it is likely the ALMA source is the same background object as observed in optical data.

8.3.2 Modeling Approach

Given the clear observed eccentricity in the Fomalhaut debris disk, we construct models that account for the orbital parameters of particles in the disk. A particle orbiting within a circumstellar disk has both a proper and forced eccentricity, e_p and e_f, respectively, as well as a proper and forced argument of periastron, ω_p and ω_f. We begin by populating the complex eccentricity plane defined by these four parameters following Wyatt et al. (1999). The forced eccentricity and argument of periastron, e_f and ω_f, are imposed on the particles by the massive perturber forcing the eccentricity in the disk, and are free parameters in our model. The proper eccentricity is also left as a free parameter, e_p, and describes the additional scatter in the eccentricity of each particle's orbit; the ω_p associated with a given e_p is assumed to be randomly distributed from 0 to 2π. By assuming a semi-major axis, a, for each particle and random mean anomalies, we iterate to find the true anomaly, f, using the `newtonm` code from `ast2body` (Vallado 2007). Then, the radial orbital locations

of each particle can be found simply using

$$r = \frac{a(1-e^2)}{1+e\cos(f)}. \tag{8.1}$$

To create our two-dimensional model, we complete this calculation for 10^4 individual disk particles. By creating a two-dimensional model, we assume that the disk structure has a negligible vertical component. This assumption is motivated by the result from Boley et al. (2012) that the vertical scale height of the disk is described by an opening angle of $\sim 1^\circ$ from the mid-plane. Adding a vertical component to the model would likely loosen the constraints we are able to place on the width of the belt (see Section 8.4.2 for further discussion).

To create an image, we bin the determined orbital locations into a two dimensional histogram with the bin size equal to the desired pixel scale and impose a radial temperature profile, $T \propto r^{-0.5}$. The belt semi-major axis ($R_{\rm belt}$) and range of semi-major axes (Δa), are both free parameters. In this eccentric disk model, the belt semi-major axis is the mean inner edge location, $R_{\rm belt} = (R_{\rm per} + R_{\rm apo})/2$, where $R_{\rm per}$ and $R_{\rm apo}$ are the radial location of the disk inner edge at pericenter and apocenter, respectively. The total flux density of the disk is normalized to $F_{\rm belt} = \int I_\nu d\Omega$. A point source with flux density, $F_{\rm star}$, is added to account for the central stellar emission. In addition to fitting for both fluxes, we fit for the geometry of the disk (inclination, i, and position angle, PA), as well as offsets of the stellar position from the pointing center of the observations ($\Delta\alpha$ and $\Delta\delta$).

For a given model image, we compute synthetic model visibilities using

`vis_sample` [1], a python implementation of the Miriad `uvmodel` task. Following our previous approach (e.g. MacGregor et al. 2013, 2016a), we evaluate these model visibilities using a χ^2 likelihood function that incorporates the statistical weights on each visibility measurement. This iterative process makes use of the `emcee` Markov Chain Monte Charlo (MCMC) package (Foreman-Mackey et al. 2013). Given the affine-invariant nature of this ensemble sampler, we are able to explore the uncertainties and determine the one dimensional marginalized probability distribution for each independent model parameter.

8.3.3 Results of Model Fits

Table 8.2 presents the best-fit model (reduced $\chi^2 = 1.1$) parameters and their 1σ (68%) uncertainties. Figure 8.2 shows the ALMA 1.3 mm data (left panel) along with the best-fit model displayed at full resolution and imaged like the ALMA data (center panels). The rightmost panel shows the imaged residuals resulting from subtracting this best-fit model from the data, which are mostly noise. The only significant peak corresponds to the background galaxy discussed in Section 8.3.1. The full MCMC output is shown in Appendix C.

The total belt flux density determined for the best-fit model is 24.7 ± 0.1 mJy (with an additional 10% uncertainty from flux calibration), consistent with previous flux measurements at slightly shorter wavelengths. Boley et al. (2012) determine a total flux density at 860 μm of ~ 85 mJy, estimated from ALMA observations of the

[1] `vis_sample` is publicly available at `https://github.com/AstroChem/vis_sample` or in the Anaconda Cloud at `https://anaconda.org/rloomis/vis_sample`

Table 8.2: Best-fit Model Parameters

Parameter	Description	Best-Fit Value
$F_{\rm belt}$	Total flux density [mJy]	24.7 ± 0.1
$F_{\rm star}$	Total stellar flux [mJy]	0.75 ± 0.02
$R_{\rm belt}$	Belt inner edge [AU]	136.3 ± 0.9
Δa	Range of semi-major axes [AU]	12.2 ± 1.6
ΔR	Belt FWHM [AU]	13.5 ± 1.8
i	Disk inclination [°]	65.6 ± 0.3
PA	Disk position angle [°]	337.9 ± 0.3
e_f	Forced eccentricity	0.12 ± 0.01
e_p	Proper eccentricity	0.06 ± 0.04
ω_f	Forced argument of periastron [°]	22.5 ± 4.3
$\Delta\alpha$	RA offset [″]	0.08 ± 0.01
$\Delta\delta$	DEC offset [″]	0.06 ± 0.01

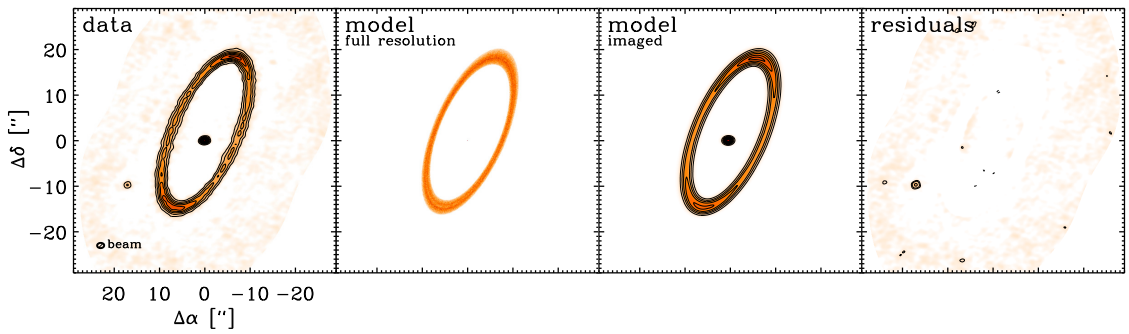

Figure 8.2: *(left)* Image of the ALMA 1.3 mm continuum emission. *(left, center)* The best-fit model at full resolution with pixel scale $\sim 0.1''$ (~ 0.8 AU). *(right, center)* The best-fit model imaged like the data with no noise. *(right)* The residuals of the best-fit model with the same imaging parameters. Contour levels in the first three panels are in steps of $5\times$ the rms noise of 14 μJy/beam. In the rightmost panel, additional contours of $\pm 3\sigma$ are added to highlight any residual structure. The labeled ellipse in the lower left corner indicates the synthesized beam size of $1\farcs56 \times 1\farcs15$, the same as in Figure 8.1.

NW half of the ring. Holland et al. (1998) and Holland et al. (2003) determine flux densities of 81 ± 7.2 mJy and 97 ± 5 mJy from SCUBA imaging at 450 and 850 μm, respectively. Assuming a millimeter spectral index of ~ 2.7 (Ricci et al. 2012), the measurement from Boley et al. (2012) extrapolates to ~ 27 mJy at 1.3 mm, consistent with our results within the uncertainties. Using ALMA observations at 233 GHz (~ 1.3 mm), White et al. (2016a) obtain a flux density of $30.8^{+3.4}_{-1.0}$ mJy by fitting directly to the visibilities and $26.3^{+4.5}_{-4.7}$ mJy by fitting in the image plane, again consistent with our results within the mutual uncertainties. For optically thin dust emission, the total dust mass is given by $M_{\rm dust} = F_\nu D^2/(\kappa_\nu B_\nu(T_{\rm dust}))$, where $D = 7.66$ pc is the distance, $B_\nu(T_{\rm dust})$ is the Planck function at the dust temperature, $T_{\rm dust}$, and κ_ν is the dust opacity. We assume a dust opacity at 1.3 mm of $\kappa_\nu = 2.3$ cm^2 g^{-1} (Beckwith et al. 1990), which may be a source of systematic uncertainty. Given the best fit radial location of the disk, 136.3 ± 0.9 AU, the radiative equilibrium temperature is ~ 48 K. Thus, the total mass of the dust belt is 0.015 ± 0.010 $M_\oplus$.

We find good agreement with all previous determinations between the belt semi-major axis, eccentricity, inclination, and position angle for our best-fit model with previous results. The best-fit belt semi-major axis from our modeling is 136.3 ± 0.9 AU. At pericenter, the inner edge of the belt is located at a radial distance of $R_{\rm per} = (1-e)R_{\rm belt} = 119.9 \pm 0.8$ AU. At apocenter, the inner edge of the belt is at $R_{\rm apo} = (1+e)R_{\rm belt} = 152.6 \pm 1.0$ AU. *HST* imaging yields a value of 136.28 ± 0.28 AU (Kalas et al. 2005, 2013), while Acke et al. (2012) obtain 137.5 ± 0.9 AU from *Herschel* observations. Boley et al. (2012) determine a semi-major axis of $135^{+1.0}_{-1.5}$ from ALMA imaging of the NW half of the disk, and

White et al. (2016a) determine a belt center location of 139^{+2}_{-3} AU from their model fits. These same observational studies yield inclination and position angles that range from $65° - 67°$ and $336° - 350°$, respectively. We obtain robust constraints on both angles of $i = 65.^{\circ}6 \pm 0.^{\circ}3$ and $PA = 337.^{\circ}9 \pm 0.^{\circ}3$. The best-fit eccentricity is 0.12 ± 0.01, consistent with both the *Herschel* result of 0.125 ± 0.006 and with the *HST* and previous ALMA results of 0.11 ± 0.01.

8.4 Discussion

For the first time, we have resolved the complete Fomalhaut outer debris disk at 1.3 mm with ALMA. This map of the dust continuum emission reveals a narrow, eccentric ring surrounding the primary star. Apocenter glow, a result of increased surface density at apocenter in an eccentric ring, is evident as a significant brightness difference between the NW and SE sides of the disk. Our modeling results place strong constraints on the disk position, width, geometry (inclination and position angle), eccentricity, and argument of periastron. We now use these new results to discuss implications for the grain composition, azimuthal structure of the disk, the directly imaged object interior to the disk, Fomalhaut b, and the central star.

8.4.1 Observational Evidence for Apocenter Glow

Our new ALMA image is the first conclusive observational evidence for apocenter glow. The Keplerian orbital velocity in an eccentric disk is slower at apocenter than at pericenter producing an overdensity of material at apocenter. At mid-infrared

wavelengths, the observed flux is strongly dependent on the grain temperature; grains at pericenter glow more brightly since they receive more flux from the star, masking the apocenter overdensity. This effect is evident as 'pericenter glow' (Wyatt et al. 1999) in *Herschel* images of the Fomalhaut disk at 70 μm, where the SE (pericenter) side of the disk appears brighter (Acke et al. 2012). In contrast, previous imaging of the Fomalhaut debris disk at longer far-infrared to millimeter wavelengths suggests a slight excess ($< 3\sigma$) of emission at the NW (apocenter) side of the disk, farthest from the star (Holland et al. 2003; Marsh et al. 2005; Ricci et al. 2012). To explain this phenomenon, Pan et al. (2016) construct a model of 'apocenter glow' where the enhancement of the surface density of the disk at apocenter results in wavelength-dependent surface brightness variations. At millimeter wavelengths, larger grains dominate the emission. Since these grains radiate efficiently at the blackbody peak, the pericenter-apocenter temperature difference has less impact on the total flux. As a result, the larger surface density at apocenter dominates and the apocenter appears brighter

Figure 8.3 shows the apocenter to pericenter flux ratio for Fomalhaut as a function of wavelength, including our new ALMA measurement at 1.3 mm of 1.10 ± 0.02. Plotted together with the observational results are curves showing the smallest (purple dotted line) and largest (red solid line) apocenter to pericenter flux ratios obtained with a grid of simulated Fomalhaut disks. A detailed description of the disk simulations is given by Pan et al. (2016); here, we include a brief overview. We created disks with the forced eccentricity e_f, radial location $R_{\rm belt}$, and semimajor axis range Δa given in Table 8.2 orbiting stars with effective temperature $T_* = 8590$ K and radius $R_* = 1.28 \times 10^{11}$ cm (Mamajek 2012). We populated the

disks with particles of sizes a following power-law size distributions $\mathrm{d}n/\mathrm{d}a \propto r^{-q}$ and grain absorptivities $Q \propto a^{-\beta}$. We drew each model disk's q and β values from a grid covering the ranges $3 \leq q \leq 4$, $1 \leq \beta \leq 3$. We then calculated the radially-integrated disk brightness as a function of longitude assuming passively heated, optically thin disks in thermal equilibrium. The ALMA flux ratio measurement falls well within the range obtained in our model grid.

As Figure 8.3 suggests, the observed apocenter to pericenter flux ratios can be diagnostic of disk grain properties including β, the grain absorptivity, and q, the size distribution power law index. The long wavelength spectral index, α_{mm}, of dust emission constrains the size distribution of dust grains in the disk. Again assuming that the differential number of grains of size a is a power law, $\mathrm{d}n/\mathrm{d}a \propto a^{-q}$, then $q = (\alpha_{\mathrm{mm}} - \alpha_{\mathrm{Pl}})/\beta_s + 3$ (Ricci et al. 2012; MacGregor et al. 2016b). Here, $\alpha_{\mathrm{Pl}} = 1.88 \pm 0.02$ (see discussion in MacGregor et al. 2016b), and $\beta_s = 1.8 \pm 0.2$, the dust opacity spectral index in the small particle limit for interstellar grain materials (Draine 2006). We note that different assumptions for the dust opacity can produce steeper grain size distributions (Gáspár et al. 2012). Ricci et al. (2012) measured the flux density of Fomalhaut at 6.66 mm with ATCA. By pairing our new ALMA flux density with this previous measurement, we determine $\alpha_{\mathrm{mm}} = 2.71 \pm 0.11$ and thus $q = 3.46 \pm 0.09$. This result is consistent with the determination of White et al. (2016a) of $\alpha_{\mathrm{mm}} = 2.73 \pm 0.13$ and $q = 3.50 \pm 0.14$. Using the flux ratios measured at 70 μm, 160 μm, and 1.3 mm respectively, and with a slight extension in the parameter range for our models, our 1σ uncertainty range in q implies $0.9 < \beta < 1.6$, $0.7 < \beta < 1.5$, and $0.7 < \beta$.[2] The overlap between these indicates an allowed range

[2]Extending our parameter grid range up to $\beta = 4$ did not increase the range of flux ratios attained

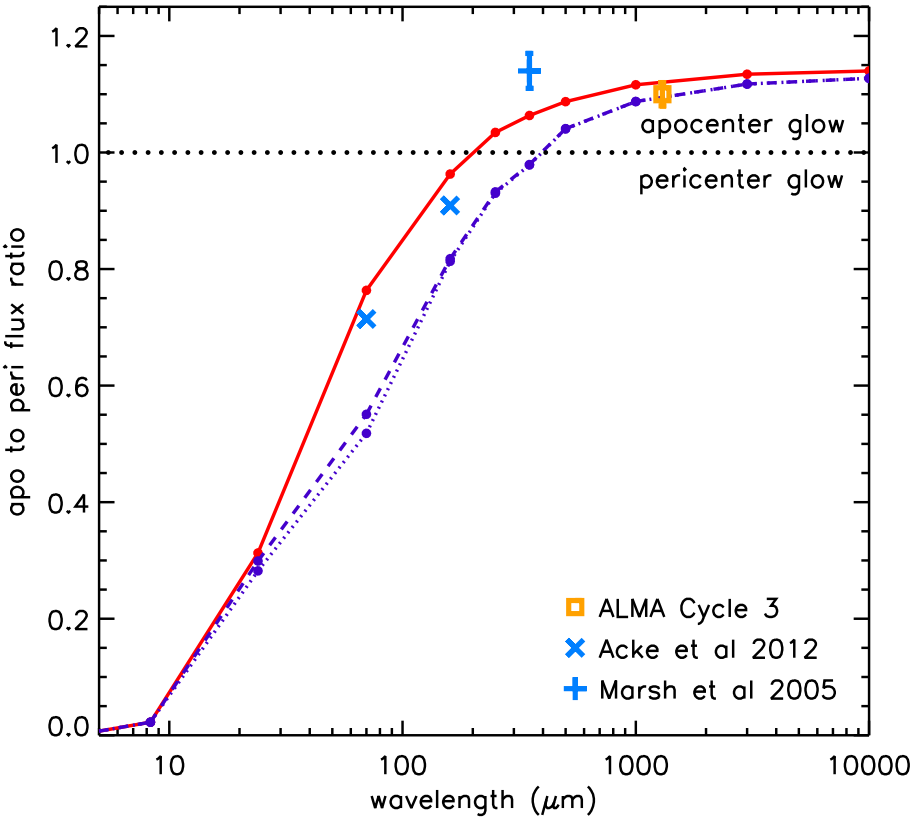

Figure 8.3: Apocenter to pericenter flux ratios (ratio of the radially integrated disk flux at apocenter to that at pericenter) as a function of wavelength. The yellow square indicates our new ALMA measurement. Blue points are measured flux ratios from *Herschel* observations at 70 and 160 μm (Acke et al. 2012) and from CSO/SHARC II observations at 350 μm (Marsh et al. 2005). Uncertainties on the *Herschel* points are smaller than the plot symbols. The curves outline the region obtained in our grid of Fomalhaut disk simulations. The red solid curve follows the maximum flux ratio values, which occur at $q = 4$, $\beta = 1$; the purple dashed/dotted curves follow the flux ratios occurring at $q = 3$ and $\beta = 2$ (dashed) or $\beta = 3$ (dotted). The $q = 3$, $\beta = 3$ flux ratios are the minimum attained on our parameter grid: extending our upper bound on β from 2 to 3 makes little difference in the overall range of model flux ratios. The observed results show broad agreement with our simulations.

of $0.9 < \beta < 1.5$, consistent within 1σ with the $\beta \simeq (q-3)\beta_s$ quoted by Draine (2006).

8.4.2 Structure of Fomalhaut's Outer Debris Disk

Constraints on Azimuthal Belt Structure

The ALMA 1.3 mm mosaic map of the outer Fomalhaut debris disk was designed to cover the complete ring with equal sensitivity, allowing us to examine azimuthal structure along the belt. After subtracting our best-fit model, any azimuthal structure should be clearly visible in the imaged residuals. Figure 8.2 shows the resulting residuals and no significant peaks are visible along the disk. Figure 8.4 shows the azimuthal profile of the disk in the sky-plane. The mean brightness is calculated in small annular sections of 10° around the ring starting in the North and moving counterclockwise to the East. Uncertainties are obtained by dividing the rms noise of the image by the square root of the number of beams in each annular sector. The two disk ansae are visible as two peaks in the SE and NW, and apocenter glow is indicated by the significant brightness difference between these two peaks. No other significant peaks or fluctuations are present. We note a slight brightness difference ($< 3\sigma$) between the NE and SW sides of the disk (along the direction of the disk minor axis). The median belt flux density measured between $170° - 270°$ (SW side) is 0.11 ± 0.01 mJy arcsec^{-2} and 0.13 ± 0.01 mJy arcsec^{-2} between $0° - 100°$ (NE side). A similar dimming of the SW side of the disk is seen by Boley et al. (2012),

in our models enough to fix an upper bound on the β values using the 1.3 mm data point.

which they interpret as resulting from a loss of sensitivity at the edges of the ALMA primary beam. However, it is likely that this slight asymmetry between the NE and SW sides of the disk presents further evidence for apocenter glow. The expected overdensity of particles at apocenter forms an arc, which would cover much of the eastern side of the disk given the observed disk geometry (Pan et al. 2016; Pearce & Wyatt 2014).

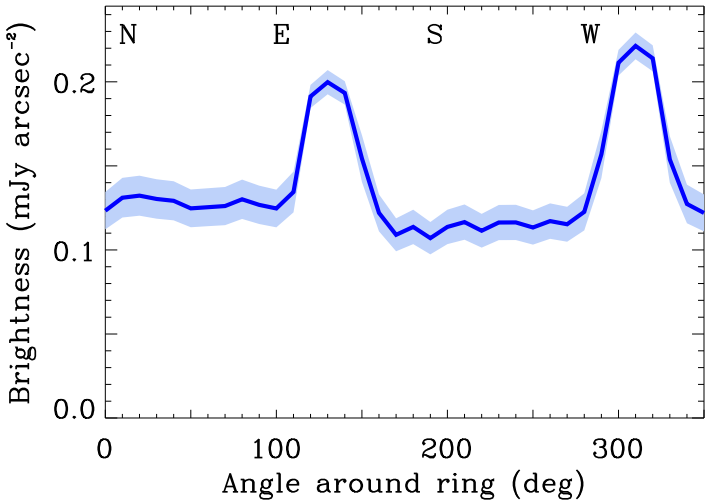

Figure 8.4: Azimuthal profile of the ALMA 1.3 mm continuum emission generated by calculating the mean brightness in 10° annular sections around the disk counter-clockwise from North to East. The disk ansae are clearly seen as two peaks, and apocenter appears brighter due to the detected apocenter glow. The shaded region indicates the $\pm 1\sigma$ confidence interval.

Previous imaging surveys at optical to infrared wavelengths have indicated several azimuthal features, which our millimeter observations do not confirm. Kalas et al. (2013) demonstrate that the dust belt has a $\sim 50\%$ deficit of optical scattered light in an azimuthal wedge at position angle $\sim 331°$, just north of the current location of Fomalhaut b. The sky-plane width of the gap is $2''$ (~ 15 AU), corresponding to a deprojected width of ~ 50 AU. One possibility is that the gap

in scattered light represents a deficit of material, where grains collect on horseshoe orbits on either side of a planet embedded in the gap. The brightness deficit could also result from self-shadowing in an optically thick, vertically thin belt. Millimeter observations are minimally affected by optical depth effects and should reveal the true surface density of grains. Since our ALMA observations do not detect the same 331° gap, it is likely that this feature results from a shadowing effect. However, we cannot rule out smaller structures $\lesssim$ 10 AU that would remain unresolved in our current map.

SCUBA imaging at 450 μm shows evidence for an arc of emission at position angle $\sim$ 141° interior to the outer belt at $\sim$ 100 AU separation from the star Holland et al. (2003). Boley et al. (2012) note a broadening of the disk width on the northwestern side of the belt, to the right of the disk ansae. We do not confirm either of these features in our ALMA map. White et al. (2016a) also note that the disk appears azimuthally smooth.

Determining the Belt Width

The FWHM width of our best-fit model is 13.5 ± 1.8 AU. Boley et al. (2012) estimate a half-maximum width for the disk of $\sim$ 11.4 AU given a power-law belt model and $\sim$ 16 AU given a Gaussian model, consistent with our results. White et al. (2016a) determine a belt width of 13 ± 3 AU from their recent ALMA data. Figure 8.5 shows the surface brightness of our ALMA image in four cuts from the star along both the disk major (SE and NW sides) and minor (SW and NE) axes. We do not see any fluctuation in width along the belt. The flux difference between apocenter and

pericenter is evident. Also of note is the offset of the star from the disk centroid to the SW by $\sim 0\farcs30$ (~ 2.3 AU) in RA and $\sim 1\farcs4$ (~ 10.7 AU) in DEC.

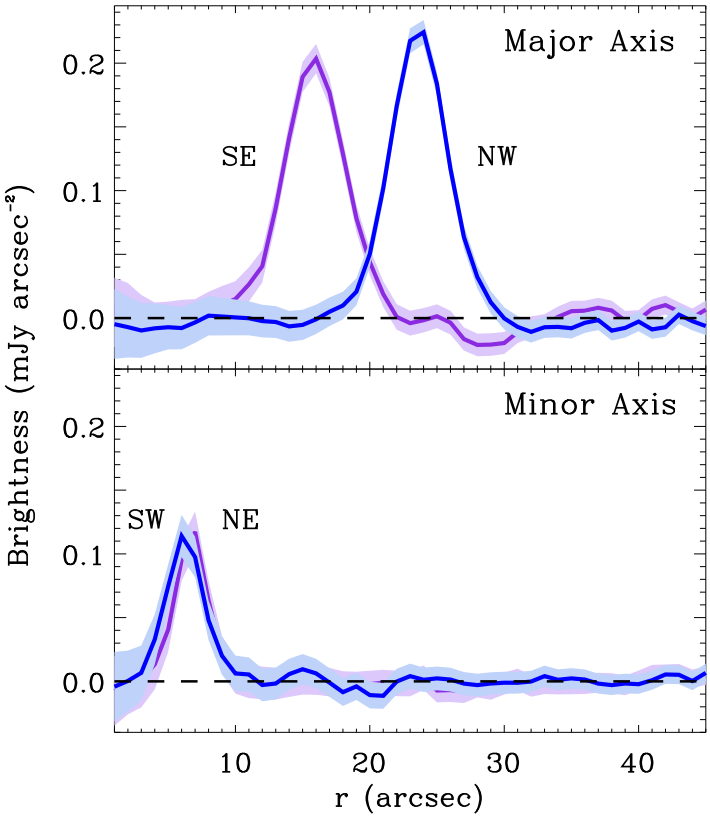

Figure 8.5: Surface brightness of the ALMA 1.3 mm continuum image in four cuts starting from the star: *(top)* along the disk major axis to the NW (apocenter) and SE (pericenter) and *(bottom)* along the disk minor axis to the SW and NE. The shaded regions indicate the $\pm 1\sigma$ confidence interval.

Given the best-fit parameters of our two-dimensional model, we can constrain the fractional width of the belt to be $\Delta R/R = 0.10 \pm 0.01$. Adding a vertical component to the model likely adds to the uncertainty of this constraint. The Fomalhaut debris disk is similarly narrow to the main classical Kuiper Belt in our own Solar System, which is radially confined between the 3:2 and 2:1 orbital resonances with Neptune implying a fractional width of ~ 0.18 (Hahn & Malhotra

2005). In contrast, both the HD 107146 (Ricci et al. 2015a) and η Corvi (Marino et al. 2017) debris disks appear much broader with fractional widths of > 0.3. Boley et al. (2012) propose that the narrow ring observed in Fomalhaut may also result from interactions with planets, namely two shepherding planets on the inner and outer edges of the belt. If the structure of the belt is indeed due to truncation by interior and exterior planets, we would expect to see sharp edges. However, given the resolution of our observations ($\sim$ 10 AU) compared with the width of the belt ($\sim$ 14 AU), we are unable to place any strong constraints on the sharpness of the disk edges.

In our models, there are two parameters that contribute to the width of the belt: the range of semi-major axes assigned to the particles (Δa) and the proper or intrinsic eccentricity (e_p) of a particle's orbit. As expected, these parameters are highly degenerate and we are unable to place strong constraints on either of these parameters independently given the moderate resolution of our observations. The best-fit values for both parameters are $\Delta a = 12.2 \pm 1.6$ AU and $e_p = 0.06 \pm 0.04$. Figure 8.6 shows the MCMC output for Δa and e_p; the degeneracy between the two parameters is clearly seen by the slope in the contours. Altering the proper eccentricity of the particles predicts azimuthal variations in the width of the belt. For a low proper eccentricity ($e_p \sim 0.01$), the particle orbits are apsidally aligned and the belt appears narrower at pericenter than at apocenter. For a high proper eccentricity ($e_p \sim 0.1$), the width of the belt is closer to uniform around the entire circumference of the ring. Future ALMA observations of the disk apocenter and pericenter locations, but with higher resolution, could distinguish between these two cases, and place the first robust constraints on the proper eccentricity of the

Fomalhaut debris disk. Whereas White et al. (2016a) have higher angular resolution in their recent ALMA observations (synthesized beam of $0''.329 \times 0''.234$), the two disk ansae are outside of the primary beam of their single ALMA pointing.

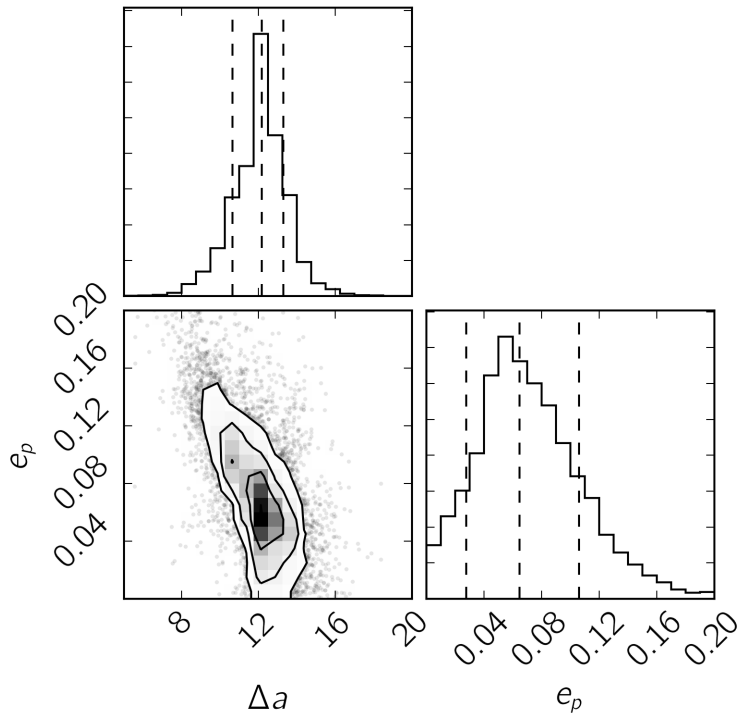

Figure 8.6: Results from $\sim 10^4$ MCMC trials. The diagonal plots show the 1D histogram for both Δa and e_p determined by marginalizing over the other parameter. The dashed vertical lines indicate the best-fit value and 1σ uncertainty. The off-diagonal plot shows the 2D projection of the posterior probability distribution for these two parameters. Contours show the 1σ, 2σ, and 3σ regions.

Geometry of the Disk: The Argument of Periastron

There has been much debate in the literature over the argument of periastron, ω_f, of the Fomalhaut ring. Acke et al. (2012) find $\omega_f = 1^\circ \pm 6^\circ$ based upon the location of the observed pericenter glow along the disk major axis. However, the resolution

of the *Herschel* 70 μm image is not high enough to detect an offset in the stellar position off the disk major axis by a few AU. Kalas et al. (2013) determine a value of $29\overset{\circ}{.}6 \pm 1\overset{\circ}{.}3$ by fitting only for the offset of the expected stellar position from the disk centroid. Boley et al. (2012) are unable to constrain the argument of periastron, since they only image half of the belt with ALMA.

Our new ALMA data provides the first resolved image of emission from both the complete outer disk and the central star with high enough angular resolution to determine an offset of the star from the disk centroid. As discussed in the previous section, the star is noticeably offset to the SW from the disk centroid. This observation is consistent with the result of Kalas et al. (2013). Adopting our modeling approach, we can fit independently for all three angles describing the disk geometry: the inclination (i), the position angle (PA), and the argument of periastron (ω_f). The best-fit argument of periastron from our models is $\omega_f = 22\overset{\circ}{.}5 \pm 4\overset{\circ}{.}3$. This value is comparable to the result from Kalas et al. (2013), and matches both the stellar position relative to the disk centroid and the position along the belt of both the observed pericenter (Acke et al. 2012) and apocenter glow. There is still a large uncertainty in this best-fit value due to the difficulty disentangling the argument of perisatron from the significant inclination of the disk ($i = 65\overset{\circ}{.}6 \pm 0\overset{\circ}{.}3$).

8.4.3 Implications for Fomalhaut b

Fomalhaut b was first discovered through *HST* direct imaging (Kalas et al. 2008) at a location consistent with theoretical predictions for a massive planet orbiting interior to the eccentric debris disk (Quillen 2006; Chiang et al. 2009). However,

follow-up observations at later epochs revealed that Fomalhaut b is instead on a highly eccentric, possibly ring-crossing orbit (Kalas et al. 2013; Beust et al. 2014). Furthermore, this object appears brighter at optical wavelengths than in the infrared, contrary to predictions from models of planetary atmospheres. Kennedy & Wyatt (2011) discuss the possibility of a collisional swarm of irregular satellites surrounding a $\sim 10\ M_{\oplus}$ planet. Alternatively, Fomalhaut b may instead be a dust cloud generated through collisions between larger planetesimals (Currie et al. 2012a; Galicher et al. 2013; Kalas et al. 2013; Kenyon et al. 2014; Tamayo 2014; Lawler et al. 2015). To date, the true nature of Fomalhaut b remains uncertain.

If Fomalhaut b is indeed a dust cloud, our ALMA observations provide useful constraints on its possible dust mass. We can place a robust 3σ upper limit on the flux density of 0.042 mJy, assuming a point source. Following the approach for optically thin emission described in Section 8.3.3, we can determine an upper limit on the potential dust mass. The current separation of Fomalhaut b is ~ 125 AU. In radiative equilibrium, this location implies a dust temperature of ~ 51 K. The resulting upper limit on the dust mass is $< 0.0019\ M_{\rm Moon}$ ($< 1.40 \times 10^{23}$ g), which is consistent with estimates of the $10^{18} - 10^{21}$ g in total sub-micron dust mass needed to account for the scattered light (Kalas et al. 2008). We can also consider optically thick dust emission and instead derive an upper limit on the size of the dust clump: $R_{\rm dust} = \sqrt{F_{\nu} D / (\pi B_{\nu}(T_{\rm dust}))}$. Given the upper limit of $F_{\nu} < 0.042$ mJy, $R_{\rm dust}$ must be < 0.021 AU for an optically thick clump.

8.4.4 Stellar Emission at Millimeter Wavelengths

The best fit flux density for the central star is 0.75 ± 0.02 mJy (with an additional 10% uncertainty for flux calibration). CHARA measurements of the stellar bolometric flux robustly determine the effective temperature to be 8459 ± 44 K (Boyajian et al. 2013). Given this effective temperature, a PHOENIX stellar atmosphere model (Husser et al. 2013) predicts a flux density of ~ 1.3 mJy at 1.3 mm (with 5% uncertainty), in excess of our flux measurement. At long wavelengths, however, this stellar model is essentially a Rayleigh-Jeans extrapolation. Boley et al. (2012) measure a stellar flux of ~ 4.4 mJy at 850 μm with ALMA in Cycle 0, which extrapolates to ~ 1.8 mJy at 1.3 mm, consistent with atmospheric model predictions, but not consistent with our ALMA flux. It is important to note, however, that this measurement is strongly influenced by the primary beam correction applied to the data, since the star is located at the edge of the single pointing. ALMA Cycle 1 observations at 870 μm by Su et al. (2016) detect a central point source as well with a lower flux density of 1.789 ± 0.037 mJy. Extrapolating to 1.3 mm, this measurement yields an expected flux density of 0.80 ± 0.02, more comparable to our result. White et al. (2016a) also determine a low stellar flux density of 0.90 ± 0.15 mJy from recent ALMA observations at a 1.3 mm (233 GHz, a slightly higher frequency than our observations). Figure 8.7 shows the flux density spectrum (top) and brightness temperature (bottom) of Fomalhaut from *Herschel* (Acke et al. 2012), ALMA (this work; Su et al. 2016; White et al. 2016a), and ATCA (Ricci et al. 2012). To calculate the brightness temperature, we follow Liseau et al. (2016) and adopt a photospheric radius of 1.842 ± 0.019 $R_\odot$ (Mamajek 2012). The stellar flux density at infrared

wavelengths from *Herschel* is inferred, since the measured flux includes contributions from both the star and the inner belt which are unresolved in these observations. Given the possible contribution from an inner warm belt at all wavelengths, we quote only upper limits on the brightness temperature. At the *Herschel* wavelengths, the brightness temperature is mostly consistent with the effective temperature. However, at millimeter wavelengths, the brightness temperature dips to < 6600 K and < 6200 K at 870 μm and 1.3 mm, respectively. The ATCA flux measurement at 6.66 mm suggests a brightness temperature of < 17900 K.

It is clear that the brightness temperature of Fomalhaut is significantly lower than the measured photospheric effective temperature at millimeter wavelengths before increasing again at longer, centimeter wavelengths. Similar behavior is seen for a number of K and M giants by Harper et al. (2013). With the advent of ALMA, there are a growing number of stars with robust millimeter flux measurements. Excess emission at long wavelengths has been observed for several other Sun-like stars, including α Cen A/B, ϵ Eridani, and τ Ceti (Liseau et al. 2015, 2016; MacGregor et al. 2015b, 2016a), which is consistent with emission from a hot stellar chromosphere. Liseau et al. (2016) observe a temperature minimum, like we observe for Fomalhaut, for both α Cen A and B at shorter, sub-millimeter wavelengths with ALMA, which they attribute to a change in the sign of the temperature gradient above the stellar photosphere, as is seen in our own Sun. At 1.3 mm wavelength, the flux densities of these stars have recovered and their brightness temperatures are similar to their effective temperature. For Fomalhaut, it seems likely that the flux density measured by ATCA at 6.66 mm is dominated by chromospheric emission. However, the long wavelength spectrum of A-type stars, like Fomalhaut, is further

complicated by ionized stellar winds, which flatten the spectral slope at radio wavelengths (Aufdenberg et al. 2002). The ability to measure these behaviors with ALMA will enable advances in our understanding of stellar radiative transfer and chromospheres, and of stellar winds.

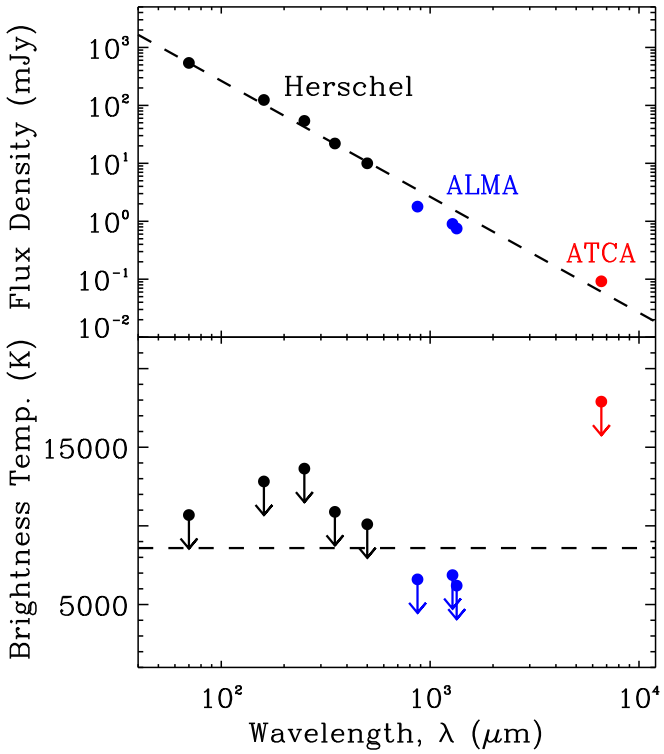

Figure 8.7: *(top)* Flux density spectrum of Fomalhaut from *Herschel* (black points, Acke et al. 2012), ALMA (blue points, this work; Su et al. 2016; White et al. 2016a), and ATCA (red point, Ricci et al. 2012). The dashed line indicates the expected spectral index for an optically thick photosphere with effective temperature 8590 ± 73 K. The uncertainty on the flux measurements lies within the size of the points. *(bottom)* Upper limits on the brightness temperature spectrum of Fomalhaut calculated by assuming a photospheric radius for the star. Again, the dashed line indicates the expectation for a classical photosphere.

For the Fomalhaut system, understanding the stellar flux contribution at long wavelengths is especially critical. *Spitzer* and *Herschel* observations reveal excess emission at infrared wavelengths (Stapelfeldt et al. 2004; Acke et al. 2012), which is attributed to a warm inner dust belt similar to the Asteroid Belt in our Solar System (Su et al. 2013). However, no inner belt has been detected or resolved with ALMA (Su et al. 2016). Robustly determining the spectral energy distribution of the star at long wavelengths will help to determine the nature of such an inner Asteroid Belt.

8.5 Conclusions

We present new ALMA observations at 1.3 mm of the continuum dust emission from the Fomalhaut system. These observations provide the first millimeter map covering the complete outer debris disk with uniform sensitivity. We adopt a MCMC modeling approach that generates models of an eccentric ring by calculating the orbital parameters of a collection of particles. The main results from this analysis are as follows.

1. The Fomalhaut outer debris disk is radially confined with a model best-fit inner edge of 136.3±0.9 AU and width of 13.5±1.8 AU, implying a fractional width of 0.10 ± 0.01. Given the measured total flux density and assuming optically thin dust emission, the total dust mass of the disk is $0.015 \pm 0.010\ M_{\oplus}$, consistent with previous measurements. Given the resolution of our observations, we do not place strong constraints on the sharpness of the belt edges.

2. Our ALMA image is the first conclusive observation of apocenter glow, a

brightness asymmetry due to a surface density enhancement at apocenter (Pan et al. 2016). We determine a best-fit eccentricity for the ring of 0.12 ± 0.01. Given the apocenter to pericenter flux ratio from our ALMA measurement and previous (sub)millimeter observations, and assuming a size distribution power law index of $q = 3.46 \pm 0.09$, we constrain the dust absorptivity power law index β to be $0.9 < \beta < 1.5$.

3. By adopting a modeling approach that accounts for the orbital parameters of disk particles, we are able to robustly constrain the geometry of the disk. The best fit values for the inclination and position angle are $65\overset{\circ}{.}6 \pm 0\overset{\circ}{.}3$ and $337\overset{\circ}{.}9 \pm 0\overset{\circ}{.}3$, respectively. By resolving both the stellar position relative to the disk centroid and both the pericenter and apocenter sides of the disk, we are able to determine the argument of periastron to be $\omega = 22\overset{\circ}{.}5 \pm 4\overset{\circ}{.}3$, consistent with the results from *HST* images (Kalas et al. 2013).

4. After subtracting our best-fit belt model from the data, the resulting residuals do not show any evidence for significant azimuthal structure. The only significant peak visible to the east of the disk is attributable to a background galaxy. We do not confirm any of the azimuthal features, including the gap at 331° position angle, that have been seen in previous imaging studies with *HST*, SCUBA, and ALMA. However, we cannot rule out smaller structure $\lesssim 10$ AU, which would be unresolved with the current resolution of our image.

5. The flux density at 1.3 mm of the central star, $F_{\rm star} = 0.75 \pm 0.02$ mJy, is significantly lower than predicted by current photospheric models. Indeed, the implied brightness temperature of Fomalhaut falls below the stellar effective

temperature at millimeter wavelengths before increasing significantly at longer, centimeter wavelengths. Similar spectra have been observed for the Sun-like stars α Cen A and B (Liseau et al. 2016). For Fomalhaut, it is especially critical to determine the long wavelength stellar spectrum in order to better constrain the contribution from the inner dust belt.

The proximity (7.66 pc) and young age ($\sim$ 440 Myr) of the Fomalhaut system make it a unique target to explore the early stages of planetary system formation and reorganization. Future ALMA observations with higher angular resolution will allow for further exploration of the outer disks's azimuthal structure, as well as enabling studies of structural variability over time.

Acknowledgments

M.A.M. acknowledges support from a National Science Foundation Graduate Research Fellowship (DGE1144152) and from NRAO Student Observing Support. L.M. acknowledges support by STFC through a graduate studentship and, together with M.C.W. and A.S., by the European Union through ERC grant number 279973. P.K. and J.R.G. thank support from NASA NNX15AC89G, NNX15AD95G/ NEXSS and NSF AST-1518332. This work benefited from NASA's Nexus for Exoplanet System Science (NExSS) research coordination network sponsored by NASA's Science Mission Directorate. G.M.K. is supported by the Royal Society as a Royal Society University Research Fellow. M.P. acknowledges support from NASA grants NNX15AK23G and NNX15AM35G. A.M.H. is supported by NSF

grant AST-1412647. A.S. is partially supported by funding from the Center for Exoplanets and Habitable Worlds. The Center for Exoplanets and Habitable Worlds is supported by the Pennsylvania State University, the Eberly College of Science, and the Pennsylvania Space Grant Consortium. This paper makes use of the following ALMA data: ADS/JAO.ALMA #2015.1.00966.S. ALMA is a partnership of ESO (representing its member states), NSF (USA) and NINS (Japan), together with NRC (Canada) and NSC and ASIAA (Taiwan) and KASI (Republic of Korea), in cooperation with the Republic of Chile. The Joint ALMA Observatory is operated by ESO, AUI/NRAO and NAOJ. The National Radio Astronomy Observatory is a facility of the National Science Foundation operated under cooperative agreement by Associated Universities, Inc. Figure 8.6 was generated using the `corner.py` code (Foreman-Mackey 2016).

9

Debris Disk Structure Around Nearby Sun-like Stars

This thesis chapter is work in progress by

M. A. MacGregor, D. J. Wilner, A. M. Hughes, S. M. Andrews,

E. Nesvold, M. Kuchner, E. Chiang

Abstract

We have assembled SMA and ALMA observations to resolve the millimeter continuum emission from a sample of the eight brightest debris disks around the closest (< 20 pc) Sun-like (FGK) main-sequence stars to probe the underlying distributions of dust-producing planetesimals. While all of these disks exhibit central clearings or gaps, it is unclear whether these structures result from collisional depletion by an outward moving front of planetoid growth, or dynamical depletion from the gravitational influence of giant planets. We will use these new data to

(1) quantify surface density structures and address the basic dynamical processes that govern debris disk evolution to Gyr ages, (2) place constraints on otherwise inaccessible wide-separation planets in these systems from signatures of disk-planet interaction, and (3) make the first systematic comparative study of planetesimal structures around Sun-like stars. Analysis of these data is ongoing, but it is already clear that these disks exhibit a range of structures. Some appear radially broad, and several show clear asymmetric structures (HD 10647 and HD 139664). Two of these sources (HD 22049 and HD 139664) have measured stellar fluxes greatly in excess of the predicted photospheric flux, possibly indicative of chromospheric emission.

9.1 Introduction

The spectral energy distributions (SED) of most debris disks show evidence for a large central cavity or gap. Surprisingly, the dominant mechanism for producing these clearings remains controversial. The leading models are (1) collisional depletion, where the formation of Pluto-sized bodies in an extended planetesimal disk initiates collisions that propagate outwards to radii of many tens of AU over Gyr timescales (Kenyon & Bromley 2002, 2008), and (2) dynamical depletion, where planetesimals are scattered by mature (possibly migrated) interior planets (Backman & Paresce 1993). These models are closely related to the fundamental question of what creates debris disks in the first place, since the planetesimals must be 'stirred' to incite destructive collisions (Wyatt 2008). Are debris disks around main sequence Sun-like stars predominantly 'self-stirred' by outwardly moving fronts of planetoid growth (Kennedy & Wyatt 2010), or are they 'planet-stirred' by the gravitational

influence of giant planets that drive initially non-intersecting planetesimal orbits to cross (Mustill & Wyatt 2009)?

The key observational discriminant between these two scenarios is the resolved spatial distribution of planetesimals. A collisional depletion front leaves a broad planetesimal disk with an outwardly increasing surface density gradient. Dynamical depletion is revealed by features that implicate giant planets, such as sharp inner disk edges (Chiang et al. 2009), asymmetries such as centroid offsets induced by the perturbations of giant planets on elliptical orbits (Wyatt et al. 1999), or azimuthal clumps from the trapping of planetesimals in mean-motion resonance (Kuchner & Holman 2003). Just as features of our own Kuiper Belt reveal the presence of Neptune and its outward migration at an early epoch (Malhotra 1995), the structure of debris disks encodes information about the formation and dynamical evolution of exoplanetary systems.

Millimeter observations provide the best way to trace the dust-producing planetesimals in debris disks. The large grains that dominate the emission at these long wavelengths cannot travel far from their parent bodies before being ground down, in contrast to the small grains detected in the optical and infrared that are redistributed rapidly by stellar radiation and winds (Wyatt 2006; Wilner et al. 2011). To explore the stirring mechanism of main sequence debris disks, we have assembled resolved millimeter continuum observations of a sample of the eight brightest debris disks around the closest (< 20 pc), Sun-like (FGK) stars to probe the underlying planetesimal distributions. We plan to use these data to (1) quantify surface density structures and address the basic dynamical processes that govern debris disk evolution to Gyr ages, (2) place constraints on otherwise inaccessible

wide-separation planets in these systems from signatures of disk-planet interaction, and (3) make the first systematic comparative study of planetesimal structures around Sun-like stars. Here we describe the sample selection, the individual targets, the new and archival millimeter observations, and we present the first images of each system. Analysis of these data is ongoing, and we defer model fitting and detailed analysis of the disk structures to future work.

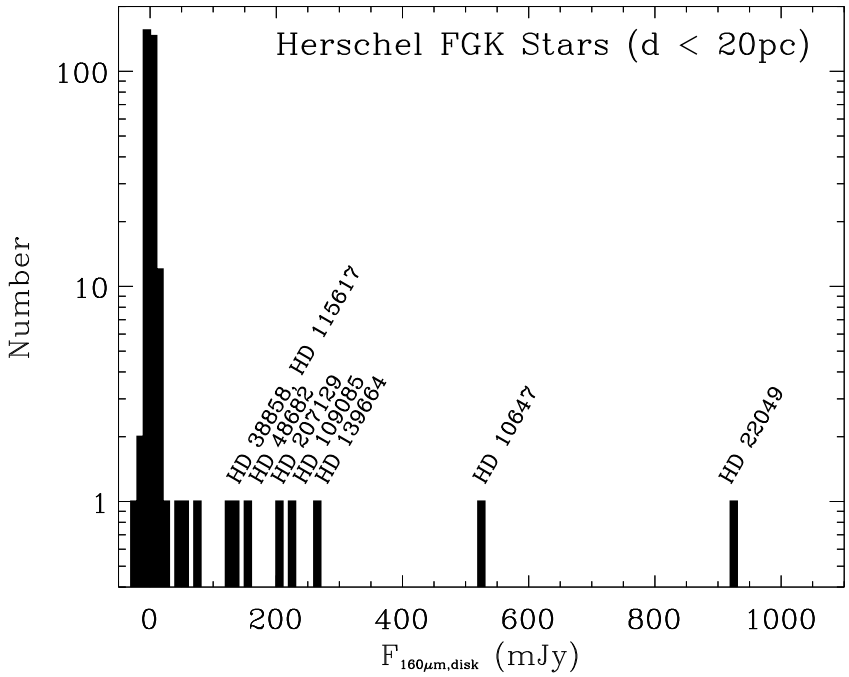

Figure 9.1: A histogram of *Herschel* 160 μm disk fluxes for FGK stars within 20 pc. The eight disks in our sample stand out within this local volume, with an abrupt drop in flux below this tier.

9.2 The Sample

Through a combination of *Herschel* programs (e.g. Eiroa et al. 2013), we have nearly complete knowledge of debris disk demographics for Sun-like (F, G, and K-type) stars within 20 pc, down to a few times Kuiper Belt levels. Figure 9.1 shows the 160 μm disk flux density, the best available proxy for cold dust content, for all 230 FGK stars within this local volume. We defined a sample of the eight brightest systems in this histogram. The 160 μm fluxes drop sharply below this tier, and imaging fainter targets with ALMA will require a more substantial effort. Table 9.1 lists the source positions and properties, and a brief discussion of each target follows. Radial velocity monitoring of these eight bright stars reveals a range of inner planetary systems, including Jupiters (HD 22049, HD 10647) and super-Earths (HD 38858, HD 115617), as well as non-detections.

9.2.1 HD 22049 (ϵ Eridani)

We discussed the HD 22049 system, the closest Sun-like star to host a debris disk, extensively in Chapter 6 of this thesis. The disk was originally detect as a far-infrared excess by *IRAS* (Aumann 1985) and subsequently resolved with JCMT/SCUBA at 850 μm, revealing a nearly face-on belt of emission peaking at 60 AU (18″) radius with several brightness enhancements or clumps (Greaves et al. 1998). Subsequent single-dish and interferometric observations from 250 to 1300 μm confirm the basic belt morphology, but not the low significance asymmetries (Schütz et al. 2004; Backman et al. 2009; Greaves et al. 2014; Lestrade & Thilliez 2015; MacGregor

Table 9.1: FGK Stars within 20 pc with 160 μm-bright Debris Disks

Source	α (J2000)	δ (J2000)	SpT	D[a] (pc)	Age (Gyr)	$F^{b}_{160\mu m}$ (mJy)
HD 22049 (ϵ Eri)	03 32 54.9	−09 27 29.4	K2	3.2	$0.4 - 0.8$	960 ± 30
HD 10647 (q^1 Eri)	01 42 29.3	−53 44 27.0	F9	17.4	$> 1 - 2$	636 ± 32
HD 139664 (g Lup)	15 41 11.4	−44 39 40.3	F5	17.5	$0.3^{+0.7}_{-0.2}$	265 ± 30
HD 109085 (η Crv)	12 32 04.2	−16 11 45.6	F2	18.2	$1 - 2$	231 ± 13
HD 207129	21 48 15.8	−47 18 13.0	G2	15.6	$1.5 - 3.2$	211 ± 2
HD 48682 (56 Aur)	06 46 44.3	+43 34 38.7	F9	16.5	$3.2^{+1.4}_{-1.9}$	182 ± 4
HD 38858	05 48 34.9	−04 05 40.7	F9	16.5	$0.2 - 9.3$	141 ± 20
HD 115617 (61 Vir)	13 18 24.3	−18 18 40.3	G7	8.6	4.6 ± 0.9	131 ± 17

[a] All distances measured by van Leeuwen (2007)
[b] Fluxes determined from the *Herschel* DEBRIS survey archive (Eiroa et al. 2013)
References for system ages: HD 22049, Mamajek (2008); HD 10647, Butler et al. (2006), and references therein; HD 139664, Mallik et al. (2003), Nordström et al. (2004); HD 109085, Mallik et al. (2003), Vican (2012); HD 207129, Marshall et al. (2011), and references therein; HD 48682, Holmberg et al. (2009); HD 38858, Takeda et al. (2007), Sousa et al. (2010), Casagrande et al. (2011); HD 115617, Wright et al. (2011), Vican (2012)

et al. 2015b; Chavez-Dagostino et al. 2016). SED modeling indicates the presence of a warm inner dust belt reaching to several AU from the star (Backman et al. 2009; Greaves et al. 2014) or inward transport from the outer belt (Reidemeister et al. 2011). In addition, radial velocity observations suggest the presence of a Jupiter-mass planet with semi-major axis of 3.4 AU (1″) (Hatzes et al. 2000), although the veracity of this detection remains controversial (Anglada-Escudé & Butler 2012).

9.2.2 HD 10647 (q^1 Eridani)

Analysis of 100 μm observations from *Herschel* indicates a highly inclined disk peaking at 85 AU with a width of 40 AU (Liseau et al. 2010). Both scattered light and far-infrared imaging offer hints that the HD 10647 debris disk is asymmetric. Stapelfeldt et al. (2007) show that the scattered light is more extended to the northeast than the southwest, though its faint and diffuse nature makes the asymmetry difficult to quantify. Augereau & *Herschel*/DUNES Team (2010), by aggressively deconvolving the *Herschel* images, show a tentative brightness enhancement on the southwest side, which may be due to 'pericenter glow,' a sign that the disk centroid may be offset northeast from the star. The system also contains a Jupiter-mass planet with a semi-major axis of ~ 2 AU and orbital eccentricity of 0.1 ± 0.01 detected via radial velocity measurements (Butler et al. 2006). Recent collisional modeling by Schüppler et al. (2016) suggests that the system may have an architecture similar to the Solar System with an inner planetesimal belt at $3-10$ AU and an outer belt at $75-125$ AU, with giant planets in between.

9.2.3 HD 139664 (g Lupus)

Initial scattered light imaging of HD 139664 with *HST* revealed a nearly edge-on disk peaking at 83 AU with a possible rising gradient to an outer edge at 109 AU (Kalas et al. 2006). Subsequent scattered light observations indicate that the disk may not be axisymmetric (Schneider et al. 2014). The eastern side of the disk is brighter and peaks closer to the central star at 2.7″ (48 AU) compared to 3.7″

(65 AU) for the western side. In addition, dust scattered light extends to a greater distance 'above' the disk midplane on the eastern side. Far-infrared images from *Herschel* are consistent with the geometry determined form scattered light, but do not show any of the same asymmetric features.

9.2.4 HD 109085 (η Corvi)

The HD 109085 system is well known to contain two distinct inner and outer dust belts. The outer belt was resolved by *Herschel* and JCMT/SCUBA-2 (Duchêne et al. 2014). Modeling of the disk gives a mean radius of $\sim$ 166 AU with an upper limit on the width of $<$ 75 AU. The hot inner dust component within $<$ 3 AU of the host star is responsible for the observed mid-infrared excess (Smith et al. 2009). Subsequent observations with the Large Binocular Telescope Interferometer and Keck Telescope suggest that the warm dust may be much closer to the star at a distance of $0.5 - 1.0$ AU (Defrère et al. 2015; Kennedy et al. 2015a; Lebreton et al. 2016). *Spitzer* IRS spectroscopy indicates that the warm component contains a significant amount of small dust grains below the expected blow-out size (Chen et al. 2006).

9.2.5 HD 207129

Both scattered light (Krist et al. 2010; Schneider et al. 2014) and far-infrared imaging (Marshall et al. 2011) indicate an emission peak at 160 AU. Power law models of the dust emission suggest an outwardly increasing radial surface density profile from $<$ 100 AU out to a sharp edge at $170 - 190$ AU (Löhne et al. 2012). However,

detailed collisional models cannot tell from the available data if this profile reflects the underlying planetesimal distribution or arises from small grains leaking inward from a narrow ring. There is no indication of starlight scattering material interior to the disk inner edge from *HST* imaging (Schwarz et al. 2016). The *Herschel* 70 μm emission shows a tentative asymmetry between the northwest and southeast sides of the ring.

9.2.6 HD 48682 (56 Aurigae)

The HD 48682 debris disk was detected at 450 and 850 μm with JCMT/SCUBA (Sheret et al. 2004), but not resolved. The disk was first resolved at far-infrared wavelengths with *Herschel* (Eiroa et al. 2013), and the highest resolution 70 μm image constrains the overall disk size and viewing geometry. It is unclear to what extent the 70 μm image traces a blowout halo of small grains. Subsequent spectral energy distribution modeling of the system indicates that the main debris belt is located at $\sim$ 140 AU (Pawellek et al. 2014). Unlike other nearby bright debris disks viewed close to edge-on, optical scattered light remains undetected from 56 Aur, even with *HST* (Stapelfeldt et al. 2012).

9.2.7 HD 38858

Spitzer imaging at 70 μm marginally resolved the HD 38858 debris disk and suggested a radius of 135 AU (Krist et al. 2012). More recent *Herschel* observations better resolve the disk structure (Kennedy et al. 2015b). However, the data is equally well fit by two models: 1) a broad belt spanning $\sim 30 - 200$ AU with a

changing surface density profile, or 2) two narrow ($\sim$ 10 AU wide) rings centered at 55 and 130 AU. SCUBA-2 observations at 850 μm marginally detect the disk, but are contaminated by significant background emission. Radial velocity data initially revealed a planet with a minimum mass of 30.55 $M_{\oplus}$ at 1 AU (Mayor et al. 2011). Additional RV measurements revised the planet's mass and semi-major axis to 12 ± 2 $M_{\oplus}$ and 0.64 AU, respectively (Kennedy et al. 2015b).

9.2.8 HD 115617 (61 Virginis)

Previous *Spitzer* observations of the HD 115617 debris disk were unable to robustly determine the disk radial location, yielding estimates that ranged from $\sim 4 - 25$ AU (Trilling et al. 2008; Lawler et al. 2009) to $\sim 96 - 195$ AU (Tanner et al. 2009). Subsequent *Herschel* observations revealed a radially broad belt spanning 30 to $>$ 100 AU, although significant background contamination is present at 160 μm (Wyatt et al. 2012). The HD 115167 system also hosts a compact system of low-mass planets at 0.05, 0.218, and 0.478 AU with minimum masses of 5.1, 18.2, and 22.9 $M_{\oplus}$ detected with radial velocity surveys (Vogt et al. 2010). Although the exact shape of the disk inner edge is not well constrained by the currently available observations, a clearing within $\sim$ 30 AU could imply the presence of additional planets in the system outside of the three already known.

9.3 Observations

We obtained either SMA or ALMA observations at $\sim$ 1 mm wavelength for each of the eight targets in the sample. Four of the targets (HD 10647, HD 139664, HD 207129, and HD 38858) were observed in ALMA Band 6 at 1.3 mm wavelength in 2016 as part of ALMA Cycle 3 project 2015.1.00307.S (PI Wilner). Both HD 109085 and HD 115617 were observed in ALMA Band 7 at 0.88 mm wavelength earlier in ALMA Cycle 1 (2012.1.00385.S, PI Wyatt) and 2 (2013.1.00359.S, PI Wyatt), respectively, with data available in the ALMA Science Archive. Analysis of the HD 109085 ALMA observations was originally present in Marino et al. (2017). We observed HD 22049 at 1.3 mm wavelength with the SMA in July–November 2014 (see Chapter 6 for further discussion of these data). HD 48682 is too far north (declination of +43°) to be accessible by ALMA. To complete the sample, we obtained SMA observations of this target at 1.3 mm in October 2015 through February 2016. Table 9.2 summarizes the essentials of these observations, including the telescope used, wavelength, observation dates, number of antennas, baseline lengths, precipitable water vapor (pwv), and gain calibrators used. The field of view for each observation is defined by the FWHM of the telescope primary beam. At 1.3 mm the SMA has a primary beam size of $\sim 52''$. ALMA has a primary beam size of $\sim 18''$ and $\sim 25''$ at 0.88 mm (Band 7) and 1.3 mm (Band 6), respectively. For all sources, except HD 109085, the phase center was chosen to be the stellar position corrected for its proper motion. The radial extent of the HD 109085 disk was slightly too large to fit in a single pointing with ALMA at Band 7, so a three-pointing mosaic was constructed. The center pointing was fixed at the stellar position, with

two additional pointings on each of the disk ansae.

The correlator was configured to maximize continuum sensitivity for all targets. However, the specific spectral set-up differs between sources. For all four targets included in ALMA project 2015.1.00307.S, the setup used four basebands, centered at 230.5, 232.5, 245, and 247 GHz, in two polarizations. We also included the ^{12}CO J= $2-1$ line (230.538 GHz) to constrain the molecular gas content of the disks. The baseband with the targeted spectral line has 3840 channels over a bandwidth of 1.875 GHz, while the other three basebands each have 128 channels over a bandwidth of 2 GHz. The set-up for observations of HD 109085 and HD 115617 were similar with four basebands centered at 335.744, 337.644, 345.798 and 347.455 GHz, in two polarizations. The ^{12}CO J= $3-2$ line (345.798 GHz) was included in one baseband with 3840 channels and a bandwidth of 1.875 GHz, while the three dedicated continuum basebands each had 128 channels and 2 GHz of bandwidth. For the SMA observations of HD 22049, we had 8 GHz of available bandwidth from $217.5-221.5$ and $229.5-233.5$ GHz. The SMA observations of HD 48682 were taken after the addition of the SWARM correlator, allowing for 16 GHz of bandwidth from $212.8-220.8$ and $228.8-236.8$ GHz.

For all of the SMA observations, the data for each track were calibrated separately using the IDL-based `MIR` software package. All of the ALMA observations were calibrated independently using the `CASA` software package. We estimate that the systematic uncertainty of the the flux calibration for all sources is $\sim 10\%$. Images for all eight targets were generated in `CASA` (version 4.7.1) using the `CLEAN` algorithm. Since we account for the primary beam in our visibility modeling, we do not apply a primary beam correction to any of these images. For some sources,

Table 9.2: SMA and ALMA Observations

Source	λ (mm)	Instr.	Obs. Date	Ant.	Baseline (m)	PWV (mm)	Gain Calib.
HD 22049	1.3	SMA	2014 Jul 28	7	6 – 35	2.2	J0339-017
			2014 Jul 29	7	6 – 35	1.7	J0339-017
			2014 Jul 30	7	6 – 35	2.0	J0339-017
			2014 Aug 05	7	6 – 35	2.5	J0339-017
			2014 Nov 19	7	6 – 56	1.7	J0339-017
HD 10647	1.3	ALMA	2016 May 26	37	15 – 641	1.3	J0210-5101
			2016 Jun 02	38	15 – 773	1.3	J0210-5101
HD 139664	1.3	ALMA	2016 May 13	38	15 – 640	1.0	J1535-4730
			2016 May 15	41	15 – 640	2.2	J1535-4730
HD 109085	0.88	ALMA	2013 Dec 15	27	15 – 445	1.2	J1215-1731
			2013 Dec 15	27	15 – 445	1.1	J1215-1731
			2014 Dec 25	38	15 – 349	0.98	J1215-1731
			2014 Dec 26	40	15 – 349	0.55	J1245-1616
			2014 Dec 29	37	15 – 349	0.72	J1245-1616
			2015 Jan 01	37	15 – 349	0.45	J1245-1616
HD 207129	1.3	ALMA	2016 May 04	41	15 – 640	2.3	J2135-5006
			2016 May 08	41	15 – 640	1.4	J2135-5006
HD 48682	1.3	SMA	2015 Oct 28	7	9 – 77	1.5	J0646+448
			2015 Dec 07	8	9 – 77	2.5	J0646+448
			2016 Jan 06	7	16 – 77	1.1	J0646+448
			2016 Feb 02	6	16 – 77	1.3	J0646+448
HD 38858	1.3	ALMA	2016 Mar 23	40	15 – 460	2.5	J0541-0541
			2016 Mar 26	39	15 – 460	0.96	J0541-0541
HD 115617	0.88	ALMA	2015 Apr 09	37	15 – 349	01.08	J1337-1257
			2015 Apr 22	41	15 – 349	0.77	J1337-1257
			2015 Apr 22	41	15 – 349	0.72	J1337-1257
			2015 Apr 22	41	15 – 349	0.75	J1337-1257

it was necessary to include a slight taper using the `uvtaper` parameter in `CLEAN` to improve surface brightness sensitivity.

Initial imaging of both HD 38858 and HD 115617 revealed significant contributions from extragalactic background sources. Figure 9.2 shows wide-field images of both HD 38858 and HD 115617 with natural weighting. For HD 38858, two background sources are evident at offset positions from the image center of $(+9\farcs9, +1\farcs1)$ and $(+9\farcs6, -17\farcs0)$ with fluxes of 0.23 ± 0.04 mJy and 0.14 ± 0.04 mJy, respectively. For HD 115617, background sources are seen at $(+0\farcs1, +4\farcs5)$ and $(-1\farcs1, +12\farcs3)$ with fluxes of 0.31 ± 0.05 mJy and 0.18 ± 0.05 mJy, respectively. Deep surveys with ALMA have established statistics on the number of background sources expected in a given field of view (Hatsukade et al. 2013; Carniani et al. 2015). For observations of a $20'' \times 20''$ field at ~ 1 mm, the expected number of sources with flux density > 0.15 mJy is $1.7^{+3.3}_{-1.2}$, consistent with the number of background sources we detect. For the purposes of isolating emission from the disk, we subtracted point source models for each apparent background source in the images using the `CASA` task `uvsub`. We then proceeded with imaging these two targets as described above.

9.4 Preliminary Results and Analysis

Figure 9.3 shows the *Herschel* 70 μm (left panels of each image pair) and either SMA or ALMA ~ 1 mm images (right panels of each image pair) for all eight debris disks in our sample. All disks are detected with a peak signal-to-noise ranging from 4σ to 10σ. Emission from the central star is detected for all sources except HD 48682 with signal-to-noise ranging from 3σ to 10σ. Table 9.3 lists the synthesized beam

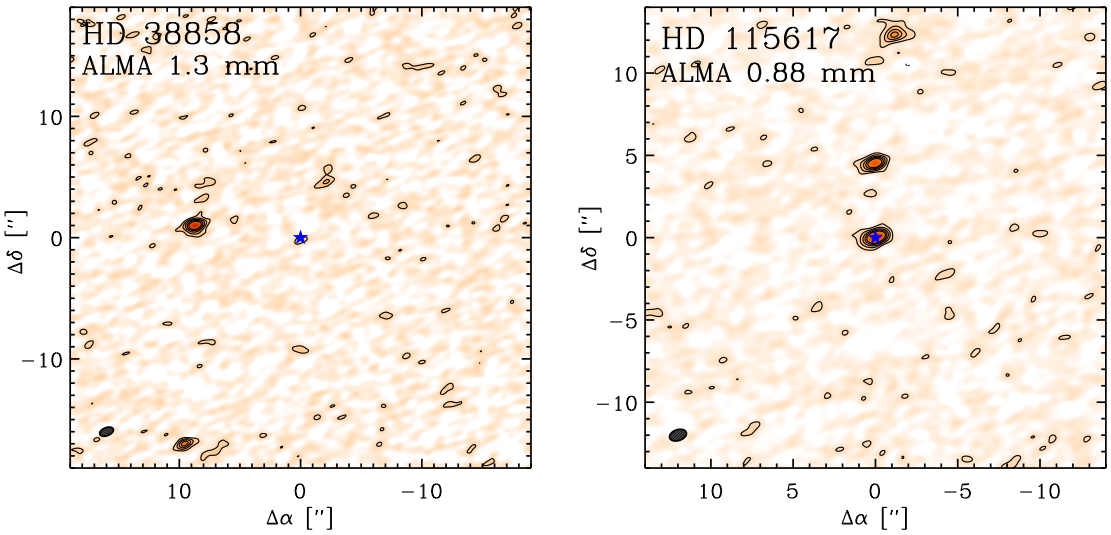

Figure 9.2: Wide-field ALMA images of HD 38858 *(left)* and HD 115617 *(right)* with natural weighting showing contamination form background sources. Contours for both images are in steps of $[2, 4, 6, 8, 10]\times$ the image rms. The stellar position for each source is marked by the blue star symbol. The dashed ellipse in the lower left corner indicates the synthesized beam size.

size with natural weighting, the beam position angle, the rms noise for each image, the expected photospheric flux, and the measured stellar flux.

All eight disks are resolved by these new millimeter observations. HD 22049 is a face-on, broad belt with a diameter of $\sim 40''$ extending beyond the primary beam of the SMA. HD 10647 has a significantly higher inclination and appears slightly asymmetric. The southwest side of the disk is brighter in the *Herschel* image and closer to the star in the ALMA image. This apparent 'pericenter glow' and centroid offset could indicate that the disk is eccentric. The HD 139664 disk is nearly edge-on and also appears asymmetric, with the southwest side of the disk extending farther from the star. Both HD 109085 and HD 207129 are closer to face-on, like HD 22049, and appear to be radially broad rings. HD 48682, HD 38858, and HD 115617 are

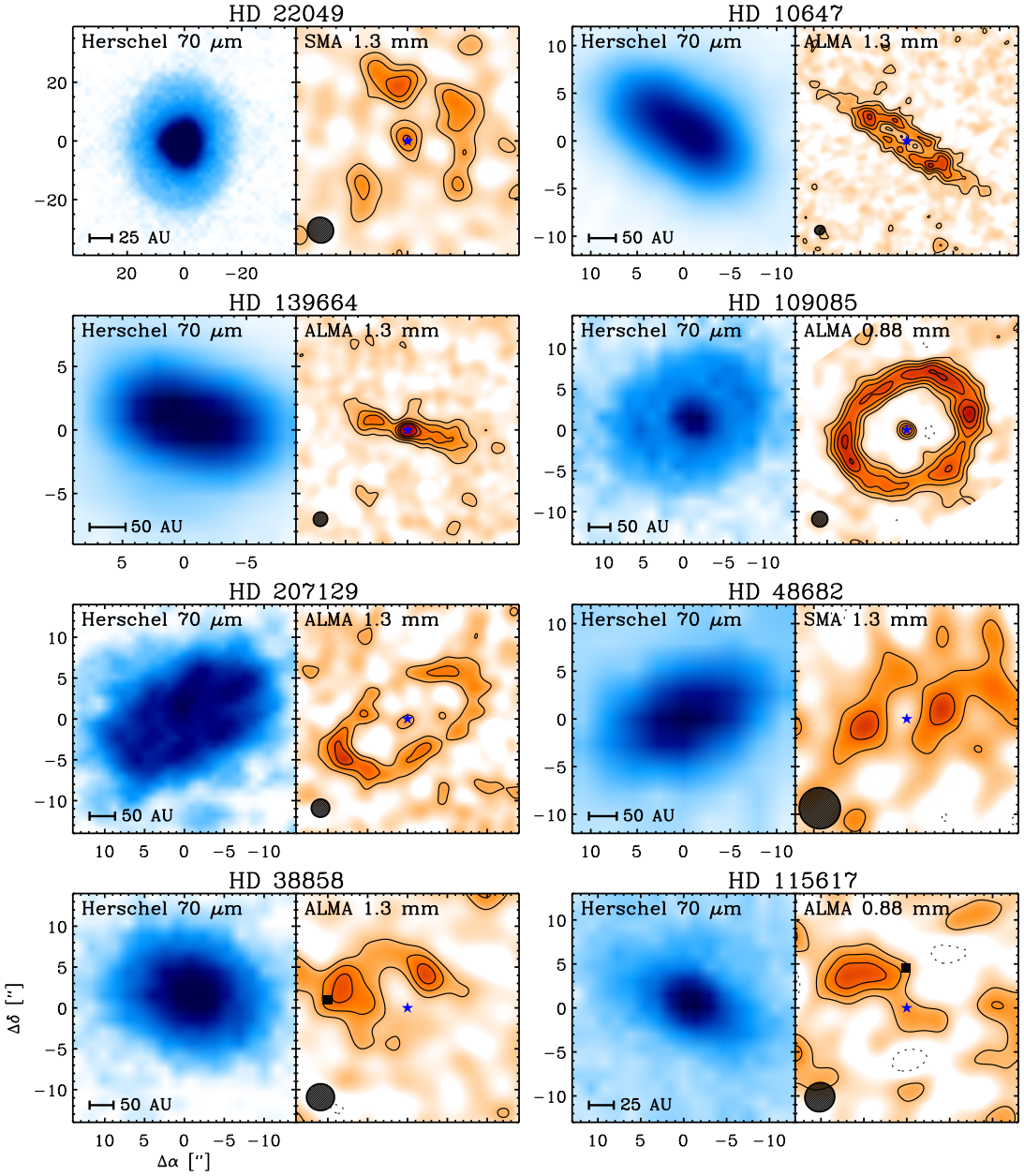

Figure 9.3: FGK debris disks in our sample imaged with *Herschel* at 70 μm *(left panels of each image pair)* and either SMA or ALMA at millimeter wavelengths *(right panels of each image pair)*. For the millimeter images, contours are in steps of $[2, 4, 6, 8, 10]\times$ the image rms listed in Table 9.3. The blue star indicates the stellar position and the dashed ellipse in the lower left corner shows the synthesized beam size. For HD 38858 and HD 115617, the black squares mark the locations of background sources subtracted from the visibilities before imaging.

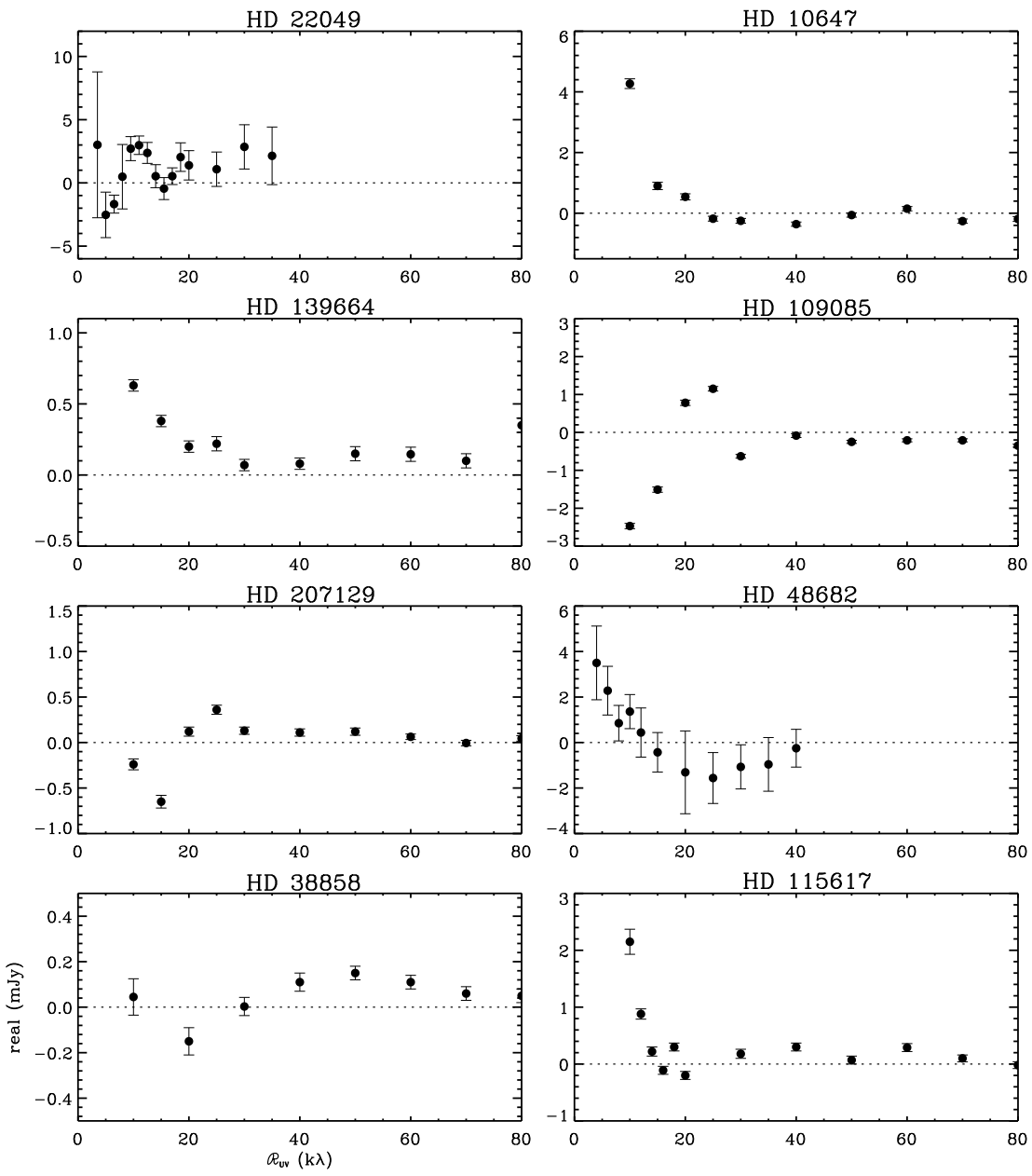

Figure 9.4: The real part of the SMA or ALMA millimeter visibilities averaged in bins of deprojected (u, v) distance for all eight debris disks in our sample of FGK stars. For HD 109085, we only plot visibilities from the central mosaic pointing that covers most of the disk extent. Although the range of baselines sampled by each observation is different, we have chosen to plot the visibilities on a fixed scale from $0 - 80$ kλ for ease of comparison.

Table 9.3: Results of the SMA and ALMA Observations

Source	Beam Size[a] ($''$)	Beam P.A.[b] ($^\circ$)	rms Noise (μJy/beam)	F^{c}_{phot} (mJy)	F_{cen} (mJy)
HD 22049	6.02×5.54	68	200	0.53	1.06 ± 0.34
HD 10647	0.69×0.55	66	15	0.076	0.082 ± 0.009
HD 139664	0.72×0.58	38	13	0.085	0.35 ± 0.02
HD 109085	1.18×0.65	89	20	0.25	0.26 ± 0.02
HD 207129	0.63×0.61	47	10	0.063	0.058 ± 0.005
HD 48682	3.76×3.29	88	150	0.080	< 0.45
HD 38858	1.46×1.09	67	14	0.047	0.055 ± 0.008
HD 115617	1.07×0.67	70	18	0.35	0.49 ± 0.17

[a] Beam size determined with natural weighting
[b] Beam position angle measured from east of north
[c] Expected photospheric flux at the observed wavelength with 2% uncertainty calculated from a PHOENIX stellar atmosphere model assuming a stellar effective temperature (Husser et al. 2013)

detected with the lowest signal-to-noise making it difficult to say much about their structure 'by eye.'

Figure 9.4 shows the deprojected real visibility profiles for all eight disks in the sample. Since HD 109085 was imaged as a mosaic, we have only plotted the deprojected visibilities for the central pointing, which covers the bulk of the disk emission with some attenuation at the ansae. For both HD 38858 and HD 115617, the visibilities have been deprojected after the background sources have been subtracted (see discussion above). All of these profiles show the characteristic shape expected for a ring: a first null followed by subsequent ringing. The location of the first null is within 50 kλ for all sources, and within 25 kλ for six sources, emphasizing the need for short baselines when imaging similar debris disks.

We fit a simple point source model to each dataset using the `CASA` task `uvmodelfit` in order to constrain the flux density of the central star. To isolate the stellar emission, we fit only to the longer baselines > 30 kλ where the star is expected to dominate over the disk. The results are included in Table 9.3 (rightmost column). For HD 48682, the star is undetected, and we can only place a 3σ upper limit on its flux density of < 0.45 mJy. Two of these sources have measured stellar fluxes greatly in excess of the predicted photospheric flux: HD 22049 and HD 139664. We discussed the nature of the central emission in HD 22049 (ϵ Eridani) in Chapter 6, concluding that the excess is likely due to chromospheric emission from the star as has been seen for other Sun-like stars including α Cen A/B (Liseau et al. 2015, 2016). It is plausible that HD 139664 exhibits similar chromospheric emission. However, the flux at 1.3 mm for HD 139664 is $> 4\times$ the expected photospheric flux, compared to only $\sim 2\times$ for HD 22049. Observations at additional wavelengths may prove necessary to pin down the spectrum and origin of this bright central source.

10

Conclusions and Future Directions

September 2011 was both the month that I began graduate school at Harvard and the month that the results from the first proposal cycle (Cycle 0) of the Atacama Large Millimeter/submillimeter Array (ALMA) were announced. In fact, the ALMA program to observe AU Mic (Chapter 4 of this thesis) was approved while I was still considering whether I wanted to devote the first few years of my Ph.D. to studying debris disks. The prospect of new telescope data certainly helped make that decision easier! The Karl G. Jansky Very Large Array (VLA) also finished its decade-long upgrade in 2011, introducing a new correlator and expanded bandwidth coverage. It was an exciting time for the entire field of circumstellar disk science and for the growing 'Disk Group' at the Harvard-Smithsonian Center for Astrophysics (CfA). After six years, the landscape has changed dramatically. ALMA continues to grow in both baseline length and frequency coverage, enabling new science goals. The Submillimeter Array (SMA) has added the new SWARM correlator, quadrupling the available bandwidth. And, our once small 'Disk Group' has recently moved to a larger conference room to accommodate its growing membership.

As a graduate student, the early days of ALMA were an ideal time to get in on the ground floor of new science. With these new observations, came the challenge of handling, analyzing, and interpreting new datasets. The size of the files was much larger, and the sensitivity and resolution unprecedented. Indeed, a large portion of my first project in graduate school was spent building the modeling framework needed to obtain meaningful constraints on debris disk structure from the millimeter visibilities. This thesis has grown from that original project, applying the same modeling toolkit to new datasets and continuing to push the capabilities of the available telescopes. Section 10.1 summarizes the significant results from this work, organized by the three overarching questions presented in Chapter 1. In Section 10.2, we discuss ongoing and future work that follows from the results presented here.

10.1 Summary of Findings

The introduction of this thesis posed three related questions concerning debris disks and planetary system evolution:

1. How are wide-separation, substellar companions formed?
2. What is the physical nature of the collisional process in debris disks?
3. Can the structure and morphology of debris disks provide probes of planet formation and subsequent dynamical evolution?

In order to explore these questions, I have used spatially resolved observations at both millimeter and centimeter wavelengths to characterize the structure and

collisional evolution of debris disks, the end-stage of circumstellar disk evolution. While working with these data sets, I have developed a modeling framework (e.g. MacGregor et al. 2013) that fits parametric models to the observed millimeter visibilities within a Markov Chain Monte Carlo (MCMC) framework. Through this combination of observations and modeling, I have taken the first steps to answer these driving questions, providing a foundation for future work.

10.1.1 Formation of Wide-Separation, Substellar Companions

In the first section of this thesis, we consider formation scenarios for the population of directly imaged low-mass, wide-separation companions. Chapter 2 presents ALMA observations of GQ Lup, one of the best characterized examples of such systems. These new observations resolve a compact disk around the primary star, GQ Lup A, but do not detect any dust around the companion, GQ Lup b. We are able to place a robust upper limit on the dust mass of any circumplanetary disk of $< 0.04\ M_{\oplus}$, an order of magnitude below any previous ALMA measurements of circumstellar disks around sources with comparable ages ($\sim$ 2 Myr) and spectral types (M5 or later). Other studies have failed to detect circumplanetary disks around similar wide-separation companions (e.g. GSC 6214-210, Bowler et al. 2015). The lack of detections disfavors models of *in situ* formation through core fragmentation or gravitational instability, which predict massive circumplanetary disks that last for several Myrs. It is possible that these massive companions formed through binary fragmentation, or formed closer in and were subsequently scattered or migrated

outwards. However, recent ALMA observations with higher resolution do not reveal an inner gap or cavity in the GQ Lup circumprimary disk, making it unlikely for the system to contain a massive inner companion needed to scatter GQ Lup b out to its current position (Wu et al. 2017).

We also detect significant amounts of ^{12}CO and ^{13}CO gas in the circumprimary disk. Forward-modeling of the Keplerian velocity field allowed us to constrain both the mass of the primary star and the geometry of the circumprimary disk. The primary star is found to have a mass of $M_* = (1.03 \pm 0.05) * (d/156 \text{ pc}) \ M_\odot$, higher than the previously assumed mass of 0.7 $M_\odot$ from stellar evolutionary models. This result and other work (Czekala et al. 2015, 2016; Rosenfeld et al. 2013) illustrates the important role ALMA can play in determining the masses of young stars and constraining models of early stellar evolution. We determine an inclination for the disk of 60°, higher than previous estimates of $20 - 30°$, which implies a much larger physical separation for the companion of ~ 220 AU if it is on a coplanar orbit.

10.1.2 Probing Collisional Processes in Debris Disks

Chapter 3 presents the results from a survey to measure the long wavelength spectral indices of a sample of 15 debris disks using VLA and ATCA observations. With this sample, we were able to place the first observational constrains on the grain size distribution power law index, q, determining a weighted mean value of $\langle q \rangle = 3.36 \pm 0.02$. This result is most comparable to the classical prediction for a steady-state collisional cascade of $q = 3.50$ (Dohnanyi 1969) and to results from recent numerical models of individual debris disk systems (Löhne et al. 2012;

Schüppler et al. 2014, 2015). Models that allow the velocity to increase for decreasing particle size or that consider collisions between bodies not dominated by material strength produce shallower distributions with q-values between $\sim 3 - 3.5$ (e.g. Pan & Sari 2005).

We explored trends in our data with a number of system properties including age, gas content, and spectral type. Although we are limited by small number statistics, we note a tentative trend of steeper q-values for earlier spectral type stars. This scatter is plausibly explained by introducing a small size cutoff in the grain size distribution, which superimposes waves on the assumed power law distribution. Using a simple analytic model, we explored the impact of varying the blowout size (from $1 - 10$ μm) on the observed grain size distribution, and found a spread in the resulting dust opacity power law index comparable to the spread in our observed values. However, in realistic systems, inhomogeneity in the grain densities and fragmentation will likely smear out this 'wave-like' modulation. Recent observations by Moór et al. (2016) determine a q-value of 3.25 ± 0.07 for HD 48370, a K0V star, adding one more late spectral type star to the sample that seems to follow the observed trend. However, robust measurements of the grain size distribution for a larger sample of debris disks, especially around G–M type stars, will be critical to explore any trends further.

10.1.3 Resolving the Millimeter Structure of Debris Disks

Chapters 4 through 9 present resolved SMA and ALMA observations at millimeter wavelengths of individual debris disk systems. Our flexible MCMC modeling

framework has allowed us to place constraints on the position, width, surface density gradient, and asymmetries in these nearby debris disk systems. The bulk of the millimeter emission in all of these disks is consistent with the presence of a 'birth ring' of planetesimals where collisional erosion produces a power law size distribution of smaller dust grains.

The first system we examined with ALMA was AU Mic (Chapter 4), one of only a handful of debris disks known around an M-type star. This edge-on ring exhibits a rising radial surface brightness profile with power law index $x = 2.3 \pm 0.3$ that is sharply truncated at 40 AU. Assuming a temperature profile that falls off with radius as $r^{-0.5}$, this result implies a rising surface density profile possibly indicative of ongoing planet formation on the inner edge of the disk (Kenyon & Bromley 2008). The ALMA continuum image also revealed an unresolved central point source with a flux density of 0.32 ± 0.06 mJy, about 6× brighter than the expected photospheric flux. AU Mic was included in our sample of disks observed with the VLA (Chapter 3). These observations at centimeter wavelengths revealed strong radio emission from the star that is variable on timescales of minutes to months (Appendix A). Given the apparent stellar activity, we conclude that the bright central source in the ALMA image results from coronal emission (Cranmer et al. 2013).

SMA observations of HD 15115 (Chapter 5) revealed an edge-on disk extending from 43 to 110 AU with a flat surface density profile. Scattered light observations of this disk show a dramatic asymmetry; the western side of the disk extends nearly 2× farther from the star than the eastern side. Fitting a symmetric belt model to the SMA data leaves a 3σ residual along the western extent of the disk, aligned with the scattered light asymmetry. Like AU Mic, HD 15115 was included in our

sample of VLA disks. Although the disk was only moderately resolved by the VLA, the resulting image suggests the same asymmetric structure. The origin of this asymmetry is still unclear. Ram pressure stripping from interstellar gas could explain the scattered light features, but is unlikely to affect larger millimeter and centimeter sized grains. If this structure is confirmed by future high resolution millimeter observations, it could suggest that the disk is shaped by interior planets or other perturbers.

In Chapters 6 and 7 we discussed the ϵ Eridani and τ Ceti systems, the closest Sun-like stars to host debris disks. Both of these disks proved challenging to image, since their angular extent was larger than the primary beam of the telescopes used. The SMA observations of ϵ Eridani reveal a broad belt of emission at 64 AU with a fractional width of 0.3. ALMA observations of τ Ceti were unable to pinpoint the precise location of the belt inner edge, but place a strong lower limit on the fractional width of > 0.75. Both of these disks are notably broad compared to our own Kuiper Belt, which has a fractional width of 0.18. This observed diversity in belt widths may tell us something about the processes that shape debris disk structure. In order to produce a narrow belt, both the inner and outer edges must be maintained by gravitational perturbers or be confined by mean-motion resonances. Without any such mechanisms, a broad belt is the expected result. Both ϵ Eridani and τ Ceti also exhibit stellar emission in excess of photospheric predictions, which we attribute to emission from a hot stellar chromosphere as has been seen for other Sun-like stars including α Cen A/B (Liseau et al. 2015, 2016).

Fomalhaut is one of the most well-studied debris disk systems. Chapter 8 presents new ALMA mosaic observations of the Fomalhaut debris disk that provide

the first complete map of the outer belt at millimeter wavelengths with uniform sensitivity. These observations enabled the first conclusive detection of apocenter glow, a brightness asymmetry due to a surface density enhancement at apocenter resulting from the disk's significant eccentricity, $e = 0.12 \pm 0.01$. Given the high signal-to-noise of these observations, we developed a new MCMC modeling approach that accounts for the eccentric orbital parameters of particles within the disk. The belt has an inner edge of 136.3 ± 0.9 AU and width of 13.5 ± 1.8 AU, yielding a fractional width of 0.10 ± 0.01, much more radially confined than the ϵ Eridani and τ Ceti debris disks. This narrow, eccentric belt is likely shaped by interactions with interior and possibly exterior planets. We also note that the flux density of the star in these observations, 0.75 ± 0.02 mJy, is significantly lower than predictions from current photospheric models. It is especially critical to constrain the long wavelength stellar spectrum for Fomalhaut, since infrared observations indicate the presence of a warm inner dust belt that has yet to be resolved at any wavelength.

In Chapter 9 we present ongoing work to make the first comparative study of debris disk structures around nearby Sun-like stars. We have defined a sample of the eight brightest debris disks around FGK stars within 20 pc from previous *Herschel* programs, and assembled resolved millimeter observations from SMA or ALMA for all sources. The first images of these systems already show a range of disk structures. Several disks appear radially broad, and two show evidence for asymmetries (HD 10647 and HD 139664). In addition, two of these sources (HD 22049 and HD 139664) exhibit stellar emission greatly in excess of the predicted photospheric flux, possibly indicative of chromospheric emission.

10.2 Future Directions

Moving forward, new observational capabilities are continuing to present exciting opportunities to further the study of circumstellar disks and their connection to planetary systems. The millimeter observations of individual debris disk systems presented in this thesis hint at large-scale trends in disk structure and dynamics. However, definitive conclusions linking observed disk structure and planetary system evolution require high quality observations of a larger sample at both millimeter and complementary wavelengths. In 2018, NASA will launch the James Webb Space Telescope (JWST), which will revolutionize our ability to study debris disks at near- to mid-infrared wavelengths. Although there are many avenues to pursue, I highlight three possible driving questions for my future research here:

1. What is the dominant mechanism stirring debris disks around main sequence stars? Are they 'self-stirred' by outwardly moving fronts of planetoid growth, or are they 'planet-stirred' by the gravitational influence of giant planets?

2. Can we infer the presence of giant planets by their influence on the surrounding debris disks?

3. Does grain composition vary radially within debris disks? How is the grain composition connected to the gas content of the disk?

To answer these questions, I hope to leverage the multi-wavelength observational capabilities that both ALMA and JWST will provide in the coming years.

10.2.1 The First Comparative Study of Debris Disk Structure

We have already begun to tackle the question of what stirs debris disks, by assembling resolved millimeter observations for the sample of FGK star debris disks discussed in Chapter 9. We will characterize the millimeter emission from these eight systems by fitting parametric models directly to the visibility data, continuing to build on the techniques that we have developed and applied to SMA and ALMA observations in this thesis. By analyzing all datasets using identical methods, we will be able to make the first truly comparative study of planetesimal structures in nearby debris disks. In particular, we aim to place strong constraints on the location, width, surface density gradient, and edge shape of each disk in the sample. This formalism is easily adapted to consider any asymmetric structures that may be seen including clumps, centroid offsets, and pericenter or apocenter glow. Since we have detected the central star in all cases but one, we are able to robustly measure any offset between the disk centroid and the stellar position. We will also make use of numerical modeling (e.g. Nesvold et al. 2013) to place constraints on any wide-separation planets that remain undetected in these systems, but may be revealed by their influence on the structure of the surrounding disks.

In addition to the continuum observations presented in Chapter 9, we have also obtained observations of the ^{12}CO spectral line for all sources except HD 48682. The growing number of debris disks with gas detections (e.g. Dent et al. 2014) has prompted a debate over whether this material is primordial, remaining behind from the gas-rich protoplanetary disk phase, or secondary, released in collisions between

icy planetesimals. Although the disks in our sample have similar spectral types, they span a range of ages from 100's of Myrs to a few Gyrs suggesting differences in their evolutionary stages. Any detections of CO gas within this sample will certainly inform our understanding of where gas originates from in such old systems. Indeed, Marino et al. (2017) present a tentative detection of CO gas at $\sim$ 20 AU in the HD 109085 system, and suggest that material may be transported inwards from the outer dust belt.

The VLA observations presented in this thesis (Chapter 3) suggest tentative differences in the grain size distributions for A–F versus G–M stars. Pawellek et al. (2014) note a similar trend at shorter wavelengths and posit that the protoplanetary disks of more massive A stars may be more efficient at forming planets that can stir the debris disks at a later evolutionary stage. Given this observational evidence, a logical extension of this current survey of FGK stars is a similar comparative survey of debris disks around A-type stars. *Herschel* provides fairly complete statistics of A star debris disks within 50 pc, allowing us to formulate a complementary sample of the eight brightest nearby systems. ALMA and SMA archival data are already available for four of these sources through previous projects. We will propose to complete the sample in upcoming ALMA cycles, allowing us to begin to examine trends of debris disk properties with spectral type.

10.2.2 Planet–Disk Interactions in the ϵ Eridani and τ Ceti Systems

As part of this thesis (Chapter 6 and 7), we have completed the first millimeter wavelength maps of the two closest Sun-like stars to host debris disks: ϵ Eridani (3.22 pc, spectral type K2) and τ Ceti (3.65 pc, spectral type G8.5). The τ Ceti system, at 5.8 Gyr, is close in age to our Solar System, while ϵ Eridani, at $0.4 - 0.8$ Gyr, offers a glimpse of what our Solar System might have been like at an earlier stage in its evolution (Mamajek & Hillenbrand 2008). Both ϵ Eridani and τ Ceti are reported to also host planets within a few AU detected by radial velocity (RV) variations, although the effects of stellar activity have generated controversy about their veracity (Hatzes et al. 2000; Anglada-Escudé & Butler 2012; Tuomi et al. 2013). In the ϵ Eridani system, RV data suggest the presence of a Jupiter-mass planet with semi-major axis 3.4 AU. τ Ceti is purported to host a compact (semi-major axes < 1.5 AU) system of five super Earths. Lawler et al. (2014) use numerical simulations to show that the τ Ceti system could be stable with an additional giant planet on a wide orbit undetectable by the current RV data. The presence of such additional giant planets and their role in the dynamical evolution of both of these nearby systems could be revealed by their influence on the surrounding debris disks.

The first millimeter images presented here have set the stage for new observations with the higher sensitivity and resolution that ALMA can provide. In the most recent ALMA proposal cycle (Cycle 4), we were awarded time to observe both disks with the Atacama Compact Array (ACA) in Band 6 (1.3 mm). Observations with

the ACA provide the short (u, v) spacings needed to constrain the position of the first null in the visibility function, and thus the inner edge and surface density gradient of the disk. With these observations we aim to resolve the millimeter emission of the τ Ceti and ϵ Eridani debris disks and robustly measure: (1) the location of the disk inner and outer edges and their relation to the proposed planetary systems, (2) the radial emission gradient of the disks, (3) any offsets between the disk centroid and the central star, and (4) any azimuthal asymmetries. By combining these data with dynamical simulations, we hope to constrain the evolution of the planetesimal belts and place limits on the presence and properties of planets beyond the proposed radial velocity systems.

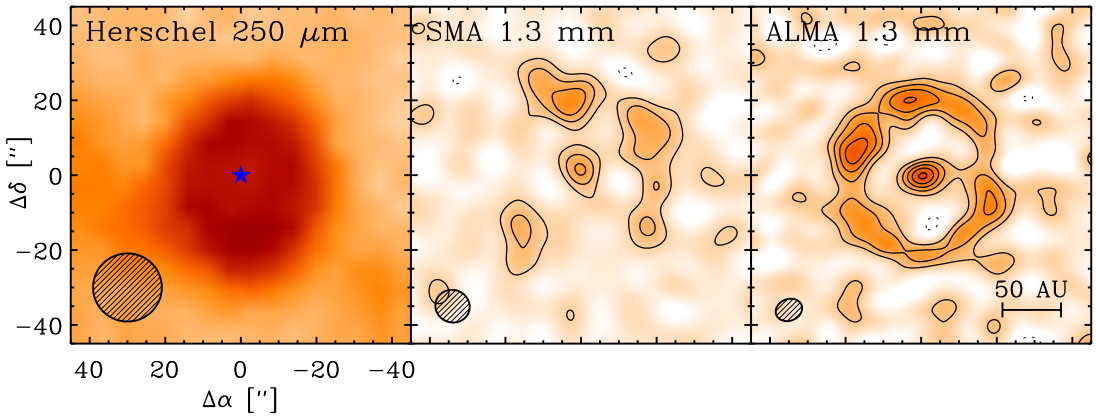

Figure 10.1: Comparison of previous observations of ϵ Eridani at 250 μm and 1.3 mm with *Herschel* (Greaves et al. 2014) and SMA (MacGregor et al. 2015b), with new ALMA observations at 1.3 mm. In the middle and right panels, contours are in steps of 2× the image rms noise of 0.2 mJy and 50 μJy, respectively. In the leftmost panel, the blue star symbol marks the stellar position. In the rightmost panel, the dashed gray circle in the lower left indicates the resolution. With these new observations, the disk is clearly detected at higher sensitivity and resolution than previous images allowing for much improved analysis and constraints on any additional planets.

These new data were taken in October–November 2016 and were just delivered in March 2017. The primary beam of the ACA is $\sim 44''$ at 1.3 mm. We cover the

entire τ Ceti disk in a single pointing. However, a small mosaic of seven pointings in a hexagonal pattern is needed to image the entire ϵ Eridani disk with uniform sensitivity. Imaging and further analysis of these data is ongoing. Figure 10.1 shows the *Herschel* 250 μm (Greaves et al. 2014) and SMA 1.3 mm (MacGregor et al. 2015b) images of the disk taken previously. The new ALMA ACA image at 1.3 mm is shown in the rightmost panel. With these new observations, the disk is clearly detected at $> 3\sigma$ around its entire circumference. We can now probe stellocentric offsets of $\lesssim 1''$ ($\lesssim 3$ AU), at least $3\times$ better than any previous observations, and approaching sensitivity to a true Uranus analog ($e = 0.05$). ϵ Eridani and τ Ceti are the closest potential analogues to our Solar System, and these detailed millimeter maps will act as 'Rosetta stones' for future larger surveys.

10.2.3 Multi-wavelength Observations with JWST

There is evidence that some debris disks have multiple components, namely distinct warm and cold belts in an architecture similar to that of the Solar System (e.g. Morales et al. 2011). One of the best studied examples is the HR 8799 system, which exhibits both warm and cold dust belts (e.g. Su et al. 2009) with four giant planets between them (Marois et al. 2008, 2010). Observations at millimeter wavelengths provide the best sensitivity to cold grains located farther away from the central star (see Figure 10.2). Close to the star, the temperature is hotter and the dust grains emit predominantly at shorter near- to mid-infrared wavelengths. As a result, observations of debris disks at mid-infrared wavelengths ($5 - 35$ μm) provide the best probe of the properties of warm dust in the habitable zones of Sun-like stars.

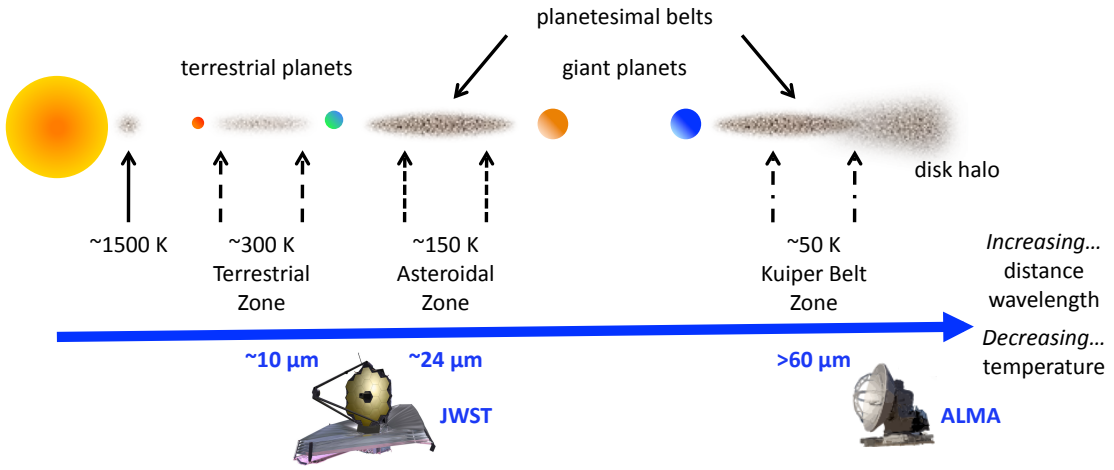

Figure 10.2: Schematic of multiple belt structure in a debris disk. Temperature decreases moving away from the star and grains emit predominantly at longer wavelengths. Observations with both ALMA and JWST probe different disk regions, providing complimentary information on disk structure.

Mid-infrared observations of debris disks have the power to not only resolve structure, but also constrain the composition, size, and crystalline fraction of grains in the disk through silicate emission features at 10 and 20 μm. Previous results suggest that the grains in debris disks may be compositionally diverse reflecting differing phases of planetary system evolution (e.g. Chen et al. 2006; Weinberger et al. 2011). Lisse et al. (2009) model the mid-infrared spectrum of HD 172555 ($\sim$ 24 Myr-old) with high-temperature and high-pressure polymorphs of silica that may indicate a recent massive collision, maybe similar to the collision thought to have formed the Moon early in the Solar System's evolution. In contrast, the η Corvi system ($\sim$ 1 Gyr-old) exhibits features of water and carbon-rich materials (Lisse et al. 2012), drawing comparison to the period of Late Heavy Bombardment (Nesvorný et al. 2010). In the well-known β Pictoris debris disk, observations indicate that grain properties within the disk may vary with increasing distance

from the central star (e.g. Weinberger et al. 2003). Recent work by Mittal et al. (2015) shows significant variations in the disk structure and dust composition of debris disks within the Sco-Cen association. Since these stars are likely coeval and formed in the same birth environment, these compositional differences may point to a diversity in planet formation and evolution within these systems.

Leveraging the multi-wavelength capabilities of both ALMA and JWST over the next several years will certainly provide many new insights into the structure and evolution of debris disks and planetary systems. In particular, mid-infrared observations with JWST will allow us to explore: (1) radial variation in grain composition within debris disks, (2) connections between grain composition and gas content, and (3) evidence for evolution or recent collisions. By combining mid-infrared observations from JWST with resolved millimeter imaging from ALMA, we will have an independent constraint on the spectral index of the disk and thus the grain size distribution, which will help break known degeneracies between grain composition and size distribution in debris disks.

A key instrument on JWST for debris disk studies will be the Mid-Infrared Instrument (MIRI). Coronagraphic imaging at 15.5 and 23 μm, will allow us to image faint disk structures close to the star that have been unresolvable until now. The inner working angle of the MIRI coronagraph is $\sim 0.5''$ at 15.5 μm, making it possible to resolve an inner dust belt at a few AU in nearby systems. Spectroscopy at mid-infrared wavelengths will cover a wealth of amorphous and crystalline spectral features, as well as several rotational lines of H_2 between 10 and 28 μm (Thi et al. 2001). Observations of both gas and silicates in a debris disk will allow us to draw connections between the distribution of solids and gas within disks, and constrain

the make-up of planetary building blocks. The results from JWST will certainly be transformational for the study of circumstellar disks, providing the first glimpse of the inner regions (< 30 AU) of debris disk systems that are virtually unexplored.

The work presented in this thesis has resulted in the first resolved millimeter images of several notable debris disk systems (AU Mic, HD 15115, ϵ Eridani, τ Ceti, and Fomalhaut). By fitting models directly to the millimeter visibilities within an MCMC framework, we have placed strong constraints on the underlying planetesimal structure of these systems. These results further our understanding of the ongoing collisional process in debris disks and their dynamical evolution. Furthermore, these nearby debris disks are the cornerstone templates for the interpretation of more distant, less accessible systems, and they will provide context for our ongoing comparative surveys of larger samples. In the future, we will leverage the capabilities of next-generation telescopes including ALMA and JWST to take the next steps towards linking the observed structure of debris disks and planetary system evolution. Perhaps the resolved structure of debris disks will enable the detection of new wide-separation exoplanets that would otherwise remain undetectable by current methods.

A

Radio Light Curves of AU Mic

AU Mic is an active M dwarf star that is known to exhibit radio-wave bursts. In quiescence, previous observations placed upper limits on the flux at radio wavelengths, $<$ 120 μJy at 3.6 cm (White et al. 1994; Leto et al. 2000). Recent ALMA observations of the system at 1.3 mm revealed a compact central emission peak with a flux of $\sim$ 320 μJy in addition to the continuum dust emission from the debris belt and greatly in excess of the expected photospheric flux at this long wavelength. Cranmer et al. (2013) model this excess emission as arising from a hot stellar corona. Schüppler et al. (2015) suggest that chromospheric emission from the star could also contribute at millimeter and radio wavelengths.

These new VLA observations of AU Mic offer a unique glimpse at the variations in radio emission from the star on minute to month-long timescales. Observations were taken at 9 mm (Ka band) in the DnC configuration on May 9 and 11, 2013 and in the C configuration on June 21, 2013. Each of the three scheduling blocks (SBs) was a total of 105 minutes in length. Observations of AU Mic were interleaved with the gain calibrator, J2101-2933, in a 4 minute cycle, with 3 minutes on-source.

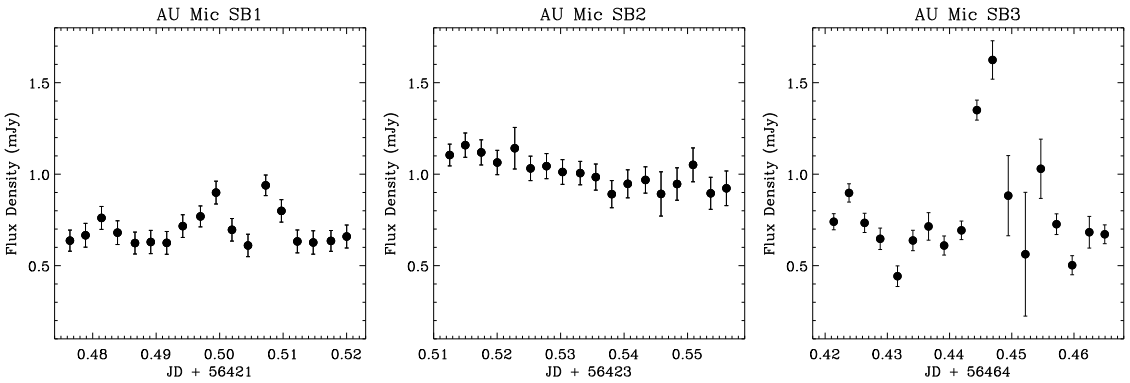

Figure A.1: Stellar light curves for AU Mic showing the variation in flux density over the course of our three observations. The flux density was determined for each 3 minute integration using the `CASA` task `uvmodelfit` to fit a point source model to the visibilities.

Figure A.1 shows the stellar light curves for each of the three SBs. To determine the flux density, we used the `CASA` task `uvmodelfit` to fit a point source model to the visibilities from each 3 minute on-source integration. There is strong radio emission from the star present in all 3 SBs with a flux of $0.5 - 1.5$ mJy. During the third SB, the star appears to have flared strongly, increasing in brightness by $100 - 150\%$.

Cranmer et al. (2013) simulated the time-steady coronal emission of AU Mic in both X-ray and millimeter bands, but they did not account for time variability. In order to begin to estimate the relative enhancements in the coronal emission during flare times, we re-ran the Cranmer et al. (2013) model for a range of imposed variations in the coronal heating. We assumed that a fractional filling factor, f, of the coronal volume was occupied by flare-like plasma, and that the photospheric driving velocity, $v_\perp$, of MHD turbulence was enhanced by a dimensionless factor, ξ, in that region. Thus, for a range of input parameters ($f \leq 1$, $\xi \geq 1$) we simulated both the total X-ray luminosity, $L_{\rm X}$, and the thermal free-free emission, I_ν, at the

observed VLA wavelength of 9 mm. The goal was to find a combination of plausible f and ξ values that would produce a relative enhancement in $L_{\rm X}$ of order 30% to 60% (to match the flare amplitudes reported by Smith et al. 2005; Mitra-Kraev et al. 2005; Schneider & Schmitt 2010) simultaneously with an increase in the 9 mm continuum of order $100 - 150\%$ (see Figure A.1).

To match the observed ranges of flux density enhancement, we found that the filling factor f must be larger than 0.48, and the boundary velocity enhancement factor ξ must be within the range of $4.1 - 8.2$. These values of ξ correspond to an increase in the total nonthermal energy input of order $20 - 70$ in the flare regions. The maximum enhanced temperature in this subset of models was found to be about 13 MK. This is reminiscent of the hottest of the three temperature components (3.37, 7.78, and 17.3 MK) inferred from *Chandra* spectra of AU Mic by Schneider & Schmitt (2010). The quiescent model of Cranmer et al. (2013) successfully predicted temperatures between the two lower *Chandra* values, but the largest value appeared to be explainable only by flare activity.

A better understanding of cool-star flare activity will depend on broader observational coverage in both time and wavelength. *Kepler* has opened up new vistas of study of how properties of white-light "superflares" on active stars may relate to the more familiar case of the Sun (Maehara et al. 2015). However, recent multi-wavelength surveys of M and K dwarf exoplanet host stars (e.g., France et al. 2015) are also revealing new information about weak flares that do not manifest at visible wavelengths. For the better-resolved case of the Sun, recent observations and simulations show that nearly *all* coronal heating activity may take the form of a distribution of flare events with a range of strengths and timescales (Fletcher et al.

2015). Even models that invoke MHD waves and turbulence appear to require the spontaneous production of nanoflare-like magnetic reconnection events as a final product of the cascade from large to small eddies (e.g., Osman et al. 2011; Velli et al. 2015).

B

Primary Beam Structure of the SMA

The SMA is composed of eight essentially identical antennas, each 6 meters in diameter. The SMA primary beam is thus the power pattern of one antenna. While the primary beam shape is often assumed to be a simple Gaussian, the actual shape is determined by illumination with a 10 dB taper at the edge of the primary dish, as well as blockage due to the secondary mirror. With these considerations, the beam power as a function of offset (in arcseconds) from the beam center is given by

$$P(x) = \left[\int_{R_p}^{R_s} 2\pi r J_0 \left(\frac{2\pi r x}{\lambda} \right) J_0 \left(\frac{1.840839 r}{R_p} \right) \right]^2 dr \qquad \text{(B.1)}$$

where, R_p is the radius of the primary dish in meters, R_s is the radius of the secondary dish in meters, and x is the offset from the dish center in radians. A complete profile of the beam power can be built up using Equation B.1 at discrete offset positions. Note that this expression does not take into account additional practical factors, such as receiver alignment, pointing jitter, and departures from perfect focus, which act to distort the primary beam shape.

Since the emission extent of the ϵ Eridani disk is comparable to the half power size of the SMA primary beam pattern, we constructed a complete beam model for use in our modeling procedure. The FWHM of accurate beam models for the LSB (218.9 GHz) and USB (230.9 GHz) are $53\farcs6$ and $50\farcs8$, respectively. For comparison, the FWHM for a uniformly illuminated circular aperture antenna is given by $1.22\lambda/D_A$, where D_A is the antenna diameter. For the SMA antennas, this predicts $50\farcs4$ and $47\farcs4$, for the LSB and USB, respectively, narrower than the FWHM of the accurate beam models. Note that tasks within the Miriad software package assume a Gaussian beam for the SMA with a FWHM given by a uniformly illuminated circular aperture.

C

MCMC Fits to Fomalhaut ALMA Visibilities

Following the modeling approach taken throughout this thesis (e.g. MacGregor et al. 2013, 2016a), we evaluated the model visibilities generated from our eccentric disk model within a Markov Chain Monte Carlo (MCMC) framework. To do this, we made use of the python package `emcee` (Foreman-Mackey et al. 2013). The best-fit model parameters and their corresponding 1σ (68%) uncertainties are listed in Table 8.2. In Figure C.1 we show the full output from $\sim 10^4$ MCMC trials. The diagonal panels show the 1D projections of the posterior probability distribution determined by marginalizing over all other parameters. In each panel, the dashed vertical lines indicate the best-fit parameter values and 1σ uncertainties. The off-diagonal panels show the 2D projections of the posterior probability distribution, or the joint probability distributions for each pair of parameters. In these panels, the contours indicate the 1σ, 2σ, and 3σ regions for each parameter pair. These regions are determined by assuming normally distributed errors, where the probability that

a measurement has a distance less than a from the mean value is given by erf $\left(\frac{a}{\sigma\sqrt{2}}\right)$.

This eccentric model provides a good fit to the ALMA visibilities with a reduced chi-squared $\chi^2 = 1.1$. The 1D histograms show symmetric, Gaussian distributions. Some parameter degeneracies are evident as diagonal contours in the 2D joint probability distributions, as is seen in the pairing between the disk inclination, i, and semi-major axis, $R_{\rm belt}$.

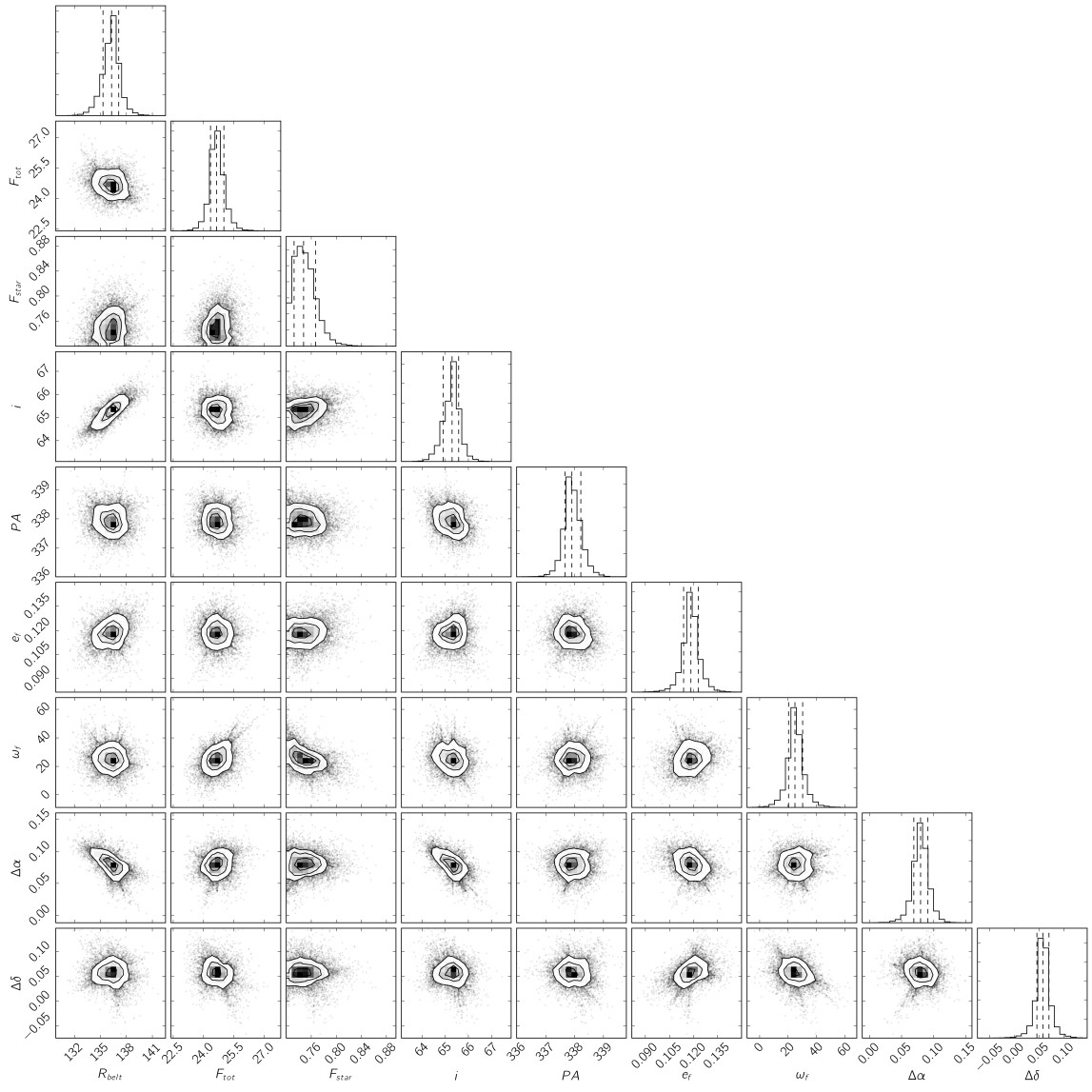

Figure C.1: The 1D (diagonal panels) and 2D (off-diagonal panels) projections of the posterior probability distributions for the best-fit eccentric model parameters. For each parameter, the 1D histogram is determined by marginalizing over all other model parameters. The dashed vertical lines indicate the best-fit values and 1σ uncertainties (listed in Table 8.2). The 2D joint probability distributions show the 1σ, 2σ, and 3σ regions for all parameter pairs.

References

Acke, B., et al. 2012, A&A, 540, A125

Alcalá, J. M., et al. 2014, A&A, 561, A2

ALMA Partnership et al. 2015, ApJ, 808, L3

Andrews, S. M., Rosenfeld, K. A., Kraus, A. L., & Wilner, D. J. 2013, ApJ, 771, 129

Andrews, S. M., & Williams, J. P. 2007, ApJ, 659, 705

Andrews, S. M., et al. 2016, ApJ, 820, L40

Anglada-Escudé, G., & Butler, R. P. 2012, ApJS, 200, 15

Ansdell, M., et al. 2016, ArXiv e-prints

Apai, D., et al. 2008, ApJ, 672, 1196

Ardila, D. R., et al. 2004, ApJ, 617, L147

Asphaug, E., & Benz, W. 1996, Icarus, 121, 225

Aufdenberg, J. P., Hauschildt, P. H., Baron, E., Nordgren, T. E., Burnley, A. W., Howarth, I. D., Gordon, K. D., & Stansberry, J. A. 2002, ApJ, 570, 344

Augereau, J.-C., & Beust, H. 2006, A&A, 455, 987

Augereau, J.-C., & *Herschel*/DUNES Team. 2010, in In the Spirit of Lyot 2010

Augereau, J. C., Nelson, R. P., Lagrange, A. M., Papaloizou, J. C. B., & Mouillet, D. 2001, A&A, 370, 447

Aumann, H. H. 1985, PASP, 97, 885

Aumann, H. H., et al. 1984, ApJ, 278, L23

Ayliffe, B. A., & Bate, M. R. 2009, MNRAS, 397, 657

Backman, D., et al. 2009, ApJ, 690, 1522

Backman, D. E., & Paresce, F. 1993, in Protostars and Planets III, ed. E. H. Levy & J. I. Lunine, 1253–1304

Baddour, N. 2009, Journal of the Optical Society of America A, 26, 1767

Bailey, V., et al. 2013, ApJ, 767, 31

Baines, E. K., & Armstrong, J. T. 2012, ApJ, 744, 138

Bannister, M. T., et al. 2015, ArXiv e-prints

Bate, M. R. 2012, MNRAS, 419, 3115

Bate, M. R., Bonnell, I. A., & Bromm, V. 2003, MNRAS, 339, 577

Beckwith, S., Gatley, I., Matthews, K., & Neugebauer, G. 1978, ApJ, 223, L41

Beckwith, S. V. W., Sargent, A. I., Chini, R. S., & Guesten, R. 1990, AJ, 99, 924

Benz, W., & Asphaug, E. 1999, Icarus, 142, 5

Bernstein, G. M., Trilling, D. E., Allen, R. L., Brown, M. E., Holman, M., & Malhotra, R. 2004, AJ, 128, 1364

Beust, H., et al. 2014, A&A, 561, A43

Biller, B. A., et al. 2015, MNRAS, 450, 4446

Binks, A. S., & Jeffries, R. D. 2014, MNRAS, 438, L11

Blitz, L. 1993, in Protostars and Planets III, ed. E. H. Levy & J. I. Lunine, 125–161

Boccaletti, A., et al. 2012, A&A, 544, A85

—. 2015, Nature, 526, 230

Bock, D. C.-J., et al. 2006, in Proc. SPIE, Vol. 6267, Society of Photo-Optical Instrumentation Engineers (SPIE) Conference Series, 626713

Boley, A. C. 2009, ApJ, 695, L53

Boley, A. C., Hayfield, T., Mayer, L., & Durisen, R. H. 2010, Icarus, 207, 509

Boley, A. C., Payne, M. J., Corder, S., Dent, W. R. F., Ford, E. B., & Shabram, M. 2012, ApJ, 750, L21

Booth, M., et al. 2013, MNRAS, 428, 1263

Boss, A. P. 2006, ApJ, 637, L137

Bottke, W. F., Durda, D. D., Nesvorný, D., Jedicke, R., Morbidelli, A., Vokrouhlický, D., & Levison, H. F. 2005, Icarus, 179, 63

Bower, G. C., Bolatto, A., Ford, E. B., & Kalas, P. 2009, ApJ, 701, 1922

Bowler, B. P., Andrews, S. M., Kraus, A. L., Ireland, M. J., Herczeg, G., Ricci, L., Carpenter, J., & Brown, M. E. 2015, ApJ, 805, L17

Bowler, B. P., Liu, M. C., Kraus, A. L., & Mann, A. W. 2014, ApJ, 784, 65

Bowler, B. P., Liu, M. C., Kraus, A. L., Mann, A. W., & Ireland, M. J. 2011, ApJ, 743, 148

Boyajian, T. S., et al. 2013, ApJ, 771, 40

Brittain, S. D., & Rettig, T. W. 2002, Nature, 418, 57

Broeg, C., Schmidt, T. O. B., Guenther, E., Gaedke, A., Bedalov, A., Neuhäuser, R., & Walter, F. M. 2007, A&A, 468, 1039

Brown, A., Jordan, C., Millar, T. J., Gondhalekar, P., & Wilson, R. 1981, Nature, 290, 34

Bryan, M. L., Bowler, B. P., Knutson, H. A., Kraus, A. L., Hinkley, S., Mawet, D., Nielsen, E. L., & Blunt, S. C. 2016, ApJ, 827, 100

Burns, J. A., Lamy, P. L., & Soter, S. 1979, Icarus, 40, 1

Butler, B. 2012, ALMA Memo Series, 594

Butler, R. P., et al. 2006, ApJ, 646, 505

Caceres, C., et al. 2015, ApJ, 806, L22

Campo Bagatin, A., Cellino, A., Davis, D. R., Farinella, P., & Paolicchi, P. 1994, Planet. Space Sci., 42, 1079

Canup, R. M., & Ward, W. R. 2006, Nature, 441, 834

Carniani, S., et al. 2015, A&A, 584, A78

Carpenter, J. M., Wolf, S., Schreyer, K., Launhardt, R., & Henning, T. 2005, AJ, 129, 1049

Casagrande, L., Schönrich, R., Asplund, M., Cassisi, S., Ramírez, I., Meléndez, J., Bensby, T., & Feltzing, S. 2011, A&A, 530, A138

Chauvin, G., Lagrange, A.-M., Dumas, C., Zuckerman, B., Mouillet, D., Song, I., Beuzit, J.-L., & Lowrance, P. 2005, A&A, 438, L25

Chavez-Dagostino, M., et al. 2016, MNRAS, 462, 2285

Chen, C. H., et al. 2005, ApJ, 634, 1372

—. 2006, ApJS, 166, 351

Chenu, J.-Y., et al. 2016, IEEE Transactions on Terahertz Science and Technology, 6, 223

Chiang, E., Kite, E., Kalas, P., Graham, J. R., & Clampin, M. 2009, ApJ, 693, 734

Choquet, É., et al. 2015, ArXiv e-prints

Clampin, M., et al. 2003, AJ, 126, 385

Comerón, F. 2008, The Lupus Clouds, ed. B. Reipurth, 295

Cranmer, S. R., Wilner, D. J., & MacGregor, M. A. 2013, ApJ, 772, 149

Crida, A., Masset, F., & Morbidelli, A. 2009, ApJ, 705, L148

Currie, T., & Kenyon, S. J. 2009, AJ, 138, 703

Currie, T., et al. 2012a, ApJ, 760, L32

—. 2012b, ApJ, 757, 28

Czekala, I., Andrews, S. M., Jensen, E. L. N., Stassun, K. G., Torres, G., & Wilner, D. J. 2015, ApJ, 806, 154

Czekala, I., Andrews, S. M., Torres, G., Jensen, E. L. N., Stassun, K. G., Wilner, D. J., & Latham, D. W. 2016, ApJ, 818, 156

Dahm, S. E., & Carpenter, J. M. 2009, AJ, 137, 4024

Dai, Y., Wilner, D. J., Andrews, S. M., & Ohashi, N. 2010, AJ, 139, 626

D'Alessio, P., Calvet, N., & Hartmann, L. 2001, ApJ, 553, 321

Dawson, R. I., Johnson, J. A., Morton, T. D., Crepp, J. R., Fabrycky, D. C., Murray-Clay, R. A., & Howard, A. W. 2012, ApJ, 761, 163

Debes, J. H., & Sigurdsson, S. 2006, A&A, 451, 351

Debes, J. H., Weinberger, A. J., & Kuchner, M. J. 2009, ApJ, 702, 318

Debes, J. H., Weinberger, A. J., & Song, I. 2008, ApJ, 684, L41

Defrère, D., et al. 2015, ApJ, 799, 42

Deller, A. T., & Maddison, S. T. 2005, ApJ, 625, 398

Delorme, P., Lagrange, A. M., Chauvin, G., Bonavita, M., Lacour, S., Bonnefoy, M., Ehrenreich, D., & Beust, H. 2012, A&A, 539, A72

Dent, W. R. F., Greaves, J. S., & Coulson, I. M. 2005, MNRAS, 359, 663

Dent, W. R. F., et al. 2014, Science, 343, 1490

Desidera, S., et al. 2011, A&A, 529, A54

di Folco, E., et al. 2007, A&A, 475, 243

Dohnanyi, J. S. 1969, J. Geophys. Res., 74, 2531

Donati, J.-F., et al. 2012, MNRAS, 425, 2948

Draine, B. T. 2006, ApJ, 636, 1114

Duchêne, G., et al. 2014, ApJ, 784, 148

Dullemond, C. P. 2012, RADMC-3D: A multi-purpose radiative transfer tool, Astrophysics Source Code Library

Dullemond, C. P., & Dominik, C. 2004, A&A, 417, 159

Dunham, M. M., et al. 2014, Protostars and Planets VI, 195

Eiroa, C., et al. 2013, A&A, 555, A11

Elmegreen, B. G., & Lada, C. J. 1977, ApJ, 214, 725

Ertel, S., Wolf, S., & Rodmann, J. 2012, A&A, 544, A61

Faber, P., & Quillen, A. C. 2007, MNRAS, 382, 1823

Fisher, R. T. 2004, ApJ, 600, 769

Fitzgerald, M. P., Kalas, P. G., Duchêne, G., Pinte, C., & Graham, J. R. 2007, ApJ, 670, 536

Flaherty, K. M., et al. 2016, ApJ, 818, 97

Fletcher, L., Cargill, P. J., Antiochos, S. K., & Gudiksen, B. V. 2015, Space Sci. Rev., 188, 211

Foreman-Mackey, D. 2016, The Journal of Open Source Software, 24

Foreman-Mackey, D., Hogg, D. W., Lang, D., & Goodman, J. 2013, PASP, 125, 306

Foreman-Mackey, D., Hogg, D. W., Lang, D., & Weare, J. 2012, arXiv:1202.3665

France, K., Parke Loyd, R. O., & Brown, A. 2015, IAU General Assembly, 22, 28599

Galicher, R., Marois, C., Zuckerman, B., & Macintosh, B. 2013, ApJ, 769, 42

Gáspár, A., Psaltis, D., Özel, F., Rieke, G. H., & Cooney, A. 2012, ApJ, 749, 14

Gáspár, A., Psaltis, D., Rieke, G. H., & Özel, F. 2012, ApJ, 754, 74

Geers, V. C., Gorti, U., Meyer, M. R., Mamajek, E., Benz, A. O., & Hollenbach, D. 2012, ApJ, 755, 8

Ginski, C., Schmidt, T. O. B., Mugrauer, M., Neuhäuser, R., Vogt, N., Errmann, R., & Berndt, A. 2014, MNRAS, 444, 2280

Gladman, B., Kavelaars, J. J., Nicholson, P. D., Loredo, T. J., & Burns, J. A. 1998, AJ, 116, 2042

Golimowski, D. A., et al. 2006, AJ, 131, 3109

Gomes, R., Levison, H. F., Tsiganis, K., & Morbidelli, A. 2005, Nature, 435, 466

Goodman, J., & Weare, J. 2010, Commun. Appl. Math. Comput. Sci., 5, 65

Goto, M., Usuda, T., Dullemond, C. P., Henning, T., Linz, H., Stecklum, B., & Suto, H. 2006, ApJ, 652, 758

Graham, J. R., Kalas, P. G., & Matthews, B. C. 2007, ApJ, 654, 595

Greaves, J. S., Hales, A. S., Mason, B. S., & Matthews, B. C. 2012, MNRAS, 423, L70

Greaves, J. S., Wyatt, M. C., Holland, W. S., & Dent, W. R. F. 2004, MNRAS, 351, L54

Greaves, J. S., et al. 1998, ApJ, 506, L133

—. 2005, ApJ, 619, L187

—. 2014, ApJ, 791, L11

Gudel, M. 1992, A&A, 264, L31

Guenther, E. W., Neuhäuser, R., Wuchterl, G., Mugrauer, M., Bedalov, A., & Hauschildt, P. H. 2005, Astronomische Nachrichten, 326, 958

Guilloteau, S. 1994, in Astronomical Society of the Pacific Conference Series, Vol. 59, IAU Colloq. 140: Astronomy with Millimeter and Submillimeter Wave Interferometry, ed. M. Ishiguro & J. Welch, 27–34

Habing, H. J., et al. 2001, A&A, 365, 545

Hahn, J. M., & Malhotra, R. 2005, AJ, 130, 2392

Halliday, A. N., & Kleine, T. 2006, Meteorites and the Timing, Mechanisms, and Conditions of Terrestrial Planet Accretion and Early Differentiation, ed. D. S. Lauretta & H. Y. McSween, 775–801

Harper, G. M., O'Riain, N., & Ayres, T. R. 2013, MNRAS, 428, 2064

Hatsukade, B., Ohta, K., Seko, A., Yabe, K., & Akiyama, M. 2013, ApJ, 769, L27

Hatzes, A. P., et al. 2000, ApJ, 544, L145

Hauschildt, P. H., Allard, F., Ferguson, J., Baron, E., & Alexander, D. R. 1999, ApJ, 525, 871

Heap, S. R., Lindler, D. J., Lanz, T. M., Cornett, R. H., Hubeny, I., Maran, S. P., & Woodgate, B. 2000, ApJ, 539, 435

Heller, R., et al. 2014, Astrobiology, 14, 798

Herczeg, G. J., & Hillenbrand, L. A. 2014, ApJ, 786, 97

Hildebrand, R. H. 1983, QJRAS, 24, 267

Hillenbrand, L. A., et al. 2008, ApJ, 677, 630

Hines, D. C., et al. 2007, ApJ, 671, L165

Ho, P. T. P., Moran, J. M., & Lo, K. Y. 2004, ApJ, 616, L1

Hodge, J. A., et al. 2013, ApJ, 768, 91

Hogerheijde, M. R., Bekkers, D., Pinilla, P., Salinas, V. N., Kama, M., Andrews, S. M., Qi, C., & Wilner, D. J. 2016, A&A, 586, A99

Holland, W. S., et al. 1998, Nature, 392, 788

—. 2003, ApJ, 582, 1141

Holmberg, J., Nordström, B., & Andersen, J. 2009, A&A, 501, 941

Housen, K. R., & Holsapple, K. A. 1999, Icarus, 142, 21

Hughes, A. M., Wilner, D. J., Andrews, S. M., Williams, J. P., Su, K. Y. L., Murray-Clay, R. A., & Qi, C. 2011, ApJ, 740, 38

Hughes, A. M., Wilner, D. J., Kamp, I., & Hogerheijde, M. R. 2008, ApJ, 681, 626

Hughes, A. M., et al. 2012, ApJ, 750, 82

Hughes, J., Hartigan, P., Krautter, J., & Kelemen, J. 1994, AJ, 108, 1071

Husser, T.-O., Wende-von Berg, S., Dreizler, S., Homeier, D., Reiners, A., Barman, T., & Hauschildt, P. H. 2013, A&A, 553, A6

Ida, S., Bryden, G., Lin, D. N. C., & Tanaka, H. 2000, ApJ, 534, 428

Ireland, M. J., Kraus, A., Martinache, F., Law, N., & Hillenbrand, L. A. 2011, ApJ, 726, 113

Isella, A., Chandler, C. J., Carpenter, J. M., Pérez, L. M., & Ricci, L. 2014, ApJ, 788, 129

Isella, A., Pérez, L. M., Carpenter, J. M., Ricci, L., Andrews, S., & Rosenfeld, K. 2013, ApJ, 775, 30

Ishihara, D., et al. 2010, A&A, 514, A1

Jackson, A. P., Wyatt, M. C., Bonsor, A., & Veras, D. 2014, MNRAS, 440, 3757

Jackson, J. M., Finn, S. C., Chambers, E. T., Rathborne, J. M., & Simon, R. 2010, ApJ, 719, L185

Jansky, K. G. 1933, Nature, 132, 66

Janson, M., Quanz, S. P., Carson, J. C., Thalmann, C., Lafrenière, D., & Amara, A. 2015, A&A, 574, A120

Jenkins, J. S., et al. 2013, ApJ, 766, 67

Jewitt, D. C., & Luu, J. X. 2000, Protostars and Planets IV, 1201

Jewitt, D. C., & Sheppard, S. S. 2002, AJ, 123, 2110

Jiang, I.-G., Laughlin, G., & Lin, D. N. C. 2004, AJ, 127, 455

Kalas, P., Deltorn, J.-M., & Larwood, J. 2001, ApJ, 553, 410

Kalas, P., Fitzgerald, M. P., & Graham, J. R. 2007, ApJ, 661, L85

Kalas, P., Graham, J. R., & Clampin, M. 2005, Nature, 435, 1067

Kalas, P., Graham, J. R., Clampin, M. C., & Fitzgerald, M. P. 2006, ApJ, 637, L57

Kalas, P., Graham, J. R., Fitzgerald, M. P., & Clampin, M. 2013, ApJ, 775, 56

Kalas, P., & Jewitt, D. 1995, AJ, 110, 794

Kalas, P., Liu, M. C., & Matthews, B. C. 2004, Science, 303, 1990

Kalas, P., et al. 2008, Science, 322, 1345

Karim, A., et al. 2013, MNRAS, 432, 2

Kennedy, G. M., & Wyatt, M. C. 2010, MNRAS, 405, 1253

—. 2011, MNRAS, 412, 2137

Kennedy, G. M., et al. 2015a, ApJS, 216, 23

—. 2015b, MNRAS, 449, 3121

Kenyon, S. J., & Bromley, B. C. 2002, ApJ, 577, L35

—. 2008, ApJS, 179, 451

—. 2016, ApJ, 817, 51

Kenyon, S. J., Currie, T., & Bromley, B. C. 2014, ApJ, 786, 70

Kharchenko, N. V., & Roeser, S. 2009, VizieR Online Data Catalog, 1280

Kóspál, Á., et al. 2013, ApJ, 776, 77

Kral, Q., Thébault, P., & Charnoz, S. 2013, A&A, 558, A121

Kratter, K. M., Murray-Clay, R. A., & Youdin, A. N. 2010, ApJ, 710, 1375

Kraus, A. L., Andrews, S. M., Bowler, B. P., Herczeg, G., Ireland, M. J., Liu, M. C., Metchev, S., & Cruz, K. L. 2015, ApJ, 798, L23

Kraus, A. L., Ireland, M. J., Cieza, L. A., Hinkley, S., Dupuy, T. J., Bowler, B. P., & Liu, M. C. 2014, ApJ, 781, 20

Krist, J. E., Stapelfeldt, K. R., Bryden, G., & Plavchan, P. 2012, AJ, 144, 45

Krist, J. E., et al. 2005, AJ, 129, 1008

—. 2010, AJ, 140, 1051

Krivov, A. V. 2007, Dust in Planetary Systems, 643, 123

Krivov, A. V., Herrmann, F., Brandeker, A., & Thébault, P. 2009, A&A, 507, 1503

Krivov, A. V., Löhne, T., & Sremčević, M. 2006, A&A, 455, 509

Krivov, A. V., Queck, M., Löhne, T., & Sremčević, M. 2007, A&A, 462, 199

Krivov, A. V., et al. 2013, ApJ, 772, 32

Kuchner, M. J., & Holman, M. J. 2003, ApJ, 588, 1110

Kuchner, M. J., & Stark, C. C. 2010, AJ, 140, 1007

Kundu, M. R., Jackson, P. D., White, S. M., & Melozzi, M. 1987, ApJ, 312, 822

Lafrenière, D., Jayawardhana, R., & van Kerkwijk, M. H. 2008, ApJ, 689, L153

Lagrange, A.-M., et al. 2010, Science, 329, 57

Lambrechts, M., & Johansen, A. 2012, A&A, 544, A32

Larwood, J. D., & Kalas, P. G. 2001, MNRAS, 323, 402

Lavigne, J.-F., Doyon, R., Lafrenière, D., Marois, C., & Barman, T. 2009, ApJ, 704, 1098

Lawler, S. M., Greenstreet, S., & Gladman, B. 2015, ApJ, 802, L20

Lawler, S. M., et al. 2009, ApJ, 705, 89

—. 2014, MNRAS, 444, 2665

Lay, O. P., Carlstrom, J. E., & Hills, R. E. 1997, ApJ, 489, 917

Lebreton, J., Beichman, C., Bryden, G., Defrère, D., Mennesson, B., Millan-Gabet, R., & Boccaletti, A. 2016, ApJ, 817, 165

Lebreton, J., et al. 2012, A&A, 539, A17

Lestrade, J.-F., & Thilliez, E. 2015, ArXiv e-prints

Leto, G., Pagano, I., Linsky, J. L., Rodonò, M., & Umana, G. 2000, A&A, 359, 1035

Levison, H. F., & Duncan, M. J. 1997, Icarus, 127, 13

Lindegren, L., et al. 2016, ArXiv e-prints

Liseau, R., De la Luz, V., O'Gorman, E., Bertone, E., Chavez, M., & Tapia, F. 2016, A&A, 594, A109

Liseau, R., et al. 2008, A&A, 480, L47

—. 2010, A&A, 518, L132

—. 2013, A&A, 549, L7

—. 2015, A&A, 573, L4

Lisse, C. M., Chen, C. H., Wyatt, M. C., Morlok, A., Song, I., Bryden, G., & Sheehan, P. 2009, ApJ, 701, 2019

Lisse, C. M., et al. 2012, ApJ, 747, 93

Liu, M. C. 2004, Science, 305, 1442

Liu, M. C., Matthews, B. C., Williams, J. P., & Kalas, P. G. 2004, ApJ, 608, 526

Löhne, T., et al. 2012, A&A, 537, A110

Luhman, K. L., et al. 2006, ApJ, 649, 894

Lynden-Bell, D., & Pringle, J. E. 1974, MNRAS, 168, 603

Lyra, W., & Kuchner, M. 2013, Nature, 499, 184

MacGregor, M. A., Lawler, S. M., Wilner, D. J., Matthews, B. C., Kennedy, G. M., Booth, M., & Di Francesco, J. 2016a, ApJ, 828, 113

MacGregor, M. A., Wilner, D. J., Andrews, S. M., & Hughes, A. M. 2015a, ApJ, 801, 59

MacGregor, M. A., Wilner, D. J., Andrews, S. M., Lestrade, J.-F., & Maddison, S. 2015b, ApJ, 809, 47

MacGregor, M. A., et al. 2013, ApJ, 762, L21

—. 2016b, ApJ, 823, 79

Maehara, H., Shibayama, T., Notsu, Y., Notsu, S., Honda, S., Nogami, D., & Shibata, K. 2015, Earth, Planets, and Space, 67, 59

Malhotra, R. 1993, Icarus, 106, 264

—. 1995, AJ, 110, 420

Mallik, S. V., Parthasarathy, M., & Pati, A. K. 2003, A&A, 409, 251

Malo, L., Doyon, R., Lafrenière, D., Artigau, É., Gagné, J., Baron, F., & Riedel, A. 2013, ApJ, 762, 88

Mamajek, E. E. 2008, Astronomische Nachrichten, 329, 10

Mamajek, E. E. 2009, in American Institute of Physics Conference Series, Vol. 1158, American Institute of Physics Conference Series, ed. T. Usuda, M. Tamura, & M. Ishii, 3–10

—. 2012, ApJ, 754, L20

Mamajek, E. E., & Bell, C. P. M. 2014, MNRAS, 445, 2169

Mamajek, E. E., & Hillenbrand, L. A. 2008, ApJ, 687, 1264

Mamajek, E. E., Quillen, A. C., Pecaut, M. J., Moolekamp, F., Scott, E. L., Kenworthy, M. A., Collier Cameron, A., & Parley, N. R. 2012, AJ, 143, 72

Maness, H. L., Fitzgerald, M. P., Paladini, R., Kalas, P., Duchene, G., & Graham, J. R. 2008, ApJ, 686, L25

Maness, H. L., et al. 2009, ApJ, 707, 1098

Marino, S., et al. 2016, MNRAS, 460, 2933

—. 2017, MNRAS, 465, 2595

Marois, C., Macintosh, B., & Barman, T. 2007, ApJ, 654, L151

Marois, C., Macintosh, B., Barman, T., Zuckerman, B., Song, I., Patience, J., Lafrenière, D., & Doyon, R. 2008, Science, 322, 1348

Marois, C., Zuckerman, B., Konopacky, Q. M., Macintosh, B., & Barman, T. 2010, Nature, 468, 1080

Marsh, K. A., Velusamy, T., Dowell, C. D., Grogan, K., & Beichman, C. A. 2005, ApJ, 620, L47

Marshall, J. P., et al. 2011, A&A, 529, A117

Martin, R. G., & Lubow, S. H. 2011, MNRAS, 413, 1447

Marzari, F., & Thébault, P. 2011, MNRAS, 416, 1890

Matthews, B. C., Krivov, A. V., Wyatt, M. C., Bryden, G., & Eiroa, C. 2014, ArXiv e-prints

Matthews, B. C., et al. 2015, ApJ, 811, 100

Mayor, M., et al. 2003, The Messenger, 114, 20

—. 2011, ArXiv e-prints

Mazoyer, J., Boccaletti, A., Augereau, J.-C., Lagrange, A.-M., Galicher, R., & Baudoz, P. 2014, ArXiv e-prints

McKee, C. F., & Ostriker, E. C. 2007, ARA&A, 45, 565

Meshkat, T., et al. 2013, ApJ, 775, L40

Metchev, S. A., Eisner, J. A., Hillenbrand, L. A., & Wolf, S. 2005, ApJ, 622, 451

Middelberg, E., Sault, R. J., & Kesteven, M. J. 2006, Publications of the Astronomical Society of Australia, 23, 147

Miotello, A., van Dishoeck, E. F., Kama, M., & Bruderer, S. 2016, ArXiv e-prints

Mitra-Kraev, U., et al. 2005, A&A, 431, 679

Mittal, T., Chen, C. H., Jang-Condell, H., Manoj, P., Sargent, B. A., Watson, D. M., & Lisse, C. M. 2015, ApJ, 798, 87

Moór, A., Ábrahám, P., Derekas, A., Kiss, C., Kiss, L. L., Apai, D., Grady, C., & Henning, T. 2006, ApJ, 644, 525

Moór, A., Kóspál, Á., Ábrahám, P., Balog, Z., Csengeri, T., Henning, T., Juhász, A., & Kiss, C. 2016, ApJ, 826, 123

Moór, A., et al. 2011, ApJS, 193, 4

Morales, F. Y., Bryden, G., Werner, M. W., & Stapelfeldt, K. R. 2013, ApJ, 776, 111

Morales, F. Y., Rieke, G. H., Werner, M. W., Bryden, G., Stapelfeldt, K. R., & Su, K. Y. L. 2011, ApJ, 730, L29

Morbidelli, A., Levison, H. F., & Gomes, R. 2008, The Dynamical Structure of the Kuiper Belt and Its Primordial Origin, ed. M. A. Barucci, H. Boehnhardt, D. P. Cruikshank, A. Morbidelli, & R. Dotson, 275–292

Morbidelli, A., Levison, H. F., Tsiganis, K., & Gomes, R. 2005, Nature, 435, 462

Morita, K.-I. 1994, in Astronomical Society of the Pacific Conference Series, Vol. 59, IAU Colloq. 140: Astronomy with Millimeter and Submillimeter Wave Interferometry, ed. M. Ishiguro & J. Welch, 18–26

Moro-Martín, A., & Malhotra, R. 2003, AJ, 125, 2255

Mouillet, D., Lagrange, A. M., Augereau, J. C., & Ménard, F. 2001, A&A, 372, L61

Mouillet, D., Larwood, J. D., Papaloizou, J. C. B., & Lagrange, A. M. 1997, MNRAS, 292, 896

Mugrauer, M., & Neuhäuser, R. 2005, Astronomische Nachrichten, 326, 701

Mundy, L. G., et al. 1996, ApJ, 464, L169

Murray, C. D., & Dermott, S. F. 1999, Solar system dynamics

Mustill, A. J., & Wyatt, M. C. 2009, MNRAS, 399, 1403

Najita, J., & Williams, J. P. 2005, ApJ, 635, 625

Napier, P. J., Thompson, A. R., & Ekers, R. D. 1983, IEEE Proceedings, 71, 1295

Nesvold, E. R., Kuchner, M. J., Rein, H., & Pan, M. 2013, ApJ, 777, 144

Nesvorný, D., Bottke, W. F., Levison, H. F., & Dones, L. 2003, ApJ, 591, 486

Nesvorný, D., Jenniskens, P., Levison, H. F., Bottke, W. F., Vokrouhlický, D., & Gounelle, M. 2010, ApJ, 713, 816

Neuhäuser, R., Guenther, E. W., Wuchterl, G., Mugrauer, M., Bedalov, A., & Hauschildt, P. H. 2005, A&A, 435, L13

Neuhäuser, R., Mugrauer, M., Seifahrt, A., Schmidt, T. O. B., & Vogt, N. 2008, A&A, 484, 281

Nilsson, R., et al. 2010, A&A, 518, A40

Nordström, B., et al. 2004, A&A, 418, 989

Nuernberger, D., Chini, R., & Zinnecker, H. 1997, A&A, 324, 1036

O'Brien, D. P., Morbidelli, A., & Bottke, W. F. 2007, Icarus, 191, 434

Offner, S. S. R., Kratter, K. M., Matzner, C. D., Krumholz, M. R., & Klein, R. I. 2010, ApJ, 725, 1485

Ono, Y., Ouchi, M., Kurono, Y., & Momose, R. 2014, ApJ, 795, 5

Osman, K. T., Matthaeus, W. H., Greco, A., & Servidio, S. 2011, ApJ, 727, L11

Pan, M., Nesvold, E. R., & Kuchner, M. J. 2016, ApJ, 832, 81

Pan, M., & Sari, R. 2005, Icarus, 173, 342

Pan, M., & Schlichting, H. E. 2012, ApJ, 747, 113

Panić, O., et al. 2013, MNRAS, 435, 1037

Pavlenko, Y. V., Jenkins, J. S., Jones, H. R. A., Ivanyuk, O., & Pinfield, D. J. 2012, MNRAS, 422, 542

Pawellek, N., & Krivov, A. V. 2015, MNRAS, 454, 3207

Pawellek, N., Krivov, A. V., Marshall, J. P., Montesinos, B., Ábrahám, P., Moór, A., Bryden, G., & Eiroa, C. 2014, ApJ, 792, 65

Pearce, T. D., & Wyatt, M. C. 2014, MNRAS, 443, 2541

Pearce, T. D., Wyatt, M. C., & Kennedy, G. M. 2015, MNRAS, 448, 3679

Pecaut, M. J., & Mamajek, E. E. 2013, ApJS, 208, 9

Pecaut, M. J., Mamajek, E. E., & Bubar, E. J. 2012, ApJ, 746, 154

Pepe, F., et al. 2011, A&A, 534, A58

Perley, R. A., Chandler, C. J., Butler, B. J., & Wrobel, J. M. 2011, ApJ, 739, L1

Phillips, T. G., & Woody, D. P. 1982, ARA&A, 20, 285

Piétu, V., di Folco, E., Guilloteau, S., Gueth, F., & Cox, P. 2011, A&A, 531, L2

Plavchan, P., Jura, M., & Lipscy, S. J. 2005, ApJ, 631, 1161

Pollack, J. B., Hubickyj, O., Bodenheimer, P., Lissauer, J. J., Podolak, M., & Greenzweig, Y. 1996, Icarus, 124, 62

Pontoppidan, K. M., Blake, G. A., & Smette, A. 2011, ApJ, 733, 84

Primiani, R. A., et al. 2016, Journal of Astronomical Instrumentation, 5, 1641006

Quillen, A. C. 2006, MNRAS, 372, L14

Redfield, S. 2007, ApJ, 656, L97

Reid, M. J., Schneps, M. H., Moran, J. M., Gwinn, C. R., Genzel, R., Downes, D., & Roennaeng, B. 1988, ApJ, 330, 809

Reidemeister, M., Krivov, A. V., Schmidt, T. O. B., Fiedler, S., Müller, S., Löhne, T., & Neuhäuser, R. 2009, A&A, 503, 247

Reidemeister, M., Krivov, A. V., Stark, C. C., Augereau, J.-C., Löhne, T., & Müller, S. 2011, A&A, 527, A57

Ricarte, A., Moldvai, N., Hughes, A. M., Duchêne, G., Williams, J. P., Andrews, S. M., & Wilner, D. J. 2013, ApJ, 774, 80

Ricci, L., Carpenter, J. M., Fu, B., Hughes, A. M., Corder, S., & Isella, A. 2015a, ApJ, 798, 124

Ricci, L., Maddison, S. T., Wilner, D., MacGregor, M. A., Ubach, C., Carpenter, J. M., & Testi, L. 2015b, ApJ, 813, 138

Ricci, L., Testi, L., Maddison, S. T., & Wilner, D. J. 2012, A&A, 539, L6

Ricci, L., Testi, L., Natta, A., & Brooks, K. J. 2010a, A&A, 521, A66

Ricci, L., Testi, L., Natta, A., Neri, R., Cabrit, S., & Herczeg, G. J. 2010b, A&A, 512, A15

Ricci, L., Testi, L., Natta, A., Scholz, A., de Gregorio-Monsalvo, I., & Isella, A. 2014, ApJ, 791, 20

Roberge, A., et al. 2013, ApJ, 771, 69

Robinson, R. D., Linsky, J. L., Woodgate, B. E., & Timothy, J. G. 2001, ApJ, 554, 368

Roccatagliata, V., Henning, T., Wolf, S., Rodmann, J., Corder, S., Carpenter, J. M., Meyer, M. R., & Dowell, D. 2009, A&A, 497, 409

Rodigas, T. J., et al. 2012, ApJ, 752, 57

Rodriguez, D. R., van der Plas, G., Kastner, J. H., Schneider, A. C., Faherty, J. K., Mardones, D., Mohanty, S., & Principe, D. 2015, A&A, 582, L5

Rosenfeld, K. A., Andrews, S. M., Hughes, A. M., Wilner, D. J., & Qi, C. 2013, ApJ, 774, 16

Rosenfeld, K. A., Andrews, S. M., Wilner, D. J., & Stempels, H. C. 2012, ApJ, 759, 119

Ryle, M. 1962, Nature, 194, 517

Ryle, M., Elsmore, B., & Neville, A. C. 1965, Nature, 207, 1024

Ryle, M., & Vonberg, D. D. 1946, Nature, 158, 339

Scherer, K. 2000, J. Geophys. Res., 105, 10329

Schmidt, T. O. B., Neuhäuser, R., Seifahrt, A., Vogt, N., Bedalov, A., Helling, C., Witte, S., & Hauschildt, P. H. 2008, A&A, 491, 311

Schneider, G., Weinberger, A. J., Becklin, E. E., Debes, J. H., & Smith, B. A. 2009, AJ, 137, 53

Schneider, G., et al. 2006, ApJ, 650, 414

—. 2014, ArXiv e-prints

Schneider, P. C., & Schmitt, J. H. M. M. 2010, A&A, 516, A8

Schüppler, C., Krivov, A. V., Löhne, T., Booth, M., Kirchschlager, F., & Wolf, S. 2016, MNRAS, 461, 2146

Schüppler, C., Löhne, T., Krivov, A. V., Ertel, S., Marshall, J. P., & Eiroa, C. 2014, A&A, 567, A127

Schüppler, C., et al. 2015, A&A, 581, A97

Schütz, O., Nielbock, M., Wolf, S., Henning, T., & Els, S. 2004, A&A, 414, L9

Schwarz, H., Ginski, C., de Kok, R. J., Snellen, I. A. G., Brogi, M., & Birkby, J. L. 2016, ArXiv e-prints

Seifahrt, A., Neuhäuser, R., & Hauschildt, P. H. 2007, A&A, 463, 309

Seperuelo Duarte, E., Alencar, S. H. P., Batalha, C., & Lopes, D. 2008, A&A, 489, 349

Sheret, I., Dent, W. R. F., & Wyatt, M. C. 2004, MNRAS, 348, 1282

Silverstone, M. D. 2000, PhD thesis, UNIVERSITY OF CALIFORNIA, LOS ANGELES

Smith, K., Güdel, M., & Audard, M. 2005, A&A, 436, 241

Smith, R., Wyatt, M. C., & Haniff, C. A. 2009, A&A, 503, 265

Snellen, I. A. G., Brandl, B. R., de Kok, R. J., Brogi, M., Birkby, J., & Schwarz, H. 2014, Nature, 509, 63

Sousa, S. G., Fernandes, J., Israelian, G., & Santos, N. C. 2010, A&A, 512, L5

Spiegel, D. S., & Burrows, A. 2012, ApJ, 745, 174

Stamatellos, D., & Herczeg, G. J. 2015, MNRAS, 449, 3432

Stapelfeldt, K., Krist, J., Bryden, G., & Chen, C. 2007, in In the Spirit of Bernard Lyot: The Direct Detection of Planets and Circumstellar Disks in the 21st Century

Stapelfeldt, K. R., Bryden, G., Eiroa, C., & Herschel/DUNES Key Project Team. 2012, in American Astronomical Society Meeting Abstracts, Vol. 219, American Astronomical Society Meeting Abstracts #219, 344.13

Stapelfeldt, K. R., et al. 2004, ApJS, 154, 458

Stark, C. C., & Kuchner, M. J. 2009, ApJ, 707, 543

Stark, C. C., Schneider, G., Weinberger, A. J., Debes, J. H., Grady, C. A., Jang-Condell, H., & Kuchner, M. J. 2014, ApJ, 789, 58

Steele, A., Hughes, A. M., Carpenter, J., Ricarte, A., Andrews, S. M., Wilner, D. J., & Chiang, E. 2016, ApJ, 816, 27

Stern, S. A. 1996, AJ, 112, 1203

Strom, K. M., Strom, S. E., Edwards, S., Cabrit, S., & Skrutskie, M. F. 1989, AJ, 97, 1451

Strubbe, L. E., & Chiang, E. I. 2006, ApJ, 648, 652

Su, K. Y. L., Morrison, S., Malhotra, R., Smith, P. S., Balog, Z., & Rieke, G. H. 2015, ApJ, 799, 146

Su, K. Y. L., Rieke, G. H., Defrére, D., Wang, K.-S., Lai, S.-P., Wilner, D. J., van Lieshout, R., & Lee, C.-F. 2016, ApJ, 818, 45

Su, K. Y. L., et al. 2005, ApJ, 628, 487

—. 2006, ApJ, 653, 675

—. 2009, ApJ, 705, 314

—. 2013, ApJ, 763, 118

Szulágyi, J., Masset, F., Lega, E., Crida, A., Morbidelli, A., & Guillot, T. 2016, MNRAS, 460, 2853

Tachihara, K., Dobashi, K., Mizuno, A., Ogawa, H., & Fukui, Y. 1996, PASJ, 48, 489

Takeda, Y., Kawanomoto, S., Honda, S., Ando, H., & Sakurai, T. 2007, A&A, 468, 663

Tamayo, D. 2014, MNRAS, 438, 3577

Tanner, A., Beichman, C., Bryden, G., Lisse, C., & Lawler, S. 2009, ApJ, 704, 109

Testi, L., Natta, A., Scholz, A., Tazzari, M., Ricci, L., & de Gregorio Monsalvo, I. 2016, ArXiv e-prints

Thébault, P. 2012, A&A, 537, A65

Thébault, P., & Augereau, J.-C. 2005, A&A, 437, 141

—. 2007, A&A, 472, 169

Thébault, P., Augereau, J. C., & Beust, H. 2003, A&A, 408, 775

Thébault, P., & Wu, Y. 2008, A&A, 481, 713

Thi, W. F., et al. 2001, Nature, 409, 60

Thi, W.-F., et al. 2014, A&A, 561, A50

Thompson, A. R., Clark, B. G., Wade, C. M., & Napier, P. J. 1980, ApJS, 44, 151

Thureau, N. D., et al. 2014, MNRAS, 445, 2558

Torres, C. A. O., Quast, G. R., Melo, C. H. F., & Sterzik, M. F. 2008, Young Nearby Loose Associations, ed. B. Reipurth, 757

Torres, R. M., Loinard, L., Mioduszewski, A. J., Boden, A. F., Franco-Hernández, R., Vlemmings, W. H. T., & Rodríguez, L. F. 2012, ApJ, 747, 18

Trilling, D. E., et al. 2008, ApJ, 674, 1086

Trujillo, C. A., & Brown, M. E. 2001, ApJ, 554, L95

Tsiganis, K., Gomes, R., Morbidelli, A., & Levison, H. F. 2005, Nature, 435, 459

Tuomi, M., et al. 2013, A&A, 551, A79

Vallado, D. A. 2007, Fundamentals of Astrodynamics and Applications

van der Plas, G., et al. 2016, ApJ, 819, 102

van Kempen, T. A., van Dishoeck, E. F., Brinch, C., & Hogerheijde, M. R. 2007, A&A, 461, 983

van Leeuwen, F. 2007, A&A, 474, 653

Velli, M., Pucci, F., Rappazzo, F., & Tenerani, A. 2015, Philosophical Transactions of the Royal Society of London Series A, 373, 40262

Vican, L. 2012, AJ, 143, 135

Villadsen, J., Hallinan, G., Bourke, S., Güdel, M., & Rupen, M. 2014, ApJ, 788, 112

Vitense, C., Krivov, A. V., Kobayashi, H., & Löhne, T. 2012, A&A, 540, A30

Vogt, S. S., et al. 1994, in Proc. SPIE, Vol. 2198, Instrumentation in Astronomy VIII, ed. D. L. Crawford & E. R. Craine, 362

Vogt, S. S., et al. 2010, ApJ, 708, 1366

Vorobyov, E. I., & Basu, S. 2010, ApJ, 714, L133

Wahhaj, Z., Koerner, D. W., & Sargent, A. I. 2007, ApJ, 661, 368

Ward-Thompson, D., et al. 2010, A&A, 518, L92

Weinberger, A. J., Becklin, E. E., Song, I., & Zuckerman, B. 2011, ApJ, 726, 72

Weinberger, A. J., Becklin, E. E., & Zuckerman, B. 2003, ApJ, 584, L33

Weinberger, A. J., Rich, R. M., Becklin, E. E., Zuckerman, B., & Matthews, K. 2000, ApJ, 544, 937

Weingartner, J. C., & Draine, B. T. 2001, ApJ, 548, 296

White, J. A., Boley, A. C., Dent, W. R. F., Ford, E. B., & Corder, S. 2016a, ArXiv e-prints

White, J. A., Boley, A. C., Hughes, A. M., Flaherty, K. M., Ford, E., Wilner, D., Corder, S., & Payne, M. 2016b, ApJ, 829, 6

White, S. M., Lim, J., & Kundu, M. R. 1994, ApJ, 422, 293

Wichmann, R., Schmitt, J. H. M. M., & Hubrig, S. 2003, A&A, 399, 983

Williams, J. P., & Andrews, S. M. 2006, ApJ, 653, 1480

Williams, J. P., & Best, W. M. J. 2014, ApJ, 788, 59

Williams, J. P., Blitz, L., & McKee, C. F. 2000, Protostars and Planets IV, 97

Williams, J. P., & Cieza, L. A. 2011, ARA&A, 49, 67

Wilner, D. J., Andrews, S. M., & Hughes, A. M. 2011, ApJ, 727, L42

Wilner, D. J., Andrews, S. M., MacGregor, M. A., & Hughes, A. M. 2012, ApJ, 749, L27

Wilson, R. W., Jefferts, K. B., & Penzias, A. A. 1970, ApJ, 161, L43

Wilson, W. E., et al. 2011, MNRAS, 416, 832

Wootten, A. 2003, in Proc. SPIE, Vol. 4837, Large Ground-based Telescopes, ed. J. M. Oschmann & L. M. Stepp, 110–118

Wright, E. L., et al. 2010, AJ, 140, 1868

Wright, N. J., Drake, J. J., Mamajek, E. E., & Henry, G. W. 2011, ApJ, 743, 48

Wu, Y.-L., et al. 2017, ApJ, 836, 223

Wyatt, M. C. 2003, ApJ, 598, 1321

—. 2006, ApJ, 639, 1153

—. 2008, ARA&A, 46, 339

Wyatt, M. C., Clarke, C. J., & Booth, M. 2011, Celestial Mechanics and Dynamical Astronomy, 111, 1

Wyatt, M. C., Dermott, S. F., Telesco, C. M., Fisher, R. S., Grogan, K., Holmes, E. K., & Piña, R. K. 1999, ApJ, 527, 918

Wyatt, M. C., et al. 2012, MNRAS, 424, 1206

Zhou, Y., Herczeg, G. J., Kraus, A. L., Metchev, S., & Cruz, K. L. 2014, ApJ, 783, L17

Zuckerman, B. 2001, ARA&A, 39, 549

Zuckerman, B., Forveille, T., & Kastner, J. H. 1995, Nature, 373, 494